

***Bentonite erosion and colloid mediated
transport of radionuclides in advection
controlled systems***

Approved version

***A Dissertation submitted to the “Fakultät für Chemie und
Biowissenschaften des Karlsruher Instituts für Technologie (KIT)”
for the Degree of Doctor of Science (Dr. rer. Nat.)***

presented by

Dipl.-Chem. Franz R. Rinderknecht

Evaluators:

Prof. Dr. Horst Geckeis

Prof. Dr. Thorsten Schäfer

Day of Disputation:

16. 10. 2017



This document is licensed under a Creative Commons
Attribution-ShareAlike 4.0 International License (CC BY-SA 4.0):
<https://creativecommons.org/licenses/by-sa/4.0/deed.en>

Erklärung/Declaration of Originality

Hiermit versichere ich, dass ich die vorliegende Arbeit mit dem Titel “Bentonite erosion and colloid mediated transport of radionuclides in advection controlled systems” selbständig verfasst und keine anderen als die angegebenen Quellen und Hilfsmittel verwendet habe. Darüber hinaus versichere ich, dass alle Stellen der Arbeit, die wörtlich oder sinngemäß aus anderen Quellen übernommen wurden, als solche kenntlich gemacht sind und dass die Arbeit in gleicher oder ähnlicher Form noch keiner Prüfungsbehörde vorgelegt wurde.

“To raise new questions, new possibilities, to regard old problems from a new angle, requires creative imagination and marks real advance in science.”

(Albert Einstein)

Acknowledgements

This PhD work was performed at the Institute for Nuclear Waste Disposal (INE) of the Karlsruhe Institute of Technology (KIT). It would not have been possible without the support of a lot of people. I would like to thank,

- Prof. Dr. Horst Geckeis for the opportunity to do my PhD at his Institute. I have gathered a lot of valuable experience working with several advanced scientific methods and technologies.
- My supervisor Prof. Dr. Thorsten Schäfer, for all his guidance, support, help, patience and constant motivation. I am honored to be supervised by him during my PhD work.
- Dr. Florian Huber, for his scientific advices, for the time which he was always able to find for my questions and discussions, for his practical support in the lab and during field trips at the Grimsel test site.
- Stephanie Heck, the good spirit of the geochemistry group, for her support in the organization of experiments, for spending hours with me in front of the glove box supporting the sampling of my experiments and for taking over the work on the long-term experiments in the busy time of writing this PhD.
- The INE analytical team, especially Cornelia Walschburger, Frank Geyer and Markus Fuß for dozens of measurements.
- The LIBD group, especially Robert Götz for teaching me the fundamentals of laser induced breakdown detection and his help and advice during numerous measuring periods at INE and during the field trips as well as his profound knowledge on handling colloid suspensions. Enjoy your well-deserved retirement!
- The INE workshop team for all technical advices and ideas.
- The field team at the Grimsel test site for advice and support during the on-site measurement campaigns.
- My colleagues in the room 108, Dipl. Geol. Madeleine Stoll, Dipl. Ing. Hector Sauri Suarez, Dipl. Chem. Felix Rieder, Dr. Andreas Schnurr and the remaining PhD students at INE for all the discussions, help and last but not least, for your friendship.
- The “BELBaR” project and the BMWI/PTKA project “Kollorado-e” are gratefully acknowledged for financial support.
- My sister, Miriam Rinderknecht, for her patience and understanding during the stressful time of writing and for simply everything.
- Dr. Alexander Krieger and Dipl. Ing. Gernot Perner for being such good friends in all the years.
- Last but not least, my family and some other not explicitly mentioned good friends and people.

Abstract

The issue of safe disposal of high level radioactive waste in a deep underground repository for $\sim 10^6$ years demands in-depth understanding of processes that may on the one hand lead to transport of contaminants away from the repository and on the other hand those processes which retain matter in the near-field. Investigations on the interaction of different transport and retention processes under repository relevant conditions are crucial in order to ensure safe storage of the high level radioactive waste for a reasonable time and to estimate the risk of a release of contaminants into the biosphere. Transport processes in crystalline rock are mainly governed by transport in advective flow fields that can be further divided in transport of solutes and colloid facilitated transport. Diffusion processes are also of importance in advective controlled systems as pollutants can be transported away from the main flow region and are as consequence effectively retained in the rock matrix. Diffusion processes furthermore dominate the transport within the bentonite buffer/backfill and gain importance if clay stone is chosen as host rock formation. Radionuclides can be retained by a multitude of processes, e.g. sorption, reduction, (co-)precipitation and matrix diffusion. These processes, often kinetically controlled, may lead to effective immobilization of radionuclides in the far-field of the repository.

Within the present study, batch radionuclide sorption reversibility experiments on natural fault gouge (FG) material under repository relevant glacial melt water conditions have been performed with the aim to quantify kinetic data of the radionuclide sorption and desorption. Therefore, aqueous solutions containing either ^{99}Tc , ^{237}Np , ^{242}Pu or ^{243}Am as single nuclide samples as well as radionuclide cocktail samples, containing in addition ^{233}U beside the before mentioned radionuclides have been prepared. FG material from the Grimsel test site has been added to investigate the desorption process after 1 day sorption up to 232 days sorption in the binary system FG – glacial melt water. Once in equilibrium, montmorillonite colloids have been added to investigate the impact of a competing colloidal surface on sorption reversibility. Distribution coefficients as well as reversibly bound radionuclide fractions and sorption/desorption rates in the binary and the ternary system have been determined. These data are supposed to provide missing information urgently needed for modeling experimental data obtained in long-term radionuclide migration studies. Notably the pronounced tailings of radionuclide colloid tracer test break through

curves, performed at the Grimsel test site, namely CFM Run 12-02 and Run 13-05 point to strong kinetic impact on sorption/desorption processes.

Natural bentonite samples without purification are taken to investigate bentonite integrity under repository relevant conditions at low flow velocities of natural Grimsel groundwater, comparable to realistic in-situ conditions. The currently ongoing long-term in-situ- test (LIT), performed within the frame of the Colloid Formation and Migration project (CFM) at the Grimsel Test Site (GTS) is described as well as supporting laboratory experiments in artificial horizontal fracture cells. Field and laboratory experiments are performed under similar conditions. Differences mainly relate to the geometry of the fracture and its composition. Beside bentonite erosion, several additional processes have to be considered due to the complexity within the system consisting of natural bentonite sample and natural glacial melt water. Dissolution of accessory mineral phases modifies the groundwater chemistry and increases the ionic strength of the contact water, which reduces colloid stability. Furthermore, natural Febex bentonite shows a Mg-Ca-Na-K dominated interlayer which is not in equilibrium with the glacial melt water and cation exchange processes are observed during all experiments.

The present work describes two bentonite erosion tests in 1 mm artificial fracture set-ups that have been performed to support the long-term in-situ test (LIT) located at the Grimsel test site. The sample geometry is therefore comparable to the LIT setup but the total sample mass is lower. A low flow velocity of $\sim 10^{-5}$ m/s was established in the artificial fracture cell. A first experiment used a compacted, natural Febex bentonite, spiked with a conservative tracer. The experiment was set-up for characterization of the erosion process and for sampling of the eroded material. A second experiment was conducted for direct comparison to LIT. Thereby the compacted bentonite sample had exactly the same composition as the sample within LIT, which is a mixture of 90% natural Febex bentonite and 10% synthetic Zn-labeled montmorillonite. A conservative tracer (Amino-G) and different radionuclides, namely $^{45}\text{Ca(II)}$, $^{75}\text{Se(IV)}$, $^{99}\text{Tc(VII)}$, $^{137}\text{Cs(I)}$, $^{233}\text{U(VI)}$, $^{237}\text{Np(V)}$, $^{241}\text{Am(III)}$ and $^{242}\text{Pu(IV)}$ were embedded within the bentonite source. The synthetic montmorillonite was selected as a tracer in order to distinguish bentonite derived colloids from natural groundwater colloids.

The erosion experiments in the artificial fracture cell can be divided into 4 phases, namely (I) outwashing of readily soluble bentonite components, (II) crystalline swelling, (III) dissolution of

accessory mineral phases and finally (IV) osmotic swelling and bentonite erosion. Colloid formation is initially suppressed due to the higher ionic strength generated from the dissolution of salt and accessory mineral phases and mixing with the bentonite pore water. Colloid concentrations increase during the subsequent erosion phase. The average bentonite erosion rate has been determined to $91 \pm 30 \text{ g}/(\text{m}^2 \cdot \text{a})$. In terms of the embedded radionuclides, only ^{99}Tc , ^{233}U and ^{237}Np have been found in the effluent and the recovery was calculated to $108 \pm 11\%$, $0.8 \pm 0.1\%$ and $1.3 \pm 0.2\%$ respectively. In case of ^{99}Tc , supporting investigations showed that the recovery is overdetermined by ICP-MS because isobaric interferences have to be taken into account. None of the strongly sorbing radionuclides (^{137}Cs , ^{241}Am and ^{242}Pu), which would indicate colloid mediated transport have been found in the effluent.

The idea behind the LIT experiment is the investigation and quantification of in-situ bentonite colloid generation and concomitant radionuclide mobilization within a well-defined and controlled shear zone, dominated by an advective flow field. A suitable site for LIT was found in the MI shear zone at the Grimsel test site. Therefore a compacted bentonite sample (Febex and Febex/Zn-Mnt-(90%/10%)-mixture) which holds a conservative tracer as well as the radionuclides, mentioned above, was placed in a water conducting shear zone and the contact water was monitored in the near-field (<10 cm distance) as well as in the far-field (~6 m distance) from the sample location. The evolution of the groundwater around the bentonite source is monitored on-site and by laboratory analyses. Most changes are found during the initial saturation phase during the first 6 months of the experiment. Constant pH, E_{HSHE} and swelling pressure values were obtained in the following. Laboratory analysis included geochemical, chemical and radiochemical investigations and colloid size distribution and concentration examination. Results obtained in the laboratory were in good agreement with the online measured data. Colloid concentrations are in average 20-40 ppb (LIBD and ICP-MS after) and surprisingly low. From the introduced radionuclides only ^{99}Tc could be found in the samples by SF-ICP-MS. AMS measurements of these samples showed that isobaric interferences cannot be neglected in the Grimsel system and that significantly less ^{99}Tc was released from the bentonite source than indicated by SF-ICP-MS.

Zusammenfassung

Das Problem der sicheren Endlagerung von hochradioaktivem Abfall in einem Endlager in tiefen geologischen Formationen für einen Zeitraum von $\sim 10^6$ Jahren erfordert ein tiefgehendes Verständnis der Prozesse, die einerseits zum Stofftransport und andererseits zur Rückhaltung von Radionukliden im Nahfeld des Endlagers führen können. Untersuchungen zum Zusammenspiel verschiedener Transport- und Rückhalteprozesse unter endlagerrelevanten Bedingungen, sind essentiell, um die sichere Lagerung von hochradioaktivem Abfall über eine sinnvolle Zeitspanne zu garantieren und um das Risiko einer Freisetzung der Schadstoffe in die Biosphäre abzuschätzen. Transportprozesse im kristallinen Gestein sind vor allem durch den Transport im advektiven Strömungsfeld bestimmt, der noch weiter in den Transport von gelösten Teilchen und den kolloidgetragenen Transport aufgeteilt werden kann. Diffusionsprozesse stellen einen weiteren wichtigen Transportprozess dar und sind im kristallinen Gestein vor allem durch die Diffusion von Stoffen aus advektiv kontrollierten Bereichen in die Gesteinsmatrix von Bedeutung. Dadurch reduzieren sie die Mobilität von Schadstoffen. Diffusionsprozesse dominieren zudem den Stofftransport im Bentonit, der als geotechnische Barriere und zur Streckenverfüllung vorgesehen ist. Diffusionsprozesse können des Weiteren nicht vernachlässigt werden, wenn die Wahl des Wirtsgesteins auf Tonsteinformationen fällt. Eine Vielzahl an weiteren Prozessen kann den Transport von Radionukliden verhindern und diese effektiv im Nahfeld eines Endlagers halten. Dazu gehören beispielsweise Sorptionsprozesse, (Mit-)Fällungsreaktionen aus übersättigten Lösungen und der Prozess der Matrixdiffusion. Diese Prozesse sind oftmals kinetisch kontrolliert und begrenzen die Radionuklidmobilität.

Eines der Referenzszenarien in den Sicherheitsanalysen des schwedischen Programms zur Endlagerung radioaktiver Abfälle ist das Vordringen von verdünnten, glazialen Schmelzwässern in die Tiefe des Endlagers und der Kontakt von diesem niedrig mineralisierten Wasser mit der Bentonitbarriere. Als Reaktion auf den Wassereintritt wird die Bentonitbarriere quellen und die Freisetzung von Bentonitkolloiden über die Bentonit-Wasser Grenzfläche wird möglich. Falls zu diesem Zeitpunkt ein defekter oder durchkorrodierter Behälter vorliegt und dadurch die eingelagerten Abfälle direkten Kontakt zur Bentonitbarriere hatten, besteht die Möglichkeit, dass Radionuklide über kolloidgetragenen Transport im advektiven Fließregime den Nahbereich des Endlagers verlassen. Die vorliegende Arbeit beschreibt die relevanten Prozesse im Falle eines

Kontakts von verdünntem, glazialem Schmelzwasser mit der geotechnischen Barriere des Endlagers.

Im Zuge der vorliegenden Arbeit wurden klassische Batchexperimente zur Sorptionsreversibilität an natürlichem Kluftfüllmaterial unter endlagerrelevanten glazialen Schmelzwasserbedingungen durchgeführt. Ziel dieser Experimente war es, kinetische Daten zur Desorptionsreaktion in Abhängigkeit von der Sorptionszeit zu erhalten. Dazu wurden sowohl Einzelnuclidproben, die ^{99}Tc , ^{237}Np , ^{242}Pu oder ^{243}Am enthielten, als auch Radionuclidcocktailproben, die alle bereits aufgeführten Radionuklide und zusätzlich ^{233}U enthielten, untersucht. Als Sorbens diente Kluftfüllmaterial („fault gouge“: FG) aus einer natürlichen Scherzone im Untertagelabor Grimsel (ULG). Die Desorption der Radionuklide wurde untersucht, nachdem sie 1 Tag bis zu 232 Tagen im binären System „Kluftfüllmaterial – glaziales Schmelzwasser“ reagieren konnten. Sobald keine weitere Radionuclid-desorption im Beobachtungszeitraum festzustellen war, wurden zusätzlich Montmorillonit-Kolloide hinzugegeben, um den Einfluss einer Konkurrenzoberfläche zu untersuchen. Verteilungskoeffizienten sowie der Anteil an Radionukliden, der reversibel an FG gebunden war und kinetische Parameter zu Sorptions- und Desorptionsreaktionen im binären und im ternären System wurden ermittelt. Diese Daten werden dringend benötigt, um die experimentellen Daten, die in den in-situ Langzeitexperimenten CFM Run 12-02 und Run 13-05 im Grimsel Felslabor für den kolloidgetragenen Transport der Radionuklide ^{237}Np , ^{242}Pu und ^{243}Am gewonnen wurden, konsistent modellieren zu können.

Weitere Experimente wurden im Labor an natürlichen, nicht aufgereinigten Bentonitproben im Kontakt mit natürlichem Grundwasser aus dem Untertagelabor Grimsel unter niedrigen Fließgeschwindigkeiten, die im Bereich der Fließgeschwindigkeiten in einer gut charakterisierten Scherzone (MI Scherzone) liegen, durchgeführt, um den Prozess der Bentoniterosion unter möglichst endlagerrelevanten Bedingungen zu untersuchen. Zudem ist dadurch die Vergleichbarkeit zwischen Labor- und Feldversuchen gewährleistet. Neben dem Prozess der Bentoniterosion spielen, aufgrund der Komplexität des Systems aus natürlichem Bentonit und natürlichem Grundwasser, einige andere Prozesse eine nicht zu vernachlässigende Rolle. So erhöht die Auflösung von akzessorischen Mineralphasen die Ionenstärke des Kontaktwassers und reduziert damit die Stabilität der Kolloide. Außerdem enthält die Zwischenschicht von natürlichem Febex Bentonit Mg, Ca, Na und K und ist nicht im Gleichgewicht mit Grimsel Grundwasser. Als Folge daraus treten in allen durchgeführten Experimenten Kationenaustauschreaktionen auf.

Die vorliegende Arbeit beschreibt zwei Bentoniterosionsexperimente, die im Labormaßstab in einer künstlichen Plexiglaszelle mit einer horizontalen Kluft mit 1 mm Apertur durchgeführt wurden, um den aktuellen Langzeitversuch (LIT), der zeitgleich im URL durchgeführt wurde, zu unterstützen. Daher ist die Probengeometrie in diesen Experimenten identisch zu der im LIT Experiment, die Gesamtprobenmasse ist jedoch geringer. Eine niedrige Fließgeschwindigkeit von $\sim 10^{-5}$ m/s wurde in der künstlichen Zelle angelegt. Im ersten Experiment wurde ein kompakterer Block aus natürlichem Febex Bentonit verwendet, der zusätzlich einen konservativen Tracer enthält. Dieses Experiment diente zum einen der Charakterisierung und Quantifizierung des Erosionsprozesses und zum anderen zur Gewinnung und Untersuchung des erodierten Materials. Ein zweites Experiment wurde zum direkten Vergleich mit LIT durchgeführt. Dabei hatte die kompaktierte Bentonitprobe die exakt gleiche Zusammensetzung, wie die Probe, die für LIT verwendet wurde. Es handelt sich dabei um eine Mischung aus Febex Bentonit (90%) und synthetischem Zn-Montmorillonit (10%). Auch hier wurde ein konservativer Tracer in die Probe eingebracht. Zudem waren verschiedene Radionuklide in der Probe enthalten. Es handelte sich um ^{45}Ca , ^{75}Se , ^{99}Tc , ^{137}Cs , ^{233}U , ^{237}Np , ^{241}Am und ^{242}Pu .

Die Bentoniterosionsexperimente in der künstlichen Kluft können in 4 Phasen unterteilt werden. Zunächst sättigt die Probe auf und Verunreinigungen werden aus dem System gewaschen (I). In der zweiten Phase quillt die Probe in die künstliche Kluft (II). Es handelt sich um kristallines Quellen, das durch den Quelldruck hervorgerufen wird. Gleichzeitig werden akzessorische Mineralphasen aufgelöst (III) bevor sich schließlich durch osmotisches Quellen eine Gelschicht bildet (IV), aus der Kolloide herausgelöst werden können. Zu Beginn wurde die Kolloidproduktion aufgrund erhöhter Ionenstärke durch die Auflösung akzessorischer Mineralphasen und die Mischung mit dem höher salinaren Porenwasser des Bentonits stark verringert. Erhöhte Kolloidkonzentrationen sind detektierbar, sobald der Auflösungsprozess abklingt und dadurch die Ionenstärke sinkt. Eine mittlere Erosionsrate von 91 ± 30 g/(m²*a) wurde für Phase IV des Erosionsversuchs bestimmt. Von den enthaltenen Radionukliden wurden ^{99}Tc , ^{233}U und ^{237}Np in den Proben gefunden. Der Wiedererhalt der Radionuklide wurde der oberen Reihenfolge entsprechend mit $108 \pm 11\%$, $0.8 \pm 0.1\%$ und $1.3 \pm 0.2\%$ berechnet, wobei im Falle der Analytik von ^{99}Tc mittels HR-ICP-MS isobare Störungen die Analyseergebnisse verfälschen (siehe hierzu auch die untenstehende Beschreibung des LIT Experiments). Keines der an Tonkolloide stark sorbierenden Radionuklide (^{137}Cs , ^{241}Am und ^{242}Pu) wurde in den Proben gefunden.

Der Grundgedanke des LIT Experiments im Grimsel Felslabor ist es, das Szenario eines Grundwasserzutritts und den Kontakt mit der Bentonitbarriere in einem Endlager für hochradioaktiven Abfall unter endlagerrelevanten Bedingungen zu simulieren und den Prozess der Bentoniterosion und das Zusammenspiel mit dem Migrationsverhalten der enthaltenen Radionuklide unter in-situ Bedingungen in einer gut charakterisierten, advektiv kontrollierten Scherzone zu beobachten. Innerhalb der MI Scherzone im ULG wurde ein geeigneter Ort für das Experiment gefunden. Die Bentonitquelle besteht aus kompaktierten Bentonitblöcken (Febex und Febex/Zn-Mnt-(90%/10%)-Mischung) und enthält sowohl einen konservativen Tracer, als auch die bereits aufgeführten Radionuklide. Die Quelle wurde in eine wasserführende Schicht eingebracht und das Kontaktwasser wurde sowohl im Nahbereich ($<0,1$ m) als auch in größerer Entfernung (~ 6 m) von der Quelle aufgefangen und untersucht. Geochemische Veränderungen im Umfeld der Quelle wurden vor Ort und im Labor untersucht. Während der Sättigungsphase zu Beginn des Experiments wurden die größten Veränderungen bezüglich pH, E_{SHE} und Quelldruck beobachtet. Diese Werte erreichten nach spätestens 6 Monaten einen stabilen Zustand und deuten auf das Erreichen eines geochemischen Gleichgewichts hin. Die nachfolgenden Analysen im Labor umfassten, neben Daten zur geochemischen Entwicklung, chemische und radiochemische Analysen der Proben sowie die Bestimmung von Kolloidkonzentrationen, mittleren Kolloidgrößen und Kolloidgrößenverteilungen. Die Ergebnisse der Laboranalysen sind im Einklang mit den vor Ort aufgenommenen Werten. Die im Nahfeld des Bentonitblocks gefundenen Kolloidkonzentrationen sind mit mittleren Werten zwischen 20 und 40 ppb (LIBD und ICP-MS) gering. Im Zuge der Radionuklidanalysen wurde in den Proben lediglich ^{99}Tc (SF-ICP-MS) detektiert. Bei Untersuchungen der gleichen Proben mit AMS wurde eine deutlich geringere ^{99}Tc -Konzentration gemessen, was darauf hinweist, dass im Grimselsystem isobare Interferenzen durch ^{99}Ru und durch Mo-Isotope mit benachbarten Massen (98 und 100) nicht ausgeschlossen werden können.

Table of Contents

| | | |
|---------|---|----|
| 1 | General Introduction | 1 |
| 2 | Theoretical background..... | 5 |
| 2.1 | Bentonite swelling and erosion..... | 5 |
| 2.2 | Retention of radionuclides at the solid-water interface..... | 13 |
| 2.2.1 | Reversible processes – Sorption/Desorption | 13 |
| 2.2.2 | Redox reactions..... | 17 |
| 2.2.3 | Matrix diffusion | 18 |
| 2.2.4 | Colloid-facilitated transport | 19 |
| 3 | State of the art | 21 |
| 3.1 | Bentonite erosion..... | 21 |
| 3.2 | Colloid mediated radionuclide transport processes | 25 |
| 3.2.1 | The CRR experiment..... | 25 |
| 3.2.2 | The CFM project | 28 |
| 4 | Aims of the PhD thesis..... | 37 |
| 5 | Methods | 41 |
| 5.1 | Inductively Coupled Plasma - Mass Spectrometry..... | 41 |
| 5.2 | Inductively Coupled Plasma - Optical Emission Spectrometry..... | 44 |
| 5.3 | Laser-based analytical methods..... | 45 |
| 5.3.1 | Laser theory and breakdown creation | 45 |
| 5.3.1.1 | Nd:YAG solid-state laser..... | 45 |
| 5.3.1.2 | Breakdown creation | 47 |
| 5.3.2 | Laser Induced Breakdown Detection (LIBD)..... | 48 |
| 5.3.2.1 | LIBD with 2D-optical data acquisition | 49 |
| 5.3.2.2 | S-curve LIBD..... | 52 |
| 5.3.2.3 | Calibration | 54 |
| 6 | Materials..... | 57 |
| 6.1 | Natural groundwater from the Grimsel Test Site (GTS, Switzerland) | 57 |
| 6.2 | Fault Gouge material from GTS..... | 58 |
| 6.3 | Clay mineral sources..... | 61 |
| 6.3.1 | Febex bentonite | 61 |
| 6.3.1.1 | Febex bentonite bulk properties..... | 61 |

| | | |
|---------|--|----|
| 6.3.1.2 | Raw Febex bentonite derived colloids | 62 |
| 6.3.2 | Synthetic montmorillonite characterization | 63 |
| 6.3.2.1 | Synthetic Ni- and Zn-montmorillonite bulk material | 63 |
| 6.3.2.2 | Synthetic Ni-montmorillonite derived colloids | 63 |
| 6.4 | Radionuclide cocktail characterization and speciation for FG sorption/desorption experiments 65 | |
| 6.5 | Batch type studies | 66 |
| 6.6 | Bentonite erosion studies | 69 |
| 6.6.1 | Pure Febex long-term bentonite erosion laboratory study | 69 |
| 6.6.1.1 | Artificial fracture set-up and sample geometry | 69 |
| 6.6.1.2 | Tracer characterization | 71 |
| 6.6.1.3 | Experimental procedure and sampling strategy | 71 |
| 6.6.2 | Long-term In-situ Test (LIT) at the Grimsel Test Site..... | 73 |
| 6.6.2.1 | Experimental layout | 73 |
| 6.6.2.2 | Bentonite sample and tracer composition..... | 76 |
| 6.6.2.3 | Background monitoring..... | 79 |
| 6.6.3 | Laboratory mock-up test in comparison to LIT | 81 |
| 7 | Results and Discussion | 83 |
| 7.1 | Radionuclide sorption reversibility studies on Fault Gouge material | 83 |
| 7.1.1 | Experimental overview..... | 83 |
| 7.1.2 | Evolution of pH-Eh _{SHE} conditions..... | 84 |
| 7.1.3 | Radionuclide speciation | 86 |
| 7.1.3.1 | ⁹⁹ Tc speciation | 87 |
| 7.1.3.2 | ²³³ U speciation | 87 |
| 7.1.3.3 | ²³⁷ Np speciation..... | 88 |
| 7.1.3.4 | ²⁴² Pu speciation | 89 |
| 7.1.3.5 | ²⁴³ Am speciation | 90 |
| 7.1.4 | RN sorption kinetics | 91 |
| 7.1.4.1 | ⁹⁹ Tc(VII), ²³³ U(VI) and ²³⁷ Np(V)..... | 91 |
| 7.1.4.2 | ²⁴² Pu(IV) and ²⁴³ Am(III)..... | 93 |
| 7.1.4.3 | Sorption data treatment | 94 |
| 7.1.5 | RN desorption kinetics in the binary system..... | 96 |
| 7.1.5.1 | ⁹⁹ Tc(VII), ²³³ U(VI) and ²³⁷ Np(V)..... | 96 |

| | | |
|---------|--|-----|
| 7.1.5.2 | $^{242}\text{Pu}(\text{IV})$ and $^{243}\text{Am}(\text{III})$ | 99 |
| 7.1.5.3 | Desorption data treatment | 101 |
| 7.1.6 | RN desorption kinetics in the ternary system | 103 |
| 7.1.6.1 | $^{99}\text{Tc}(\text{VII})$, $^{233}\text{U}(\text{VI})$ and $^{237}\text{Np}(\text{V})$ | 103 |
| 7.1.6.2 | $^{242}\text{Pu}(\text{IV})$ and $^{243}\text{Am}(\text{III})$ | 105 |
| 7.2 | Bentonite Erosion experiments..... | 109 |
| 7.2.1 | Bentonite erosion in artificial fracture set-up..... | 109 |
| 7.2.1.1 | Monitoring of bentonite swelling distance and pressure | 109 |
| 7.2.1.2 | Hydro-geochemical monitoring – pH, flow rate and conservative tracer..... | 113 |
| 7.2.1.3 | Bentonite erosion processes | 113 |
| 7.2.2 | LIT | 121 |
| 7.2.2.1 | LIT - online monitoring | 121 |
| 7.2.2.2 | LIT - sample analysis | 127 |
| 7.2.3 | LIT mock-up | 137 |
| 7.2.3.1 | Swelling pressure and distance | 137 |
| 7.2.3.2 | Hydro-geochemical monitoring – pH, flow rate and conservative tracer evolution | 140 |
| 7.2.3.3 | Elemental characterization..... | 142 |
| 7.2.3.4 | Radiochemical characterization | 147 |
| 8 | Conclusions..... | 151 |
| 9 | Open questions and future directions of research | 155 |
| 10 | References..... | 157 |
| 11 | Annex..... | 165 |
| 12 | List of Publications..... | 178 |

List of Figures

| | |
|---|----|
| Figure 1: (left) Conceptual model for the postglacial evolution at the Forsmark site (Sweden) The figure shows possible flow lines during deglaciation [1] and (right) the KBS-3V repository concept, showing a water conducting fracture intersecting a deposition hole [5]. | 2 |
| Figure 2: The “Colloid ladder”[16] shows the colloid related processes that have to be investigated in order to decide whether colloids have an impact on radionuclide mobility and have to be taken into account to the HLRW safety analysis. | 3 |
| Figure 3: Basic structure of montmorillonite [23]. | 7 |
| Figure 4: (left) the structure of the diffuse electrical double layer at the surface of a montmorillonite particle and (right) distribution of the concentration of cations and anions with distance from the surface..... | 8 |
| Figure 5: Ion sorption processes on the mineral surface. Mobility and reversibility decreases with increasing bond strength (from top to bottom) [35]...... | 14 |
| Figure 6: Flow velocity distribution in an idealized smooth, parallel plate type water conducting fracture. Parabolic flow field with highest flow velocities in the middle of the fracture. Velocity decreases towards the fracture wall..... | 20 |
| Figure 7: Conceptual model of the CRR experiment [11]. | 26 |
| Figure 8: (left) schematic cut through the mega packer system, sealing the MI shear zone and (right) picture taken from inside the mega packer system. | 29 |
| Figure 9: (top) location of the radiation controlled zone (encircled) within the GTS, (bottom, left) the dipole which was used in the radionuclide migration test Run 12-02 [64] and (bottom, right) Run 13-05 [65]. | 30 |
| Figure 10: Breakthrough curves of conservative tracer Amino-G; solid black line on-site fluorescence monitor data and open black circles INE off-site fluorescence measurements using an Amico-Bowman Series II spectrofluorimeter (AB2). Gamma-spectrometry data from PSI-LES and INE for Na-22, Ba-133 and Cs-137 are inserted and respective recoveries are given [66]. .. | 31 |
| Figure 11: Breakthrough curve of the colloid-associated trivalent ²⁴³ Am(III) and the tetravalent ²⁴² Pu(IV). ²³⁷ Np is additional shown, which was injected in the pentavalent state. All data are normalized to the injected mass M ₀ for comparison and recoveries are given [66]. | 32 |
| Figure 12: ²³⁷ Np and ²⁴² Pu breakthrough curve of CFM Run 12-02 measured with SF-ICP-MS and extension to longer monitoring times in the tailing using RIMS and AMS. Long-term concentrations clearly differ from the COFRAME model [67]. | 32 |
| Figure 13: Detailed geological mapping of the MI shear zone between tunnel meters AU93 and AU100 with surface packer locations [63]...... | 35 |
| Figure 14: Modelling of CFM Run 12-02 with the COFRAME model (Personal communication with Ulrich Noseck, GRS). The Accelerator Mass Spectrometry (AMS)- [73] and Resonance Ionization Mass Spectrometry (RIMS)-derived long-term data (Reich et al., unpublished) lie below the modelled concentrations. | 39 |
| Figure 15: Schematic diagram of a quadrupole mass filter. Only ions of a single m/z have a stable path and exit the quadrupole [76]...... | 42 |

| | |
|---|----|
| Figure 16: Energy level diagram of Nd:YAG [89]. | 46 |
| Figure 17: Nd:YAG laser induced breakdown event in a bentonite colloid suspension. | 47 |
| Figure 18: Fundamental LIBD functionality (http://www.innovation.kit.edu/img/Setup_LIBD.png) | 49 |
| Figure 19: Scheme of LIBD with optical data acquisition. | 50 |
| Figure 20: Contour plot of equal power area-density. The numbers indicate the relative energy density. [94] | 51 |
| Figure 21: Breakdown distribution of (left) 20 nm and (right) 500 nm polystyrene standards along the laser beam axis (top) and the same data ordered in a histogram. Size information is gained over the full width at half maximum of the gaussian fit [91] (bottom). | 51 |
| Figure 22: Scheme of the S-curve LIBD device with acoustic data acquisition. | 53 |
| Figure 23: Scheme of the mobile s-curve LIBD device with acoustic data acquisition. | 54 |
| Figure 24: Calibration range of the mobile LIBD with optical data acquisition. | 55 |
| Figure 25: ESEM images of the 250-500 μm grain size fraction of FG. EDX verifies quartz, feldspars and phyllosilicates. | 59 |
| Figure 26: Scheme of the experimental procedure concerning the FG sorption reversibility experiment (Me = Metal ion). Step 2 is triggered by water exchange which can be seen as a disturbance of the sorption equilibrium. | 66 |
| Figure 27: Flow velocity distribution in the 1mm artificial fracture erosion experiments calculated with COMSOL Multiphysics for the initial condition before swelling into the fracture | 70 |
| Figure 28: (left) Schematic arrangement of the bentonite erosion experiment and (right) bentonite erosion experiment set-up as installed in the lab. Pressure monitoring sensor on top (white cable). | 70 |
| Figure 29: (left) Bentonite sample with holes on side of the ring containing filled glass vials. (right) Top view of the bentonite ring in the swelling stage. | 72 |
| Figure 30: LIT experimental layout (www.grimsel.com). LIT enables bentonite erosion and colloid generation directly from compacted bentonite instead of colloid suspension under realistic flow conditions. | 74 |
| Figure 31: Arrangement of the boreholes relevant for LIT. A schematic overview (left) and a picture of the site (right) is pictured. The bentonite source is located in the central borehole and the surrounding boreholes (CFM 11.00X) are for near-field observation. Overcoring and retrieval of the source is an option for the late phase of the experiment. | 75 |
| Figure 32: Conceptual design of the emplacement packer system and location in the borehole CFM 06.002 (NAB 14-092). The source is sealed with two hydro-mechanical packers (P1 and P2) and the hydraulic packer (P3) is located close to the tunnel wall. | 76 |
| Figure 33: Photograph of the geochemistry cabinet (left) and schematic overview of the surface equipment setup for the nearfield monitoring system (right). | 79 |
| Figure 34: Sample preparation for the LIT-mock-up test. Tracer vials are already emplaced. The breaking points are still visible (left) and filled up with pulverized Febex-Zn-montmorillonite mixture (right). | 81 |

| | |
|---|-----|
| Figure 35: Closed cell with installed sample before transfer to the Ar glovebox. The pressure sensor will replace the screw above the bentonite source. | 82 |
| Figure 36: Schematic overview of the sorption reversibility studies. Sorption and desorption experiments are performed successively during the first 232 days of the experiment. Ni-mnt colloids are introduced as competing ligand at a run-time of 400 days (ternary system). | 83 |
| Figure 37: (a) pH evolution for the sorption experiments (symbols), desorption in the binary system (light grey area) and desorption in the ternary system (dark grey area), respectively. (b) E_{SHE} evolution for the sorption (symbols) binary (grey area) and ternary desorption (symbols) experiments, respectively. | 85 |
| Figure 38: (left) Predominance diagram for ^{99}Tc under the given conditions. The region of interest is marked with the light grey area and (right) thermodynamic speciation calculation. | 87 |
| Figure 39: (left) Predominance diagram for ^{233}U under the given conditions. The region of interest is marked with the light grey area and (right) thermodynamic speciation calculation. | 88 |
| Figure 40: (left) Predominance diagram for ^{237}Np under the given conditions. The region of interest is marked with the light grey area and (right) thermodynamic speciation calculation. | 89 |
| Figure 41: (left) Predominance diagram for ^{242}Pu under the given conditions. The region of interest is marked with the light grey area and (right) thermodynamic speciation calculation. | 89 |
| Figure 42: (left) Predominance diagram for ^{243}Am under the given conditions. The region of interest is marked with the light grey area and (right) thermodynamic speciation calculation. | 90 |
| Figure 43: Results of (a) ^{99}Tc , (b) ^{233}U and (c) ^{237}Np batch sorption kinetic experiments. | 92 |
| Figure 44: Results of ^{242}Pu (a) and ^{243}Am (b) batch kinetic sorption experiments. | 93 |
| Figure 45: Uranium speciation in GW calculated with Hydra-Medusa. The relevant pH region in the sorption experiment is located within the grey shaded area. There is no change in the oxidation state but it is obvious that calcium complexes which are not observed in the predominance diagram cannot be neglected. | 97 |
| Figure 46: Results of (a) ^{99}Tc and (b) ^{233}U batch kinetic desorption experiments. | 97 |
| Figure 47: Results of (a) ^{237}Np single radionuclide and (b) ^{237}Np cocktail kinetic desorption experiments, respectively. | 98 |
| Figure 48: Results of (a) ^{242}Pu single radionuclide, (b) ^{242}Pu cocktail and (c) ^{243}Am single radionuclide kinetic desorption experiments, respectively. The legend in (a) is valid for all diagrams. | 100 |
| Figure 49: Results of ^{99}Tc (a), ^{233}U (b) and ^{237}Np (c) desorption experiments of the radionuclide cocktail sample series. A combination of the desorption in the binary (open symbols) and the ternary system (filled symbols) over the desorption time only. The legend in (a) is valid for all diagrams. | 105 |
| Figure 50: Results of ^{242}Pu (cocktail (a) and single nuclide (b)) and ^{243}Am (single nuclide (c)) desorption experiments. A combination of the desorption in the binary (open symbols) and the ternary system (filled symbols) over the desorption time only. The description in (a) is valid for all diagrams. | 106 |

| | |
|--|-----|
| Figure 51: Pictures taken from the Febex bentonite erosion experiment (top, left) of the open fracture cell prior beginning of the experiment (top, right) at a run-time of three days and (bottom, left) at a run-time of 20 days. | 110 |
| Figure 52: (a) Swelling distance and pressure during the first month of the erosion experiment, (b) a closer look on initial pressure changes due to the removal of air bubbles, (c) pH evolution and (c) flow rate through the artificial 1 mm fracture and fluorescence signal of the conservative tracer uranine. | 112 |
| Figure 53: Evolution of Na (a), Cl ⁻ and SO ₄ ²⁻ (b) during the experiment. | 115 |
| Figure 54: Calcium (top) and magnesium (bottom) evolution during the experiment. | 117 |
| Figure 55: (a) Colloid concentration measured by LIBD and s-curve LIBD. The s-curve measurement gives a total concentration and a size distribution. The size fraction is given in the respective stacked diagram. The gap in the s-curve data is due to a software update during the experiment. (b) Colloid concentration calculated from the Mg and Al signal measured by ICP-MS. | 118 |
| Figure 56: Swelling pressure evolution within the LIT bentonite source. | 122 |
| Figure 57: (a) pH and (b) redox potential evolution (Eh _{SHE} , corrected to standard hydrogen electrode) in the near-field of the bentonite source and on the tunnel wall respectively. | 124 |
| Figure 58: (top) electrical conductivity in the near-field of the bentonite source as well as on the tunnel wall and (bottom) conservative tracer evolution in the near-field of the bentonite sample. | 126 |
| Figure 59: Comparison of online and laboratory data concerning (top) the conservative tracer concentration and (bottom) pH values. | 128 |
| Figure 60: (top) Magnesium, aluminum and zinc evolution in comparison to the respective background value of Pinkel and (bottom) calcium and sulfate molar concentrations. The respective background concentrations (0.09 mM Ca and 0.06 mM SO ₄ from Pinkel, n=21) are subtracted to compare the molar ratios regarding the dissolution of gypsum. Background values are given in Table 2. | 131 |
| Figure 61: Colloid mean sizes and concentrations derived by LIBD with optical data acquisition. | 132 |
| Figure 62: ⁹⁹ Tc release from LIT in the Grimsel test-site Sampling borehole CFM11.02. | 135 |
| Figure 63: LIT-mock-up experiment (left) at a run-time of four days and (right) at a run-time of 56 days. | 138 |
| Figure 64: Results on swelling distance (top) in the 1 mm aperture and swelling pressure (bottom) within the set-up. | 139 |
| Figure 65: Evolution of pH, volumetric flow rate (top) and conservative tracer concentration and total recovery (bottom). | 141 |
| Figure 66: Elemental evolution of the main cations Na, Ca and Mg (a), the source forming cations Zn and Al (b), anions (c) as well as molar ratios of the components of the accessory mineral gypsum (d). | 146 |
| Figure 67: Radionuclide concentration in case of ⁹⁹ Tc, ²³³ U and ²³⁷ Np. ⁹⁹ Tc initially as Tc(VII), ²³³ U initially as U(VI) and ²³⁷ Np initially as Np(V). | 148 |

Figure 68: Uranium speciation for the LIT mock-up experiment calculated with Hydra/Medusa. Speciation changes over the run-time of the experiment. 149

A-Figure 1: Calibration curves for polystyrene particles in different concentrations and particle sizes on the stationary s-curve LIBD. 165

A-Figure 2: Calibration curves for polystyrene particles in different concentrations and particle sizes on the mobile s-curve LIBD. 166

A-Figure 3: Flow velocity distribution in the Febex 1mm artificial fracture erosion experiment calculated with COMSOL Multiphysics for the equilibrium condition after swelling into the fracture. 167

A-Figure 4: Flow velocity distribution in the LIT mock-up 1mm artificial fracture erosion experiment calculated with COMSOL Multiphysics for the equilibrium condition after swelling into the fracture. 167

A-Figure 5: Flow velocity distribution of the bentonite erosion experiments in artificial 1mm fracture set-ups calculated with COMSOL Multiphysics. Flow velocities are given over the maximum cross section perpendicular to the flow direction. The initial condition before swelling (continuous line) and the equilibrium conditions after swelling is shown for the Febex bentonite erosion test (7.2.1, red dotted line) and for the LIT mock-up experiment (0, blue dotted line) 168

A-Figure 6: Shear stress distribution of the bentonite erosion experiments in artificial 1mm fracture set-ups calculated with COMSOL Multiphysics. Shear stress values are given over the maximum cross section perpendicular to the flow direction. The initial condition before swelling (continuous line) and the equilibrium conditions after swelling is shown for the Febex bentonite erosion test (7.2.1, red dotted line) and for the LIT mock-up experiment (0, blue dotted line) 168

A-Figure 7: Line-up of the LIT samples with extraction point and sampling time for off-site analysis. 176

List of Tables

| | |
|---|-----|
| Table 1: Radionuclide tracer cocktail components used in the in-situ tracer runs #31 and #32 within the CRR experiment..... | 27 |
| Table 2 GGW composition | 58 |
| Table 3: Results of XRF analysis, the main components are given in weight-% of the respective oxides. | 60 |
| Table 4: Specific surface area of the FG material used in the batch experiments. | 60 |
| Table 5: Mineralogical composition of the Febex bentonite [59]..... | 61 |
| Table 6: Exchangeable cation composition of the smectite's interlayer within the Febex bentonite. Total CEC and the main cations for charge compensation are listed [56]...... | 62 |
| Table 7: Colloid concentration and average diameter. ICP-OES derived data are calculated from the Al, Mg and Fe signal and the mean value is given..... | 62 |
| Table 8: Concentration and mean size of synthetic Ni labelled montmorillonite colloids. ICP-OES derived concentrations are calculated over the elemental composition. The respective element is given below the values..... | 64 |
| Table 9: Concentration of the radionuclides and stock solutions used in the different batch experiments , combined with the respective solubility in GGW [39]..... | 65 |
| Table 10: Synthetic Febex porewater composition [102]. | 77 |
| Table 11: Within LIT emplaced activity and license limits. | 78 |
| Table 12: Overview on the radiochemical analysis with occurring isobaric interferences and respective background value in GGW (n=4)..... | 78 |
| Table 13: Maximum sorption values and distribution coefficients of the RN sorption samples. Duplicates have been prepared and a value for each sample is given..... | 94 |
| Table 14: Radionuclide sorption rates fitted to the batch sorption experiment results. | 95 |
| Table 15: Overview of the fitted desorption rates and measured radionuclide recoveries. Recovery denotes the radionuclide fraction found in solution after the desired contact time of desorption. | 102 |
| Table 16: Overview of the fitted desorption rates and measured radionuclide recoveries after desorption in the binary and the ternary system. Recovery denotes the radionuclide fraction found in solution after the desired contact time of desorption. | 107 |
| Table 17: Colloid mean concentration measured by three different methods over the bentonite erosion phase (t > 200 d). Mean values, lowest and highest limits are given. | 119 |
| Table 18: Elemental composition of the bentonite rings emplaced within LIT..... | 133 |
| Table 19: Radionuclide recoveries over the first 320 days of the LIT mock-up experiment. | 150 |
| | |
| A-Table 1: XRF analysis of FG material in different size fractions. | 169 |
| A-Table 2: Input file for Hydra/Medusa calculations of ⁹⁹ Tc speciation and predominance diagrams in GGW systems..... | 170 |

| | |
|--|-----|
| A-Table 3: Input file for Hydra/Medusa calculations of ^{233}U speciation and predominance diagrams in GW systems..... | 171 |
| A-Table 4: Input file for Hydra/Medusa calculations of ^{237}Np speciation and predominance diagrams in GW systems..... | 173 |
| A-Table 5: Input file for Hydra/Medusa calculations of ^{242}Pu speciation and predominance diagrams in GW systems..... | 174 |
| A-Table 6: Input file for Hydra/Medusa calculations of ^{243}Am speciation and predominance diagrams | 175 |
| A-Table 7: Line-up of the sample transfer from GTS to the laboratory. | 176 |

1 *General Introduction*

In the past decades high level radioactive waste (HLRW) was produced worldwide mainly as spent nuclear fuel in nuclear power plants and as vitrified waste after reprocessing. Further sources of nuclear waste are the nuclear weapon industry, decommissioning of nuclear facilities, medicine and research. In order to protect human beings and the environment from the radiotoxic material in high-level nuclear waste, it has to be isolated safely from the geosphere for $\sim 10^6$ years due to the long life times of transuranic elements, fission and activation products. There is a consensus nowadays that nuclear waste should be disposed in deep geological formations.

Possible host rock formations currently discussed internationally are sedimentary rocks (indurated or plastic clays/claystones), evaporites (rock salt) and crystalline rocks (i.e. granite, gneiss). Crystalline rock is the dominating rock formation in the Scandinavian region and thus represents the reference host rock for the disposal of spent nuclear fuel in Sweden and Finland. The enclosure of radiotoxic waste in a so called multi-barrier system is considered to ensure safe disposal, containment and isolation of the waste from the biosphere. The multi-barrier system [1] consists of three barriers, namely the technical, the geotechnical and the geological barrier. The vitrified waste or spent fuel will be encapsulated in stainless steel or copper coated canisters. The technical barrier is built by the high level waste matrix itself (spent fuel rods or vitrified waste) and the surrounding container. The backfill material forms the geotechnical barrier and is planned to fill the cavities around the waste container and the shafts/drifts. Compacted bentonite is considered to be suitable for this purpose due to its swelling properties that prevents advective flow conditions and controls the transport of water by diffusion and due to its high sorption capacity for radiotoxic elements. The geological barrier is formed by the surrounding host rock and possibly overlaying formations [1, 2].

In the case of a corroded canister, radionuclides can get in contact with groundwater and compacted bentonite. Sorption onto mineral surfaces will take place under porewater conditions. The scenario of canister corrosion must be considered within safety analysis exercises, even though in the Scandinavian disposal concept the Cu coating is regarded as thermodynamically stable and designed to guarantee a lifetime of $> 10^5$ a [3]. Canister failure might for instance be due to manufacturing defects. A reference scenario of the future climate development is

glaciation/deglaciation induced intrusion of dilute glacial melt water down to repository depths (Figure 1). This low mineralized potentially oxidized water may come in contact with the compacted bentonite and cause swelling, gel layer formation in the contact zone and successive bentonite erosion. In advective flow fields colloidal bentonite particles might be transported away from the bentonite buffer contact zone and colloid associated radionuclides from defect containers might be released to the repository far-field [4].

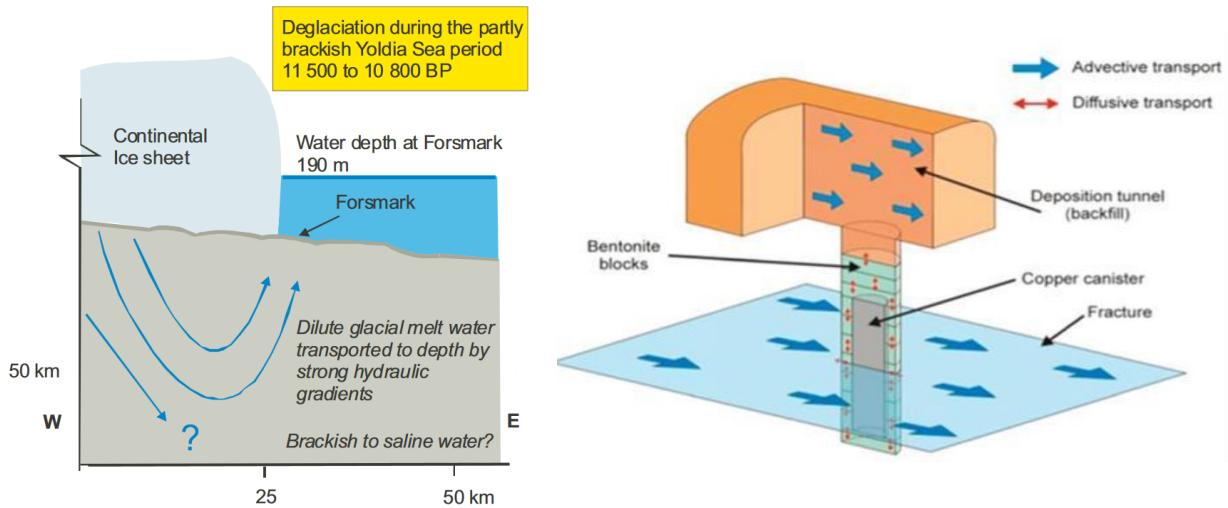


Figure 1: (left) Conceptual model for the postglacial evolution at the Forsmark site (Sweden) The figure shows possible flow lines during deglaciation [1] and (right) the KBS-3V repository concept, showing a water conducting fracture intersecting a deposition hole [5].

In order to ensure safe disposal within the HLRW repository under the given scenario, it is important to explore and quantify the erosion process of the bentonite buffer in terms of colloid generation and all kinds of RN uptake as well as RN and colloid retention processes on the way to the biosphere. The relevant processes concerning the importance of colloids for the safety assessment are shown in Figure 2. The so-called “Colloid ladder” illustrates the five requirements that must be fulfilled for colloid-facilitated radionuclide transport to be significant for the safety-case. The requirements will be addressed in the following from the bottom to the top. Although there are still a lot of open questions, a statement can be made for most requirements:

- It has been shown that natural colloids are omnipresent in aquifers and the concentration can increase with increasing the groundwater flow rate [6]. It has furthermore been proved

that colloids are produced when the bentonite barrier gets in contact with low mineralized groundwater [7].

- Mobility of the colloids is mainly driven by colloid stability, groundwater flow velocity, and retardation (colloid filtration) processes during transport like attachment to the rock surface or size exclusion from nano porous medium [8].
- In regard of a glacial melting period, described above, one has to consider that colloids can be present and stable under the dilute glacial melt water conditions [8].
- The kinetics of radionuclide uptake on colloids have been investigated extensively in laboratory batch and column experiments as well as in field studies within the Colloid and Radionuclide Retardation experiment (CRR) and the Colloid Formation and Migration project (CFM) [9-14]. There are a couple of studies focussing on the reversibility of this process [4, 8, 15].

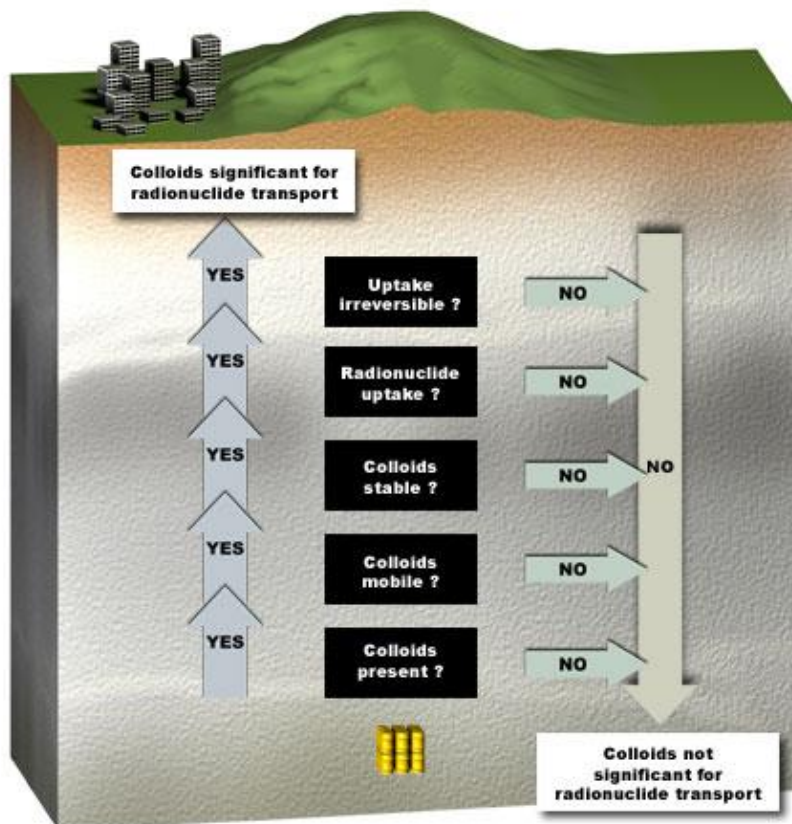


Figure 2: The “Colloid ladder”[16] shows the colloid related processes that have to be investigated in order to decide whether colloids have an impact on radionuclide mobility and have to be taken into account to the HLRW safety analysis.

Mechanisms that are responsible for colloid generation and the interaction with radionuclides as well as possible transport and retardation processes on the way from the HLRW repository to the biosphere will be discussed within the theoretical background in Chapter 2.2.

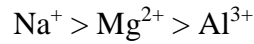
2 *Theoretical background*

The theoretical part will give an overview of the main colloid-facilitated radionuclide transport mechanisms within a HLRW repository in crystalline rock after a canister failure. Processes within the bentonite buffer, namely swelling and erosion will be explained as well as interactions at the water-solid interface and finally possible transport processes in fractured rocks.

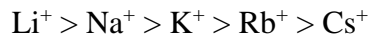
2.1 *Bentonite swelling and erosion*

Bentonite can be described as an aluminum phyllosilicate clay and is the product of rocks or volcanic ash weathering. It consists mainly of montmorillonite with a significant amount of accessory minerals like quartz, feldspar, calcite and gypsum. Montmorillonite is a member of the smectite family and built up as a 2:1 layer silicate. This means that one tetrahedrally coordinated silica layer on each plane surrounds an inner octahedral sheet that is mainly composed of aluminum, six-fold coordinated by oxygen [17]. The idealized structural formula of montmorillonite is $M^+_y nH_2O(Al_{2y}Mg_y)Si_4O_{10}(OH)_2$ [18]. A single montmorillonite unit layer is due to the arrangement of tetrahedral and octahedral sheets classified as TOT (tetrahedral – octahedral – tetrahedral) layer. Unit layers are thin platelets with a height of approximately one nanometer while the dimensions in direction of the sheet can vary between some tens to several hundred nanometers. Stability of the unit layer is achieved by covalent bonds and shared oxygen atoms between the octahedral and tetrahedral sheets. Unit layers are stacked face-to-face to form the crystal lattice. Nearby unit layers are only weakly bound by Van der Waals forces and secondary valences between neighboring atoms [19]. A negative net-charge is achieved by substitution of the trivalent aluminum in the octahedral sheet against divalent cations like magnesium or iron as well as by substitution of silica within the tetrahedral sheets against aluminum. The negative potential on the surfaces of the unit layers increase the space between two layers in the crystal lattice and is responsible for the built up of an interlayer. Due to the high surface charge of typically 1 charge equivalent per 1 kg smectite the interaction between neighboring unit layers is weak and allows water penetration in the interlayer. Cations near the surface of the unit layer compensate the negative charge. Alkaline earth metals like Ca^{2+} or Mg^{2+} or alkaline metals like Na^+ are most of the times found in a mixture of the

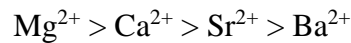
mentioned ions for charge compensation. In aqueous suspensions the charge balancing ions can be exchanged by ions found in solution. Exchangeability of the cations depends on the valence:



Higher charged cations are stronger bound to the interlayer than lower charged cations. If cations show the same valence, the effective ionic radius including the hydration shell or in other words the charge density determines the exchangeability. Larger ions exchange more easily [20]:



and



The amount of exchangeable cations and the interlayer composition is characteristic for different bentonites and known as the cationic exchange capacity (CEC) [21].

Aside the permanent negative layer charge an additional variable pH dependent charge is located at the broken edge of the montmorillonite platelets. Mainly octahedral Al-OH and tetrahedral Si-OH sites are situated at the broken edges. In suspension these edge sites can be protonated or deprotonated depending on the pH of the suspension. Under acid conditions aluminol groups are protonated inducing positive edge charges. Under alkaline conditions both aluminol and silanol groups are deprotonated and produce an additional negative layer charge [22].

The accessibility of the interlayer surface is a unique property of montmorillonite clay [19]. In dry bentonite unit layers are stacked close together with a face to face distance typically below 1 nm or less when compacted. The interlayer cations form an alternate charged layer between the negatively charged TOT-units to stabilize the stacked structure by electrostatic forces. When wetted or placed in a moist atmosphere, complexing water intrudes the interlayer to form hydration shells around the cations and hydration layers on the smectite particle surfaces. The interlayer space expands with increasing saturation until an equilibrium depending on factors like ionic strength or the elemental composition of the interlayer cations is reached. The moving apart of the clay particles in a parallel arrangement is known as bentonite swelling. This process is more pronounced in case of monovalent, highly hydrated interlayer cations like Li^+ or Na^+ . Nearly free, unlimited swelling can be observed in this case. Polyvalent interlayer cations in contrast hinder extensive

swelling because electrostatic attraction between the cations and the montmorillonite surfaces outrun the repulsive effect of ion hydration.

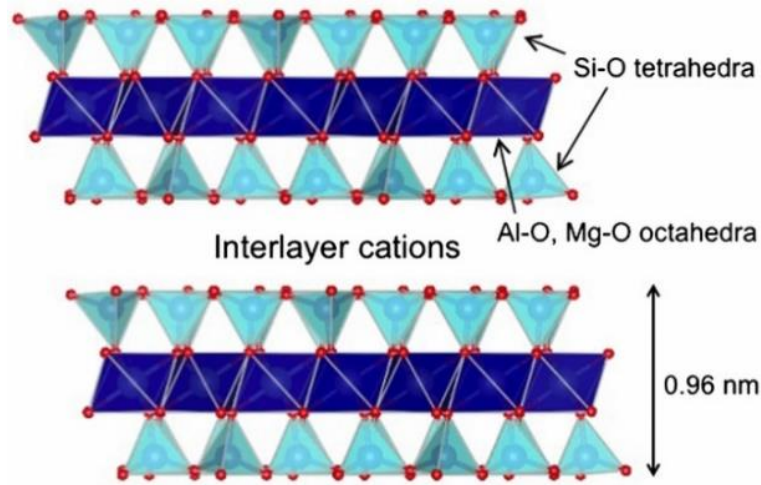


Figure 3: Basic structure of montmorillonite [23].

In order to describe the interactions between clay platelets, different effects have to be taken in account, especially interparticle repulsive forces due to the formation of an electrical double layer competing against attractive Van der Waals forces.

Regarding a charged surface in an electrolyte, contrary charged ions will approach the surface to balance the surface potential. The resulting layer in front of the charged surface is with the exception of the first adsorbed layer (Stern layer) not rigid as the oppositely charged ions are highly concentrated compared to the bulk solution and tend to diffuse into the electrolyte where the concentration is lower. The resulting arrangement is therefore called electrical diffusive double layer and was described by Gouy and Chapman in the beginning of the last century [24, 25]. At the same time the respective counter-ion concentration near the charged surface is decreased due to repulsion between the surface potential and the equally charged ions. Concentrations of the electrolyte components converge with distance from the surface. The theory of Gouy and Chapman predicts an exponential decay of the electrical potential Ψ [mV] of the solution with distance x from the plane surface to merge with the electrical potential of the bulk solution [19]:

$$\Psi = \Psi_0 \exp(-\kappa x) \quad \text{Equation 1}$$

Ψ_0 [mV] describes the surface potential and κ^{-1} , also called inverse Debye-Hückel-length, the thickness of the double layer. κ^{-1} depends on the electrolyte concentration (c_i), the valence of the ions (z_i), the dielectric constant of the medium (ϵ_0) and the absolute temperature (T) according to the equation:

$$\frac{1}{\kappa} = \sqrt{\frac{\epsilon_0 RT}{F^2 \sum_{i=n} c_i z_i^2}} \approx \frac{0.3 \text{ nm}}{\sqrt{I}} \quad \text{Equation 2}$$

where F is the Faraday constant, R the gas constant and I the ionic strength. A schematic presentation of the electrical diffusive double layer and the evolution of the ion concentration in dependence of the distance from a negatively charged surface is shown in Figure 4.

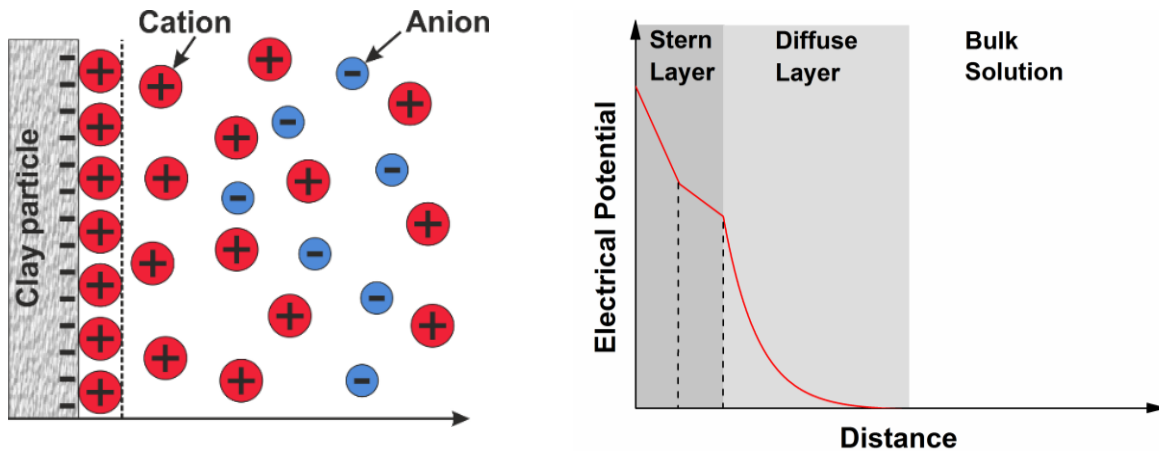


Figure 4: (left) the structure of the diffuse electrical double layer at the surface of a montmorillonite particle and (right) distribution of the concentration of cations and anions with distance from the surface.

From Equation 2 can be concluded that the double layer is compressed if the concentration of the electrolyte or the valency of the electrolyte cations increase and vice versa. As direct result charged particles can move closer in concentrated solutions. This is an important issue as particle interactions are strongly depending on the distance the particles can approach as it directly influences the stability of particles in suspension as well as the accessibility of the interlayer pore space. With decreasing distance intermolecular attractive Van-der-Waals forces gain importance. Three different forces are merged together as Van der Waals forces, namely dipole-dipole interactions, dipole-induced dipole interactions and London dispersion forces which are the reason

for nearly all Van der Waals attraction forces in colloidal suspensions. Thereby fluctuation in the charge distribution of one molecule induces a change of the charge distribution in a neighboring molecule. The London dispersion forces between two plane plate-like particles can be expressed as:

$$V_A = -\frac{A}{12\pi} \left(\frac{1}{H^2} + \frac{1}{(H+2t)^2} - \frac{1}{(H+t)^2} \right) \quad \text{Equation 3}$$

where A is the Hamaker constant [26], H the distance between the surfaces and t the thickness of the plates [19].

Regarding the bentonite swelling process, a comparison of attractive and repulsive forces between the montmorillonite unit layers is mandatory. As has been shown in Equation 2 the thickness of the diffuse double layer depends on the electrolyte concentration, the valence of the electrolyte cations and the temperature. Increasing the electrolyte concentration or the valence of the oppositely charged ions, both leads to a compression of the diffuse double layer. The surface charge of the clay particle is not affected by this change. It is simply a decrease in the thickness of the diffuse double layer and allows charged particles to approach to a closer distance. Temperature within a HLRW repository changes due to decay heat over 1 million years after operation. Most changes are expected during the first 1.000 years followed by a long-lasting convergence towards the surrounding rock temperature. Temperature changes are slow in comparison to the bentonite swelling process and temperature can be simplified as a constant value during bentonite swelling. Most changes in temperature are expected within the first 10,000 years after operation of the repository. In the following temperatures will decrease to reach initial rock temperature over the following ten millennia [27]. Glacial melt water intrusion down to repository depths and bentonite swelling and erosion in course of the KBS-3 repository is not expected for roughly 50.000 years after the closure [28].

Going back to the swelling properties of a bentonite, the interlayer cation composition as well as the electrolyte concentration and cation valency is responsible for the dimension of swelling. In very dilute electrolytes (< 1mM ionic strength) montmorillonite saturated with polyvalent cations in the interlayer, typically Ca^{2+} , will not expand further than to an interlayer spacing of 1 nm. Changing the interlayer composition to monovalent cations, typically Li^+ or Na^+ , leads to higher interlayer spacing above 10 nm [29]. Under these conditions a bentonite gel layer forms on the

bentonite-water interface. Thereby the particles orient themselves in an arrangement of minimum free energy under the influence of Brownian motion [30]. As attractive interlayer forces decrease with increasing distance, the particles are only loosely bound to neighboring particles and can be removed from the bulk under advective conditions or even by diffusion. This process is named bentonite erosion as it will result in a loss of material. Erosion of montmorillonite unit layers or erosion of stacks of unit layers is possible depending on the interlayer cation. Na-dominated montmorillonites form single unit layers or small stacks while Ca-dominated montmorillonites on the contrary tend to form larger tactoids.

The eroded material is typically colloidal in the nanoparticle size range which means that one or more dimensions of the particles are smaller than 100 nanometer while the remaining dimensions are quite variable [8]. However, transport of eroded particles over longer distances is only possible if these particles form stable suspensions. With increasing electrolyte concentration the diffuse layer shrinks and at some distance attractive Van der Waals forces become stronger than the repulsive forces. As result, the particles get closer and come into contact with one another to form agglomerates. The suspension is stable below this threshold concentration, which is known as critical coagulation concentration (CCC). It is beside ionic strength a function of electrolyte ion valency and pH. Suspensions are stable if the electrolyte concentration is below and start to agglomerate if the concentration exceeds the CCC. The CCC varies for different cations in the electrolyte and is in case of monovalent cations higher in comparison to polyvalent cations. Surface charges have a major impact on interparticle interactions and are, despite permanent charges, pH dependent because protonation and deprotonation processes are driven by the content of OH^- and H_3O^+ in solution. Based on long-term safety evaluation for KBS-3 repositories in Sweden colloidal stability is much decreased as well as bentonite buffer stability enhanced if the concentration of divalent cations, like Ca^{2+} and Mg^{2+} , exceeds 1 mM. Montmorillonite particles are not stable at concentrations above that limit. In case of divalent cations the respective CCC is independent of pH [1].

In case of NaCl electrolyte a pH dependent Na-CCC is determined. Lower CCC values are found for low pH values and increase with pH. The reason can be found in the pH dependent edge-charge of the montmorillonite particles. In acid media the edge of the platelets is protonated. The positively charged edges can interact with the negatively charged faces of the montmorillonite particles. Aggregates are formed if the diffuse layer is not thick enough to separate the particles. This is

known as edge to face (EF) interaction. Under alkaline conditions the edges of the montmorillonite platelets are deprotonated. The produced negative edge-charge stabilizes the particles in suspension and EF interaction can be neglected. The pH dependent Na-CCC is determined as 15 ± 5 mM at pH 6, 20 ± 5 mM at pH 7, 200 ± 50 mM at pH 8, 250 ± 50 mM at pH 9 and 350 ± 100 mM at pH 10, respectively [8].

The low mineralized, high pH groundwater from the migration shear zone at the Grimsel Test Site in Switzerland can be seen as reference water in case of intrusion of glacial melting water in the KBS-3 repository. Low ionic strength around 1.2 mM, dominated by sodium (0.64 mM) and calcium (0.14 mM) and alkaline pH of 9.6 support the stability of colloidal suspensions which is the reason for the importance of this groundwater in studies concerning the safety assessment of a HLRW repository [31].

2.2 *Retention of radionuclides at the solid-water interface*

Radionuclide retention processes at the solid-water interface are of special interest for the performance assessment of a future HLRW repository as they limit the radionuclide mobility. The processes of radionuclide sorption, desorption and reduction on the solid water interface will be discussed.

2.2.1 *Reversible processes – Sorption/Desorption*

The immobilization of matter at the solid-water interface is known as (ad)sorption whereas desorption denotes the release of matter from the surface into the surrounding bulk water phase. Thereby, matter can be in the gaseous, dissolved or solid phase [32]. Mobility of contaminants in trace concentrations, e. g. radionuclides, is controlled in particular by the interaction with the solid-water interface and radionuclide concentration can be significantly reduced by the retention on mineral surfaces. The term “sorption” comprises a variety of possible processes and does not give information on the underlying sorption mechanism. Aside from sorption especially radionuclide reduction which limits the solubility of many radionuclides and changes the sorption behavior has to be taken into account as additional retention mechanism. Possible ion sorption processes on the mineral surface are schematically shown in Figure 5. A distinction is drawn between outer-sphere attachment and inner-sphere surface complexation which differ in the binding forces between sorbate (mineral surface) and sorbent (radionuclide or colloidal particle) [33].

Outer-sphere sorption describes electrostatic interactions between charged species and a charged surface. Thereby the sorbed ion maintains its full hydration shell. The electrostatic forces, which are responsible for outer-sphere sorption, are dipole-dipole, ion-dipole, van-der-Waals-interaction and ion-bonding [34]. Inner-sphere sorption however describes a surface complexation whereby the sorbent loses part of the water molecules of the first coordination sphere which is replaced by chemical binding to functional groups of the sorbate. Forces between sorbate and sorbent in an inner-sphere surface complexation shows significant ionic or covalent contribution and is strong in comparison to outer-sphere attachment [33]. This strong binding results in decreased sorption reversibility and affects desorption kinetics, compared to outer-sphere sorption.

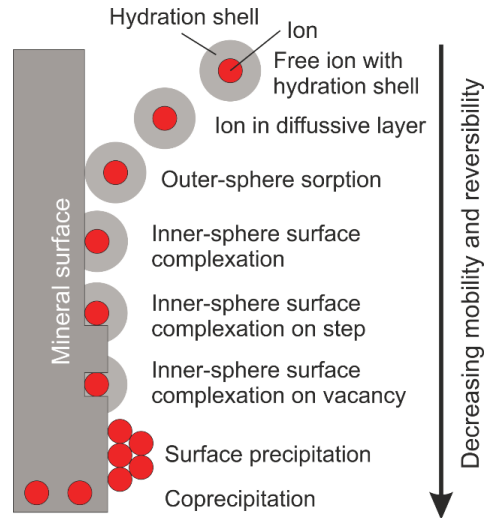


Figure 5: Ion sorption processes on the mineral surface. Mobility and reversibility decreases with increasing bond strength (from top to bottom) [35].

Replacement of sorbed ions at the solid-water interface against ions from the bulk solution is called ion exchange. This sorption process is often considered in case of permanently charged sorbates like clay particles or layer double hydroxides as an example for cation and anion exchangers, respectively. The cation exchange process is described in terms of the bentonite swelling process in 2.1.

The extent and type of sorption depends on [34]:

- Chemical parameters of the dissolved species, namely concentration, speciation, valence state and charge.
- Properties of the absorbing surface, like mineralogy, morphology, surface charge, functional surface groups that built up different sorption sites and ratio between these sorption sites (strong/weak sites).
- General chemical and physical parameters of the liquid phase, e.g. pH, E_{SHE} , ionic strength, temperature, pressure and the concentration of accessory components. Additional reactive components can on the one hand act as competing ligands and occupy the sorption sites or on the other hand interact with the sorbent and form stable complexes. In both cases interaction between sorbate and sorbent is hindered.

Batch type sorption studies are suitable to obtain reliable distribution coefficients (K_d values) and kinetic rates which both provide input data for the development of mechanistic sorption models,

crucial for the performance assessment of a HLRW repository. Thereby a defined amount of solid material that will act as sorbate is given to a solution with defined sorbent concentrations. After equilibration between the sorbate and the sorbent a steady state will be reached between the sorbent which is bound on the surface of the sorbate (q) and the sorbent remaining free in solution (c). The distribution coefficient can be expressed by the following Equation 4.

$$K_d = \frac{q}{c} \quad \text{Equation 4}$$

Such K_d -values are very sensitive to changes of system parameters and therefore only applicable at trace concentration ranges, when sorbate and sorbent are in equilibrium, for fully reversible sorption reactions and for constant geochemical conditions.

Sorption to mineral surfaces represents, besides precipitation and coprecipitation phenomena, one of the most important retention processes for radionuclides in a HLRW repository [36]. Depending on the radionuclide oxidation state the interaction to a mineral surface is more or less pronounced. Tri- and tetravalent radionuclides like e. g. Am, Th or Pu show high tendency to sorb on mineral surfaces. In contrast penta-, hexa- and heptavalent actinides show much less interaction with mineral surfaces and are therefore more mobile in the environment. As an example Np, U and Tc are present in the oxidation states Np^{5+} , U^{6+} and Tc^{7+} under GW conditions. A reason for the different sorption properties can be found in the respective radionuclide speciation. Tri- and tetravalent actinides form more or less spherical aquo-ions with 9-10 water molecules in the first coordination sphere. In contrast, penta- and hexavalent actinides form actinyl cations with covalently bound axial oxygen atoms while the equatorial plane is 4- to 6-fold coordinated. This results in a reduction of the charge density on the actinide cation in addition to steric hindrance [33]. Heptavalent Tc is the most stable oxidation state under oxidizing conditions, forming mobile TcO_4^- anions over the entire pH range with very weak sorption properties towards negatively charged mineral surfaces [37, 38].

In case of a geochemical equilibrium, sorption and desorption processes are present but show equal reaction rates. Thereby, the equilibrium between sorbed species the ratio free in solution remains constant. A change of geochemical conditions like pH, E_{SHE} , temperature or solution chemistry are possible disturbances of the equilibrium condition and can force the system to build up a new equilibrium. In case of classical batch sorption reversibility studies, sorption equilibrium is disturbed by exchange of the sorbent containing solute against a sorbent-free solution. The system will then try to reestablish the distribution equilibrium of sorbent at the surface and in solution by releasing part of the sorbed amount into the solute. Adding an additional mineral phase to a mineral surface and sorbent containing solution in equilibrium, can also trigger desorption. The new mineral phase will act as competing ligand. Thereby, the sorbent concentration is decreased by sorption to the additional surface. As a consequence, sorbent will be released from the first and subsequent sorbed to the additional mineral phase until a new equilibrium in the ternary system is reached. Sorption processes are deemed to be fully reversible but differ in desorption rates. In case of outer-sphere sorption, the sorbate's hydration shell remains intact, while the hydration shell is in regard of an inner-sphere sorption species partly replaced (Figure 5). The need to detach from the mineral surface and to rebuild the hydration shell of the sorbate before desorption is the reason for slower reaction rates in comparison to outer-sphere sorption [33].

Additional immobilization mechanisms can be found in surface precipitation and coprecipitation of the sorbent if the solute is supersaturated in respect of a secondary phase or dissolution/recrystallization processes of the sorbate that gain importance if the sorbate is not in equilibrium with the solute. Even in chemical equilibrium, mineral surfaces cannot be considered as inert and dissolution and recrystallization are omnipresent. In this case, surface sorbed species can be ultimately incorporated and immobilized into the bulk matrix of the sorbate. Release of the incorporated species is then controlled by the solubility of the mineral phase which holds the contaminants.

2.2.2 Redox reactions

The migration behavior of redox sensitive RNs like e. g. Tc, U, Np or Pu is mainly determined by the respective oxidation state which is in turn set by the geochemical conditions (i. e. pH, E_{SHE}) prevailing. The reduced oxidation states show in most cases but not in general lower solubility and higher tendency for sorption as discussed in 2.2.1 [39]. Radionuclide reduction of e. g. pentavalent Np to the low soluble tetravalent oxidation state is an effective mechanism to reduce radionuclide mobility. It has to be mentioned that changes in the geochemical conditions can also lead to radionuclide re-oxidation and mobilization as it was observed e. g. in the Swedish site investigation program for Oskarshamn [40].

The redox potential of a given system is determined as potential against the standard hydrogen electrode (E_{SHE}) or in logarithmic units of the electron activity a_{e^-} ($pe = -\log a_{e^-}$) in analogy to e. g. the definition of the pH ($pH = -\log a_{\text{H}^+}$). A relationship between Eh and pe is found in the following Equation 5:

$$Eh = \frac{RT}{F} \ln a_{e^-} = \frac{RT \ln(10)}{F} pe \quad \text{Equation 5}$$

in which R is the gas constant [$\text{J}\cdot\text{mol}^{-1}\cdot\text{K}^{-1}$], T the temperature [K] and F the Faraday constant [$\text{C}\cdot\text{mol}^{-1}$] [34].

The redox state of a radionuclide in solution is conveniently depicted in a predominance or Pourbaix diagram (pe over pH diagram). Besides the redox state the respective dominant species within a pH-Eh region but not the full speciation can be found in this kind of diagram. Examples for a variety of radionuclides under relevant conditions can be found in 7.1.1.

In addition, radionuclide reduction is possible although reduction is unlikely in regard to the geochemical conditions of the solute. In this case a coupled sorption/reduction process is responsible for radionuclide reduction, which strongly reduces the radionuclide mobility. This process is known as surface-induced radionuclide reduction. Various examples have been given by Geckeis et al. [33] and Marsac et al. [41] who found Np(IV) on the illite surface although the solution was in the stability field of Np(V) and a recent study in case of reduction of Tc(VII) to

Tc(IV) published by Huber et al. [42]. Surface induced oxidation has also to be taken into account. Especially Mn(IV) containing minerals are considered as oxidizing agents [33]. This process is especially relevant under acidic conditions and therefore only mentioned but of minor relevance for this study.

2.2.3 *Matrix diffusion*

Solute movement in groundwater is in general driven by advection and diffusion. In highly impermeable crystalline rocks, the groundwater flow takes place exclusively in fractured zones. Rates for diffusive solute movement in fractured crystalline rock are typically orders of magnitude lower than advective velocities and can therefore be neglected concerning transport in the fractured system. Diffusion has to be taken into account in regard of transport processes in the bentonite barrier, in which diffusion is the only notable transport path. The importance of diffusion in the fractured zone is based on matrix diffusion processes which guide contaminants away from advective dominated regions into the stagnant groundwater in the porous matrix [43]. This process is known as matrix diffusion and leads to the retardation of contaminants (radionuclides or to a lesser extent colloids) by moving them from the main paths of the advective flow to regions of significantly lower velocities and thereby significantly increasing the residence time [44]. Solutes, once transferred to the porous matrix, are in contact with a much higher surface area compared to the main flow paths and further retardation processes like sorption, reduction and (co)precipitation can take place and increase the residence time. In addition, solutes in the porous matrix show much lower effective diffusion coefficients in comparison to the free diffusion coefficient in water. The pore diffusion coefficients (D_p [$\text{m}\cdot\text{s}^{-2}$]) can be calculated from the free diffusion coefficient (D_0 [$\text{m}\cdot\text{s}^{-2}$]), corrected by the constrictivity (δ) and the tortuosity (τ) as given in Equation 6 [45]:

$$D_p = D_0 \frac{\delta}{\tau^2} \quad \text{Equation 6}$$

The ratio between the constrictivity and the tortuosity is known as the geometric factor (G) and always smaller than one. An empirical relation can be drawn between G and the accessible porosity (ϵ) in crystalline rock [46]:

$$G = 0.71\varepsilon^{0.58} \quad \text{Equation 7}$$

The rock-matrix within this study is the so-called Grimsel granodiorite. An average porosity of $\varepsilon=0.6\%$ was reported for this material [47] but for negatively charged species, which is valid for bentonite colloids, the ion accessible porosity usually is smaller. For negatively charged clay colloids a value being one order of magnitude lower has been suggested [48]. This can be explained by anionic exclusion between the negatively charged granite surface and the equally charged colloids. Furthermore, taking in account that colloids are bigger in comparison to anions, part of the nanopores which are included in the ion accessible porosity are not available for colloids. This reduces the ion accessible porosity to only 0.06%. The pore diffusion coefficient (D_p) is linked with the accessible porosity (ε) to form the effective diffusion coefficient (D_e) by:

$$D_e = \varepsilon D_p \quad \text{Equation 8}$$

2.2.4 Colloid-facilitated transport

In terms of radionuclide transport in fractured rocks, colloid formation and subsequent colloid mediated radionuclide transport cannot be neglected [49]. Colloids are formed by alteration or physical erosion of mineral phases or by direct precipitation in groundwater. Colloid composition is therefore typically very comparable to the host rock and the fracture filling minerals and typically comprise of silica, clay minerals, calcite and Fe-oxyhydroxides. Additional colloid sources within a HLRW repository can be found for instance as bentonite colloids from erosion of the geotechnical barrier or corrosion products from the waste holding canister and the waste matrix itself [8].

In saturated, advection controlled flow regimes, colloid mobility is mainly influenced by colloid stability (2.1) and retardation processes during transport, like e. g. sorption on the fracture surface or matrix diffusion. Colloid retention depends on the geochemical conditions as electrostatic attraction and repulsion strongly depends on the surface charge of the fracture filling minerals. Under favorable conditions, which means that the pH is close or below the point of zero charge of the respective mineral phase, the surfaces are neutral charged or protonated and as a consequence strong adsorption of negatively charged colloids is observed. Colloid facilitated transport will not

take place. Under unfavorable conditions which can be found for instance in case of natural groundwater from GTS (GGW), mineral surfaces and colloids are both negatively charged and show pronounced repulsion. As a consequence colloids do not interact with the fracture surface and are transported away in the natural flow field. In natural granitic systems, however, colloid retention was found to be strongly depending on small scale chemical effects, roughness or non-uniform distribution of charge sites [8, 50, 51].

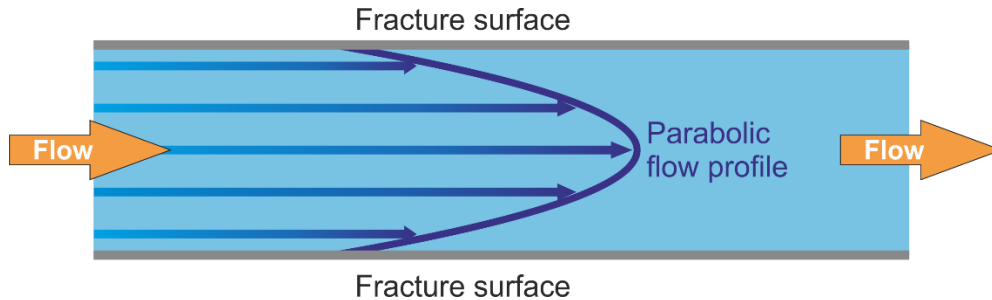


Figure 6: Flow velocity distribution in an idealized smooth, parallel plate type water conducting fracture. Parabolic flow field with highest flow velocities in the middle of the fracture. Velocity decreases towards the fracture wall.

As consequence of the repulsive forces between colloids and fracture filling mineral surface, it is possible that the colloid breakthrough maximum is observed even before the conservative tracer. This observation can be explained with the Flow velocity distribution within an idealized fracture. Under the assumption of laminar flow under the prevailing low average flow velocities, highest flow velocity can be found in the middle between the surfaces and decrease closer to the fracture surface (Figure 6). As explained before, colloids will not approach the surface wall and will be transported in the inner, faster region of the flow field. A conservative tracer does in contrast not at all interact with the mineral surface and is transported with the mean flow velocity, only slowed down by matrix diffusion.

3 *State of the art*

3.1 *Bentonite erosion*

Bentonite is widely accepted as suitable buffer material for surrounding the canisters with spent nuclear fuel in a HLRW repository [52-55]. The purpose of the bentonite barrier is the safe enclosure of the waste canister. A couple of properties are favorable to choose bentonite as backfill material, namely low permeability, high sorption capability, very good swelling properties, high buffer capability concerning Eh and pH, high plasticity and compressibility. In case of water intrusion in a prospective HLRW repository, the bentonite buffer will expand, thus sealing the emplacement chamber. In addition, gel formation at the bentonite groundwater interface and penetration into open rock fractures can furthermore contribute to separating the waste from the surrounding water. Besides all this positive aspects, the high swelling capability also shows a disadvantage as the bentonite buffer may erode in advection controlled systems and release colloidal particles from the interface between gel and water. This may lead to weakening of the bentonite barrier and radionuclide transport to the geosphere. Buffer erosion is a process that may not be neglected and was a major topic within recent EU projects, for instance FUNMIG (FUNdamental processes of radionuclide MIGration, FP6-516514) and BELBaR (Bentonite Erosion: effects on the Long-term performance of the engineered Barrier and Radionuclide transport, contract number: 295487).

A number of different factors influencing bentonite erosion have been identified, namely groundwater chemistry, bentonite dry density, interlayer composition of the bentonite and the flow-velocity at the gel-water interface. Recent research on bentonite erosion puts a lot of effort on all the mentioned issues in order to develop a model that describes the erosion process which is essential for the long-term safety of a HLRW repository. Simple erosion experiments have been performed in artificial fracture set-ups with varying fracture height. Parallel plate set-ups with smooth, in some cases also rough or seldom even real granite surfaces were used. Different sorts of bentonites have been investigated in these studies ranging from unpurified over purified to synthetic samples. The same diversity is found in the contact water distribution that ranges from ultra-pure water over diluted salt brines to synthetic or even natural groundwaters.

A Spanish research group from CIEMAT (www.ciemat.es, Madrid) published their investigation on the generation and stability of bentonite colloids at the bentonite/granite interface in 2003 [53]. Two set-ups were developed to facilitate the differentiation between diffusive and advective controlled colloid generation. The experiments under advection control consisted of half cylinders from natural Febex bentonite and granite that were faced and kept joined during the experiment. Two sintered stainless steel filters were placed on the bottom and the top of the sample to prevent swelling. Water was introduced between bentonite and granite and could flow along the interface. A low mineralized synthetic groundwater with moderately alkaline pH was pumped through slowly through the cell. In these studies the concentration of the eroded particles increased with the water flow rate indicating the presence of a mechanic erosion process. Colloid concentrations in the effluent were always below 1 ppm.

A couple of small-scale, flow-through, artificial fracture bentonite erosion tests have been carried out by B+Tech Oy, a company that is working on the development of the technical barriers used to isolate nuclear waste from the environment in Finland (www.btech.fi, Helsinki). The experiments were performed in order to simulate the potential extrusion and erosion behavior of the bentonite buffer at a transmissive fracture interface. The effect of different solution and material compositions as well as the flow velocity on bentonite swelling and erosion were part of these studies. Some of the experiments are summarized in [31]. Most experiments were conducted using purified homoionic exchanged sodium-saturated montmorillonite or in some cases a 50/50 mixture of calcium and sodium saturated montmorillonite. Cylindrical bentonite samples were prepared (diameter = 2 cm, height = 2 cm) in a dry density 1.6 g/cm^3 . The artificial fracture was arranged horizontally and has a height of 1 mm. Groundwater composition ranged from deionized water up to 10 g/L NaCl solution and even a Grimsel groundwater simulant relative to sodium and calcium concentrations only was used. Flow velocity in thirteen experiments was adjusted between $6 \cdot 10^{-6}$ up to $2 \cdot 10^{-4}$ m/s. No erosion was observed for the experiments with concentrated NaCl solution of 0.5 g/L (8.6 mM) or higher. Erosion was observed in case of the experiments with less concentrated solutions and mass loss rates have been determined between $5 \cdot 10^{-7}$ and $3 \cdot 10^{-6}$ g/s. Two additional tests with untreated bentonite samples lead to limited erosion rates by more than one order of magnitude in comparison to the behavior of the purified sample.

A summary of the knowledge on bentonite erosion achieved during the FUNMIG project is given in [8]. A broad collection of parameters influencing the erosion behavior of compacted bentonite

have been investigated. These are amongst others dry density of the bentonite sample, the interlayer cation composition, the clay type, the surface area exposed to hydration and the contact water solution chemistry concerning ionic strength, pH and cation composition. Several requirements valid for stability of colloidal suspensions could be transferred to the bentonite erosion process. Colloid generation is for instance only observed for cation concentrations below the CCC. It is remarkable that the colloid concentration in the mentioned erosion experiments reach a plateau over time indicating a steady state of the colloid generation process. Thereby the plateau colloid concentration increased with the initial bentonite dry density. Erosion rates have been determined and were compared by normalizing values to the contact area between the rim of the swelling phase and the contact water. In case of bentonite dry densities above 1.6 g/cm^3 , highest bentonite erosion rates of $1.2 \cdot 10^{-6} \text{ mg cm}^{-2} \text{ s}^{-1}$ were at least one order of magnitude below modelled erosion rates. These experimental results created the basis for improvements of these bentonite erosion models.

The BELBaR project is the most recent project dealing with bentonite erosion processes to be described here. It took place from 2012 to 2016 with the main aim to increase the knowledge on the processes that control clay colloid generation, stability and the ability to transport radionuclides. The project was divided in 6 work packages and one of those packages solely dealt with bentonite erosion and another one with the modelling of this process. Detailed reports are available on the BELBaR web page (<http://www.skb.se/belbar>).

Beside numerous bentonite erosion tests in artificial fracture set-ups to facilitate bentonite swelling and experiments in closed set-ups without fracture to investigate erosion without or only with little swelling, the Full-scale Engineered Barriers EXperiment (FEBEX) was investigated in regard of colloidal release. This project is located at the GTS and was conducted to demonstrate the feasibility of actually manufacturing and assembling an engineered barrier system in crystalline rock and to gain data for modelling work. It was emplaced in 1996 and was slowly saturating due to the uptake of surrounding groundwater from water conducting fissures. Very low colloid concentrations have been observed in the near-field by analyzing Al concentrations as an indicator for suspended aluminosilicate particles. Although GGW favors the stability of bentonite colloids due to low salinity and alkaline pH, maximal concentrations of only 0.8 ppm have been determined under the unlikely assumption that all aluminum is colloid associated. It was assumed that the existence and the dissolution of accessory phases like halite or gypsum in the natural unpurified

bentonite increases the ionic strength in the near-field of the experiment and reduces stability of the colloid suspensions and hinders colloid release [56].

3.2 *Colloid mediated radionuclide transport processes*

A number of recent studies investigated colloid mediated migration of radionuclides in fractured granite systems on the laboratory scale [10, 57-59]. Thereby clay, silica, iron oxide/hydroxide and organic (humic/fulvic acids) nanoparticles have been identified as relevant colloidal species [9]. The description here will focus on the field experiments conducted at the GTS within the CRR and CFM projects as they represent the background for the present experiments. Further details on the experiments can be found in the Nagra Technical Reports or on the Grimsel web page (<http://www.grimsel.com/>).

3.2.1 *The CRR experiment*

The CRR experiment was devoted to the study of the in situ migration behavior of selected actinides and fission products in the absence and presence of bentonite derived colloids in a natural water-conducting shear zone in GTS. The experiment included radionuclides of the elements U, Th, Pu, Am, Np, Sr, Cs, I and Tc and the impact of smectite bentonite colloids by two in-situ tracer tests in a well characterized dipole. A conceptual model of the CRR experiment can be found in Figure 7 and it becomes obvious that the migration behavior of radionuclides and bentonite colloids in a repository's far-field is focus of the experiment but not the processes which are responsible for the generation of these colloids.

Besides the field experiments, an extensive experimental program on the laboratory scale as well as a modelling program which mainly focused on RN solubility, flow field and reactive transport modelling [60], were established to support the in-situ experiments. The laboratory program mainly focused on batch experiments with different mineral phases in the absence and presence of bentonite colloids [61].

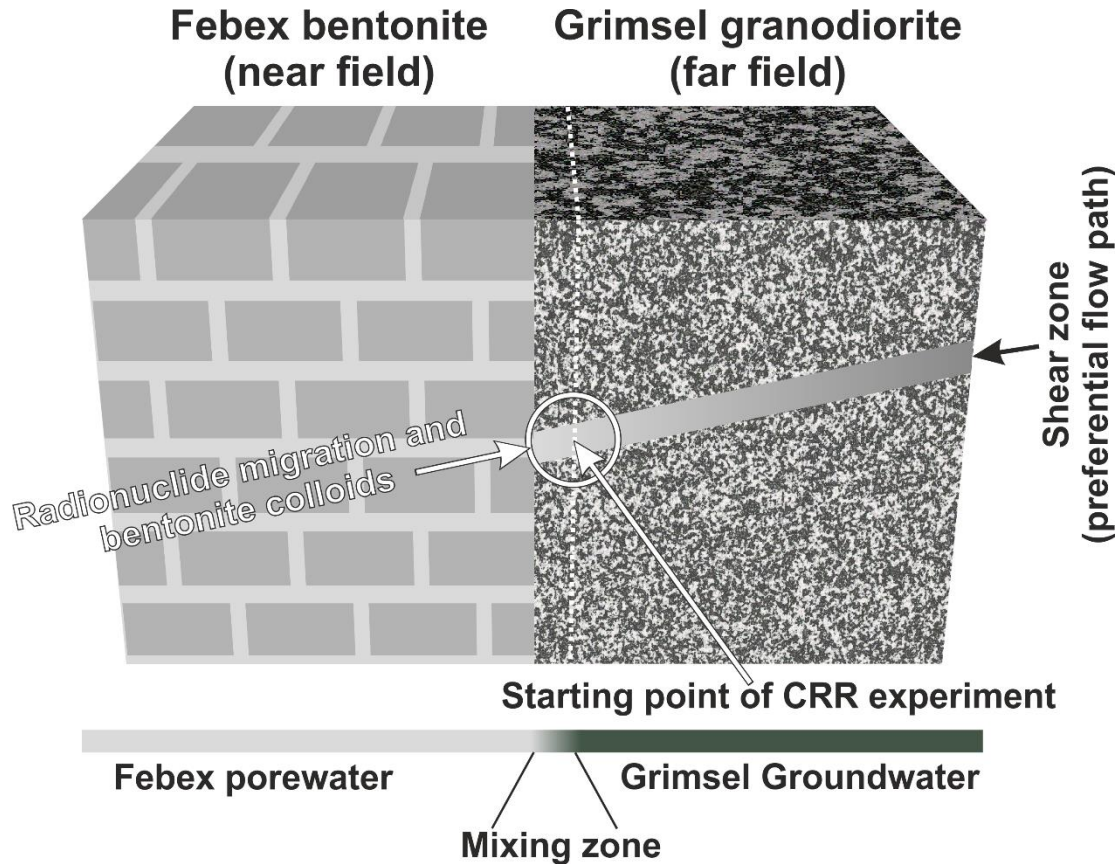


Figure 7: Conceptual model of the CRR experiment [11].

The final in-situ radionuclide tracer tests have been carried out after characterization of the CRR test site in order to choose the suitable borehole arrangement for the experiment. Results of the field tests are described in detail in the Nagra Technical Report 03-01 [62] and only a short summary is given here. A dipole with a straight-line length of 2.23 m was chosen. Thereupon, several conservative tracer and colloid runs have been carried out in this dipole before the two final in-situ radionuclide tracer tests have been carried out. The tracer composition is given in Table 1. The main difference in the described radionuclide tracer runs consists in the bentonite colloids that have only been added to the second experiment. Different isotopes of the respective radionuclides have been used in both RN tracer runs, if possible (e. g. $^{233}\text{U}/^{238}\text{U}$ or $^{242}\text{Pu}/^{244}\text{Pu}$), to reduce artefacts from radionuclide concentrations in the later run due to a possible long lasting tailing or cross contaminations. A flow field between the injection borehole and the extraction point was established by injection of 10 mL/min, while 150 mL/min were extracted at the end of the dipole.

Table 1: Radionuclide tracer cocktail components used in the in-situ tracer runs #31 and #32 within the CRR experiment.

| CRR-Run #31 | CRR-Run #32 |
|---|---|
| $^{243}\text{Am(III)}$ | $^{243}\text{Am(III)}$ |
| $^{237}\text{Np(V)}$ | $^{237}\text{Np(V)}$ |
| $^{238}\text{Pu(IV)}$, $^{242}\text{Pu(IV)}$ | $^{238}\text{Pu(IV)}$, $^{244}\text{Pu(IV)}$ |
| $^{238}\text{U(VI)}$ | $^{233}\text{U(VI)}$ |
| $^{85}\text{Sr(II)}$ | $^{85}\text{Sr(II)}$ |
| $^{131}\text{I(I)}$ (conservative tracer) | $^{131}\text{I(I)}$ (conservative tracer) |
| $^{232}\text{Th(IV)}$ | $^{232}\text{Th(IV)}$ |
| | $^{99}\text{Tc(IV)}$ |
| | $^{137}\text{Cs(I)}$ |
| No bentonite colloids | 20 mg/L bentonite colloids |

In the absence of bentonite colloids (Run #31), the tri- and tetravalent actinides ^{243}Am , ^{232}Th and $^{238/242}\text{Pu}$ showed a migration behavior different to the other elements, namely less recovery (20-30%), less tailing and the maximum of the breakthrough was about 10 minutes earlier than those found for the conservative tracer. The early breakthrough indicates partly colloidal transport although bentonite colloids have not been part of the tracer cocktail. In presence of bentonite colloids (Run #32) the same behavior was observed for the tri- and tetravalent actinides but recoveries were significantly higher (70-90%) due to a larger colloid bound actinide fraction. The peak time of these elements coincided with the peak time of the bentonite colloids. In contrast to the tri- and tetravalent actinides ^{137}Cs was only partly colloid bound and showed the release of two different species, a colloid bound species was visible at the peak time of the bentonite colloids as well as a second retarded fraction. Migration behavior of the remaining radionuclides and more details to the mentioned radionuclides can be found in [9, 62].

The main findings of the CRR experiment were the following:

- Colloids are for the conditions within the MI shear zone at the Grimsel Test Site stable, mobile and interact with radionuclides.
- Colloids show a significant influence on the in-situ retardation behavior of tri- and tetravalent actinides, meaning that the migration behavior of these elements is strongly mediated by the presence of bentonite colloids. Recoveries increase as a consequence of selective radionuclide sorption on the bentonite colloids.
- Cs is present in the dissolved state as well as colloid associated.
- The mean travel time of colloids and colloid associated radionuclides is faster than the transport of dissolved species and the conservative tracer under the fast flow conditions established.
- With regard to the colloid ladder (Figure 2), it has not been verified within the hydraulic conditions licensed within CRR if full reversibility of the bentonite colloid adsorbed radionuclides is given under repository relevant conditions.

3.2.2 *The CFM project*

The CFM project started as follow-up project of the CRR experiment in 2004. Relevant processes are in contrast to CRR one step closer to the engineered barrier system (EBS) as colloid generation rates and mechanisms at the EBS and the transport under HLRW repository relevant conditions are investigated in-situ. The project moreover enlarges the time scale from former residence times of days (CRR) to years as a deeper insight in the long-term geochemical behavior of radionuclides at the EBS – host rock interface is a major topic within CFM.

Three project phases are comprised within CFM to date. Field activities at GTS during the first phase focused on selection of a suitable site, site characterization and preparation. The MI shear zone was selected as suitable experimental site as several experiments had been conducted within this feature (MI, Ep and CRR projects) and it was therefore already well characterized. A further benefit was that part of the old boreholes could be used for ongoing hydraulic characterization. A series of tracer tests were performed in the MI shear zone to find suitable flow fields for the migration experiment. The shear zone was mapped (Figure 13) at the intersection with the tunnel wall in order to begin the most challenging part of the site preparation which was the sealing of the

tunnel surface to minimize the heads towards the tunnel wall and to achieve control over the flow velocity within the shear zone. A surface packer was installed between the packer system and the tunnel wall to provide control over the flow velocity by variation of the extraction rate. A first try to seal the tunnel wall was undertaken within CFM phase one. A sealing resin was applied directly to the tunnel surface but it did not withstand the hydraulic forces from the shear zone. As consequence it was decided to install a steel tube of 5 m length with cement filled Bullflex® (BuM Beton- und Monierbau GmbH, Herten, Germany) packers at each end. Permanent (i.e. for a couple of years) sealing of the shear zone with this new designed packer was inadequate and an improvement of the packer design was needed.

The final version of the mega packer system was realized during CFM phase 2. Moreover, the preparation work on the experimental site was completed, the experimental design was finalized and additional migration experiments including tests with colloids and radionuclides took place. In order to realize a long-term (> 4 a) controllable repository relevant flow system which is characterized by low flow velocities, the mega packer system needed some improvement. This issue was successfully realized by exchanging the Bullflex® packers against large inflatable “O-ring type” packers at each end. Detailed information on the installation of the mega packer system can be found in NAB 10-04 [63] and the system is shown in Figure 8.

Sealing packer Reinforcement of steel tube

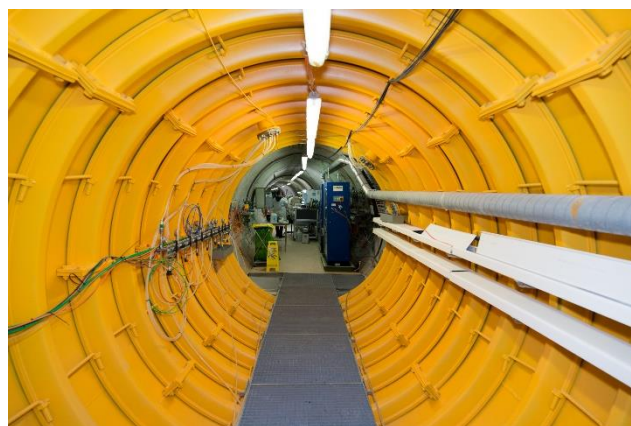
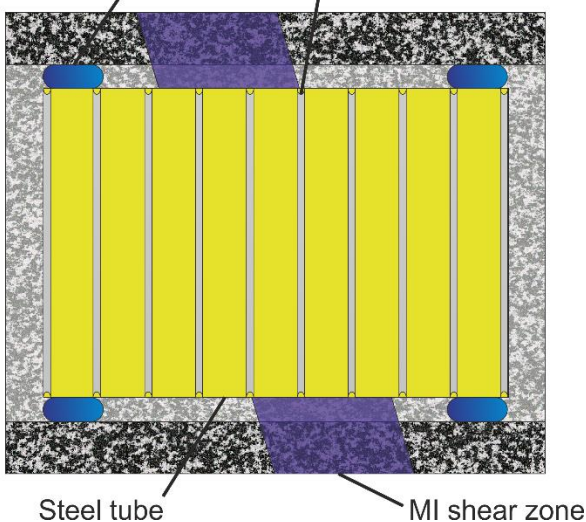


Figure 8: (left) schematic cut through the mega packer system, sealing the MI shear zone and (right) picture taken from inside the mega packer system.

Once the shear zone was successfully sealed and the flow conditions within the shear zone controllable, two radionuclide colloid tracer tests have been conducted, namely Run 12-02 [64] and Run 13-05 [65] (Figure 9).

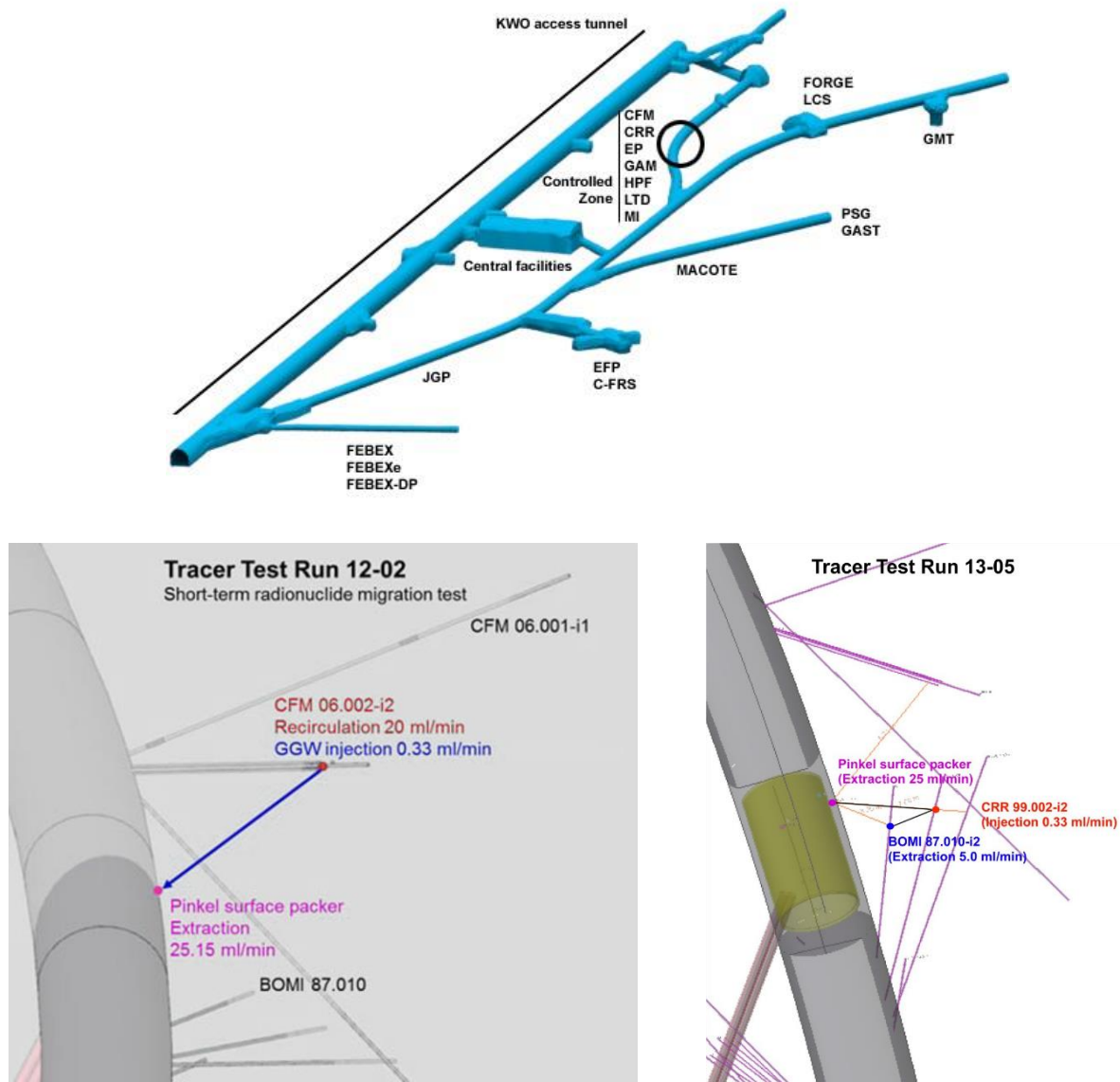


Figure 9: (top) location of the radiation controlled zone (encircled) within GTS, (bottom, left) the dipole which was used in the radionuclide migration test Run 12-02 [64] and (bottom, right) Run 13-05 [65].

Radionuclide colloid tracer test Run 12-02 was conducted in the same flow path as foreseen for the long-term in-situ test. A radionuclide containing colloid suspension (^{22}Na , ^{133}Ba , ^{137}Cs , ^{237}Np , ^{232}Th , ^{242}Pu and ^{243}Am) was injected (re-circulation technique) in the borehole CFM 06.002-i2 and extracted at the Pinkel surface packer. The distance of the dipole was 6.08 m. The tracer run took place in this dipole to optimize the experimental setup, to clearly prove the overall control of the system and to confirm that colloids once generated can be mobile in this section of the shear zone.

Breakthrough curves of the main components of the radionuclide colloid tracer suspension are given in Figure 10 and Figure 11.

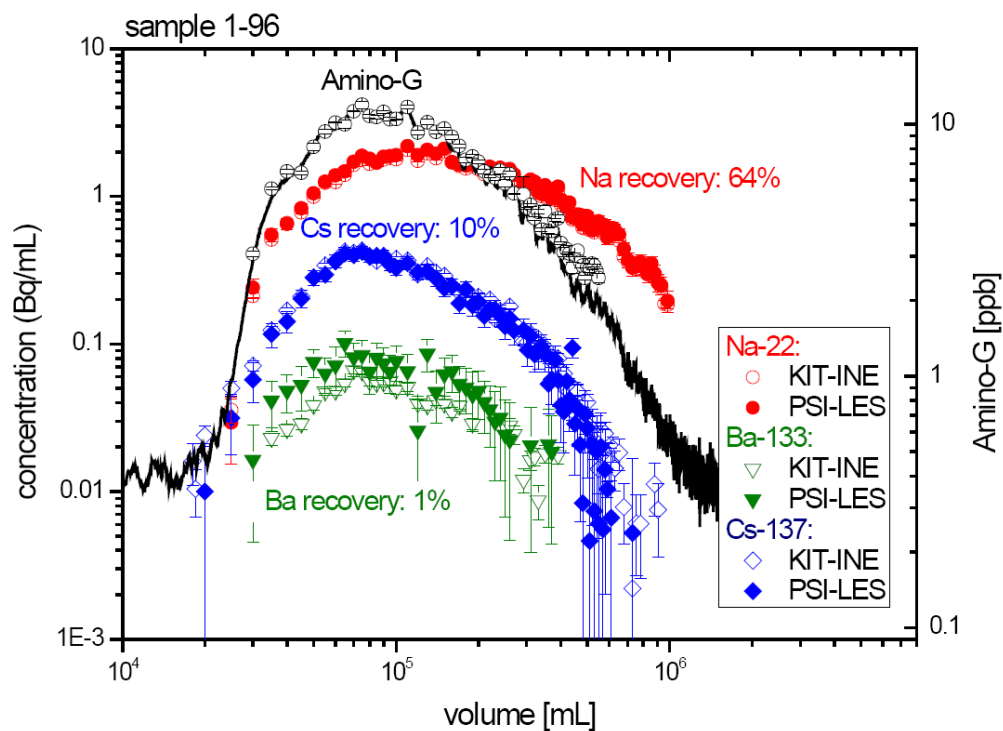


Figure 10: Breakthrough curves of conservative tracer Amino-G; solid black line on-site fluorescence monitor data and open black circles INE off-site fluorescence measurements using an Amico-Bowman Series II spectrofluorimeter (AB2). Gamma-spectrometry data from PSI-LES and INE for Na-22, Ba-133 and Cs-137 are inserted and respective recoveries are given [66].

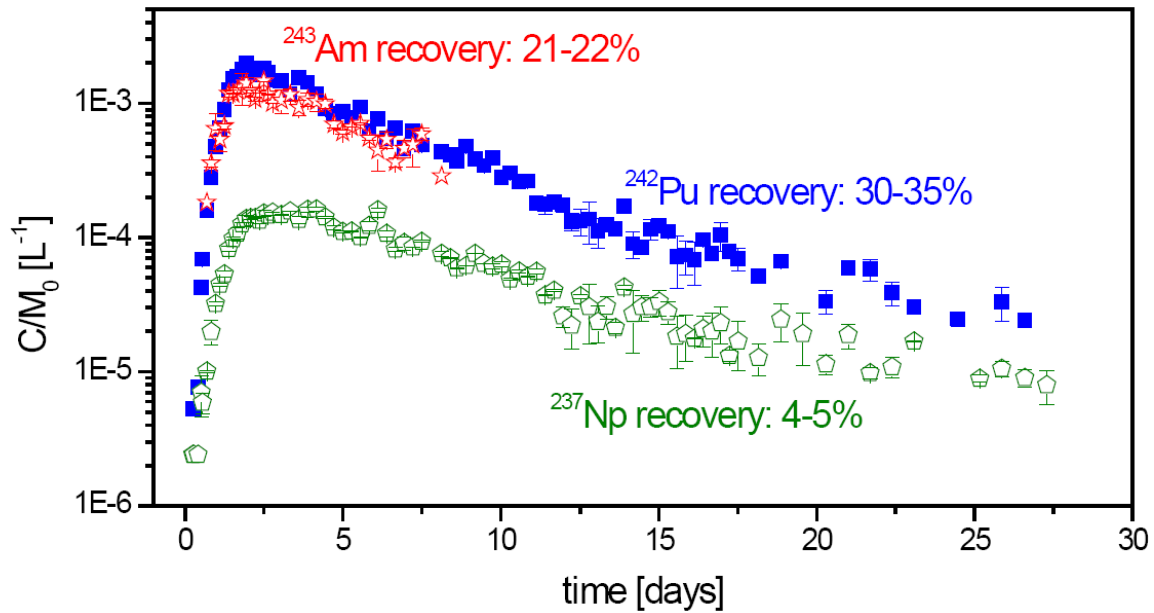


Figure 11: Breakthrough curve of the colloid-associated trivalent $^{243}\text{Am}(\text{III})$ and the tetraivalent $^{242}\text{Pu}(\text{IV})$. ^{237}Np is additional shown, which was injected in the pentavalent state. All data are normalized to the injected mass M_0 for comparison and recoveries are given [66].

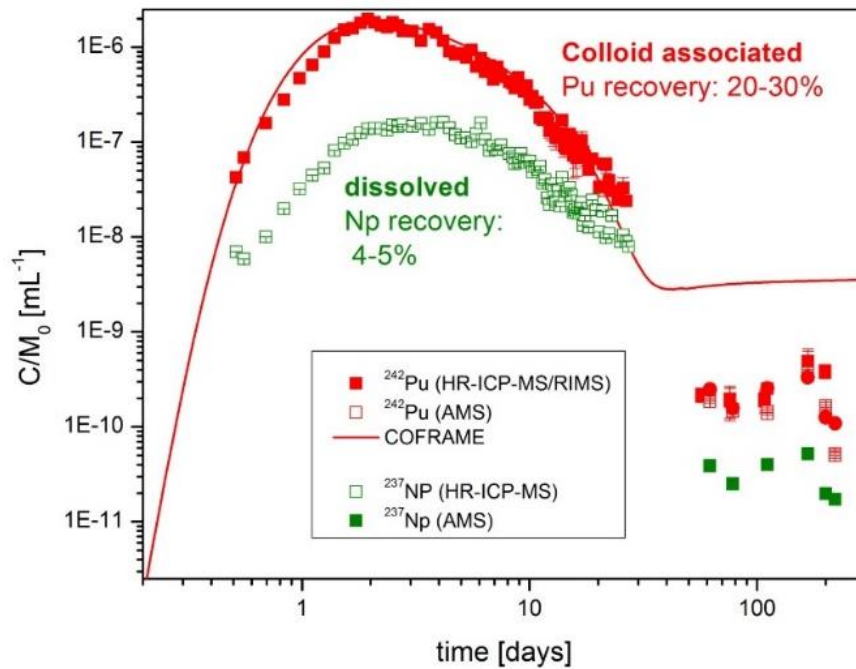


Figure 12: ^{237}Np and ^{242}Pu breakthrough curve of CFM Run 12-02 measured with SF-ICP-MS and extension to longer monitoring times in the tailing using RIMS and AMS. Long-term concentrations clearly differ from the COFRAME model [67].

Breakthrough curves of the colloid attached radionuclides have been modeled with the transport code COFRAME. A detailed description of the parameters, assumptions and simplifications can be found in Reiche et al. [68]. Regarding the long-term concentrations derived by AMS and RIMS, the COFRAME model calculations clearly overpredicted the dissolved fraction (Figure 12). This observation makes further improvement of the model concerning relevant RN immobilization and remobilization processes as well as the experimentally derived input parameters necessary.

The main conclusions of Run 12-02 are listed below. For a detailed overview of the results reference is made to the final reports of the Kollorado-2 [66] and Kollorado-e projects [67]:

- Control of the hydraulic system has allowed a further decrease in gradients and consequent decrease in flow velocities.
- The established flow velocity in the MI shear zone was with a 1% gradient and $\sim 10^{-5}$ m/s more relevant to the post-closure situation of a HLRW-repository. Thereby conservative tracer recoveries remained high.
- Colloid associated RN transport was detectable in the shear zone even after months after injection.
- RN recoveries were found to be lower for trivalent actinides compared to tetravalent actinides so that it can be concluded that the desorption rates were faster for the trivalent as compared to the tetravalent actinides.
- As a consequence of more reducing conditions in-situ at GTS, reduction processes were faster compared to supporting laboratory results
- The overall aim to prove that the megapacker sealing system performed well and was ready for the LIT experiment was confirmed.

Radionuclide colloid tracer test Run 13-05 was conducted in the same dipole configuration that was used within the CRR experiment but due to the meanwhile installation of the mega packer system, under much lower flow rates. A brief description of the tracer test can be found in the Kolorado-e final report [67] and only a summary of the major conclusions in comparison to the CRR experiment and the Run 12-02 is given here:

- The change of the residence time (80 min in CRR #32 to 2640 min in Run 13-05) within the fracture due to reduced flow rate had no effect on the conservative tracer recovery (92% for CRR and 92.6% for 13-05).
- In comparison to CRR #32 colloid mobility was clearly decreased from 85-100% to only 36-38% as consequence of the increased residence time.
- $^{233}\text{U(VI)}$ and $^{237}\text{Np(V)}$ recoveries were significantly lower in comparison to CRR #32. The decrease can be explained by reduction during the much longer residence time within the shear zone.

Ten years of site preparation, characterization and work on the experimental design finally lead over to CFM phase three and to the main experiment. This is the latest phase of the CFM project and deals with the installation and operation of the long-term in-situ test (LIT) and is to date still ongoing. The LIT experiment is a main part of this thesis and described in detail below.

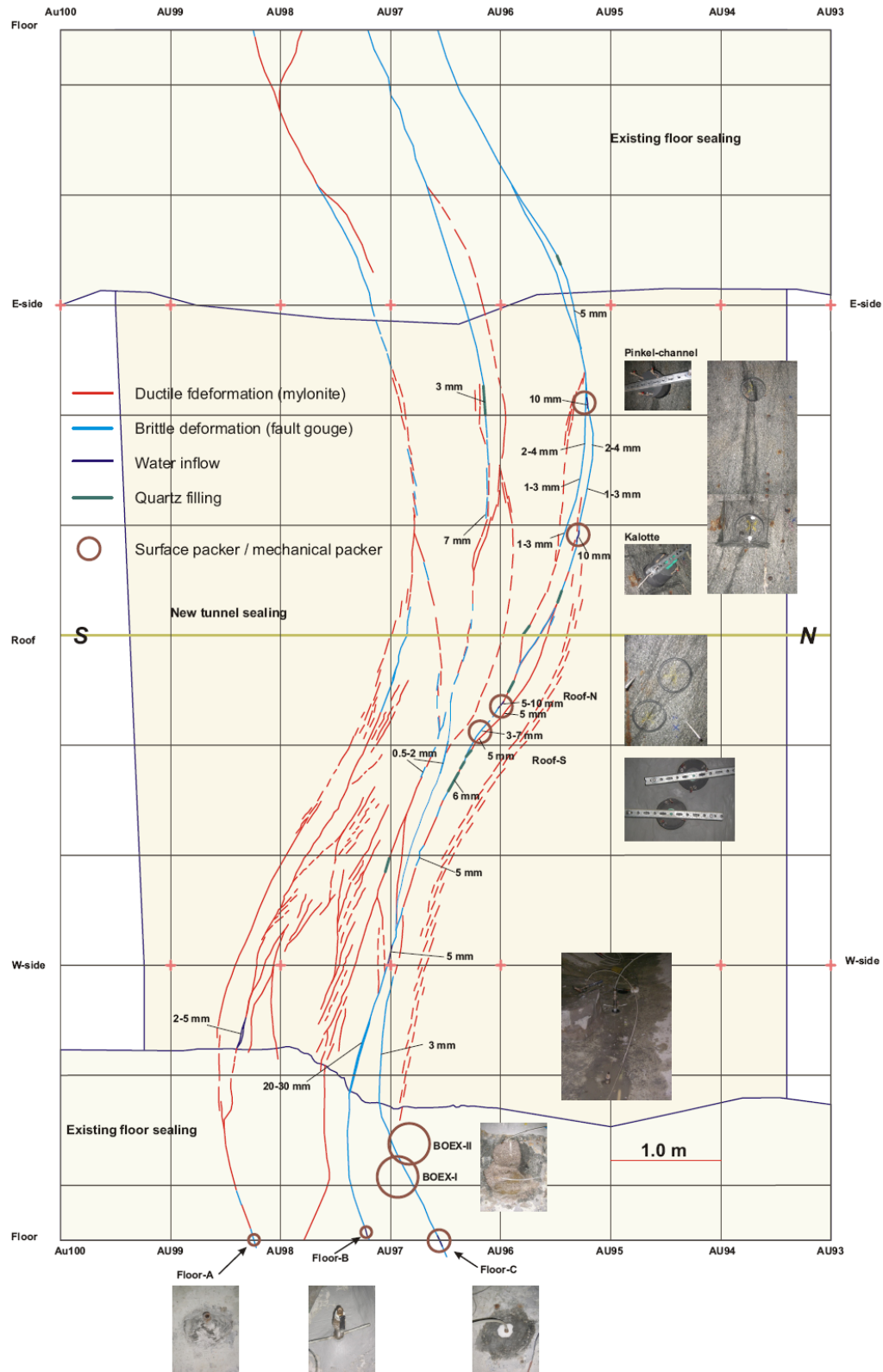


Figure 13: Detailed geological mapping of the MI shear zone between tunnel meters AU93 and AU100 with surface packer locations [63].

4 *Aims of the PhD thesis*

As part of the normal evolution scenario of a deep geological repository in the Scandinavian countries (i. e. Sweden, Finland), diluted glacial melt waters will reach down to repository depths. This process is induced by the strong hydraulic gradients originating from the ice sheet coverage of future glaciation. These low mineralized groundwaters will induce bentonite swelling at the contact zone between the bentonite buffer and a water conducting feature. Bentonite swelling can under low mineralized glacial melt water conditions lead to generation of bentonite colloids that can be transported away from the repository under advective conditions [1].

Over the last couple of years research at INE focused on:

- Erosion of compacted bentonite as a function of bentonite dry density, exchangeable cation composition, bentonite type, contact water and flow velocity [58, 69, 70]. The main focus was on providing experimental erosion rates and process understanding to improve modelling of the erosion process. A status of these experiments is given in 3.1.
- Separation of bentonite derived colloidal suspensions by centrifugation/sedimentation techniques and interaction of these colloids with radionuclides [8] under glacial melt water conditions have been explained in detail in 3.2. The experiments included also reversibility studies (radionuclide desorption from clay colloids) by addition of fracture filling minerals (fault gauge, FG) or natural organic matter (humic acid, fulvic acid) [4, 12, 15]. The surfaces of the added materials acted as competing ligands for the clay colloid bound radionuclides.
- Quantifying the mobility of bentonite derived montmorillonite particles in natural fractures in laboratory column experiments as well as field experiments at the GTS. These experiments have been conducted in the frame of the CRR and the CFM project. These studies confirmed the mobility of montmorillonite colloids from the cm-scale to the meter-scale and highlighted the effects of sorption reversibility [9-11, 59, 71, 72] (see 3.2).

Based on the current state-of-the-art knowledge presented in Chapter 3.1 a good understanding of bentonite derived montmorillonite colloid stability, radionuclide interaction and transport under dilute glacial melt water conditions has been obtained.

On the one hand side the expansion of the current knowledge concerning bentonite erosion processes to more relevant systems is an aim of this PhD. After the RN-colloid migration tests performed within the CFM project where a pre-produced RN-colloid suspension was injected in the shear zone, an experiment that combines in-situ colloid generation combined with a radionuclide tracer source became mandatory and was realized with the Long-term In-situ Test (LIT) in the time frame of this PhD. Experimental laboratory bentonite erosion mock-up tests are conducted in order to validate experimental data from the field and to support the interpretation of this data.

On the other hand side batch experiments dealing with the kinetics of radionuclide sorption to and desorption from colloids in the presence of natural FG material are part of this PhD. The aim is a more precise quantification of kinetic parameters like time dependent distribution coefficients as well as sorption and desorption rates in different systems to describe the long-term interaction of radionuclides with FG material. As has been shown within the latest migration experiments in the frame of the CFM project, namely CFM Run 12-02 and Run13-05, the radionuclide concentrations appearing in the effluent after 0.1 a are significantly overestimated by the modelled COFRAME data. Short time data (< 0.1 a) are dominated by colloid mediated radionuclide transport while the long-term (> 0.1 a) concentrations originate either from a slow desorption of radionuclides from initially sorbed colloids on the fracture wall or from a slow desorption process directly from the fracture filling minerals. Goal of this PhD thesis is the improvement of the model by the implementation of desorption kinetic data obtained in RN-FG sorption reversibility experiments. Thereby radionuclides get in contact with natural FG material from GTS in the binary system RN-FG and in the ternary systems RN-FG-montmorillonite colloids over a long time-scale. The experiment was carried out under natural granitic groundwater from GTS. Sorption time depending desorption kinetic data was collected by varying the contact time during sorption between 1 d and 232 d and one desorption experiment after each sorption time step, respectively. Studying the binary system was stopped after a total experimental time of 400 days, including both sorption and

desorption time. At this point, synthetic montmorillonite particles were added as competing surface in order to trigger desorption in the ternary system.

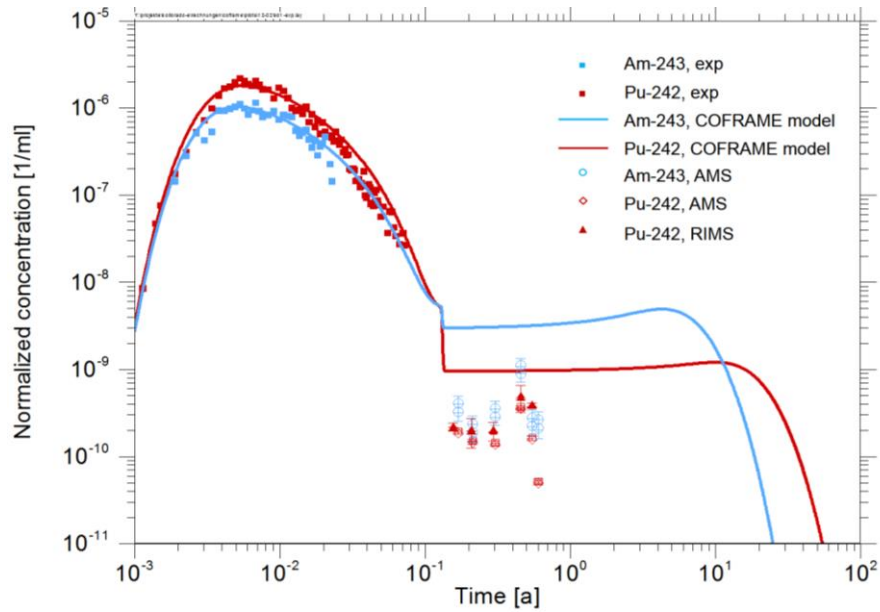


Figure 14: Modelling of CFM Run 12-02 with the COFRAME model (Personal communication with Ulrich Noseck, GRS). The Accelerator Mass Spectrometry (AMS)- [73] and Resonance Ionization Mass Spectrometry (RIMS)-derived long-term data (Reich et al., unpublished) lie below the modelled concentrations.

5 *Methods*

5.1 *Inductively Coupled Plasma - Mass Spectrometry*

Inductively coupled plasma - mass spectrometry (ICP-MS) is accepted as a powerful multi-element analytical technique, capable of true multi-elemental determinations within minutes. ICP-MS detects elemental compositions at ultra-trace concentrations. The basic principle of ICP-MS is elemental differentiation by weight differences in atomic mass. While atoms of one element may consist of different isotopes, the natural isotopic composition of each element is usually well known and can be taken to calculate element concentrations [74, 75]. Differentiation between neutral atoms is not possible. Therefore, in a first step atoms are ionized to form detectable positively charged ions. This is performed by sample injection in an inductively coupled plasma (ICP) at very high temperature (5000 - 10000 K).

Samples have to undergo six essential steps within an ICP-MS analysis. These are:

- Conversion of the liquid sample into an aerosol before introduction into the plasma
- Drying, atomization and ionization within the plasma
- Ion extraction from the plasma
- Focusing of the ions and transport to the mass spectrometer
- Separation of the charged particles according to the mass-to-charge ratio (m/z)
- Detection and quantification of the produced ions by the detector

A closer look to available separation methods will follow because the instruments used in this study differ in terms of the ion separation. A summary of all the mentioned processes is given by Linge et al. [76].

In order to quantify each element, the respective ions of a distinct mass-to-charge ratio must be separated from the ion beam. The most common mass spectrometer used in ICP-MS is the quadrupole mass filter. It consists of four metal rods, oriented in parallel to the ion beam. The rods are equidistant from the beam [77]. A scheme of the quadrupole mass filter can be found in Figure 15. Voltages applied to the rods build up a magnetic field and cause the ions entering the quadrupole to oscillate. Only ions with a stable trajectory depending on the current voltage of the rods will leave the quadrupole mass filter. The voltage within the mass filter must be varied to scan

over the elemental composition of a sample. This scanning process is very rapid and data over a broad mass distribution (0-300 u) can be collected in less than a second.

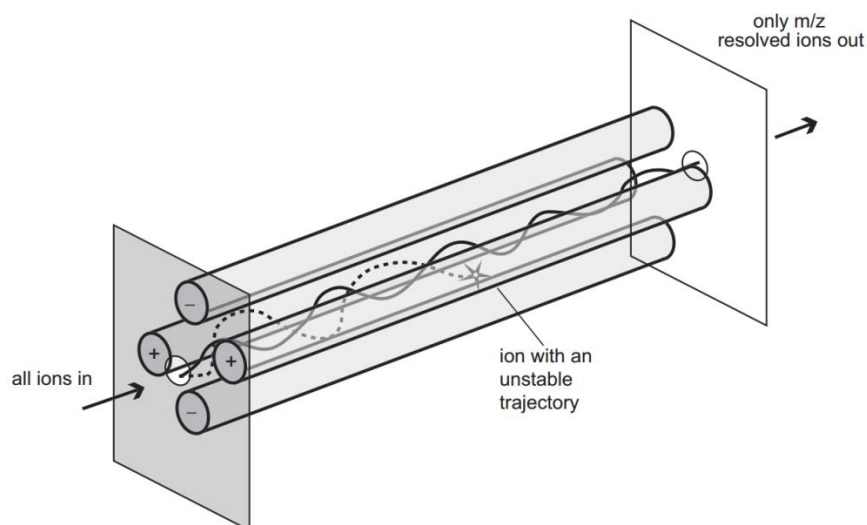


Figure 15: Schematic diagram of a quadrupole mass filter. Only ions of a single m/z have a stable path and exit the quadrupole [76].

An even more sensitive ion separation method applied within this study can be found in the high resolution magnetic sector field ICP-MS (SF-ICP-MS). In this case the ions are separated using the mass-to-charge ratio in a laminated magnet as well as by the difference of the kinetic energy of the ions by using an electrostatic analyzer [78, 79]. A magnetic field is applied perpendicular to the ion beam and forces the ions to move on a circular path. The radius of the movement depends on the magnetic field, m/z and the velocity of the ions. Only ions travelling on a distinct circular path will pass through a narrow slit and reach the detector.

Sector field ICP-MS is a very sensitive method and can resolve differences in m/z to 0.01 - 0.001 u. In comparison a quadrupole ICP-MS can resolve only to 0.5 - 1 u. Detection limits of the sector-field ICP-MS are typically in the ppq range and at least one order of magnitude below the detection limit of a quadrupole ICP-MS. It also shows less electronic noise and lower background but on the other hand slower scan speed and higher costs in comparison to ICP-MS. It is typically applied to determine a limited group of elements, rather than scanning for multi element overview. The precision of trace element analysis with ICP-MS is normally in the order of 2-5% [76].

Both types of ICP-MS devices mentioned above have been used for sample analysis within this work:

- Most samples were measured with a Thermo Scientific XSERIES 2 quadrupole ICP-MS. It was suitable to determine bentonite colloids by the concentrations of the main elemental components (Mg, Al, Fe, Zn, and Ni) as well as changes in the background concentrations by applying the TotalQuant method that is described in the next section. Detection limits are often below 1 ppt but typically element and water matrix dependent.
- Most radionuclide concentrations were determined on a Thermo Scientific Element XR High resolution sector-field ICP-MS. Detection limits for most actinides are in the ppq-range ($\sim 10^{-15}$ M).

The TotalQuant method describes a semi-quantitative scan over the total elemental concentrations within an analyte. This method makes the determination of an overview concerning the elemental composition simple, fast and flexible. A standard solution that contains typically ten analytes is used for calibration. During the following measurement the system can determine semi-quantitative concentrations for around 70 analytes using a peak-jumping acquisition method. Results for certified stock solutions in the semi-quantitative measurement show good agreement with known values. The expected error of this method is $\leq 30\%$ [80].

Samples have been measured without pretreatment or up to 5-fold diluted in 2% HNO₃ (suprapur, Merck KGaA, diluted from 65% with ultrapure water) if the sample volume was limited. HF has been added to the bentonite colloid containing samples in order to dissolve the clay nanoparticles. Hydrofluoric treatment was not necessary in case of the SF-ICP-MS measurements because direct injection of the colloid containing suspensions into the plasma was possible in case of this device.

5.2 Inductively Coupled Plasma - Optical Emission Spectrometry

Inductively coupled plasma - optical emission spectrometry (ICP-OES) is a powerful technique in elemental analysis, suitable for the determination of roughly 70 different elements in varying matrices and was applied for quantification of higher concentrated colloid suspensions in the range of several ppm to 1,000 ppm. An inductively coupled plasma is like in case of the ICP-MS techniques applied for ion generation. Differences to the ICP-MS can be found in the detector system. Elements are excited within the plasma to emit photons, which are used to identify the elemental components by their element specific characteristic wavelength after spectral separation. Quantitative analysis is achieved over the intensity of the emitted light. In ICP-OES, simultaneous analysis of a multitude of elements is possible as all elements within the sample are excited in the plasma at the same time. Therefore the time-span of a measurement is short which is the major advantage of this method but quantification of ultra-trace amounts like in the case of ICP-MS is not possible [81]. Two ICP-OES devices have been used within this thesis, namely ICP-OES Optima 8300DV (Perkin Elmer Inc.) and ICP-OES Optima 4300DV (Perkin Elmer Inc.).

5.3 *Laser-based analytical methods*

The word laser is an acronym for light amplification by stimulated emission of radiation and its history can be traced back to Max Planck and the publication of his work on the law of radiation in 1901 [82] as well as Albert Einstein, who developed the theory of stimulated emission [83]. Einstein thereby established the fundamental principle behind the laser. It took however over 40 years until his theory was proven and the first working laser was built [84].

5.3.1 *Laser theory and breakdown creation*

Over 50 years after it was invented, the laser became an indispensable technique in many aspects of analytical chemistry. The most important demands on a laser system for analytical issues are tunability, feasible power density, monochromaticity, coherence, directionality and in the case of pulsed lasers pulse to pulse stability [85]. All lasers consist of three main parts, namely a pumping source, the lasing medium and an optical cavity or resonator. Pumping describes the input of energy into the lasing medium. Pumping by electrical discharge, the use of flash lamps or other lasers as pump source is possible. Thereby population inversion in the lasing medium is established. Laser classification by the different lasing media is one possibility and results in dye, gas, semiconductor and solid-state lasers. The further explanation will focus on the pulsed Nd:YAG solid-state laser as it is the most important system for this work but a detailed overview on laser systems can be found elsewhere [85, 86].

5.3.1.1 *Nd:YAG solid-state laser*

The Nd:YAG laser is of special interest as it is the laser type used for breakdown creation in all LIBD devices described and used in this work. It has been chosen as Nd:YAG lasers are small and portable, show short, high energy pulses combined with high beam quality and high pulse-to-pulse stability [87]. The lasing medium is a neodymium-doped (0.5 - 1.5% Nd³⁺) yttrium aluminum garnet (Y₃Al₅O₁₂:Nd³⁺) and can be described as a four-level laser system. Nd:YAG shows three possible transitions for laser operation. The ⁴F_{3/2} to ⁴I_{11/2} transition at ~1.06 μm is the commonly used lasing transition but the ⁴F_{3/2} to ⁴I_{13/2} transition at ~1.33 μm and the ⁴F_{3/2} to ⁴I_{9/2} transition at ~0.94 μm, which is seldom used, are also applicable [88] (Figure 16). In all cases optical pumping raises the neodymium ions from the ground state to a higher energy level followed by radiation

5.3.1.2 Breakdown creation

Soon after the development of the ruby laser, experiments showed that focusing a laser beam resulted in the creation of a breakdown in air and on metals. Laser-induced breakdown can be defined as the generation of a totally ionized gas, a plasma. Thereby a glow or flash is observed in the focal region (Figure 17). Plasmas created by the focused radiation from pulsed laser beams were first reported in 1963 by [90].

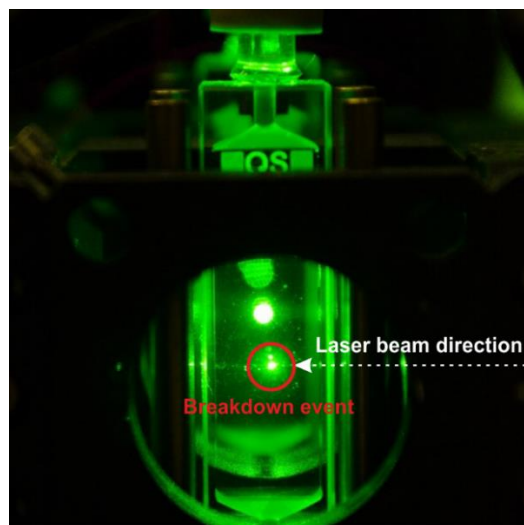


Figure 17: Nd:YAG laser induced breakdown event in a bentonite colloid suspension.

There are two main mechanisms for electron generation and growth, namely cascade ionization and multiphoton ionization. The first mechanism describes absorption of laser radiation by electrons and ionization of the sample if the electrons gain enough energy (Equation 9). The electron concentration will increase exponentially with time.



In fact, two criteria must be fulfilled for cascade ionization. The electron energy has to exceed the ionization threshold of the sample and initial electrons have to be present in the focal region. Initial electrons can be generated by multiphoton ionization, the simultaneous absorption of a sufficient

number of photons by an atom or a molecule, present in the focal region, to cause ionization (Equation 10).



Both cascade and multiphoton ionization require high laser irradiances of at least 10^8 W/cm² but breakdown of solids can be observed already at two orders of magnitude less laser irradiances caused by a third mechanism, called thermal runaway. This mechanism is caused by self-focusing in solid particles and affects the beam to focus in a smaller volume than expected by the laws of classical optic.

5.3.2 *Laser Induced Breakdown Detection (LIBD)*

The laser-induced breakdown detection method has been developed particularly for the characterization of aquatic colloids in dilute concentrations. LIBD is based on the generation of dielectrical breakdowns in the focus of a triggered laser beam. As the threshold energy to create a breakdown for a solid is lower than for a liquid or a gas, the breakdown can be generated selectively on particles dispersed in solution at suitable pulse energies [91]. Therefore, the laser energy is chosen below the threshold energy needed to generate breakdowns of the liquid phase but occur when nano-particles enter the focus of the laser beam only. The breakdown probability is the ratio between breakdown events and total number of laser shots. It is used to determine colloid concentration, mean size or even size distribution of a sample. Breakdown events can be detected either by the acoustic signal produced by the rapid expansion of the plasma or by the emitted light during the plasma recombination. A distinction is drawn between optical detection of the breakdown position along the laser beam axis at fixed laser energy and photoacoustic or optical breakdown detection while stepwise increasing the laser energy. The first method gives particle mean size and concentration. By varying the laser energy, it is possible to gain information about a sample's particle size distribution but measurement time will increase.

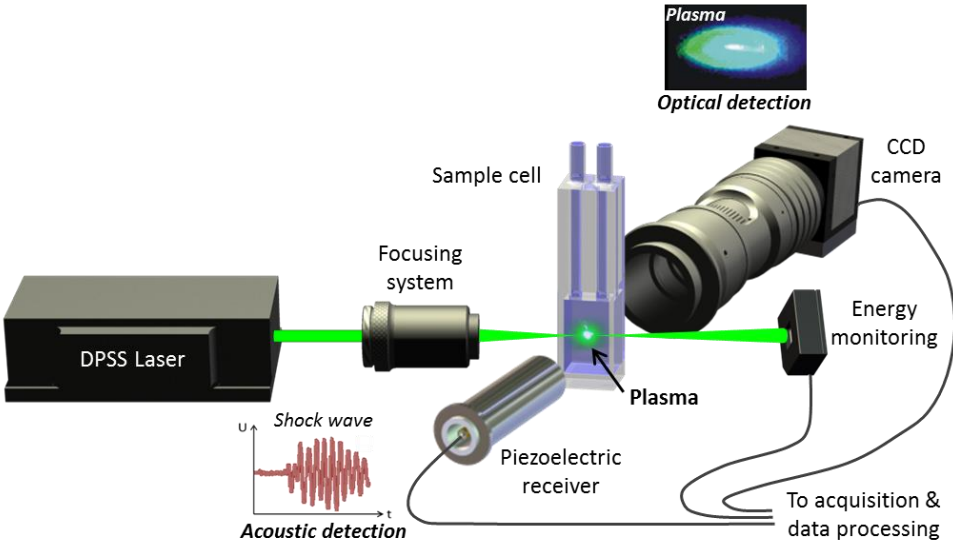


Figure 18: Fundamental LIBD functionality
 (http://www.innovation.kit.edu/img/Setup_LIBD.png)

5.3.2.1 LIBD with 2D-optical data acquisition

All LIBD devices consist of a laser source, an optical pathway with the focusing system, the sample cuvette and a breakdown analyzer (Figure 18). LIBD with optical data acquisition uses a high energy Q-switched Nd:YAG laser (Minilite™ Series, Continuum) with a repetition rate of 15 Hz for breakdown creation in combination with a CCD camera to record the emitted light during plasma recombination. The optical pathway is simple. It consists of two components only, namely a semi-transmissive mirror and a focus lens. A small part of the laser beam is separated by the mirror and used to control and to adjust the laser energy. The focus lens is located in front of the sample cuvette and focusses the laser beam into the cuvette. The CCD camera is located perpendicular to the laser beam axis and records the breakdown events along the laser beam axis. The compact setting of the LIBD with optical data acquisition is shown in Figure 19 and makes it a robust, reliable system which is installed on a mobile table to be suitable for field experiments.

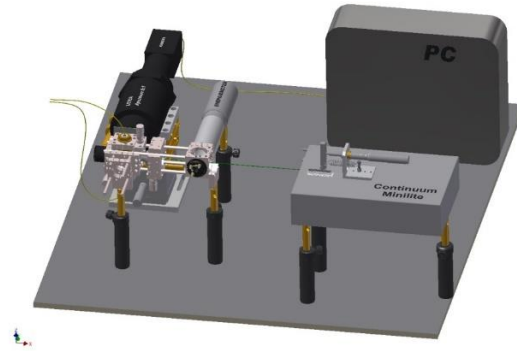


Figure 19: Scheme of LIBD with optical data acquisition.

Through optical data acquisition, size information is gained by measuring the spatial distribution of the breakdown events along the laser beam axis at constant laser pulse energy [91-93]. As the laser beam is focused in the sample, highest laser energy density is located in the focal region and decreases over the distance from the focal point. A CCD camera is oriented perpendicular to the laser beam axis and records the position of the breakdown events along this axis (Figure 19). Breakdowns produced by small particles are concentrated selectively near the focal region, whereas bigger particles form breakdowns at lower energy densities (Figure 20). This is caused by the reciprocal correlation between particle size and breakdown generation threshold and produces a broader distribution along the laser beam axis for bigger particles. The evaluation of the recorded data is in contrast to the s-curve LIBD a simple task. The position of the breakdown events is plotted in a histogram and the full width at half maximum of the Gaussian fit of the resulting distribution is used to calculate the mean particle diameter (Figure 21). The colloidal concentration of the sample is accessible over the mean particle diameter in combination with the breakdown probability. LIBD with optical data acquisition is a statistical method and it is recommended to record at least 1000 breakdown events to achieve reliable and reproducible results. Taking into account that most aquifers naturally contain at least $1 \cdot 10^8$ particles/mL it is obvious that only a very small sample volume is analyzed (1000 breakdowns correlate to a sample volume of $0.01 \mu\text{L}$). Therefore sample homogenization during the measurements is a crucial task.

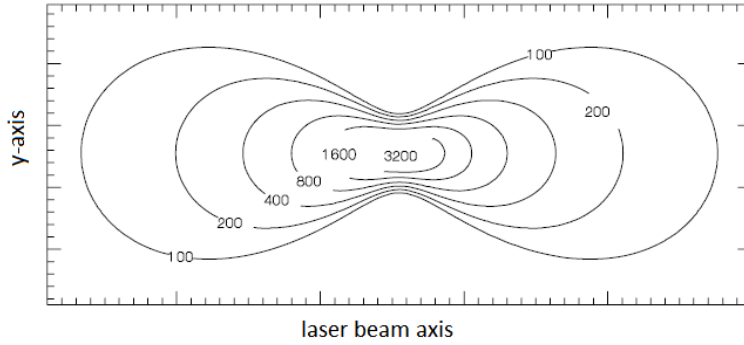


Figure 20: Contour plot of equal power area-density. The numbers indicate the relative energy density. [94]

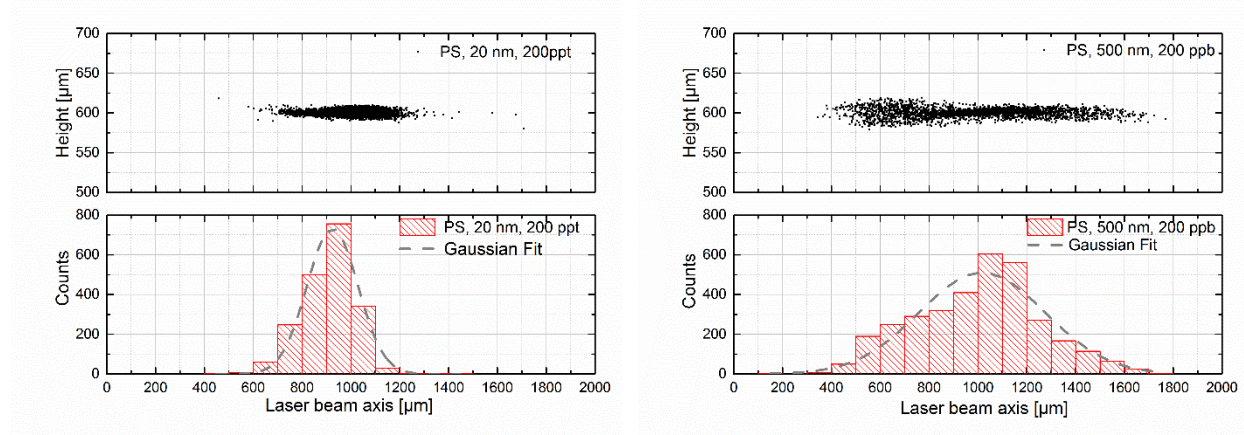


Figure 21: Breakdown distribution of (left) 20 nm and (right) 500 nm polystyrene standards along the laser beam axis (top) and the same data ordered in a histogram. Size information is gained over the full width at half maximum of the Gaussian fit [91] (bottom).

The breakdown probability (h_{bd}) is correlated with the particle number density (c_p), the particle volume (V_p) under the assumption of spherical particles and the particle size specific effective focus volume (V_{eff}) in accordance with the formula

$$h_{bd} = 1 - (1 - c_p \times V_p)^{V_{eff}/V_p} \quad \text{Equation 11}$$

and

$$c_p = (1 - (1 - h_{bd})^{V_p/V_{eff}}) * 1/V_p \quad \text{Equation 12}$$

The effective focus volume describes the volume within which a particle of a certain size will be excited by a laser pulse exceeding the respective power density. V_{eff} increases with increasing

particle diameter and laser energy but is independent of the particle number density for a wide range of concentrations. V_{eff} can be calculated according to [95] by

$$V_{eff} = V_p \frac{\log(1 - h_{bd})}{\log(1 - c_p * V_p)} \quad \text{Equation 13}$$

Plotting V_{eff} against the particle diameter (d_p) and treating the data with an allometric fit leads to a direct dependency between V_{eff} and d_p [nm].

$$V_{eff} = 375 * d_p^{1.10} \quad \text{Equation 14}$$

5.3.2.2 *S-curve LIBD*

S-curve LIBD is an advanced LIBD method to investigate colloidal size distributions in multimodal size suspensions by variation of the laser pulse energy. As bigger particles form breakdowns at lower laser energy, size distributions can be analyzed by recording the breakdown probability while step-wise increasing the laser pulse energy followed by computational data evaluation. The method is called s-curve LIBD as the resulting breakdown probability plotted over the laser pulse energy has an s-curve shape in the diagram. The threshold energy of the s-curve which is needed to create first breakdowns is characteristic for the particle size and the concentration is given by the slope. In a multimodal size suspension, the measured curve can be described by the combination of several unimodal s-curves. In order to facilitate this approach, a number of calibration measurements at different particle densities for each particle size is needed. The measured calibration curves for the latest calibration performed within this study can be found in A-Figure 1 and A-Figure 2. Two s-curve LIBD devices have been available. Main differences can be found in laser pulse energy and frequency of the pulsed Nd:YAG lasers, the dimension of the optical pathway, possible additional features and especially the mobility of the systems. In the following, the systems will be differentiated as the stationary and the mobile s-LIBD.

The stationary s-LIBD system is fixed on a table under a cleanroom ventilation system without the possibility to change the site of the device. As all LIBD systems, the stationary s-LIBD consists of the laser, the optical pathway, the energy analyzer, the sample cuvette and a breakdown detection device (Figure 22). The laser is a low power diode pumped Nd:YAG system (BMI, Soliton, DIVA) and is pulsed at a repetition rate of 20 Hz [94]. Main differences to the former explained LIBD with optical data acquisition can be found in the necessity to fine-tune the laser energy. This is realized by the installation of a computer-controlled polarizer in the optical pathway. The laser energy is step-wise increased while the breakdown probability is recorded for each energy step, respectively. Size distribution is determined by the shape of the resulting breakdown curve, more precisely by the threshold energy and the slope of the s-curve. The position of the breakdown event on the laser beam axis is not relevant for this method. Therefore, optical data acquisition is not mandatory and is replaced by photoacoustic detection with a piezo element. Additional instruments are located behind the sample cuvette in order to ensure to a best possible measurement conditions including for example a continuous wave laser for optimization of the optical path and a beam profiler to ensure good beam quality.

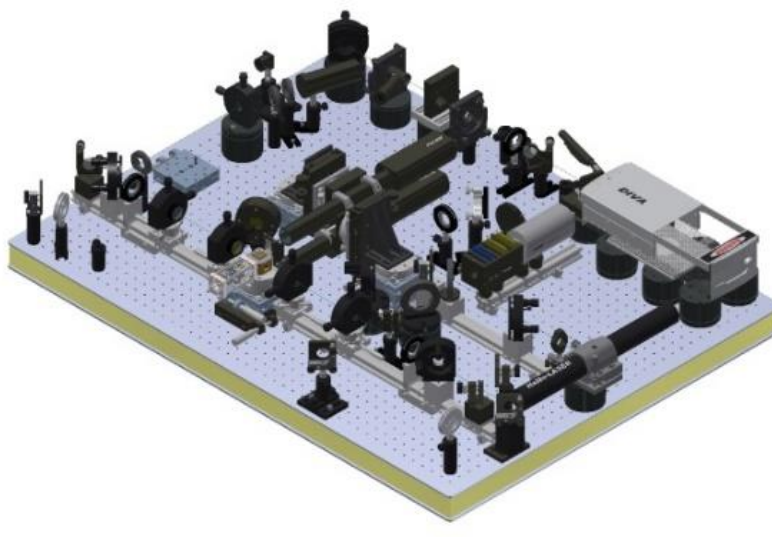


Figure 22: Scheme of the S-curve LIBD device with acoustic data acquisition.

The second s-curve LIBD was built as a robust, portable system and developed as completion of the LIBD systems regarding the possibility to use s-curve LIBD within field experiments (Figure

23). The mobile s-LIBD is the prototype for a commercially available nanoparticle analyzer, produced and distributed under the label Magellan by Cordouan Technologies (www.cordouan-tech.com). A diode pumped Nd:YAG laser (Flare 532-40-100, Coherent Inc.) is used for breakdown creation at a pulse frequency of 100 Hz. The remaining parts are similar to the first mentioned s-curve LIBD and breakdown detection is facilitated with the same kind of piezo element.

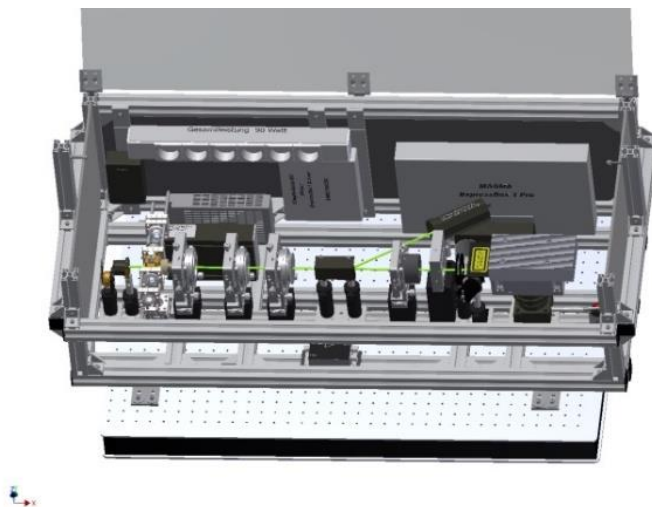


Figure 23: Scheme of the mobile s-curve LIBD device with acoustic data acquisition.

5.3.2.3 Calibration

Calibration of the LIBD systems was carried out on the three described LIBD devices. The mobile devices have been transported in the course of this thesis several times from KIT-INE to the Grimsel Test Site (Guttanen, CH) to observe the colloidal composition during on-site measurement campaigns.

Monodisperse spherical polystyrene (PS) microspheres (Nanosphere Size Standards, Distrlab B. V.) in the particle size range from 20 nm up to 900 nm were used for calibration purposes at various concentrations for each particle size class. A selection of eight spherical PS particle sizes was used (Figure 24). LIBD is a particle number density sensitive technique. Therefore, initial mass concentrations and the concentration range for each particle size differ. Detection limits of $5 \cdot 10^6$ particles/mL for the smallest 20nm particles down to $1 \cdot 10^5$ particles/mL for the biggest 900 nm particles were found.

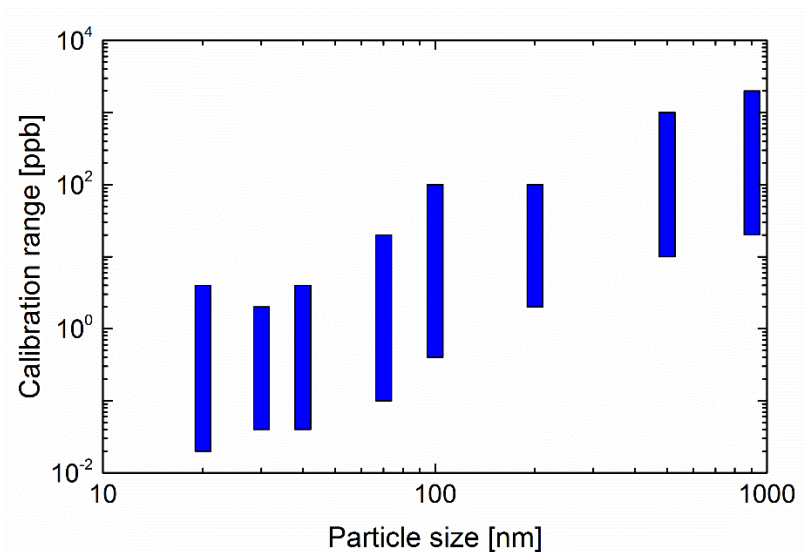


Figure 24: Calibration range of the mobile LIBD with optical data acquisition.

To make sure that all LIBD devices measure the same sample, the test solution was circulating through the three laser systems and measured in flow-through cuvettes on all devices simultaneously. The devices were connected in the order of increasing laser pulse frequency to minimize the laser damage on the sample and the appearance of artefacts. For each particle size a 400 mL reservoir of the test solution was provided beginning with the measurement of ultra-pure water (Milli-Q; $< 16.2 \mu\text{S}/\text{cm}$) to reassure that an acceptable threshold value for the breakdown probability was achieved during washing and the ultra-sonic cleaning. One sample solution was used for each particle size, respectively. Particle concentrations were measured from lowest to highest values. Thereby, particle concentration was increased by adding a specific amount of the PS standard to reach the next higher concentration after each measurement.

6 *Materials*

One of the reference scenarios in the Swedish safety case is the intrusion of dilute glacial melt water down to repository depths and the contact of this low mineralized water with the bentonite buffer/backfill material which will result in bentonite swelling and erosion of colloidal particles. If the canister within the respective bentonite buffer was not intact and the radionuclides were in contact with the buffer material, radionuclides attached to the eroded colloids may be transported away from the repository in the advective flow field. Relevant concomitant processes relate to the sorption of radionuclides to bentonite colloids as well as the interaction of radionuclides in a system consisting of fracture filling minerals, groundwater and colloidal matter. This thesis aims at describing the relevant processes in case of dilute groundwater intrusion into the repository.

6.1 *Natural groundwater from the Grimsel Test Site (GTS, Switzerland)*

Natural granitic groundwater (GGW) from GTS is used for bentonite erosion experiments as well as for radionuclide sorption reversibility studies. The groundwater is a $\text{Na}^+/\text{Ca}^{2+}\text{-HCO}_3^-/\text{SO}_4^{2-}$ groundwater type (Table 2) with a pH of 9.6 and an E_{hSHE} below -200mV. Low salinity of 1.2 mM makes this groundwater comparable to expected glacial melting water that may in the Scandinavian scenario reach down to repository depths within the relevant time span of a repository [1, 96].

The water was filled in 50 L Teflon coated Al- barrels which were cleaned and filled with Argon gas thoroughly before they were transported to the GTS for sampling. Sampling was performed under low flow rates ($< 10\text{mL}/\text{min}$) similar to the minimal-draw down procedure established by USEPA [97] in order to sample artifact-free the natural mobile colloid fraction. Once filled, the barrels remained for several days on the opened sampling line and the water was flushed through the barrels in order to exclude any interaction with oxygen or CO_2 that may still have been inside the barrels.

Table 2 GGW composition

| | Barrel 4-14 | Barrel 4-16 | Literature [98] |
|----------------------------------|-------------|-------------|-----------------|
| pH | 9.33 | 9.18 | 9.67 |
| Eh _{SHE} | 201 mV | 260 mV | |
| Ionic strength | | | 1.2 mM |
| [Mg ²⁺] | 21.2 µg/L | 34.5 µg/L | 12.6 µg/L |
| [Ca ²⁺] | 7.5 mg/L | 8.1 mg/L | 5.3 mg/L |
| [Na ⁺] | 8 mg/L | 12.4 mg/L | 14.7 mg/L |
| [Al ³⁺] | 12.6 µg/L | - | 42.9 µg/L |
| [Fe ^{2+/3+}] | - | - | < d. l. |
| [Sr ²⁺] | 210 µg/L | 145 µg/L | 182 µg/L |
| [Cl ⁻] | 0.9 mg/L | 1.6 mg/L | 6.7 mg/L |
| [SO ₄ ²⁻] | 5.9 mg/L | 7.8 mg/L | 5.8 mg/L |
| [F ⁻] | 4.5 mg/L | 4.6 mg/L | 6.3 mg/L |
| [Si] | 4.2 mg/L | 2.7 mg/L | 5.6 mg/L |
| [HCO ₃ ⁻] | 3.6 mg/L | 4.0 mg/L | 3.0 mg/L |

6.2 *Fault Gouge material from GTS*

The FG material was collected at the Grimsel Test Site (GTS), Switzerland. The main rock type in the Grimsel area is the so-called Grimsel granodiorite [99]. It consists of plagioclase, quartz, K-feldspar, biotite and accessory minerals like muscovite/sericite, apatite, sphene, epidote, zircon, calcite and opaque minerals (e.g. Fe-oxides like magnetite) [100]. The material was extracted from an outcrop of the Colloid Formation and Migration (CFM) project MI shear zone at the AU tunnel wall outside the controlled area. FG was transferred to KIT-INE, crushed and separated under ambient conditions using sieves with meshes between 63 µm up to 5 mm. Thereby, FG in seven different grain sizes (< 63 µm (VII), 63-125 µm (VI), 125-250 µm (V), 250-500 µm (IV), 500-1000 µm (III), 1-2 mm (II) and 2-5 mm(I)) was generated. Only the size fraction IV was used for the radionuclide sorption and reversibility experiments. These fractions were washed and equilibrated using natural Grimsel groundwater (GGW) over a period of two weeks and exchanged regularly five times to remove any fines in the supernatant.

Environmental Scanning Electron Microscopy (ESEM, QUANTA 650 FEG) analysis of the size fraction was carried out. The FG material was dried at 60°C and transferred to the ESEM device. Results are shown in Figure 25 corroborating the sieved size fraction of 250µm - 500µm. By

application of energy-dispersive X-ray spectroscopy (EDX) element analysis was possible and used to estimate the FG mineralogy yielding mainly feldspar, plagioclase, quartz and phyllosilicates. As expected the artificially and freshly crushed grains show a very rough and irregular shape.

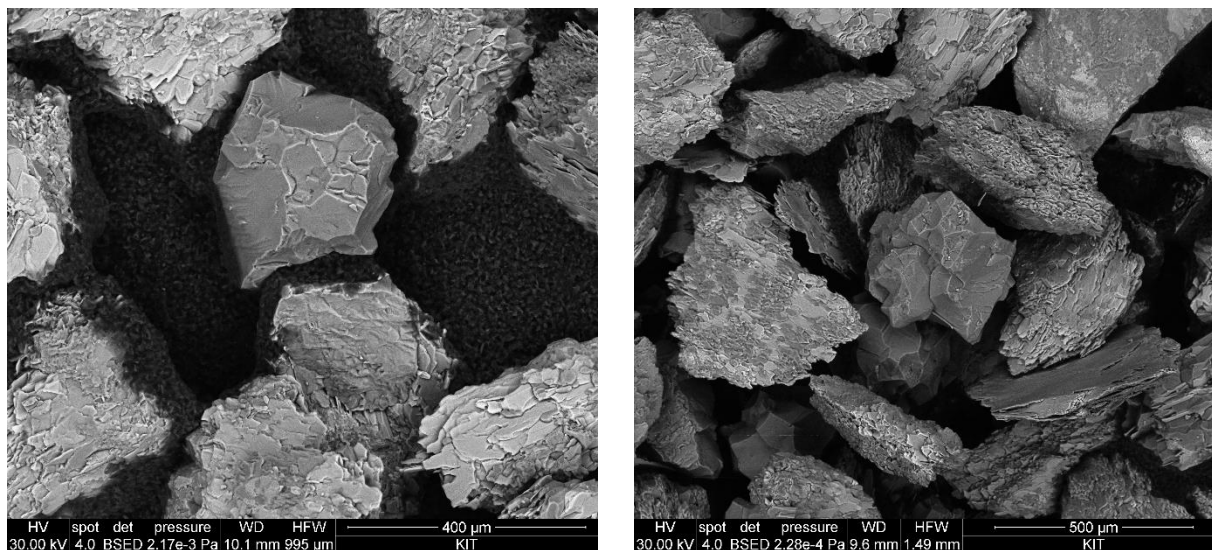


Figure 25: ESEM images of the 250-500 μm grain size fraction of FG. EDX verifies quartz, feldspars and phyllosilicates.

Powder X-ray diffraction analysis was conducted to determine the mineralogical composition of the size fraction used. XRD spectra were recorded from $5^\circ - 90^\circ 2\theta$ with a Siemens D5000 powder diffractometer equipped with a scintillation detector and $\text{Cu K}\alpha$ radiation. Results of the analysis yield mainly mineral phases like quartz, plagioclase, K-feldspar in line with literature data. Chemical composition of FG was quantified by XRF (MagiXPro, PANalytical B. V.) concerning the major and trace elemental composition of the FG material used (Table 3). In line with general granitic rock composition SiO_2 , Al_2O_3 , Na_2O , Fe_2O_3 and K_2O dominate reflecting the main minerals plagioclase, feldspar and quartz. The dominating Fe redox state is Fe(II) with 2.71% of 3.87% total Fe present in the sample as determined by photometric analysis.

Table 3: Results of XRF analysis, the main components are given in weight-% of the respective oxides.

| Component | FG, 500 - 1000 μm grain size | FG, 250 - 500 μm grain size |
|--------------------------------|---|--|
| SiO ₂ | 65.3% | 64.6% |
| Al ₂ O ₃ | 15.8% | 15.7% |
| Fe ₂ O ₃ | 3.8% | 3.9% |
| MgO | 2.4% | 2.4% |
| CaO | 1.6% | 1.7% |
| Na ₂ O | 4.7% | 4.5% |
| K ₂ O | 3.7% | 3.7% |

The specific surface area of the FG was measured by classical 5 point BET N₂-adsorption. All samples were heated to 90°C and degassed for 18h. Using multi point analysis the BET isotherm was fitted to obtain the surface area. A total surface area of $> 1 \text{ m}^2$ was used in all measurements. Results of the BET analysis is given in Table 4. Additionally, the geometrical surface area was calculated assuming a density of 2.7 g/cm^3 for the FG. Comparing the measured BET with the calculated specific surface area it is obvious that the FG material specific surface area is fully dominated by inner porosity in pores or cracks rather than the surface area only. In addition to the BET measurements, the ESEM pictures for the FG material grains shown above support this conclusion and allow the direct comparison of different size fractions in terms of mass based K_d values to similar experiments using the same type of FG material but with a different size fraction (1160 μm) [99].

Table 4: Specific surface area of the FG material used in the batch experiments.

| FG grain size fraction (μm) | Specific surface area (m^2/g) | |
|--|---|---|
| | BET | calculated (sphere) |
| 250 - 500 | 22.8 ± 1.1 | $8.8 \cdot 10^{-3}$ (250 μm) / $4.4 \cdot 10^{-3}$ (500 μm) |

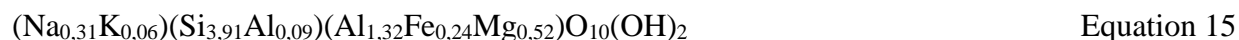
6.3 *Clay mineral sources*

6.3.1 *Febex bentonite*

In the course of the Full-scale Engineered Barriers EXperiment (FEBEX) which started in 1997 at the GTS (www.grimself.com), a suitable bentonite for the construction of the engineered barrier system was selected. The so-called Febex bentonite originating from the Cortijo de Archidona deposit exploited by Minas de Gádor, located in south Spain was chosen as the most suitable material and was also used in this experiment.

6.3.1.1 *Febex bentonite bulk properties*

Characteristics of the Febex bentonite is a very high montmorillonite content, large swelling pressure, low permeability, good retention properties and the ease of compaction. Febex bentonite consists mostly of smectite with minor quantities of quartz, plagioclase, cristobalite and gypsum; for reference see [101] and Table 5. The structural formula of the Febex bulk after homoionic exchange of the interlayer cations against Na is given as [21]



but with different interlayer composition valid for natural Febex bentonite. The interlayer composition of the smectite phase (Table 6) is crucial as exchange processes with the contacting water cannot be neglected.

Table 5: Mineralogical composition of the Febex bentonite [59].

| Mineral | Content [%] |
|--------------|-------------------|
| Smectite | 93 ± 2 |
| Quartz | 2 ± 1 |
| Plagioclase | 3 ± 1 |
| Cristobalite | 2 ± 1 |
| Gypsum | 0.14 ± 0.01 [102] |

Table 6: Exchangeable cation composition of the smectite's interlayer within the Febex bentonite. Total CEC and the main cations for charge compensation are listed [56].

| Exchangeable Cation | Content to CEC [meq/100g] |
|----------------------|---------------------------|
| Ca ²⁺ | 42 ± 3 |
| Mg ²⁺ | 32 ± 2 |
| Na ⁺ | 25 ± 2 |
| K ⁺ | 2.5 ± 0.3 |
| CEC _{total} | 102 ± 4 |

6.3.1.2 Raw Febex bentonite derived colloids

To prepare colloids which are similar in size and composition to the colloids formed by bentonite erosion, compacted Febex bentonite was pulverized and sieved until a uniform grain size below 63 μm was reached. The material was dispersed in de-ionized water (Milli-Q; < 16.2 $\mu\text{S}/\text{cm}$) (1 weight-% bentonite) for one day in order to remove soluble phases. In the first three washing steps the supernatant was removed by centrifugation at 4,000 rpm for 30 minutes (2,800 g). Additional centrifugation was under these conditions due to decreasing ionic strength and therefore increasing colloid stability not possible. Dialysis until conductivity was below 5 $\mu\text{S}/\text{cm}$ completed the washing procedure.

Centrifugation at 2,800 g was used to separate the colloidal phase from the bigger particles. A test showed that centrifuging for 10 minutes yielded best results. The size distribution and concentration of the colloidal dispersion was determined by LIBD, S-curve LIBD and ICP-OES. In the case of ICP-OES measurements, the colloid concentration was determined by the structural formula (Equation 15) of the bentonite for the results of Mg²⁺, Al³⁺ and Fe³⁺ and the mean value of these elements was formed. The results are given in Table 7.

Table 7: Colloid concentration and average diameter. ICP-OES derived data are calculated from the Al, Mg and Fe signal and the mean value is given.

| Centrifugation time [min] | C _{ICP-OES} [g/L] | C _{LIBD} [g/L] | d _{LIBD} [nm] | C _{s-LIBD} [g/L] |
|---------------------------|----------------------------|-------------------------|------------------------|---------------------------|
| 5 | 1.57 | 2.37 | 125 | 1.66 |
| 10 | 0.87 | 1.19 | 118 | 1.54 |
| 30 | 0.36 | 0.70 | 91 | 0.70 |

6.3.2 *Synthetic montmorillonite characterization*

6.3.2.1 *Synthetic Ni- and Zn-montmorillonite bulk material*

Bentonite erosion experiments are conducted under GGW conditions (Table 2). Monitoring the eroded Febex colloids over concentrations of the main elements silicon, aluminum and magnesium the effluent in combination with its elemental composition is difficult as there are a number of additional interactions. Si is ubiquitous in natural waters and the dissolved natural background in GGW is comparable high to the expected colloid concentrations (~4 ppm). Therefore, the additional contribution from the eroded colloids is small and the measurement could only be given with high uncertainties. Al is also part of the groundwater but in this case the background is low (Table 2) and Al solubility at GGW conditions is limited to roughly $3 \cdot 10^{-4}$ M [103]. It therefore can be used for monitoring bentonite erosion and colloidal release from the system. Mg values are not reliable to calculate the released bentonite mass. Natural Febex bentonite is part of all erosion experiments described in this work and Mg is the main component in the Febex interlayer as can be seen in Table 6. Therefore, a cation exchange reaction as additional Mg source cannot be neglected. In order to implement an additional element for detection in the system, the bentonite sources are spiked or even partly replaced by synthetic Zn or Ni containing montmorillonites. The respective bivalent cations thereby replace Mg in the octahedral sheets. These montmorillonites are produced in acidic and fluoride medium under mild-hydrothermal conditions (493 K, autogenous pressure) [104, 105]. For the characterization of the colloidal size fraction it is referred to Huber et al. (2015) [4].

6.3.2.2 *Synthetic Ni-montmorillonite derived colloids*

Synthetic Ni-bearing montmorillonite colloids in GGW have been produced from Ni-montmorillonite suspensions in a repeated four time cycles of suspending, centrifugation for 30 minutes at 4000 rpm (2.800 g) and re-suspending of the separated phase in GGW. The initial suspension contained 2 g montmorillonite in 200 mL GGW and was equilibrated prior the first centrifugation for 7 days. In contrast to the preparation of Febex colloids (6.3.1.2), dialysis was not part of the synthetic colloid preparation. The final colloid containing supernatant was taken as colloid stock and diluted to the desired concentration of 35.9 mg/L according to ICP-OES data of

the main elements (Si, Al and Ni). Element ratios of 24.8% (Si), 9.8% (Al) and 5.1% (Ni) are derived by the elemental composition $\text{Na}_{0.3} [\text{Al}_{1.64}\text{Ni}_{0.39}\square_{0.97}]-[\text{Si}_{4.00}]\text{O}_{10} (\text{OH}_{1.95}\text{F}_{0.05})\cdot 4\text{H}_2\text{O}$. A comparison between ICP-OES, LIBD and s-curve LIBD can be found in Table 8.

Table 8: Concentration and mean size of synthetic Ni labelled montmorillonite colloids. ICP-OES derived concentrations are calculated over the elemental composition. The respective element is given below the values.

| | ICP-OES (N = 2) | Optical LIBD (N = 3) | Stationary curve LIBD (N = 2) | s- Mobile LIBD (N = 1) |
|---------------------------------|---|-------------------------|-------------------------------------|---------------------------------|
| Dilution | --- | 1000 | 100 - 1000 | 100 |
| Colloid concentration [mg/L] | 34.7 ± 0.7 (Si) 35.4 ± 1.0 (Al) 37.5 ± 0.7 (Ni) | 17.0 ± 3.9 | 18.3 ± 6.8 | 5.2 ± 1.0 |
| Mean colloid size [nm] | --- | 73 ± 6 | 44 ± 9 | 51 ± 10 |

A thorough characterization of the separated colloids was reported by Huber et al. [4] including ICP-MS, PCS, AFM, AsFIFFF and LIBD.

6.4 Radionuclide cocktail characterization and speciation for FG sorption/desorption experiments

Two experimental series were prepared: (i) single radionuclide and (ii) radionuclide cocktail samples, respectively. The radionuclides used are listed in Table 9 in conjunction with their respective concentration and the oxidation states at the time of the addition. The concentrations are very similar in both sample series. ^{233}U was used in the cocktail experiments only. Radionuclide concentrations have been selected to not exceed the solubility limit under the geochemical conditions given therefore avoiding any precipitation which could bias the analysis of the experiments and the experimental results itself. Measurement of the radionuclide concentrations in the samples was done by either ICP-MS (THERMO X-Series II) or high-resolution (HR) ICP-MS (THERMO Element XR).

Table 9: Concentration of the radionuclides and stock solutions used in the different batch experiments, combined with the respective solubility in GGW [39].

| Nuclide | $C_{\text{single radionuclide}}$ [M] | $C_{\text{RN-cocktail}}$ [M] | RN-solubility [M], (solid phase) | Stock solutions [M] |
|------------------------|---|---|--|------------------------|
| $^{99}\text{Tc(VII)}$ | $1.5 \cdot 10^{-7} \pm 4.5 \cdot 10^{-9}$ | $1.5 \cdot 10^{-7} \pm 6.0 \cdot 10^{-9}$ | $9.6 \cdot 10^{-4}$ ($\text{TcO}_2 \cdot 1.6 \text{H}_2\text{O}$) | $1.0 \cdot 10^{-5}$ |
| $^{233}\text{U(VI)}$ | Not used | $8.2 \cdot 10^{-8} \pm 3.3 \cdot 10^{-10}$ | $2 \cdot 10^{-4}$ ($\text{UO}_2(\text{OH})_2$) | $1.5 \cdot 10^{-4}$ |
| $^{237}\text{Np(V)}$ | $5.5 \cdot 10^{-9} \pm 1.8 \cdot 10^{-10}$ | $5.4 \cdot 10^{-9} \pm 2.1 \cdot 10^{-10}$ | $2 \cdot 10^{-4}$ ($\text{NpO}_2\text{OH (am)}$) | $1.6 \cdot 10^{-5}$ |
| $^{242}\text{Pu(IV)}$ | $5.9 \cdot 10^{-10} \pm 3.1 \cdot 10^{-11}$ | $6.4 \cdot 10^{-10} \pm 2.6 \cdot 10^{-11}$ | $1 \cdot 10^{-10} - 2 \cdot 10^{-9}$ ($\text{PuOH}_4(\text{am})$) | $4.4 \cdot 10^{-7}$ |
| $^{243}\text{Am(III)}$ | $4.2 \cdot 10^{-10} \pm 8.4 \cdot 10^{-12}$ | $3.3 \cdot 10^{-10} \pm 1.3 \cdot 10^{-11}$ | $1 \cdot 10^{-7}$ ($\text{AmOHCO}_3(\text{am})$) | $1.6 \cdot 10^{-4}$ |

Radionuclide solubility data is given in Table 9. All RN, despite Pu(IV), are well below the solubility limit for the most stable oxidation state under GGW conditions, respectively. A predominance diagram for each RN can be found in Figure 38 to Figure 42. In case of Pu the limit is not strictly determined and ranges from $1 \cdot 10^{-10}$ M to $2 \cdot 10^{-9}$ M [39]. In the case of an oversaturated Pu solution, precipitation is unlikely as Pu(IV) forms highly stable $\text{Pu}(\text{OH})_4$ colloids that show similar sorption behavior as dissolved Pu(IV) [15].

6.5 Batch type studies

Both batch sorption and desorption (reversibility) experiments have been conducted in a glovebox under anaerobic conditions (Argon atmosphere) and room temperature (22°C). Separate samples have been prepared using HDPE 20 mL vials (ZINSSER) for each sampling time. This allows the use of the sorption samples subsequently as samples in the desorption experiments. A duplicate has been prepared for each sample to check for reproducibility. A scheme of the experimental procedure can be found in Figure 26.

Experimental approach

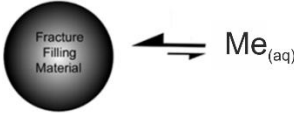
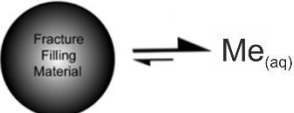
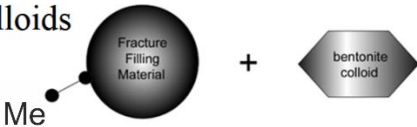
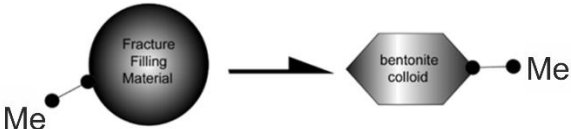
- Step 1: RN sorption on FFM
 
- Step 2: RN desorption from FFM
 
- Step 3: Addition of bentonite colloids
 
- Step 4: Desorption of RN from FFM and sorption to bentonite colloids
 

Figure 26: Scheme of the experimental procedure concerning the FG sorption reversibility experiment (Me = Metal ion). Step 2 is triggered by water exchange which can be seen as a disturbance of the sorption equilibrium.

Diluted stock solutions (RN-GGW) for each single radionuclide and for the cocktail sample series were prepared by mixing fresh GGW with the concentrated radionuclide stock solutions to reach the desired radionuclide concentrations. Afterwards pH of the RN-GGW solutions were re-adjusted to the original Grimsel pH of ~9.5. In each vial 1.5 g (dry weight) of the FG (250-500 μm size fraction) was brought in contact with 8.5 mL of the different RN-GGW solutions yielding a V/m ratio of 5.7 mL/g. The samples prepared were stored in the glove box during the whole experimental duration. Sampling times were as follows: 1 d, 3 d, 7 d, 14 d, 28 d, 100 d, 200 d and

300 d (Figure 26, step 1). After the desired contact time, pH and E_{SHE} have been monitored before taking an aliquot for further analysis. pH was measured in each sample using a semi-micro Ross electrode (81-03, Orion Co.) in combination with a digital pH meter (720A, Orion Co.) to check for any drift over the experimental duration. Calibration of the pH setup was carried out using at least five commercial buffer solutions (Merck). Eh measurements have been carried out with a Pt combined electrode (Metrohm) connected to the pH meter (Orion). Raw Eh data was corrected to a standard hydrogen electrode by addition of 207 mV. E_{SHE} was consistently monitored in the blank samples until a plateau value was reached within ~120 minutes. Afterwards, an aliquot of the sample was diluted in 2% HNO_3 and analyzed by (HR)-ICP-MS. After each sorption time, the remaining solution in each vial was discarded carefully and fresh RN free GGW was added (8.5 mL to keep the V/m ratio constant). A similar sampling schedule was chosen in the desorption experiments as used in the sorption experiments, namely 1 d, 3 d, 7 d, 14 d, 28 d, 100 d, 200 d and 300 d (Figure 26, step 2). That is, for the 7 d sorption sample for instance, after a desorption time of e.g. 1 d an aliquot was taken for RN analysis by (HR)-ICP-MS and pH of the sample was measured. Subsequently, the remaining solution was completely discarded from the sample vial and fresh GGW was added. After additional two days (that is 3 d desorption time in total), the same procedure of sampling, pH measurement and exchange of solution with fresh GGW was carried out. This procedure was repeated for all samples and desired desorption times. In other words, every sample out of the sorption series experiments was exchanged with fresh GGW 8 times (once for each desorption time) within the desorption experiment series. Subsequently to the desorption kinetics experiments under pure GGW conditions, the FG material containing sorbed RN (only for the single radionuclide series of Am, Pu and cocktail series samples, respectively) was brought in contact with 8.5 mL of synthetic Ni montmorillonite containing GGW colloid suspension [4, 105] to study a possible remobilization of RN due to the presence of an additional concurrence surface (Figure 26, steps 3&4). The colloid concentration in the sample was 35.9 mg/L. The samples were taken after 1 d, 5 d, 14 d, 28 d and 211 d and afterwards immediately prepared for elemental composition analysis.

6.6 *Bentonite erosion studies*

Bentonite erosion studies in order to investigate the stability of the bentonite buffer under realistic conditions concerning low flow velocities, natural contact water (GGW) and the use of natural unpurified compacted bentonite samples have been performed on the laboratory and the field scale.

6.6.1 *Pure Febex long-term bentonite erosion laboratory study*

Bentonite erosion studies have been conducted in an artificial fracture set-up to simulate the intrusion of dilute glacial melt water in a repository. Natural Febex bentonite and GGW was used for this type of experiments to keep it close to the expected scenario in a prospective repository.

6.6.1.1 *Artificial fracture set-up and sample geometry*

The artificial fracture set-up consists of an acrylic glass housing that is built up by three parts, namely a lower and an upper plate and a cylindrical spacer that is placed inside the arrangement (Figure 28). A ring shaped compacted bentonite sample with inner diameter of 40 mm, outer diameter of 80 mm and 25 mm in height is located in the middle of the setup and the spacer is placed in the center of this ring to avoid any kind of swelling towards the center of the setup. The parts of the housing around the bentonite ring are not in contact. Thereby a slit with an aperture of 1 mm height and 180 mm in diameter is formed that mimics a parallel-plate synthetic fracture around the bentonite source and allows the granitic groundwater to reach the bentonite. Natural Grimsel groundwater is pumped through the synthetic fracture with constant flow rate of 50 $\mu\text{L}/\text{min}$. Modelling the flow velocity at the water-bentonite interface from the given volume flux with COMSOL Multiphysics yields a maximum velocity of $1.2 \cdot 10^{-5}$ m/s (A-Figure 5) and a maximum shear stress of $3.3 \cdot 10^{-5}$ Pa (A-Figure 6). The flow velocity distribution within the 1 mm fracture set-up at the initial stage before the bentonite extrudes into the fracture is shown in Figure 27. The shear stress for instance determines if particles are removed from the gel-water interface in advection controlled systems [106]. The dimensions of the compacted bentonite ring are identical to the long-term in-situ test (LIT) which is running since May, 2014 within the CFM project located at GTS.

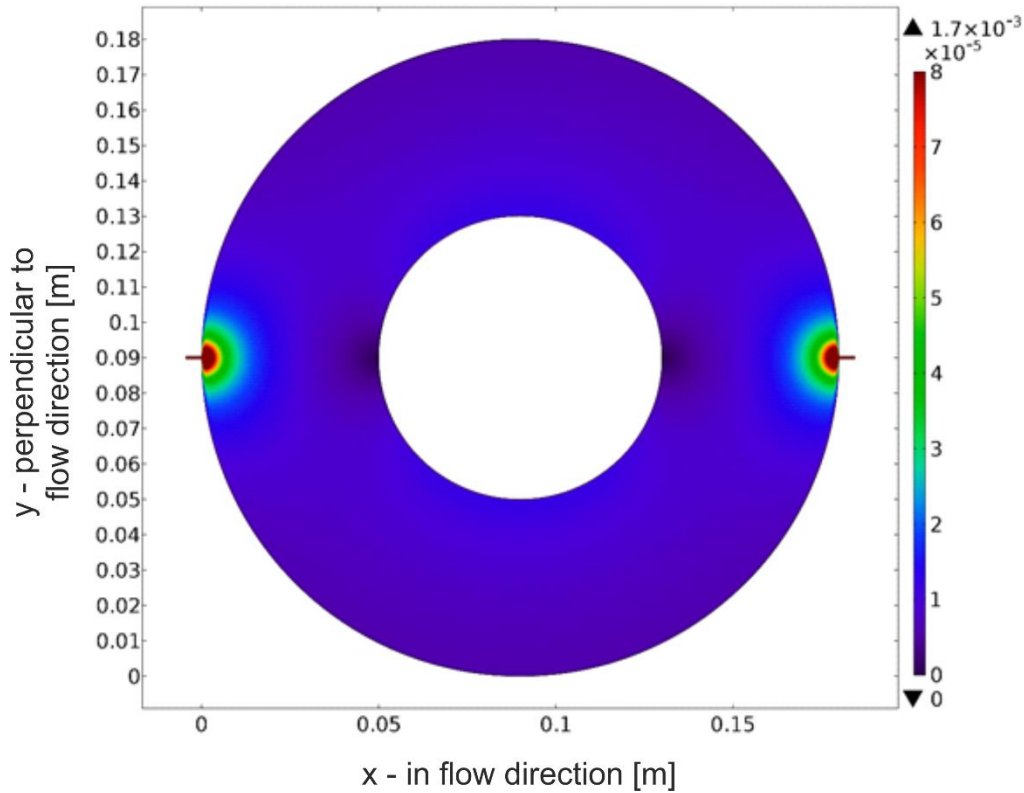


Figure 27: Flow velocity distribution in the 1mm artificial fracture erosion experiments calculated with COMSOL Multiphysics for the initial condition before swelling into the fracture

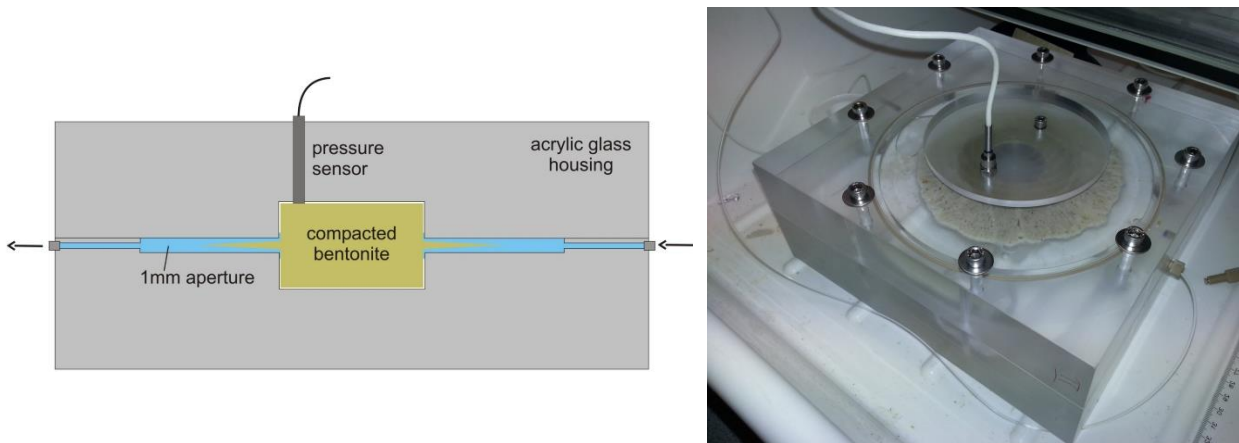


Figure 28: (left) Schematic arrangement of the bentonite erosion experiment and (right) bentonite erosion experiment set-up as installed in the lab. Pressure monitoring sensor on top (white cable).

6.6.1.2 *Tracer characterization*

Eight thin glass vials (VWR International, product number 548-0347, 7,8 mm outer diameter, 35 mm height, shortened to 10 mm) containing 220 mg synthetic Ni-labelled montmorillonite (as paste) ([105]) spiked with 10 mg uranine powder in each vial as conservative tracer and the homologues Eu, Th, Hf and Tb (18.3 μg per vial, respectively under the assumption of quantitative sorption) were emplaced in the bentonite ring. Therefore, a 3 g/L Ni-montmorillonite suspension (1 L sample volume) was spiked with 250 μL of 1 g/L homologue solution, respectively. The suspension was left for one week to facilitate quantitative sorption of the homologues on the montmorillonite particles. The suspension was meanwhile regularly homogenized by shaking. The labeled solid phase was then separated by centrifugation for 40 min at 4,000 rpm ($\sim 2,800\text{ g}$) and filled with the conservative tracer into the glass vials. For tracer vial emplacement, 8 holes were drilled laterally in the sample ring to mount the glass vials (Figure 29). Due to the swelling of the clay the glass vials were supposed to break and release the labelled montmorillonite and associated homologues as well as the conservative tracer.

6.6.1.3 *Experimental procedure and sampling strategy*

The experiment is continuously running since October 29th, 2013. As the bentonite used contains a high amount of swellable clay (smectite), a swelling pressure builds up in the cell during the saturation of the bentonite with GGW. The bentonite swelling pressure evolution is monitored by a pressure sensor (Disynet XP1103-A1-100BG) installed on the top housing part of the cell above the bentonite ring (Figure 28). The experiment is conducted at room temperature ($\sim 21\text{ }^\circ\text{C}$) under ambient conditions for the first seven months and afterwards transferred to anoxic conditions in a glove box under Ar atmosphere ($< 1\text{ ppm O}_2$). The pH measurements were undertaken using a semi-micro Ross electrode (81-03, Orion Co.) in combination with a digital pH meter (520A, Orion Co.). The set-up was calibrated using five commercial buffer solutions covering a pH region of 2 to 10. Samples are taken daily for the first 11 weeks of the experiment and weekly afterwards. During the first seven months, samples are taken in 15 mL sample vials and the remaining effluent is discarded. Once the set-up is in the glove box all the effluent has to be collected and in order to recover as much released colloidal material as possible the total effluent is sampled weekly ($\sim 500\text{ mL}$ per week). The samples are analyzed with regard to pH, fluorescence intensity (conservative tracer), and chemical composition by ICP-MS and IC. Eluted colloid size, colloid size distribution

and colloid concentration were determined by LIBD systems. Flow rate is determined over the eluted volume weighted on a balance during each sampling period.



Figure 29: (left) Bentonite sample with holes on side of the ring containing filled glass vials. (right) Top view of the bentonite ring in the swelling stage.

6.6.2 *Long-term In-situ Test (LIT) at the Grimsel Test Site*

The Colloid Formation and Migration project (CFM) studies the formation and migration of bentonite derived colloids in natural fractured rocks and colloid facilitated transport of radionuclides in this system. A series of hydraulic and tracer tests including well-defined bentonite colloids, conservative and radionuclide tracers have been performed so far. The latest step includes the implementation of a radionuclide tracer containing compacted bentonite colloid source in the water-bearing feature for better understanding of the real in-situ processes in a bentonite-based engineered barrier. The Long-term In-situ Test (LIT) includes in-situ bentonite swelling, erosion and the transport of the eroded material under advection dominated conditions.

6.6.2.1 *Experimental layout*

LIT is located in the radiation controlled zone at the GTS. The borehole CFM 06.002 was chosen for the emplacement of the bentonite source. It shows a diameter of 96 mm and intersects the migration shear zone at a depth of approximately 6.75 ± 0.05 m from the tunnel wall. It is surrounded by three 56 mm boreholes (CFM 11.001, CFM11.002 and CFM11.003) which are located in parallel to CFM 06.002 at a distance of only 40 mm and used for observation and sampling in the near-field. Each monitoring borehole is equipped with a 54 mm triple packer system including two hydro-mechanical packers of 0.2 m sealing length and one hydraulic packer of 1 m length near the tunnel wall. The migration shear-zone intersects the boreholes between the hydro-mechanical packers. Stainless steel lines are integrated in each packer system for water extraction as well as pressure monitoring and resin injection which is planned around the radioactive bentonite source in the last phase of the experiment just before overcoring. An additional option for sampling can be found in the Pinkel extraction point at a distance of 6.08 m from the source located at the tunnel wall within the mega-packer system. A scheme of the experimental layout can be found in Figure 30. The analytical program for these samples is limited in comparison to the near-field samples as dilution is due to the long distance much higher.

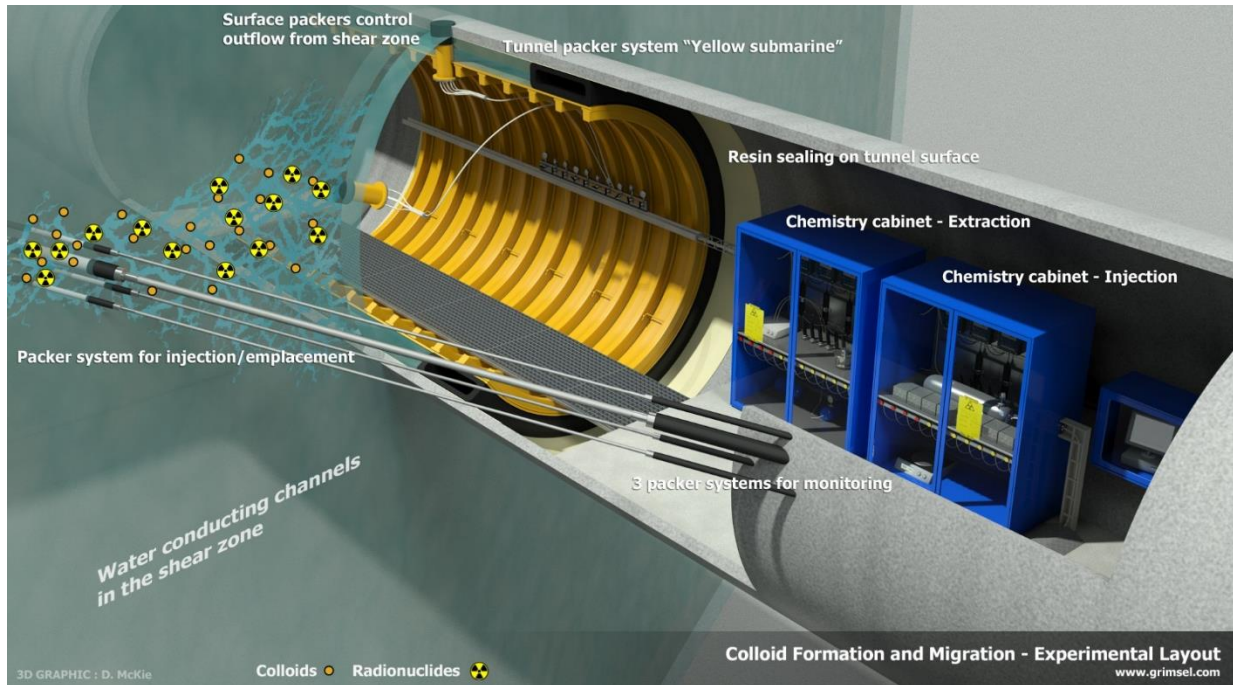


Figure 30: LIT experimental layout (www.grimsel.com). LIT enables bentonite erosion and colloid generation directly from compacted bentonite instead of colloid suspension under realistic flow conditions.

The source emplacement borehole CFM06.002 is instrumented with a triple packer system and includes two hydro-mechanical packers of 0.27 m sealing length and one hydraulic packer of 1 m length located at the borehole mouth. The system was designed to facilitate emplacement, monitoring and subsequent overcoring of the radionuclide labelled bentonite source. Several stainless steel lines are located within the packer for water extraction and pressure monitoring. Therefore, two total pressure cells are installed at each end of the source interval. The interval consists of a carbon steel mandrel (ST52) of 44 mm diameter and 400 mm length to hold a total of 16 bentonite rings, each with 25 mm thickness. Sinter filters are placed between the sample and the respective packer. The total length of this interval from sealing element to sealing element is 520 mm.

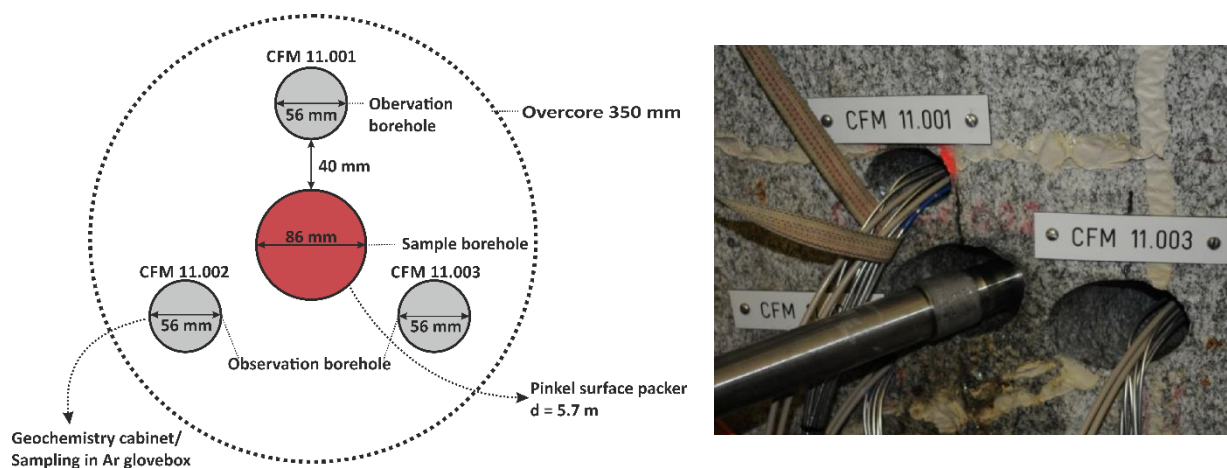


Figure 31: Arrangement of the boreholes relevant for LIT. A schematic overview (left) and a picture of the site (right) is pictured. The bentonite source is located in the central borehole and the surrounding boreholes (CFM 11.00X) are for near-field observation. Overcoring and retrieval of the source is an option for the late phase of the experiment.

Pre-tests showed that the observation borehole CFM 11.002 features the best connection to CFM 06.002 and is therefore used for near-field monitoring and sampling. Low extraction rates of only 0.02 mL per minute are applied in order to keep the flow regime around the bentonite source undisturbed. The outflow is either channeled through the geochemistry cabinet for online monitoring (Chapter 6.6.2.3) or sampled in a fraction collector within an Ar glovebox for later analysis. Samples are transferred to KIT and undergo an extensive analytical routine including the samples pH, $E_{h_{SHE}}$, fluorescence, elemental composition (IC, ICP-MS), radiochemical composition (LSC, Gamma, SF-ICP-MS and AMS) as well as size and concentration of the colloidal fraction (LIBD, s-curve LIBD).

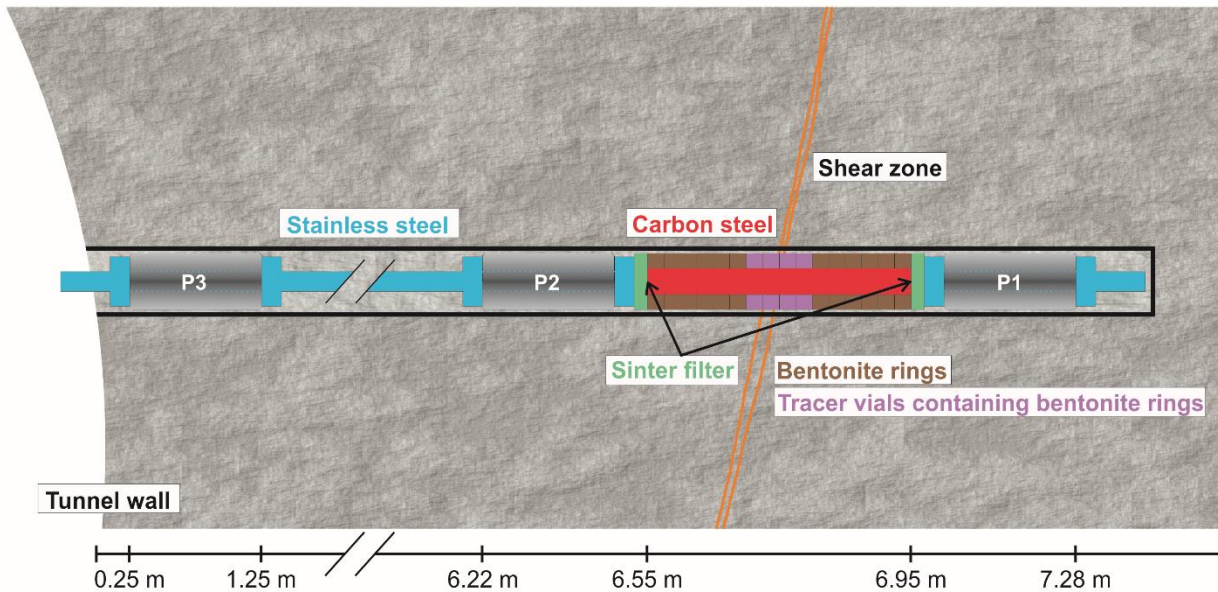


Figure 32: Conceptual design of the emplacement packer system and location in the borehole CFM 06.002 (NAB 14-092). The source is sealed with two hydro-mechanical packers (P1 and P2) and the hydraulic packer (P3) is located close to the tunnel wall.

6.6.2.2 Bentonite sample and tracer composition

The bentonite source within LIT consists of 16 compacted bentonite rings with a compaction density of 1600 kg/m^3 which are stacked on the mandrel of the packer system. Combination of the bentonite rings results in a 400 mm high bentonite rod with an inner diameter of 43 mm and an outer diameter of 83 mm. A total of 2613.6 g bentonite composed of 2549.9 g natural Febex bentonite and 63.7 g synthetic Zn-labeled montmorillonite is emplaced in the migration shear zone. The fact that the contact area between bentonite source and migration shear zone is located on the four central sample rings is the reason for special interest and deviating sample composition in this region. The midst sample rings contain not only pure Febex but an admixture of 10% synthetic Zn-montmorillonite. Holes have been drilled laterally in the Zn-montmorillonite containing bentonite rings to host the tracer containing glass vials. A total of 16 vials are equipped, 4 in each Zn-labeled bentonite ring. The caps of the glass vials have been removed prior mounting to facilitate contact between the tracer and the surrounding ground water and the closed side points to the outside surface of the bentonite rings. Under high swelling pressure, the vials are supposed to break and the radionuclide tracer will be released.

The tracer is composed of a radionuclide containing bentonite paste and Amino-G (Sigma Aldrich, order no. 14,664-7, Monopotassium-7-amino-1,3-naphthalenedisulfonate hydrate) as conservative fluorescence tracer. A mixture of natural Febex bentonite in the grain size $< 63 \mu\text{m}$ and synthetic Ni-labeled bentonite [105] was used in equal ratios (50% each). A 5g/L suspension of the mixture was prepared with synthetic Febex porewater (Table 10) [102], resulting in an ionic strength of 0.9 M and near-neutral pH.

Table 10: Synthetic Febex porewater composition [102].

| | |
|-------------------------------|-----------------------|
| pH | 7.44 |
| Ionic strength | 0.66 M |
| Na ⁺ | $3.3 \cdot 10^{-1}$ M |
| K ⁺ | $2.6 \cdot 10^{-3}$ M |
| Mg ²⁺ | $8.1 \cdot 10^{-2}$ M |
| Ca ²⁺ | $6.8 \cdot 10^{-2}$ M |
| Si ²⁺ | $6.1 \cdot 10^{-4}$ M |
| Cl ⁻ | $4.2 \cdot 10^{-1}$ M |
| SO ₄ ²⁻ | $1.9 \cdot 10^{-2}$ M |
| C _{inorg.} | $3.1 \cdot 10^{-4}$ M |
| Si | $1.8 \cdot 10^{-4}$ M |

The bentonite suspension was first equilibrated with the strongly sorbing radionuclide tracers ²⁴¹Am(III), ¹³⁷Cs(I) and ²⁴²Pu. Pu was added in the trivalent oxidation state after electrochemical reduction. The suspension was equilibrated for 26 hours and the solid phase was separated by centrifugation at 2.800 g for 60 min. The centrifugate was stored in a fume cupboard to remove remaining water. Then, the bentonite paste was transferred in an Ar glovebox and the weakly sorbing radionuclides ⁹⁹Tc(VII), ⁷⁵Se(VI), ⁴⁵Ca(II), ²³³U(VI) and ²³⁷Np(V) were added. The resulting mixture with 5g/5mL was homogenized using a spatula. Afterwards the glass vials (VWR International, product number 548-0347, 7,8 mm outer diameter, 35 mm height, shortened to 10 mm) were filled with 8.55 ± 0.10 mg Amino-G powder per vial and 222 mg of the radionuclide containing bentonite slurry respectively by using a syringe (5 mL, Luer solo, B. Braun, order no. 4606051V). The glass vials were closed with a plastic lid and transported to GTS in a full confinement. A total of 19 glass tracer vials were prepared, 16 of them for the LIT experiment and the remaining vials for the laboratory mock-up test. The activities of all of the emplaced radionuclides are under the licensed limits (Table 11).

Table 11: Within LIT emplaced activity and license limits.

| Nuclide | Total activity in LIT (16 vials) [Bq] | Max. activity based on license [Bq] |
|-------------------|--|--|
| ⁴⁵ Ca | $7.10 \cdot 10^5$ | $1.0 \cdot 10^6$ |
| ⁷⁵ Se | $4.78 \cdot 10^4$ | $1.0 \cdot 10^6$ |
| ⁹⁹ Tc | $5.40 \cdot 10^3$ | $1.0 \cdot 10^4$ |
| ¹³⁷ Cs | $4.39 \cdot 10^3$ | $1.1 \cdot 10^5$ |
| ²³³ U | $7.10 \cdot 10^2$ | $1.0 \cdot 10^3$ |
| ²³⁷ Np | $1.07 \cdot 10^3$ | $1.5 \cdot 10^3$ |
| ²⁴¹ Am | $8.81 \cdot 10^2$ | $8.5 \cdot 10^3$ |
| ²⁴² Pu | $2.13 \cdot 10^2$ | $3.0 \cdot 10^2$ |

Gamma spectroscopy and high resolution ICP-MS were applied for radiochemical characterization of the samples. Gamma spectroscopy focused only on the quantification of ⁷⁵Se, ¹³⁷Cs and ²⁴¹Am because the remaining radionuclides are due to a missing gamma emission not suitable for this technique. None of the before mentioned radionuclides was found. All samples were below the detection limit. SF-ICP-MS was applied for all radionuclides within LIT. Due to the detection of the atomic mass several isobaric interferences are possible and have to be taken into account (Table 12).

Table 12: Overview on the radiochemical analysis with occurring isobaric interferences and respective background value in GGW (n=4).

| Nuclide | Isobaric interference (GGW value in brackets) | Results SF-ICP-MS | Results Gamma-Spec. |
|-------------------|--|-------------------------------|---------------------|
| ⁴⁵ Ca | ⁴⁵ Sc (0.66 ± 0.06 ppb) | GGW level (⁴⁵ Sc) | --- |
| ⁷⁵ Se | ⁷⁵ As (1.77 ± 0.13 ppb) | Detected | Not detected |
| ⁹⁹ Tc | ⁹⁹ Ru (< detection limit) | Detected | --- |
| ¹³⁷ Cs | ¹³⁷ Ba (0.13 ppb) | Detected | Not detected |
| ²³³ U | | Not detected | --- |
| ²³⁷ Np | | Not detected | --- |
| ²⁴¹ Am | | Not detected | Not detected |
| ²⁴² Pu | | Not detected | --- |

6.6.2.3 Background monitoring

The installed monitoring system includes beside the Ar glovebox with the fraction collector, a flow control and a geochemistry cabinet. All components were installed before the start of LIT to monitor the chemical parameter changes in the nearfield monitoring intervals within CFM 11.001, CFM 11.002 and CFM 11.003. Switching from one observation borehole to another is possible manually by a valve. Due to the low flow rates the parallel use of geochemistry cabinet and fraction collector is not possible and an electrical switch is programmed to switch between water sampling and online monitoring. The geochemistry cabinet is equipped with a turbidity meter, a fluorimeter, pH, EC and E_{SHE} probes (Figure 33).

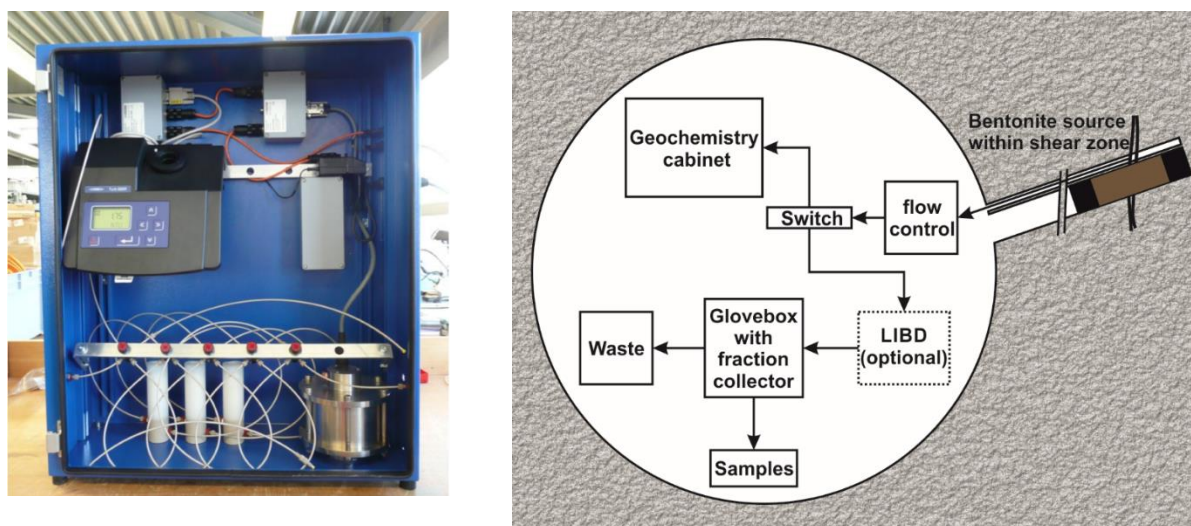


Figure 33: Photograph of the geochemistry cabinet (left) and schematic overview of the surface equipment setup for the nearfield monitoring system (right).

6.6.3 Laboratory mock-up test in comparison to LIT

Complementary to LIT, a bentonite erosion mock-up test has been installed in the laboratory. The artificial fracture set-up, described in Chapter 6.6.1.1, is applied. The experiment started on February 25th, 2016. It is located in an Ar glovebox and constantly flushed with natural GGW at a low flow rate of 50 $\mu\text{L}/\text{min}$. A pressure sensor is installed on top of the bentonite source in order to record the evolution of the swelling pressure and a camera takes pictures for monitoring the swelling distance regularly. The effluent was sampled daily in 15 mL sample vials and the remaining effluent was collected in a 500 mL bottle which was exchanged once a week. Daily sampling was stopped after 90 days but sampling continued once or twice per week.

In contrast to the bentonite erosion experiment, described in chapter 6.6.1, the bentonite source and the tracer composition differ. A leftover unfortunately broken Zn-montmorillonite labelled Febex bentonite ring from the installation of LIT as well as the three remaining tracer vials (Chapter 6.6.2.2) have been installed. A fourth glass vial was necessary because the ring was already prepared to hold four tracer vials. It contained pure Zn-labelled montmorillonite. Cavities have been filled up with pulverized remainings of the Febex-Zn-montmorillonite mixture.

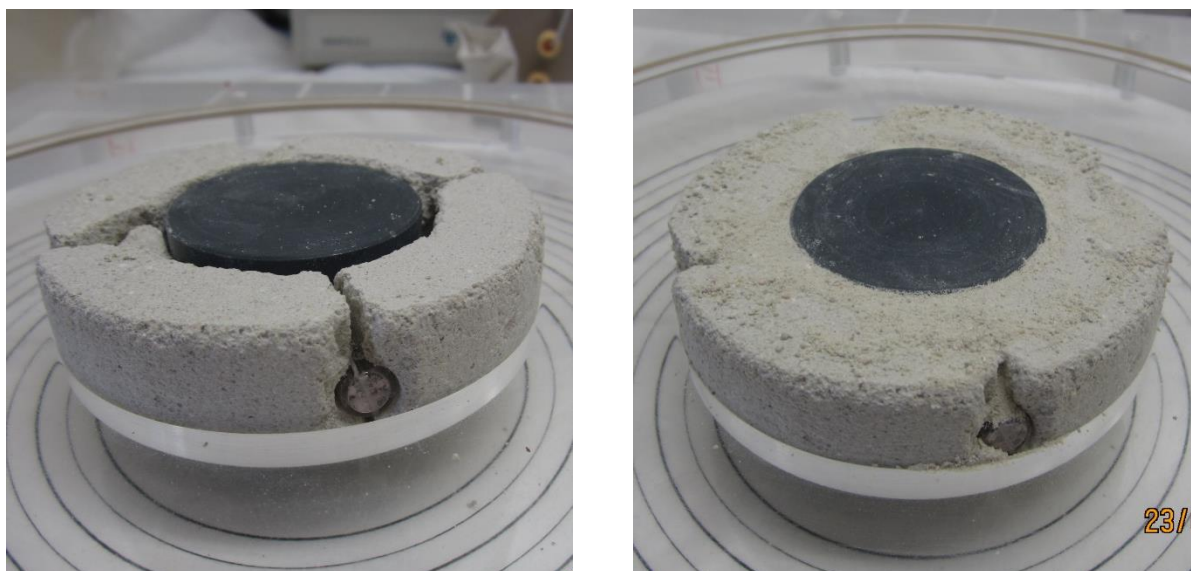


Figure 34: Sample preparation for the LIT-mock-up test. Tracer vials are already emplaced. The breaking points are still visible (left) and filled up with pulverized Febex-Zn-montmorillonite mixture (right).

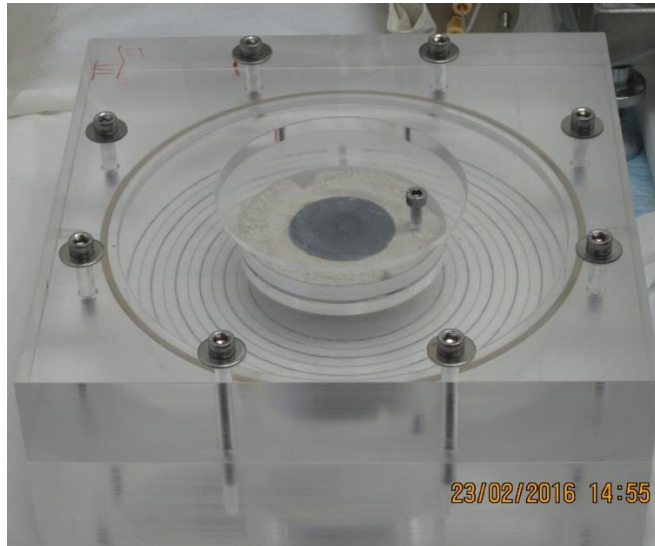


Figure 35: Closed cell with installed sample before transfer to the Ar glovebox. The pressure sensor will replace the screw above the bentonite source.

7 Results and Discussion

7.1 Radionuclide sorption reversibility studies on Fault Gouge material

7.1.1 Experimental overview

The radionuclide sorption reversibility studies are divided in three phases (Figure 36):

1. Sorption of the RNs on FG takes place during the first 232 days of the experiment. Thereby a sample duplicate is prepared for each sorption time step and for each RN solution. The sorption experiment is divided in 6 sorption time steps varying between 1 day and 232 days.
2. Desorption in the binary system GGW-FG starts as soon as the first sorption time step, which is one day of sorption, is over and lasts until a total experimental time of 400 days. The longer reacting sorption samples are added subsequently to the desorption experiment but desorption time is not extended accordingly. Therefore sorption and desorption in the binary system GGW-FG take place in parallel within the first 232 days of the experiment. A fraction of the RNs remained on the FG surface at the end of desorption in the binary system but did not change between the last samplings.
3. Desorption in the ternary system GGW-FG-Ni-mnt is the final phase of the sorption reversibility study. In order to remobilize part of the remaining FG-attached RNs, Ni-mnt colloids are added as competing surface. Only the strong sorbing RN samples (Pu and Am) and the RN cocktail containing samples are included in the final phase of the study. Desorption in the ternary system is investigated for the following 211 days, leading to a total experimental duration of 611 days.

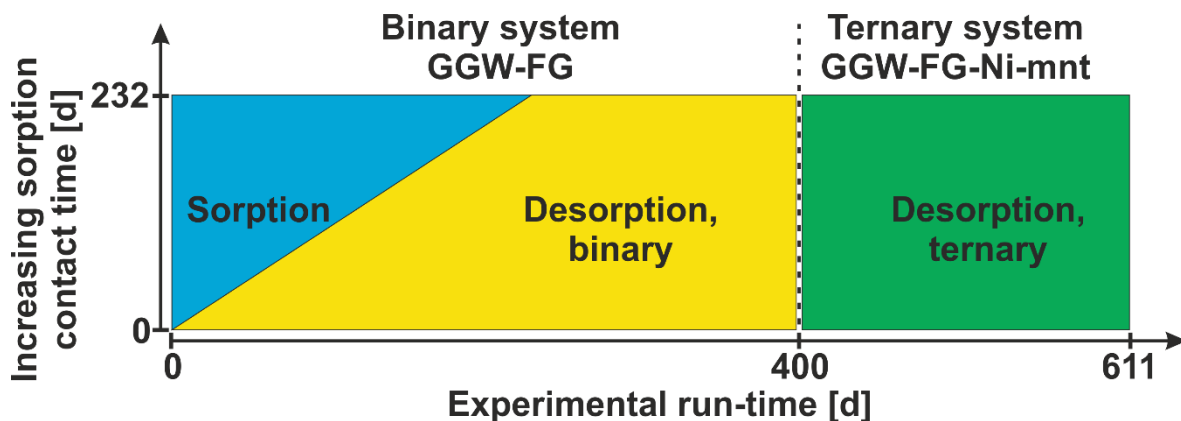


Figure 36: Schematic overview of the sorption reversibility studies. Sorption and desorption experiments are performed successively during the first 232 days of the experiment. Ni-mnt colloids are introduced as competing ligand at a run-time of 400 days (ternary system).

7.1.2 Evolution of $pH-Eh_{SHE}$ conditions

pH evolution of both the sorption and desorption experiments are shown in Figure 37. In case of the sorption samples, each pH data point shown is an average of 34 single samples in total. Regarding the very small error bar (~ 0.1 pH unit) of the measured pH values for each time step, pH evolution is very reproducible. A constant pH was observed within the first 28 d contact time. Afterwards a drift from initially pH of ~ 9.3 down to pH of ~ 8.2 was detectable during the contact time of 232 d. This drift might be attributed to two possible reasons:

- (i) a disequilibrium between the FG and the GGW inducing mineral dissolution and precipitation processes which consume OH^- ions shifting pH to lower values or
- (ii) intrusion of trace amounts of CO_2 (which could be present in the glove box Ar atmosphere) into the samples by diffusion.

The former explanation might be favored over the latter explanation when looking at the pH evolution during the desorption experiments. Here, the pH stayed very much constant ($9.3 \pm \sim 0.1$ pH unit) over 600d despite having contact to the FG all the time. This effect can be explained by the sampling strategy of the desorption experiment. In contrast to the sorption experiment, which included duplicate samples for each sorption time step, contact times during desorption are short. The contact water is exchanged after each desorption time step and an equilibrium between the FG and the GGW cannot be established. Therefore, the disequilibrium cannot be resolved in the first desorption samples and aligned when it came to longer contact times. The pH during the desorption experiments in both the binary and the ternary system is shown in Figure 37 as greyish areas instead of single values. This was necessary since for each sorption time 14 pH values (7 samples with duplicates) have been measured for each desorption step for each single radionuclide and cocktail samples (5 RN series sums up to > 700 values).

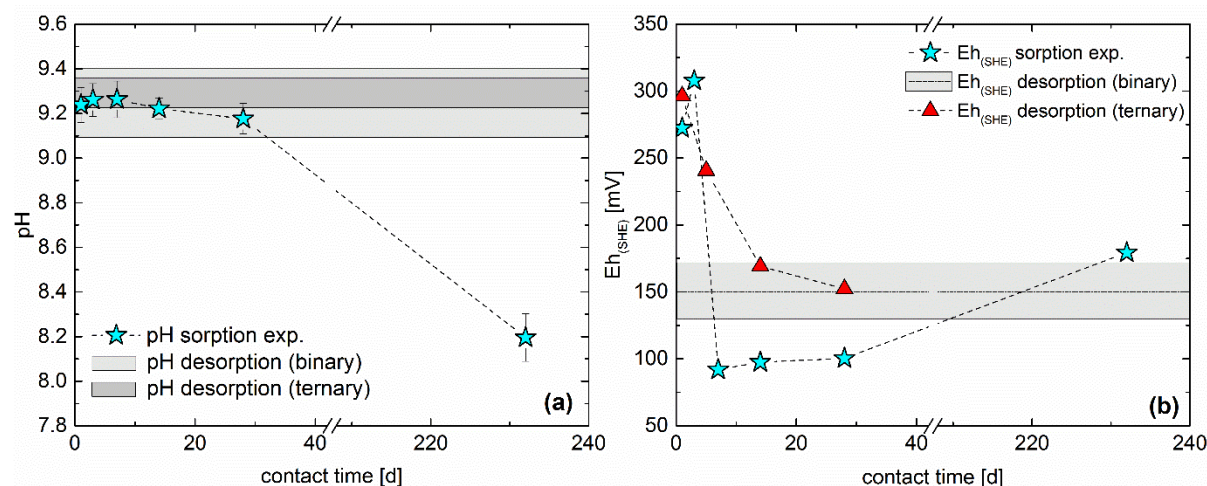


Figure 37: (a) pH evolution for the sorption experiments (symbols), desorption in the binary system (light grey area) and desorption in the ternary system (dark grey area), respectively. (b) $Eh_{(SHE)}$ evolution for the sorption (symbols) binary (grey area) and ternary desorption (symbols) experiments, respectively.

The redox potential was measured in blank samples (GGW and FG only) in absence of RN to evaluate only the influence of the FG material on the Eh_{SHE} evolution and to avoid any leakage of the electrode inner filling electrolyte (3M KCl) into the sample solution during long measurement times. With respect to the sorption experiments, an initial drop from $\sim +250$ mV down to $\sim +90$ mV was detected within the first 7 d which stayed constant until 28 d. Afterwards Eh_{SHE} drifted to a value of $\sim +175$ mV after 232 d. The drift for the long term samples might be explained by trace amounts of O_2 diffusing into the vials. Regarding the desorption experiments in the binary system, Eh_{SHE} was very constant over the whole experimental duration in line with the pH behavior. In case of the desorption experiment in the ternary system, higher $Eh_{(SHE)}$ values similar to the sorption experiments (~ 300 mV) are observed for the short contact times and converge to the values in the binary system within 28 d. Eh_{SHE} data for the latest sampling is missing because the electrode was not in use for a couple of months and needed a revision to give reliable results. This was not possible when sampling took place. Generally speaking, the measured redox potentials of the GGW are much more positive than the in-situ Eh_{SHE} value measured in the field. Here values of around -300 mV have been measured by Mōri et al. (2003) [11]. Similar low redox potentials have also been measured within very similar laboratory batch experiments by Huber et al. (2015) [4]. The discrepancies between the measured values in this study and reported values in the literature display

the general high uncertainties in reliably measuring $E_{h(SHE)}$ values in systems where only very small concentrations of redox active elements like e.g. Fe(II)/Fe(III) are present. For a thorough discussion on this topic the reader is referred to e.g. Grenthe et al. (1992) [107].

7.1.3 Radionuclide speciation

Predominance diagrams as well as speciation diagrams for the radionuclides used in the sorption reversibility experiments were calculated for the experimental conditions (Chapter 7.1.1) using the GW composition given in Table 2 with the geochemical speciation code Hydra-Medusa [108]. The radionuclide concentrations are given in Table 9. The relevant pH- $E_{h(SHE)}$ region is between pH 8.2 and pH 9.3 and $E_{h(SHE)}$ between +100 mV and +300 mV (Figure 37). The thermodynamic constants used are taken from the NEA database only [108] (except for U where two additional species were included (see discussion below)). In all speciation diagrams shown only species with a fraction of at least 10% are included. The input files for the respective radionuclides can be found in the Annex in A-Table 2 to A-Table 6.

7.1.3.1 ^{99}Tc speciation

The dominant ^{99}Tc species is TcO_4^- over the entire pH and E_{SHE} region of interest. ^{99}Tc predominance and speciation diagram can be found in Figure 38 which shows that there is no relevant species except TcO_4^- under the experimental conditions prevailing. Reduction of Tc(VII) (TcO_4^-) to Tc(IV) followed by precipitation of $\text{TcO}_2 \cdot 1.6 \text{H}_2\text{O}_{(\text{s})}$ is unlikely given the distance to the 50/50 borderline where both species are present in equal amounts.

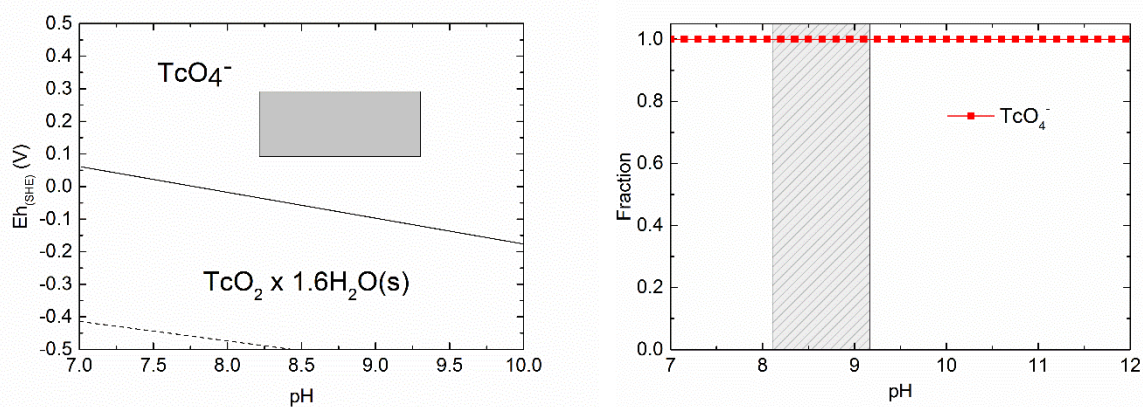


Figure 38: (left) Predominance diagram for ^{99}Tc under the given conditions. The region of interest is marked with the light grey area and (right) thermodynamic speciation calculation.

7.1.3.2 ^{233}U speciation

The predominance diagram for ^{233}U shows two relevant species within the region of interest (Figure 39). In case of pH values below 9, the negatively single charged $(\text{UO}_2)_2\text{CO}_3(\text{OH})_3^-$ complex is dominant. At the highest pH values of 9.3, relevant for most of the samples, the negatively single charged $\text{UO}_2(\text{OH})_3^-$ dominates. The speciation diagram for ^{233}U reveals two additional relevant species (Figure 39). The calcium containing complexes $\text{CaUO}_2(\text{CO}_3)_3^{2-}$ and $\text{Ca}_2\text{UO}_2(\text{CO}_3)_{3,\text{aq}}$ have to be taken into account additionally since they have been shown to be of importance under near-neutral pH conditions and in presence of Ca^{2+} in aqueous environments [109]. Equilibrium constants for these complexes are currently not implemented in the NEA database used and have been added using the thermodynamic constants from Endrizzi et al. [110]. At pH 9.3 slightly more than 50% of the uranium is bound in the Ca-containing complexes, separated in 22% and 30% for the negatively double charged $\text{CaUO}_2(\text{CO}_3)_3^{2-}$ and the neutral complex $\text{Ca}_2\text{UO}_2(\text{CO}_3)_{3,\text{aq}}$, respectively. The maximum concentration of these complexes coincides with the pH value of all

samples except the long-term sorption sample series. At the lower limit of the pH region, the ratio decreases to 6% and 9% in case of the negatively double charged and the neutral complex, respectively. All described complexes contain uranium in the oxidation state +VI and reduction to U(IV) is thermodynamically not expected. Moreover, it has been shown that the Ca-UO₂-CO₃ complexes are very stable towards reduction [111].

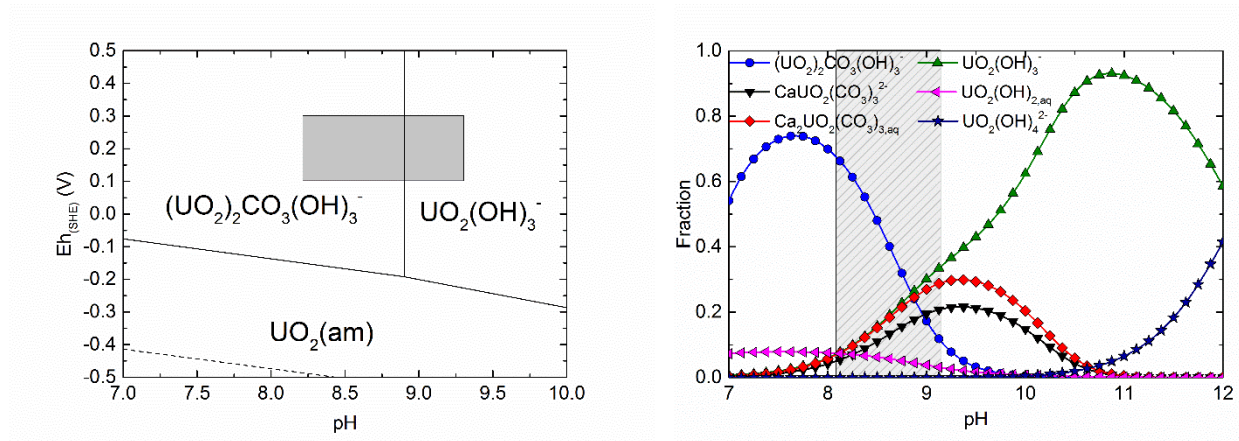


Figure 39: (left) Predominance diagram for ²³³U under the given conditions. The region of interest is marked with the light grey area and (right) thermodynamic speciation calculation.

7.1.3.3 ²³⁷Np speciation

The predominance diagram for ²³⁷Np shows only the pentavalent species, NpO₂⁺ (Figure 40, left) under the experimental conditions. Lowest Eh_{SHE} values are close (< 50mV) to the transition borderline from Np(V) to Np(IV) but still in the stability field of Np(V). Np speciation shows NpO₂⁺ in a ratio of 95% at pH 8.2 and still 67% at pH 9.3 with NpO₂CO₃⁻ as the second dominating species (Figure 40, right).

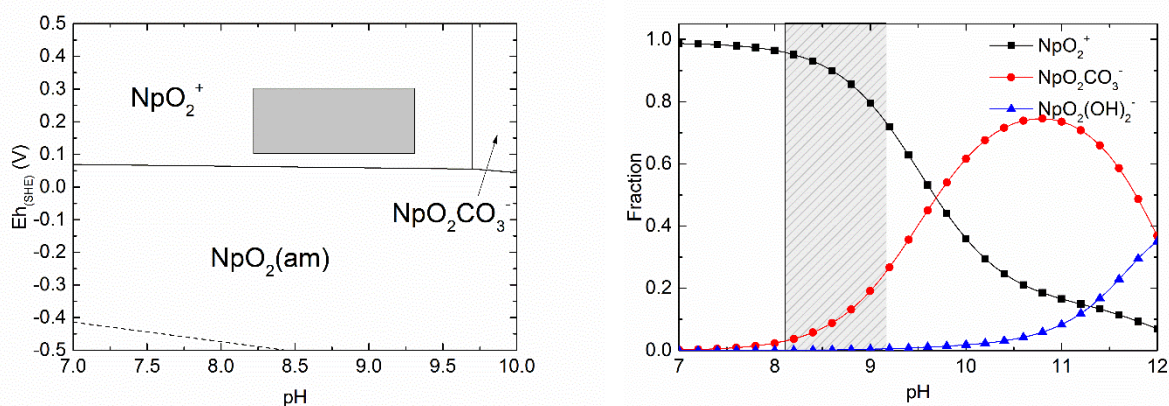


Figure 40: (left) Predominance diagram for ^{237}Np under the given conditions. The region of interest is marked with the light grey area and (right) thermodynamic speciation calculation.

7.1.3.4 ^{242}Pu speciation

The predominance diagram for ^{242}Pu can be found in Figure 41 (left). A Pu(IV) stock solution was used in the experiments and the dominant complex $\text{Pu}(\text{OH})_4$ does not show a change of the oxidation state under the conditions prevailing. Due to the distance to the Pu(IV)/Pu(III) borderline, reduction is not expected. Calculation of the speciation under the given conditions show that the $\text{Pu}(\text{OH})_4$ neutral complex is the only relevant one in the system (Figure 41, right).

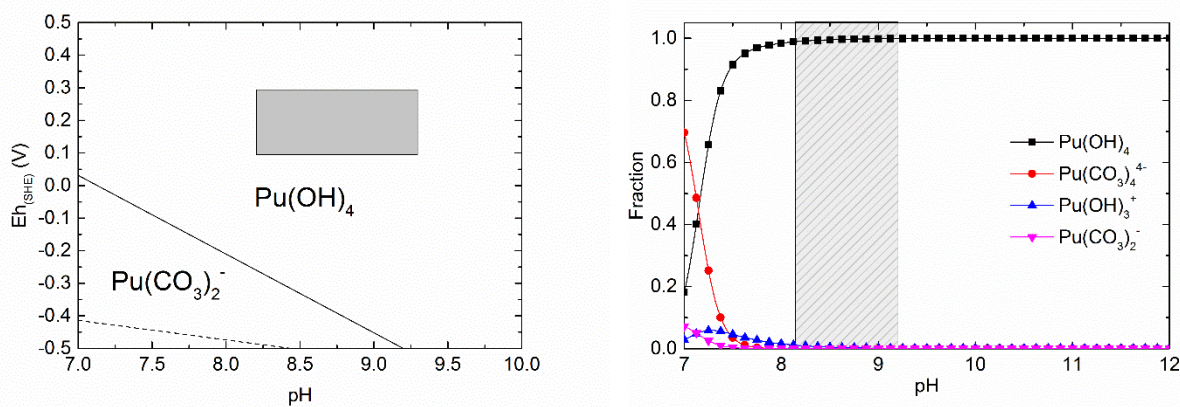


Figure 41: (left) Predominance diagram for ^{242}Pu under the given conditions. The region of interest is marked with the light grey area and (right) thermodynamic speciation calculation.

7.1.3.5 ^{243}Am speciation

The predominance diagram for ^{243}Am (Figure 42, left) shows two relevant species, namely AmCO_3^+ at pH values below 8.5 and $\text{Am}(\text{OH})_2^+$ at pH values above pH 8.5. At low pH values a third complex (AmOH^{2+}) gains minor importance ($\sim 15\%$) as can be seen in the speciation diagram in Figure 42 (right). Precipitation or a change of the oxidation state is in case of ^{243}Am not expected.

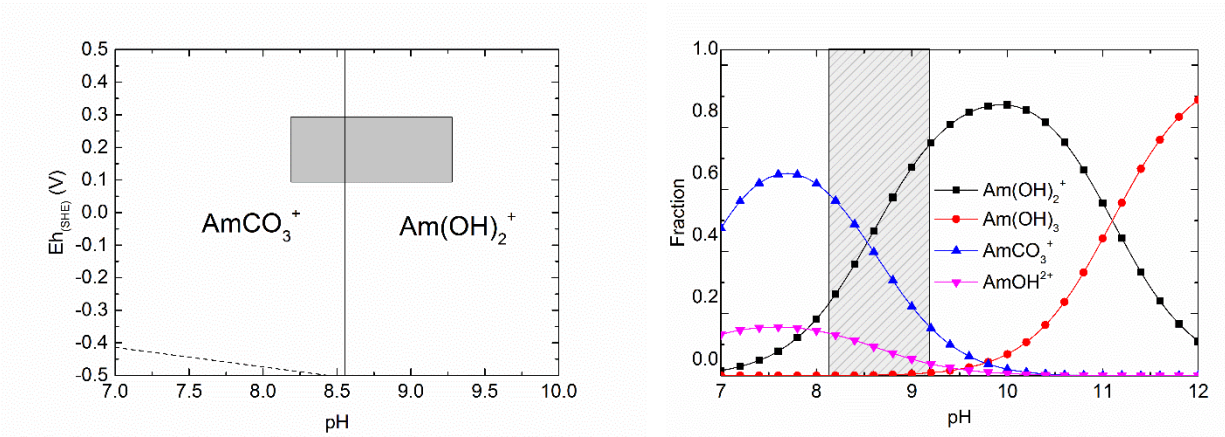


Figure 42: (left) Predominance diagram for ^{243}Am under the given conditions. The region of interest is marked with the light grey area and (right) thermodynamic speciation calculation.

7.1.4 RN sorption kinetics

7.1.4.1 $^{99}\text{Tc(VII)}$, $^{233}\text{U(VI)}$ and $^{237}\text{Np(V)}$

The results for the $^{99}\text{Tc(VII)}$ sorption kinetics are shown in Figure 43a for both the single RN experiments and the RN cocktail experiments. Less than 10% sorption was observed for the cocktail samples after 28 d contact. The same is true for the single RN samples except the values after 28 d, which is around 17%. For the long-term sample after 232 d both the single RN experiments yielded values of 60% and ~45% for the RN cocktail samples, respectively. Regarding the thermodynamic modelling, a reduction of Tc(VII) to Tc(IV) is rather unlikely since the measured redox potentials are more than 200 mV above the 50/50% borderline for Tc(VII)/Tc(IV) reduction. The removal process leading to the decrease in aqueous $^{99}\text{Tc(VII)}$ concentration is most probably a surface-induced redox transformation of $^{99}\text{Tc(VII)}$ to $^{99}\text{Tc(IV)}$. It is well known that a dramatic change in the sorption properties is accompanied with the reduction process [112]. While Tc(VII) behaves like a conservative tracer and is therefore not interacting with the FG surface, Tc(IV) shows a very strong sorption behavior. Thus, it seems likely that during the experimental duration a coupled process of reduction and subsequent sorption occurred (sorptive reduction). As potential redox partner Fe(II) might be responsible which is found in the Grimsel FG material as verified by XRF measurements (2.7 wt-% FeO). A similar behavior of ^{99}Tc sorptive reduction in the same system has been observed e.g. by Huber et al. (2011, 2015) [4, 113]. Regarding thermodynamic simulation results, no reduction should be expected based on the measured pH-Eh range. This is apparently in agreement with measurements for short contact times. For longer contact times, however, calculations and experiment differ. One has to state clearly that the determination of the redox potential in natural systems is associated with very high uncertainties due to local redox disequilibrium as discussed for example Grenthe et al. (1992) [107]. A study by Marsac et al. (2015) [41] investigated Np(V) interaction with illite and found that although the measured redox potential measured in solution would predict Np(V), the reduced Np(IV) species was detected on the illite surface. This observation was explained by the occurrence of a very stable Np(IV) surface complex. A similar behavior for Tc(VII) surface reduction was just recently reported by Huber et al. [42]. Another possible explanation would be that the redox potential measured in solution with a redox electrode can be different to the redox potential prevailing at the solid-liquid interface and that it is reducing enough to build up Np(IV) surface species.

Sorption kinetics for $^{233}\text{U(VI)}$ are shown in Figure 43b. Only values for the cocktail samples are shown since no single RN experiment has been conducted for $^{233}\text{U(VI)}$. A maximum of ~40% sorption was observed which was obtained already after 14 d contact time. Afterwards only a very small increase could be observed until 232 d (~2%). This might be interpreted as a faster initial sorption followed by a very slow sorption reaction. Regarding the thermodynamic modelling a reduction of U(VI) to U(IV) as shown for ^{99}Tc is rather unlikely since the measured redox potentials are more than 100 mV above the 50/50% borderline for U(VI)/U(IV) reduction. It seems more reasonable to assume the sorption of U(VI) species. It has been shown that the CaUO_2CO_3 species is rather weakly sorbing and thus also very stable against reduction when assuming a sorptive reduction process. This would be in line with the results observed.

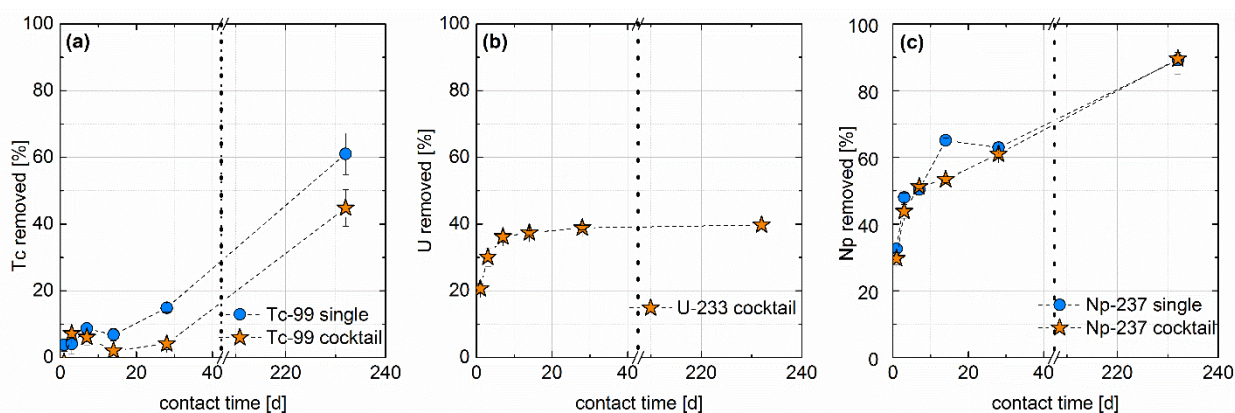


Figure 43: Results of (a) ^{99}Tc , (b) ^{233}U and (c) ^{237}Np batch sorption kinetic experiments.

Both single RN and cocktail experiments have been conducted for $^{237}\text{Np(V)}$. Results are depicted in Figure 43c. The results indicate the absence of an equilibrium state within the experimental duration of 232 d. There is a steady increase in sorption for $^{237}\text{Np(V)}$ up to ~90% after 232 d contact time. No difference is observable between the cocktail and the single RN samples indicating the absence of any competition effects. Since the pentavalent Np is known to sorb rather weakly the removal process might again be explained by a sorptive reduction process to Np(IV) at the surface of the FG material. This seems to be corroborated by thermodynamic considerations which predict Np(IV) species at around 60 mV in the pH range 8 to 10. Given the uncertainties of the $E_{\text{h(SHE)}}$ measurements as noted above, the measured values are relatively close to the Np(V)/Np(IV)

borderline. A transformation of Np(V) to Np(IV) and a subsequent sorption to the FG material can therefore be hypothesized as Np removal process.

7.1.4.2 $^{242}\text{Pu(IV)}$ and $^{243}\text{Am(III)}$

With respect to ^{99}Tc , ^{233}U and ^{237}Np , $^{242}\text{Pu(IV)}$ shows a much faster sorption reaction since more than 80% is already sorbed after 3 d contact time as can be seen in Figure 44. The high degree of sorption was expected since the tri- and tetravalent RNs are known to sorb very strongly onto various mineral phases [33]. The sorption increases to more than 90% after 7 d to 14 d possibly reaching already a steady state equilibrium process. After 232 d contact time, the sorption is even slightly higher at around 98%. This increase between 28 d and 232 d might indicate a very slow sorption reaction step. Again, no difference was observed between single RN experiments and cocktail experiments, respectively.

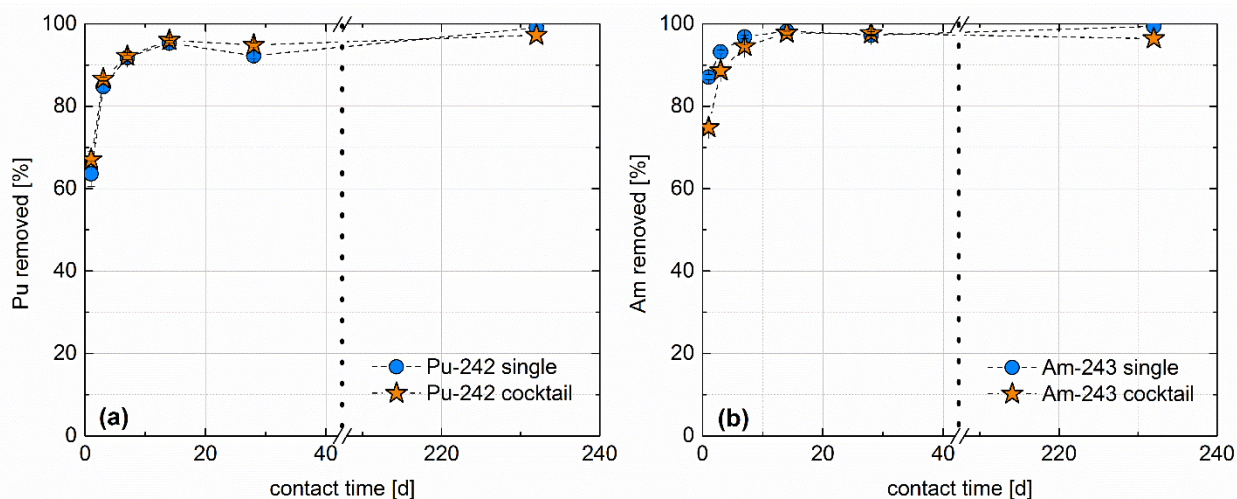


Figure 44: Results of ^{242}Pu (a) and ^{243}Am (b) batch kinetic sorption experiments.

A very similar sorption behavior was found for $^{243}\text{Am(III)}$ compared to $^{242}\text{Pu(IV)}$. After 7 to 14d, the sorption is $> 95\%$ reaching a plateau which can be interpreted as an equilibrium state. No difference is found between single RN experiments and cocktail experiments. A summary of the

sorption values and associated distribution coefficients are listed in Table 13. The possibility of colloidal species has not been ruled out by centrifugation during sampling. Therefore, K_d values are minimum values. Regarding the maximum sorption values of up to 99%, only 1% of the total activity is left in the supernatant and either dissolved or sorbed on a colloidal phase. Considering the extreme that the remaining RN fraction is quantitatively colloid associated will have a great impact on the distribution coefficients. Assuming that the maximum distribution between mineral sorbed and colloid sorbed RN is 100:1 and that is valid for all radionuclides, only a minor effect on the distribution coefficients is expected in case of ^{99}Tc , ^{233}U and ^{237}Np .

Table 13: Maximum sorption values and distribution coefficients of the RN sorption samples. Duplicates have been prepared and a value for each sample is given.

| | Max. sorption [%] | | K_d min [L/kg] | K_d max [L/kg] |
|----------------|----------------------|------------------------|---------------------|---------------------|
| | | $^{242}\text{Pu(IV)}$ | | |
| Single RN exp. | 99 | | 487 | 727 |
| Cocktail exp. | 98 | | 122 | 322 |
| | | $^{243}\text{Am(III)}$ | | |
| Single RN exp. | 99 | | 183 | 253 |
| Cocktail exp. | 96 | | 71 | 171 |
| | | $^{233}\text{U(VI)}$ | | |
| Cocktail exp. | 40 | | 3.6 | 3.8 |
| | | $^{237}\text{Np(V)}$ | | |
| Single RN exp. | 89 | | 32 | 81 |
| Cocktail exp. | 90 | | 38 | 60 |
| | | $^{99}\text{Tc(VII)}$ | | |
| Single RN exp. | 60 | | 6.8 | 11.6 |
| Cocktail exp. | 45 | | 3.7 | 5.8 |

7.1.4.3 Sorption data treatment

Using an exponential growth equation (Equation 16) sorption rates k [1/t] were fitted to the experimental datasets.

$$y = A_1 \cdot e^{\frac{x}{t_1}} + y_0 \quad \text{with } k = \frac{1}{t_1} \quad \text{Equation 16}$$

where y_0 is the radionuclide fraction in equilibrium that was removed by sorption.

The fitting results of the sorption data are given in Table 14. Sorption rates are given as negative values because the data is fitted over the radionuclide concentrations which are dissolved in solution. Therefore, the concentration will decrease with increasing sorption and negative rates are needed to describe this decline. These rates are needed as input parameters in numerical codes for performance assessment calculations like e.g. COFRAME [68]. The fastest rates were found for Pu with values of ~ -0.52 to -0.54 [1/d]. Am and U show very similar rates of -0.37 to -0.45 [1/d] ($^{243}\text{Am(III)}$) and -0.38 [1/d] ($^{233}\text{U(IV)}$). Although the rates for $^{243}\text{Am(III)}$ and $^{233}\text{U(IV)}$ are very similar the amount of sorbed species is totally different for these two radionuclides. That is, because the sorption rate is not sensitive to the final amount sorbed on the FG but to the gradient of the sorption data. Rates of around one order of magnitude lower were found in case of Np yielding values of -0.027 to -0.037 [1/d]. For $^{99}\text{Tc(VII)}$, the fitting routine was not successful due to the very low amount of $^{99}\text{Tc(VII)}$ sorbed within the first month of the experiments which can be seen as induction time for the higher sorption values that occurred after 232 days sorption.

Table 14: Radionuclide sorption rates fitted to the batch sorption experiment results.

| | Rate [1/d] | | Error [\pm] | R ² [-] |
|----------------|---------------|------------------------|---------------------|-----------------------|
| | | $^{242}\text{Pu(IV)}$ | | |
| Single RN exp. | -0.52 | | 0.15 | 0.948 |
| Cocktail exp. | -0.54 | | 0.1 | 0.976 |
| | | $^{243}\text{Am(III)}$ | | |
| Single RN exp. | -0.37 | | 0.088 | 0.962 |
| Cocktail exp. | -0.45 | | 0.059 | 0.934 |
| | | $^{233}\text{U(VI)}$ | | |
| Cocktail exp. | -0.38 | | 0.053 | 0.98 |
| | | $^{237}\text{Np(V)}$ | | |
| Single RN exp. | -0.037 | | 0.017 | 0.84 |
| Cocktail exp. | -0.027 | | 0.011 | 0.9 |
| | | $^{99}\text{Tc(VII)}$ | | |
| Single RN exp. | | | No fitting possible | |
| Cocktail exp. | | | No fitting possible | |

7.1.5 RN desorption kinetics in the binary system

Subsequent to the sorption studies, desorption experiments were conducted to examine a possible sorption reversibility as function of the overall RN - FG contact time. The desorption data is presented in the following way: (i) the amount sorbed after the selected contact time is set to 100%, (ii) the amount desorbed after each desorption step is plotted as cumulative concentration as a function of time.

7.1.5.1 $^{99}\text{Tc(VII)}$, $^{233}\text{U(VI)}$ and $^{237}\text{Np(V)}$

Desorption kinetics for $^{99}\text{Tc(VII)}$ are depicted in Figure 46. As in all sorption samples contacted for < 28 days, the fraction of sorbed Tc is rather low, the desorption data are not considered reliable and highly affected by uncertainties. A reasonable trend of desorption rates with increasing contact time is therefore hard to be derived. For long contact periods (232 d), however, it is evident that the dissociation of Tc from the FG to solution is slow. In contrast to $^{99}\text{Tc(VII)}$, data for $^{233}\text{U(VI)}$ show a clearer trend between the sorption time and the reversibility. For short contact time samples coinciding desorption rate curves are obtained. Uranium desorbs, however, not completely until ~400 days, where only about 70% are removed from the FG surface. Uranium desorption rates decrease significantly after a contact time of 168 d and only 30% of uranium could be desorbed after 232 days sorption. This result highlights that the previous sorption time has a direct influence on the desorbable amount. A possible explanation for this observation might be found in a coupled sorption reduction transformation over time. That is, ^{233}U was sorbed initially as hexavalent $^{233}\text{U(VI)}$ on the FG material and was reduced to U(IV) by e.g. Fe(II) during the course of the experiment especially for the long-term samples. Since $^{233}\text{U(IV)}$ is showing a stronger sorption behavior as $^{233}\text{U(VI)}$, the total desorption and the desorption rate is expected to be less which is in line to the results described above. Provided that a change of the uranium oxidation state can be neglected, the lower total desorption in the 232 d sorption sample can be explained by alteration of the mineral surfaces. Thereby part of the radionuclides are incorporated in the mineral matrix.

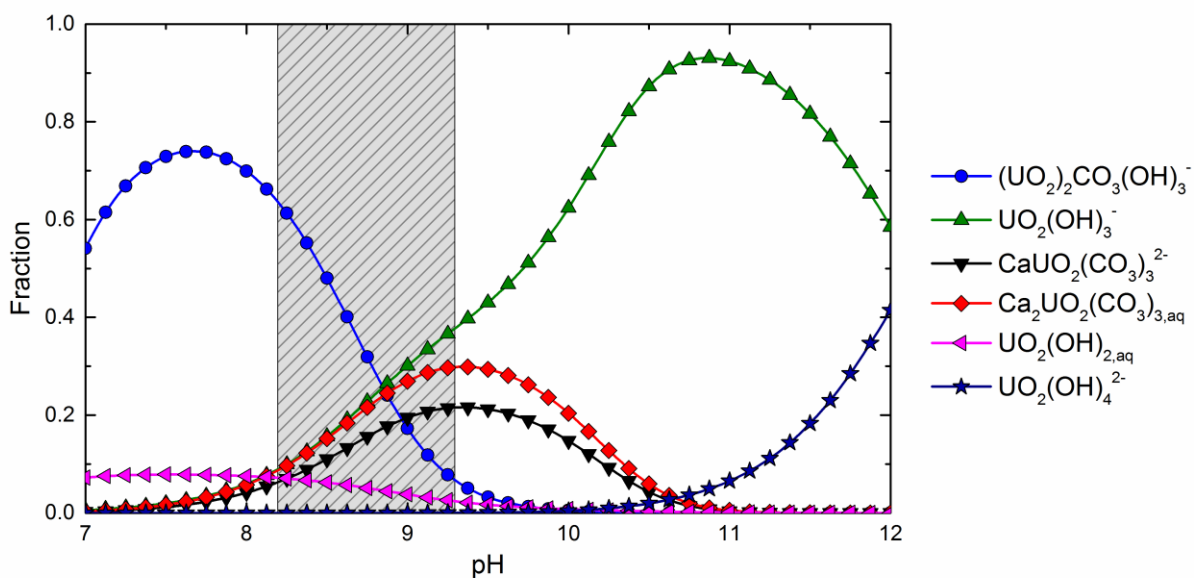


Figure 45: Uranium speciation in GW calculated with Hydra-Medusa. The relevant pH region in the sorption experiment is located within the grey shaded area. There is no change in the oxidation state but it is obvious that calcium complexes which are not observed in the predominance diagram cannot be neglected.

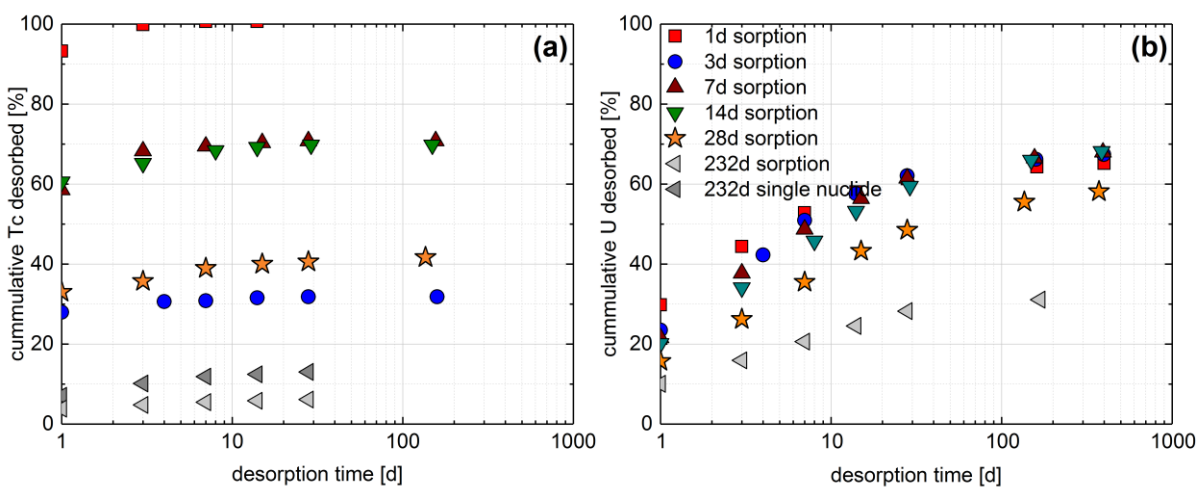


Figure 46: Results of (a) ^{99}Tc and (b) ^{233}U batch kinetic desorption experiments.

An even clearer correlation between the previous sorption time and desorption rates is found for $^{237}\text{Np(V)}$ as shown in Figure 47. The longer the sorption time, the slower the desorption. The maximum desorption increases from ~30% after 1 d desorption up to ~68% after 399 d desorption for the 1 d sorption sample. For the 232 d sorption samples, the desorption values increase only from below 10% after 1 d up to a maximum of only ~20% after 168 d desorption. Moreover, the desorption kinetics slow down between 28 d and 168 d desorption time indicating near equilibrium conditions. Regarding short sorption times until 28 days, slightly higher desorption values (~5 to 10%) were observed for the cocktail samples compared to the single RN samples. A very similar explanation for the correlation between the sorption time and the Np desorption behavior is postulated as above for Tc. Np(V) was reduced to Np(IV) during the sorption experiments and removed via sorption to the FG material. The increasing amount of stronger sorbing Np(IV) for longer contact times during the sorption experiments is directly visible in the decreasing amount of desorbed Np for the longer contact times of the sorption samples within the desorption experiments.

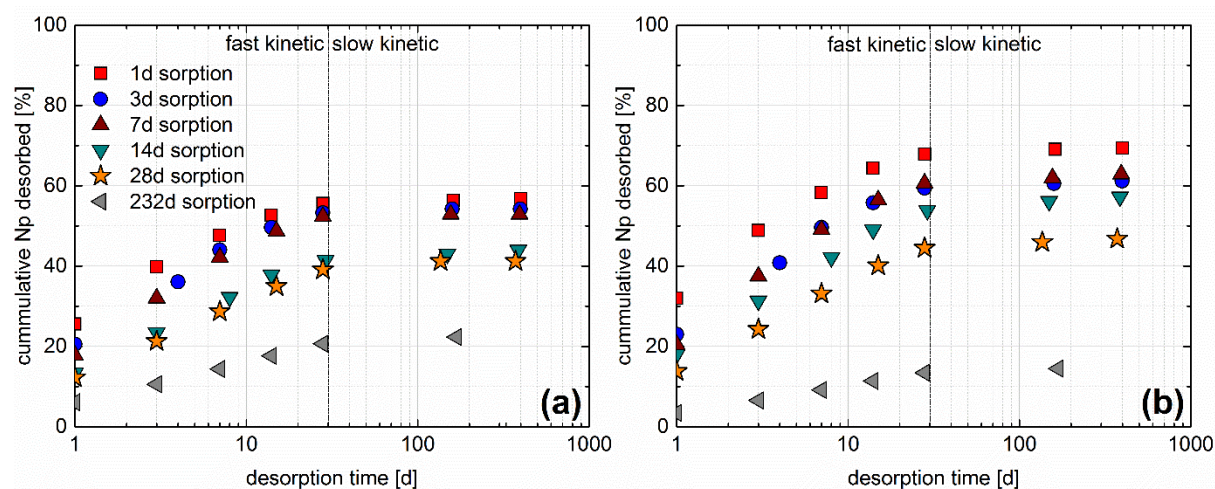


Figure 47: Results of (a) ^{237}Np single radionuclide and (b) ^{237}Np cocktail kinetic desorption experiments, respectively.

Distribution coefficients have been calculated after each desorption time step of the 232 days sorption samples. These samples have been chosen because lowest recoveries have been observed in comparison to shorter sorption times and consequently highest K_d values. Distribution coefficients during desorption are in case of ^{99}Tc with values of 460 ± 340 L/kg (Single RN) and

1060±610 L/kg (RN cocktail) up to two orders of magnitude increased, supporting the theory of a surface induced reduction to Tc(IV). Distribution coefficients are in case of ^{233}U with a value of 97±26 L/kg and ^{237}Np with values of 150±56 L/kg (Single RN) and 240±100 L/kg (RN cocktail) also increased. The maximal difference of only one order of magnitude is closer to the sorption derived distribution coefficients. Comparison to the distribution coefficients during sorption and desorption supports the theory of surface induced reduction in particular in regard of the ^{99}Tc sorption reversibility.

7.1.5.2 $^{242}\text{Pu(IV)}$ and $^{243}\text{Am(III)}$

The results of the desorption experiments for both $^{242}\text{Pu(IV)}$ and $^{243}\text{Am(III)}$ show a very similar trend (Figure 48). Both radionuclides are strongly and fast sorbing in the sorption experiments. Desorption increases from ~1% after 1 d desorption time to a maximum of ~15% (or even less) after 232 d desorption time. No clear dependence of desorption extent and rate on the contact time was observed. A very slow desorption kinetic might be seen in case of the single RN experiments especially for Pu. Even slower kinetics were observed for the cocktail experiment samples for Pu and Am single RN experiments. Unfortunately, no results for ^{243}Am cocktail sample series have been obtained due to very little amount of desorption lying below the detection limit of the ICP-MS, which is given with 0.3 ng/L. Distribution coefficients have been calculated after each desorption time step of the 232 days sorption samples. These samples have been chosen because lowest desorption has been observed in comparison to shorter sorption times, except in case of the ^{242}Pu cocktail sample whereat all desorption samples are close together (Figure 48b). Average distribution coefficients of 670±300 and 810±450 L/kg have been obtained for the single nuclide and the radionuclide cocktail samples of ^{242}Pu , respectively. These values match with the distribution coefficients that have been determined during the sorption experiment (Table 13). An average distribution coefficient of 2700±1150 L/kg is determined in case of the ^{243}Am single nuclide desorption samples. This value is one order of magnitude above the distribution coefficient that has been observed during the sorption experiment. The difference of the K_d -values indicates the possibility of a colloidal species in the sorption samples and therefore under-determined distribution coefficients. Higher K_d values during desorption can also be explained by an alteration process, which immobilized part of the sorbed RNs by incorporation into the FG matrix. This effect

was not observed in case of the ^{242}Pu samples and is therefore less probable. To conclude, both radionuclides show only very weak desorption in the range of the K_d values that have been observed during the sorption experiment. Therefore, experiments adding montmorillonite colloids as concurrence ligand to the RN containing FG material samples were conducted to investigate if the desorption could be enhanced. Sorption time dependence in the desorption process has not been observed.

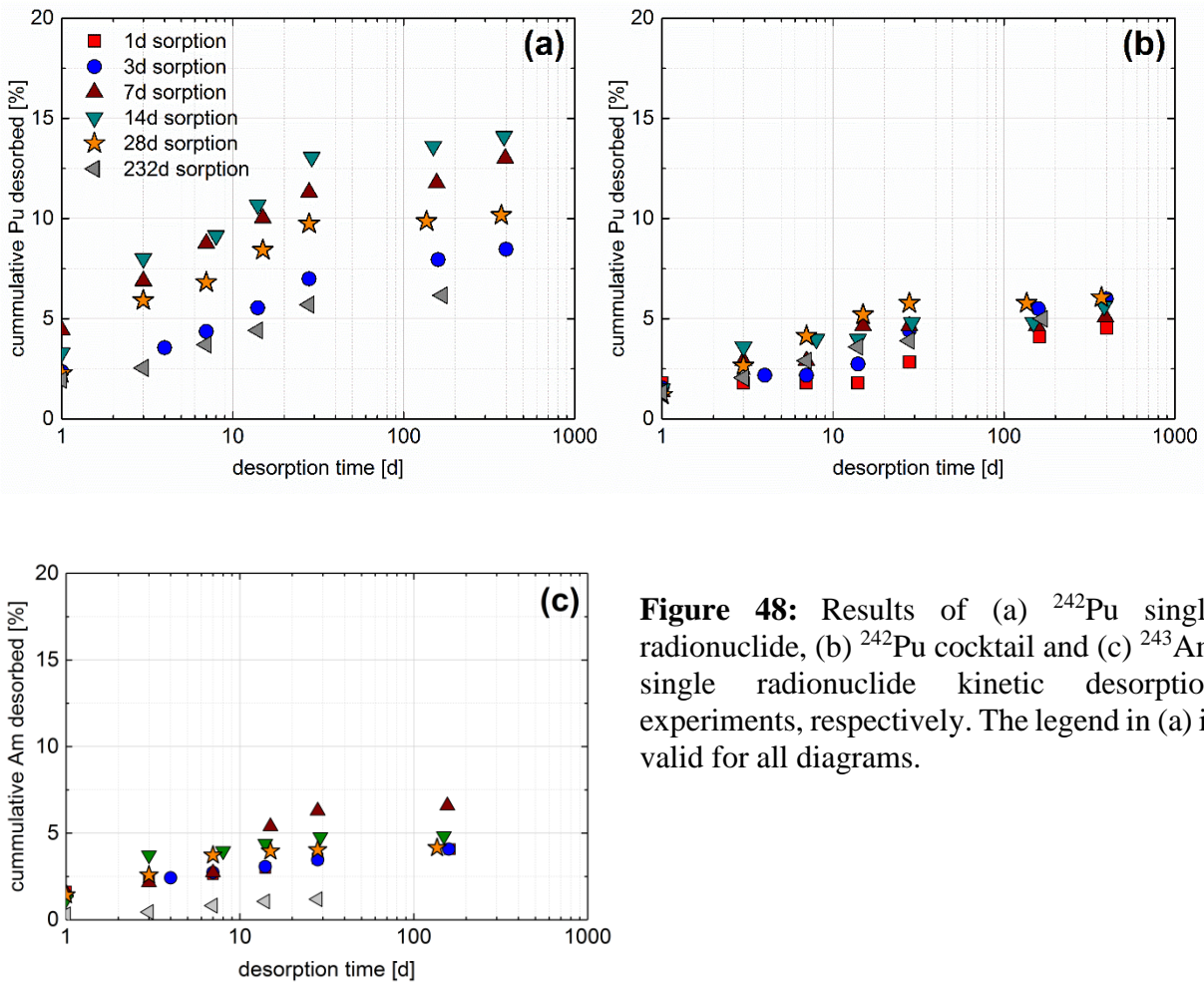


Figure 48: Results of (a) ^{242}Pu single radionuclide, (b) ^{242}Pu cocktail and (c) ^{243}Am single radionuclide kinetic desorption experiments, respectively. The legend in (a) is valid for all diagrams.

7.1.5.3 Desorption data treatment

Desorption data was fitted using an exponential decay equation (Equation 17):

$$y = A_1 \cdot e^{-\frac{x}{t_1}} + y_0 \quad \text{with } k = \frac{1}{t_2} \quad \text{Equation 17}$$

Fitting the desorption data with Equation 17 was not successful for all radionuclides. Especially data of the redox-sensitive nuclides neptunium and uranium were not described satisfactorily. Therefore, a two-rate fit (Equation 18) was applied for these radionuclides because desorption of two oxidation states (e. g. Np(V) and Np(IV) in parallel cannot be neglected in case of the redox-sensitive radionuclides. Desorption of different surface associated species as shown in the speciation diagram of uranium (Figure 39) that show different desorption behavior have to be taken into account and lead to a two-site desorption kinetic:

$$y = A_1 \cdot e^{-\frac{x}{t_3}} + A_2 \cdot e^{-\frac{x}{t_4}} + y_0 \quad \text{with } k_1 = \frac{1}{t_3} \text{ and } k_2 = \frac{1}{t_4} \quad \text{Equation 18}$$

Table 15: Overview of the fitted desorption rates and measured radionuclide recoveries. Recovery denotes the radionuclide fraction found in solution after the desired contact time of desorption.

| Sorption time [d] | Desorption time [d] | Single nuclide samples | | | | RN cocktail samples | | | |
|-------------------------|------------------------|-------------------------------------|------------------------------|----------|-----------------|------------------------------|------------------------------|----------|-----------------|
| | | 1-rate fit k [1/a] | 2-rate fit k_1 [1/a] | | Recovery [%] | 1-rate fit k [1/a] | 2-rate fit k_1 [1/a] | | Recovery [%] |
| ²³⁷Np | | | | | | | | | |
| 1 | 399 | 147 ± 24 | 409 ± 23 | 48 ± 4 | 57 | 150 ± 26 | 424 ± 28 | 47 ± 4 | 70 |
| 3 | 397 | 96 ± 13 | 479 ± 117 | 57 ± 8 | 55 | 96 ± 13 | 446 ± 115 | 56 ± 9 | 61 |
| 7 | 393 | 100 ± 89 | 296 ± 24 | 47 ± 3 | 53 | 95 ± 13 | 254 ± 24 | 38 ± 4 | 63 |
| 14 | 386 | 66 ± 11 | 351 ± 75 | 39 ± 5 | 44 | 68 ± 12 | 336 ± 57 | 36 ± 4 | 57 |
| 28 | 372 | 58 ± 10 | 323 ± 30 | 33 ± 2 | 42 | 69 ± 10 | 319 ± 48 | 37 ± 3 | 46 |
| 232 | 168 | 50 ± 9 | 331 ± 36 | 29 ± 2 | 22 | 48 ± 7 | 273 ± 13 | 29 ± 1 | 15 |
| ²³³U | | | | | | | | | |
| 1 | 399 | no single nuclide samples for U-233 | | | | 132 ± 29 | 403 ± 52 | 33 ± 6 | 65 |
| 3 | 397 | | | | | 76 ± 13 | 301 ± 61 | 30 ± 7 | 67 |
| 7 | 393 | | | | | 69 ± 14 | 250 ± 31 | 23 ± 3 | 68 |
| 14 | 386 | | | | | 47 ± 10 | 275 ± 62 | 21 ± 4 | 68 |
| 28 | 372 | | | | | 37 ± 8 | 260 ± 69 | 19 ± 4 | 58 |
| 232 | 168 | | | | | 52 ± 12 | 376 ± 52 | 25.4 ± 3 | 31 |
| ⁹⁹Tc | | | | | | | | | |
| 232 | 168 | 163 ± 42 | 380 ± 61 | 18.9 ± 8 | 14 | 217 ± 62 | 654 ± 128 | 32 ± 10 | 6.5 |
| ²⁴²Pu | | | | | | | | | |
| 1 | 399 | 41 ± 16 | 622 ± 148 | 14 ± 3 | 13 | 9 ± 4 | No fitting possible | | 5 |
| 3 | 397 | 27 ± 5 | 664 ± 297 | 20 ± 3 | 9 | 15 ± 3 | No fitting possible | | 6 |
| 7 | 393 | 51 ± 14 | 351 ± 132 | 23 ± 8 | 13 | 57 ± 14 | 386 ± 530 | 39 ± 27 | 5 |
| 14 | 386 | 48 ± 11 | 253 ± 117 | 21 ± 9 | 14 | 52 ± 19 | 196 ± 53 | 1 ± 3 | 6 |
| 28 | 372 | 65 ± 12 | 227 ± 115 | 28 ± 14 | 10 | 65 ± 6 | 159 ± 82 | 41 ± 12 | 6 |
| 232 | 168 | 38 ± 8 | 1024 ± 1101 | 27 ± 5 | 6 | 32 ± 8 | 195 ± 86 | 12 ± 6 | 5 |
| ²⁴³Am | | | | | | | | | |
| 1 | 399 | 36 ± 12 | 494 ± 74 | 15 ± 2 | 4 | below ICP-MS detection limit | | | |
| 3 | 397 | 39 ± 11 | 308 ± 58 | 11 ± 2 | 4 | | | | |
| 7 | 393 | 32 ± 5 | No fitting possible | | 7 | | | | |
| 14 | 386 | 100 ± 27.0 | 175 ± 44 | 3 ± 3 | 5 | | | | |
| 28 | 372 | 113 ± 12 | 138 ± 12 | 3 ± 3 | 4 | | | | |
| 232 | 168 | 34 ± 5 | 75 ± 38 | 9 ± 12 | 1 | | | | |

7.1.6 RN desorption kinetics in the ternary system

Due to the strong binding and the slow release of the tri- and tetravalent actinides $^{242}\text{Pu}(\text{IV})$ and $^{243}\text{Am}(\text{III})$, a competing surface has been added to the system in order to force and to quantify the release rates of the RN from the FG. Single nuclide samples of $^{242}\text{Pu}(\text{IV})$ and ^{243}Am as well as the RN-cocktail samples have been included in this experiment. Therefore, the supernatant of each sample was exchanged after a total run-time of 400 days (sorption and desorption in the binary system) by a 35.9 mg/L Ni-labelled montmorillonite colloid containing suspension in GGW (Chapter 6.3.2.2). ^{99}Tc and ^{237}Np single nuclide samples have not been included in this study because of difficulties in the quantification of the desorbed concentration due to low sorption values (^{99}Tc) or because a significant amount already desorbed in the binary system (^{237}Np). Nevertheless both radionuclides are part of the radionuclide cocktail samples. After each desorption time step two samples were taken and the remaining supernatant was exchanged against fresh Ni-montmorillonite containing GGW. One sample was measured after centrifugation (18.000 rpm, 1h) and the remaining sample was measured without further treatment to differentiate between colloid bound and dissolved fractions. Collected kinetic data will be used to improve the input parameters of the transport code COFRAME [68].

7.1.6.1 $^{99}\text{Tc}(\text{VII})$, $^{233}\text{U}(\text{VI})$ and $^{237}\text{Np}(\text{V})$

Desorption data for ^{99}Tc in the ternary system is depicted in Figure 49a. As explained in Chapter 6.1.3.1 desorption data values are attached with a high uncertainty. This results in recoveries above 100% which have been found in part of the shorter sorption time samples (≤ 28 d). Samples with a sorption time of 232 d deliver once again the only reliable data and show an increase of the desorbed fraction from 6% in the binary to 40% in the ternary system for the latest sampling respectively. Desorption equilibrium in the binary system was established within the first days of desorption. A fast kinetic was found but in case of the ternary system equilibrium is not reached within 211 days of desorption. Therefore, the desorption rate is only preliminary and smaller in comparison to the binary case although the 6-fold amount of Tc was desorbed from the FG. Analysis of ultra-centrifuged samples and analysis of the centrifugate showed that 91% of the desorbed Tc is associated to montmorillonite colloids only 9% are free in solution. This can be interpreted as a hint for the surface reduction process from weak sorbing Tc(VII) to strong sorbing

Tc(IV), already mentioned in 7.1.5.1. In the ternary system Tc(IV) desorbs from the FG to attach selectively to the higher charged montmorillonite colloids.

Desorption data for ^{233}U in the ternary system is depicted in Figure 49b. Uranium desorption in the ternary system shows only minor differences in comparison to the latest values in the binary case. An additional fraction of 2% for the short time sorption samples going up with increasing sorption time to 9% for 232 d sorption in relation to the initial sorbed amount was remobilized. The last desorption value after 211 days desorption is set as equilibrium although there is still a small increase and desorption rates are derived in the range of 21 ± 5 1/a for all samples. These values are smaller compared to the desorption in the binary system. A sorption time dependence is not detectable. Under the assumption of a combined sorption and partial surface reduction process from U(VI) to U(IV) and the remobilization of the weaker sorbed U(VI) in the binary desorption experiments mainly U(IV) should be on the FG at the beginning of the ternary desorption. Analysis of the centrifuged samples showed that $76 \pm 10\%$ of the desorbed U is Ni-montmorillonite colloid associated while $24 \pm 10\%$ are free in solution. The relatively high diluted ratio is a hint for the presence of U(VI) in solution as one would expect U(IV) as sorbed species. Nevertheless, an analysis of this issue is due to very low concentrations ($< 1 \cdot 10^{-10}$ M in solution) not possible.

Desorption data for ^{237}Np in the ternary system is depicted in Figure 49c. The behavior of ^{237}Np is very similar to ^{233}U . A small additional fraction of 3% to 8% in relation to the values in the binary system, which is increasing with higher initial sorption time is released during desorption in the ternary system. The last desorption value after 211 days desorption is set as equilibrium value and desorption rates are derived in the range of 32 ± 7 1/a for all samples which is significantly lower compared to the rates in the binary system. Analysis of the centrifuged samples showed that $60 \pm 12\%$ of the desorbed Np is Ni-montmorillonite colloid associated while $40 \pm 12\%$ free in solution. The relatively high dilution ratio is a hint for the presence of Np(V) in solution as one would expect Np in the oxidation state +IV as sorbed species. As in the case of U further analysis of this issue is due to very low concentrations ($< 1 \cdot 10^{-10}$ M in solution) not possible.

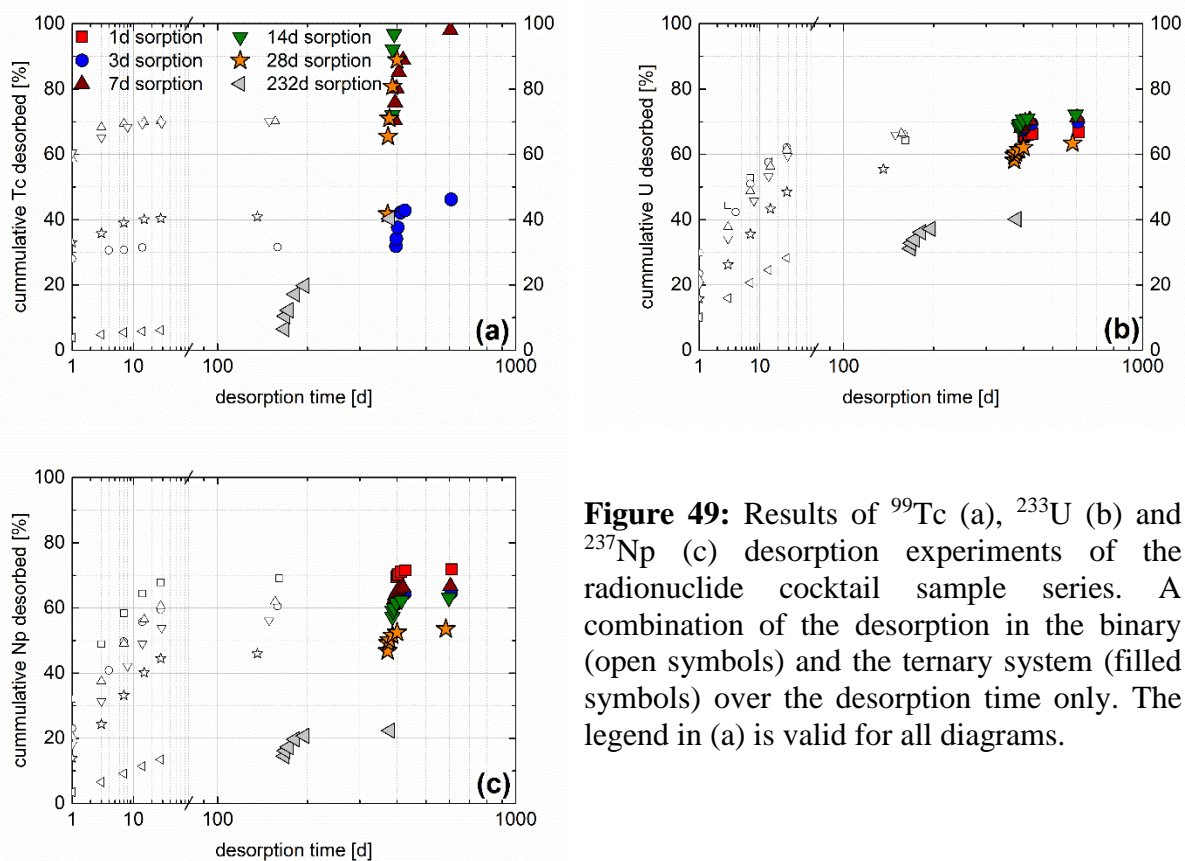


Figure 49: Results of ^{99}Tc (a), ^{233}U (b) and ^{237}Np (c) desorption experiments of the radionuclide cocktail sample series. A combination of the desorption in the binary (open symbols) and the ternary system (filled symbols) over the desorption time only. The legend in (a) is valid for all diagrams.

7.1.6.2 $^{242}\text{Pu}(\text{IV})$ and $^{243}\text{Am}(\text{III})$

The results of ^{242}Pu and ^{243}Am desorption experiments are depicted in Figure 50. Both Pu and Am samples show significant desorption triggered by the addition of and the tendency of both radionuclides to sorb on the Ni-montmorillonite particles. The three- to five-fold Pu fraction is released from the FG during desorption in the ternary system in comparison to the desorption in the binary system for both cocktail and single nuclide experiments. This is an average increase of the recovery from 5% after desorption without, to 25% in the presence of montmorillonite particles for the cocktail experiments and from 11% to 31% in case of the single nuclide experiments, respectively. Desorption is not sorption time dependent and desorption rates are with an average value of $40 \pm 9 \text{ l/a}$ (cocktail samples) and $52 \pm 30 \text{ l/a}$ (single nuclide samples) very close to the average value found in the binary system. Analysis of the centrifuged samples found that $\geq 97\%$ of the released Pu is colloid associated. In case of the Am single nuclide sample series, the reversible bound fraction increased from $4 \pm 3\%$ to $12 \pm 4\%$ by the addition of Ni-montmorillonite particles. The desorption rate is in the ternary system with a mean value of $23 \pm 6 \text{ l/a}$ even lower in

comparison to desorption rate in the binary system with a mean value of 59 ± 12 l/a. Centrifugation of the samples found that $> 99\%$ of the released Am is colloid associated.

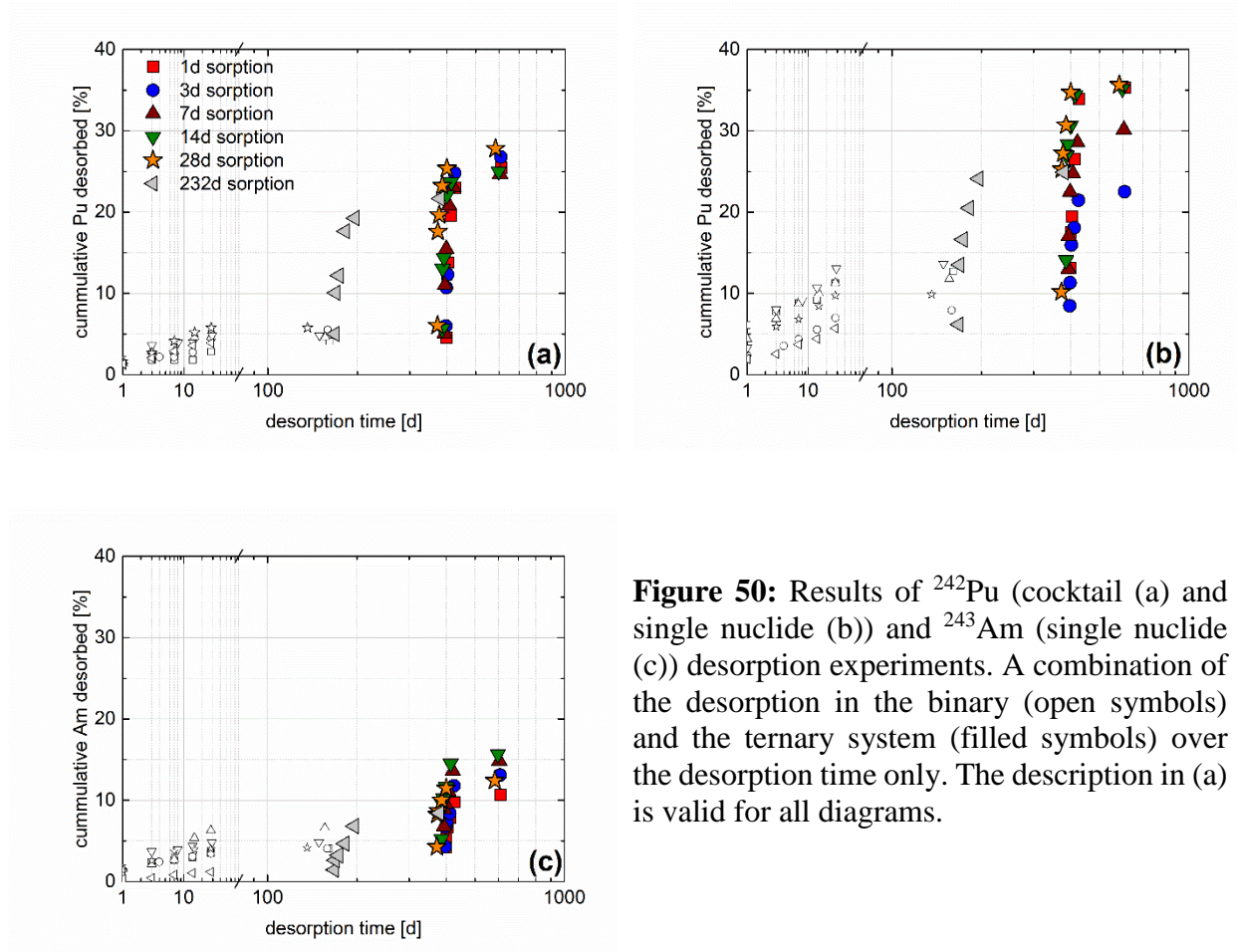


Figure 50: Results of ^{242}Pu (cocktail (a) and single nuclide (b)) and ^{243}Am (single nuclide (c)) desorption experiments. A combination of the desorption in the binary (open symbols) and the ternary system (filled symbols) over the desorption time only. The description in (a) is valid for all diagrams.

Table 16: Overview of the fitted desorption rates and measured radionuclide recoveries after desorption in the binary and the ternary system. Recovery denotes the radionuclide fraction found in solution after the desired contact time of desorption.

| Sorption time [d] | Desorption time, binary [d] | Rate, binary k [1/a] | Recovery [%] | Desorption time, ternary [d] | Rate, ternary k [1/a] | Recovery [%] |
|---|-----------------------------------|----------------------------|-----------------|------------------------------------|--------------------------------|-----------------|
| ⁹⁹Tc, cocktail experiments | | | | | | |
| 1 | 399 | - | 102% | 211 | - | 109% |
| 3 | 397 | - | 32% | 211 | - | 46% |
| 7 | 393 | - | 70% | 211 | - | 98% |
| 14 | 386 | - | 72% | 211 | - | 141% |
| 28 | 372 | - | 42% | 211 | - | 125% |
| 232 | 168 | 217 ± 62 | 6% | 211 | 6.5 ± 1 | 40% |
| ²³³U, cocktail experiments | | | | | | |
| 1 | 399 | 132 ± 29 | 65% | 211 | 17 ± 2 | 67% |
| 3 | 397 | 76 ± 13 | 67% | 211 | 22 ± 3 | 70% |
| 7 | 393 | 69 ± 14 | 68% | 211 | 27 ± 6 | 71% |
| 14 | 386 | 47 ± 10 | 68% | 211 | 20 ± 4 | 72% |
| 28 | 372 | 37 ± 8 | 58% | 211 | 21 ± 6 | 63% |
| 232 | 168 | 52 ± 12 | 31% | 211 | 16 ± 3 | 40% |
| ²³⁷Np, cocktail experiments | | | | | | |
| 1 | 399 | 150 ± 26 | 69% | 211 | 27 ± 4 | 72% |
| 3 | 397 | 96 ± 13 | 61% | 211 | 35 ± 6 | 65% |
| 7 | 393 | 95 ± 13 | 63% | 211 | 39 ± 9 | 67% |
| 14 | 386 | 68 ± 12 | 57% | 211 | 33 ± 7 | 63% |
| 28 | 372 | 69 ± 10 | 47% | 211 | 33 ± 12 | 54% |
| 232 | 168 | 48 ± 7 | 14% | 211 | 24 ± 4 | 22% |
| ²⁴²Pu, cocktail experiments | | | | | | |
| 1 | 399 | 9 ± 4 | 5% | 211 | 31 ± 9 | 25% |
| 3 | 397 | 15 ± 3 | 6% | 211 | 34 ± 7 | 27% |
| 7 | 393 | 57 ± 14 | 5% | 211 | 45 ± 9 | 25% |
| 14 | 386 | 52 ± 19 | 6% | 211 | 43 ± 12 | 25% |
| 28 | 372 | 65 ± 6 | 6% | 211 | 53 ± 27 | 28% |
| 232 | 168 | 32 ± 8 | 5% | 211 | 33 ± 7 | 22% |
| ²⁴²Pu, single nuclide experiments | | | | | | |
| 1 | 399 | 41 ± 16 | 13% | 211 | 26 ± 4 | 35% |
| 3 | 397 | 27 ± 5 | 8% | 211 | 37 ± 7 | 23% |
| 7 | 393 | 51 ± 14 | 13% | 211 | 36 ± 8 | 30% |
| 14 | 386 | 48 ± 11 | 14% | 211 | 85 ± 51 | 35% |
| 28 | 372 | 65 ± 12 | 10% | 211 | 84 ± 47 | 36% |
| 232 | 168 | 38 ± 8 | 6% | 211 | 44 ± 14 | 25% |
| ²⁴³Am, single nuclide experiments | | | | | | |
| 1 | 399 | 36 ± 12 | 4% | 211 | 23 ± 3 | 11% |
| 3 | 397 | 39 ± 11 | 4% | 211 | 19 ± 5 | 13% |
| 7 | 393 | 32 ± 5 | 7% | 211 | 21 ± 4 | 15% |
| 14 | 386 | 101 ± 27 | 5% | 211 | 25 ± 9 | 16% |
| 28 | 372 | 113 ± 12 | 4% | 211 | 32 ± 14 | 12% |
| 232 | 168 | 34 ± 5 | 1% | 211 | 17 ± 2 | 8% |

7.2 *Bentonite Erosion experiments*

The implementation of a natural compacted bentonite sample into a natural water conducting feature was the reasonable continuation of the CFM project. In-situ investigation of bentonite saturation, swelling and erosion as well as interaction with and migration of radionuclides is a major aim of the experiment. The erosion process in simplified systems was widely investigated but interactions in a more realistic scenario, using natural bentonite and natural low mineralized groundwater are not satisfactorily investigated. This is why the LIT field experiment was supported by two additional mock-up experiments to gain better understanding of the erosion process in this complex system.

7.2.1 *Bentonite erosion in artificial fracture set-up*

The objective of this bentonite erosion experiment was the investigation of the bentonite erosion process. Side reactions, like e.g. dissolution or anionic exchange reactions have been observed and may not be neglected as they influence the erosion process.

7.2.1.1 *Monitoring of bentonite swelling distance and pressure*

Swelling of the bentonite ring took place during the first weeks of the experiment and the intrusion distance into the artificial fracture was monitored visually for ~200 d, while the experiment was running under ambient conditions. Pictures have been taken regularly every 20 minutes for the first three weeks and every 3 hours afterwards (Figure 51). Swelling started immediately upon contact of the bentonite sample with GW in conjunction with the built-up of a swelling pressure. The biggest difference in swelling distance was observed during the first days of the experiments. After 2 d the sample expanded already 6.1 mm into the fracture (Figure 52a). From this point on the swelling distance linearly increases over time with a rate of 0.7 mm per day and reaches a steady state at a distance of 18 mm after ~21 d.

Within the first 10 h after the start of the experiment the swelling pressure increased up to ~2500 kPa. During the following days pressure decreased to a constant value between 1700 to 1800 kPa

(Figure 52a) implying steady state conditions after 5 days. The pressure drop coincided with the bentonite swelling into the fracture. A maximum swelling pressure of 5000 to 6000 kPa is expected according to Agus et al. [114] for a bentonite sample with the dry density of 1.65 g/cm^3 without swelling. Experimental data is due to the expansion within the sample pocket and into the aperture below the literature values.

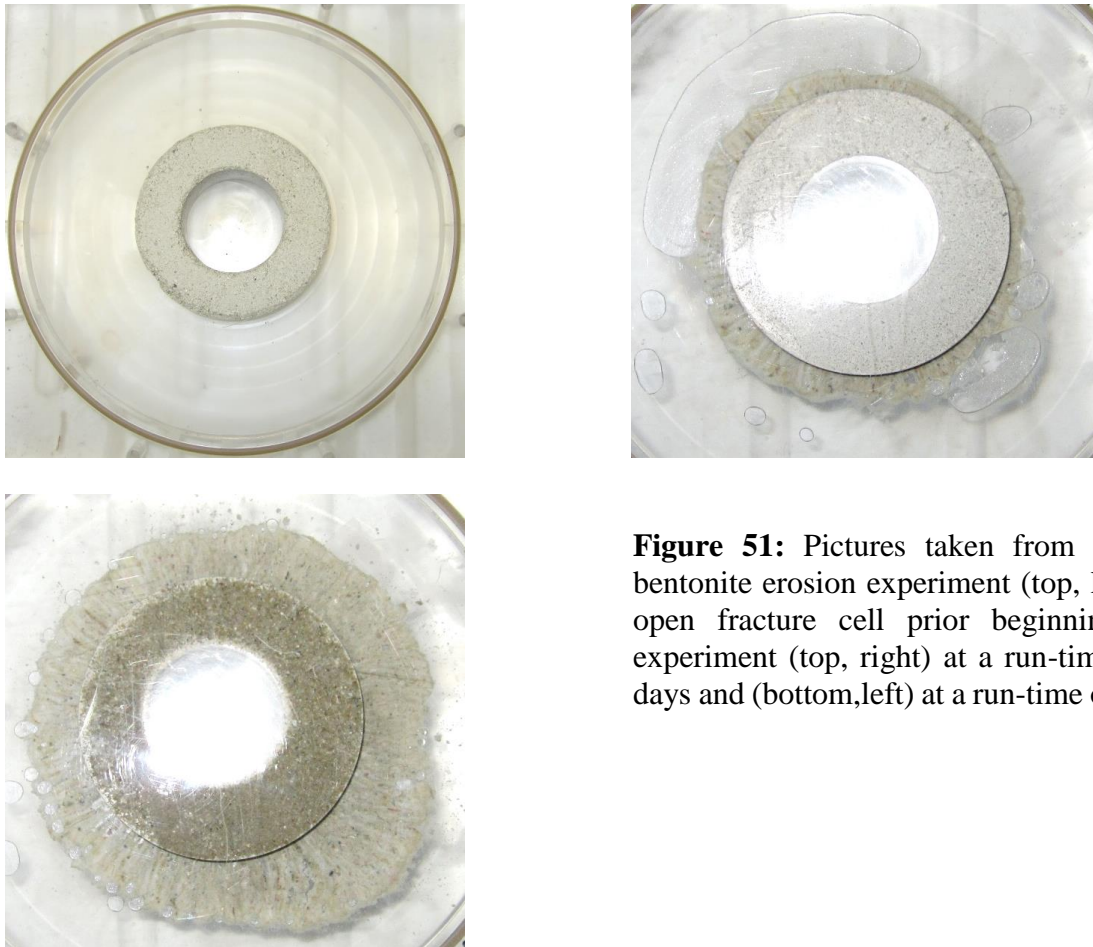


Figure 51: Pictures taken from the Febex bentonite erosion experiment (top, left) of the open fracture cell prior beginning of the experiment (top, right) at a run-time of three days and (bottom, left) at a run-time of 20 days.

As an unsaturated Febex bentonite sample was used in the experiment, a water saturation process took place in the initial phase of the experiment in parallel to the crystalline swelling. This process can be observed by the color change of the bentonite source in Figure 51. The unsaturated sample shows a lighter grey tone in comparison to the saturated sample. GGW was sucked into the Febex cavities and replaced entrapped air. As a consequence, air bubbles occurred regularly at the rim of the swelling zone during the first days of the experiment (Figure 51, top right) which were removed by slightly tilting of the set-up and moderately increasing the flow rate in parallel. This was

necessary as the air bubbles otherwise would have stayed in the system effectively preventing the bentonite swelling process. The bentonite ring was fully saturated after three weeks and the swelling distance reached a steady state. Pressure drops on the third, the fourth and the sixth day can be explained by the removal of air bubbles (Marked in Figure 52b). This procedure had only a minor effect on the system as the swelling pressure recovered within 3 hours after each manual disturbance. Pressure monitoring was stopped in May, 2014 as the setup was moved to the glove box.

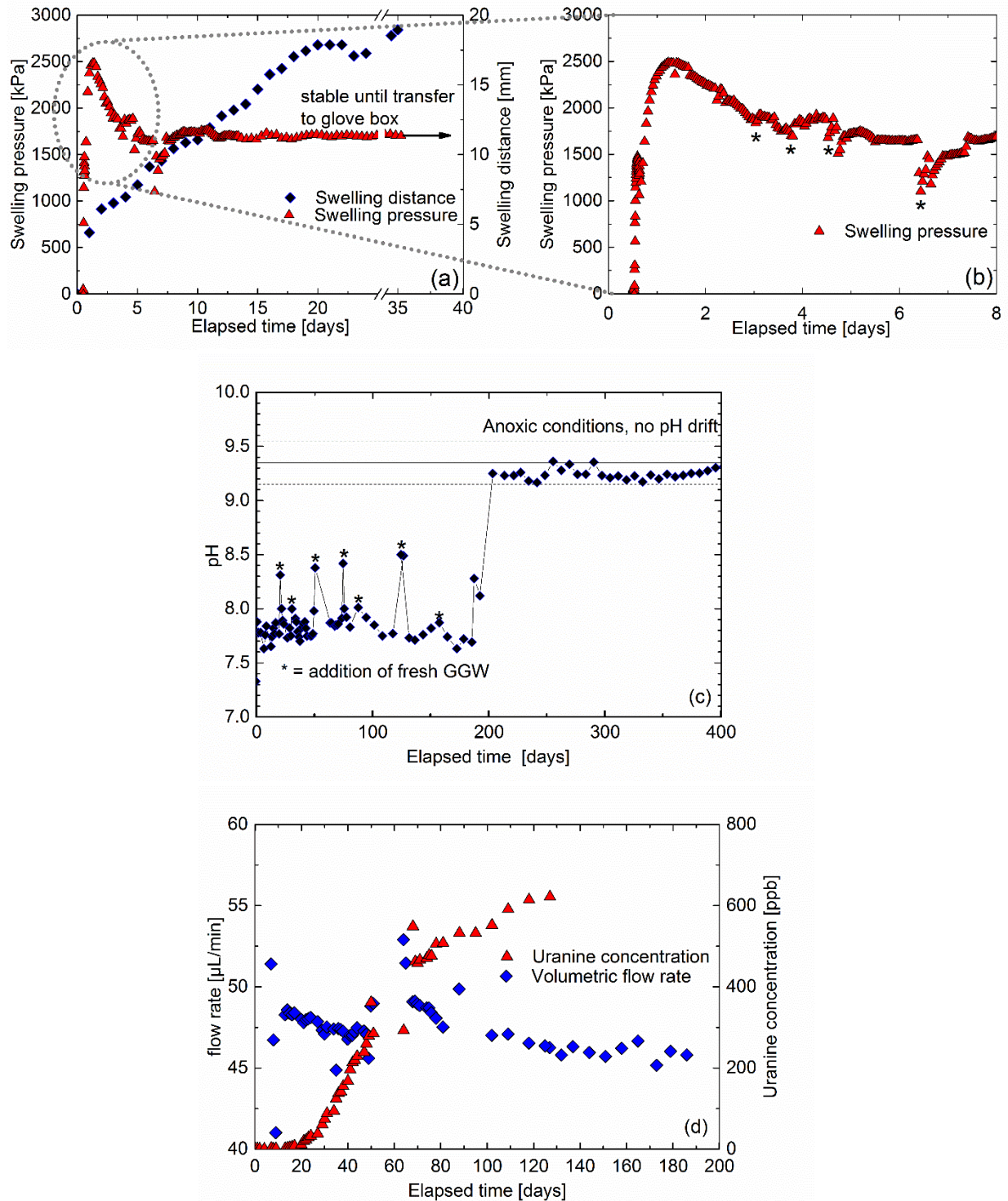


Figure 52: (a) Swelling distance and pressure during the first month of the erosion experiment, (b) a closer look on initial pressure changes due to the removal of air bubbles, (c) pH evolution and (c) flow rate through the artificial 1 mm fracture and fluorescence signal of the conservative tracer uranine.

7.2.1.2 *Hydro-geochemical monitoring – pH, flow rate and conservative tracer*

pH evolution in the erosion experiment is shown in Figure 52b. GGW is continuously pumped through the artificial fracture from a 1 L GGW reservoir which is refilled if necessary. As the experiment is set up under ambient conditions for the first months, air CO₂ interacted with the reservoir water resulting in a fast pH drift towards values around 7.8 due to carbonization. The repeatedly addition of fresh GGW led to an immediate increase in pH. This pH drift disappeared once the experiment was transferred to an argon glove box in order to run the experiment under realistic conditions (anoxic and CO₂- free). Measured pH-values stayed close to the GGW value during the further run-time of the experiment. Flow rates were monitored during each sampling as the eluted mass over time gives the average volumetric flow rate. It was initially adjusted to 49 μL/min but decreased to 46 ± 0.5 μL/min within the first months (Figure 52c). After the transfer to the glove box and exchange of tubing, the same trend was observed from initially 49 μL/min down to 45 ± 0.5 μL/min within four weeks. Modelling the flow velocity at the water-bentonite interface from the given volume flux with COMSOL Multiphysics yields a maximum velocity of 1.2·10⁻⁵ m/s (A-Figure 5) and a maximum shear stress of 3.3·10⁻⁵ Pa (A-Figure 6). The flow velocity distribution within the 1 mm fracture set-up at the equilibrium swelling distance is shown in A-Figure 3. These are input parameters for modelling the erosion mechanism. The conservative tracer uranine was detected after 13 days and was continuously rising to a values around 600 ppb after 120 days experimental run-time (Figure 52c) indicating that at least one of the tracer containing glass vials broke under the swelling pressure and released the tracer to the GGW. The constant increase of the uranine concentration indicates that the tracer containing glass vials broke within a short period but it cannot be excluded that some of the glass vials stayed intact. This will be clarified in terms of the concluding post-mortem analysis. After the transfer to the argon glove-box, determination of uranine concentrations was stopped as the light-sensitive tracer within the set-up could not be protected from surrounding light.

7.2.1.3 *Bentonite erosion processes*

Based on the results obtained the experiment can be divided into four consecutive (in part with overlap) phases namely (i) an initial washing phase in which loosely bound particles are removed, (ii) crystalline swelling into the fracture (iii) a dissolution phase in which Febex bentonite accessory minerals start to dissolve and finally (iv) an osmotic swelling phase with increased bentonite colloid

release. Additionally, a cation exchange process occurs during the total duration of the experiment. Here, magnesium and sodium in the smectite interlayer are exchanged constantly with calcium.

Phase I (Washing phase):

As the raw and un-purified bentonite ring material gets in contact with the GGW, loosely bound particles of the bentonite ring were washed out. The colloidal size distribution and concentration monitored by optical LIBD and s-curve LIBD during the first weeks of the experiment is depicted in Figure 55. During the first days a high colloid concentration was detected by LIBD (initially ~10 mg/l) which is explained by the release of loosely aggregates and accessory minerals during the saturation of the artificial fracture. The washing phase is followed by a decrease of colloid concentration to values around 0.02 to 0.3 mg/l within 10 d which coincided with increased divalent cation release (Ca^{2+} and Mg^{2+} , Figure 54).

Phase II (Crystalline swelling phase):

Crystalline swelling is observed as soon as the bentonite sample is in contact with water and it takes 21 days to reach steady state (Figure 52). Thereby, the sample expands 18 mm into the 1mm artificial fracture. The heterogeneity of the expanded material (Figure 51) indicates that there is no phase separation during the swelling but the material is unselectively pushed out of the sample pocket in consequence to the swelling pressure evolution. Erosion of bentonite colloids is hindered in this period due to the chemical composition of the water which is described in detail in the following section.

Phase III (Dissolution phase):

The third phase of the bentonite erosion experiment is dominated by the dissolution of accessory minerals like halite and gypsum which are accessory components of natural Febex [52] bentonite. Simultaneously a cation exchange process takes place in which Ca is intercalated and Na and Mg are released from the Febex interlayer and the bentonite porewater mixes with the contact water. The cation interlayer binding selectivity coefficients ($K_{\text{Gaines-Thomas}}$) for the Febex bentonite are in the order: $\text{Mg} > \text{Ca} > \text{Na}$ [115]. According to the selectivity coefficients, Mg is not expected to be replaced by Ca but due to the fact that the molar background concentration of calcium is 250-fold higher concentrated than the one for magnesium in GGW (Table 2) the interlayer composition is pushed towards a homoionic calcium saturated bentonite. The Febex porewater was described by

Fernandez et al. [102] and is under the investigated compaction density of the bentonite a Na-Ca-Mg-Cl-SO₄ type water with nearly neutral pH (7.44) and high ionic strength (0.66) in comparison to GGW. Dissolution of accessory minerals can be followed by the evolution of sodium, calcium, chloride and sulfate concentrations, respectively (Figure 53). This process dominates the experiment during the first 3 months of the total run-time and reaches maximum values between 7 days (Na and Cl evolution, Figure 53) for readily soluble phases like halite and 35 days in the case of slightly soluble minerals like gypsum (SO₄, Figure 53). These concentrations decrease and reach steady states after 200 days.

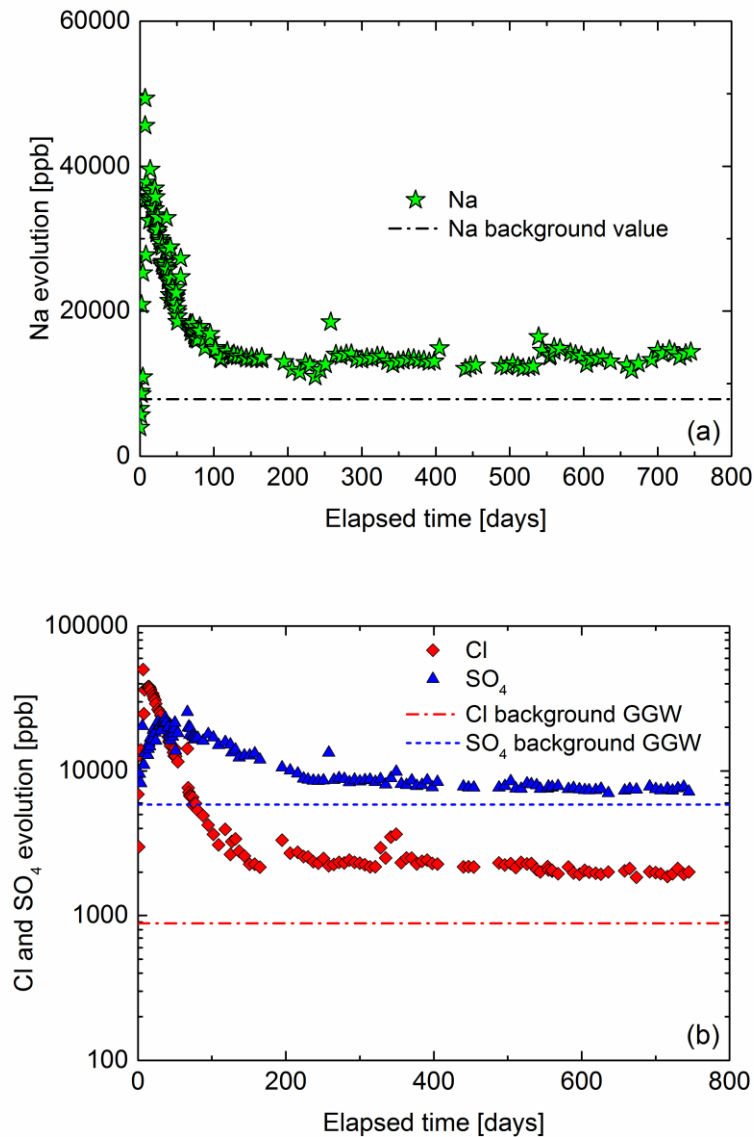


Figure 53: Evolution of Na (a), Cl⁻ and SO₄²⁻ (b) during the experiment.

It is remarkable that in the case of Na, Cl and SO₄ steady state values are still above the respective background levels. Assuming that all sulfate originates from gypsum a total amount of 2.3 mmol is dissolved within 750 days. This sums up to a total gypsum content of 0.19% in good agreement to literature data ($0.14 \pm 0.1\%$ [101]). Over this period 16 mmol sodium but only 5.4 mmol chloride have been collected in the effluents.

An additional sodium source can be found in the bentonite itself as 24% of the interlayer is Na-occupied and the bentonite porewater shows a Na concentration of 0.33 M [102]. In the course of the experiment sodium is exchanged against divalent cations and released from the interlayer. Under the assumption that the total amount originates from the Febex interlayer, 40% of the interlayer inventory is exchanged at most but mixing with the porewater during the early stage of the experiment cannot be neglected and reduces the exchanged amount. Limited calcium concentrations (Figure 54) that drop after a previous increase due to mixing with the porewater (0.068 M Ca in the Febex porewater [102]) as well as dissolution processes of accessory minerals even under the GGW background level and reach steady state at this reduced concentration are an additional indication for the cation exchange process and demonstrate that it is still ongoing.

Besides Na and Ca, Mg with a ratio of 30% is based on the CEC part of the Febex interlayer composition. Mg is also with a concentration of 0.081 M part of the Febex porewater. Mg concentrations are displayed in Figure 54 only for the first 200 days of the experiment. These values can be correlated to dissolved Mg from the cation exchange processes and the mixing with the porewater. Colloid release is suppressed as dissolution results in higher ionic strength decreasing colloid stability. A maximum ionic strength of 2.9 mM is reached during the dissolution phase. Regarding the calcium concentration only, the highest concentration of 0.32 mM alone is already sufficient to inhibit colloid release [116]. Colloids as additional Mg-source turn out to gain importance in the continuation of the experiment and are discussed in detail later. The evolution of magnesium and calcium concentrations both show a maximum after 25 days of the experiment and decrease to reach steady state after 150 days. Released magnesium sums up to a total amount of 0.2 mmol over the first 200 days which correlates to 0.8% of the interlayer Mg-inventory at most.

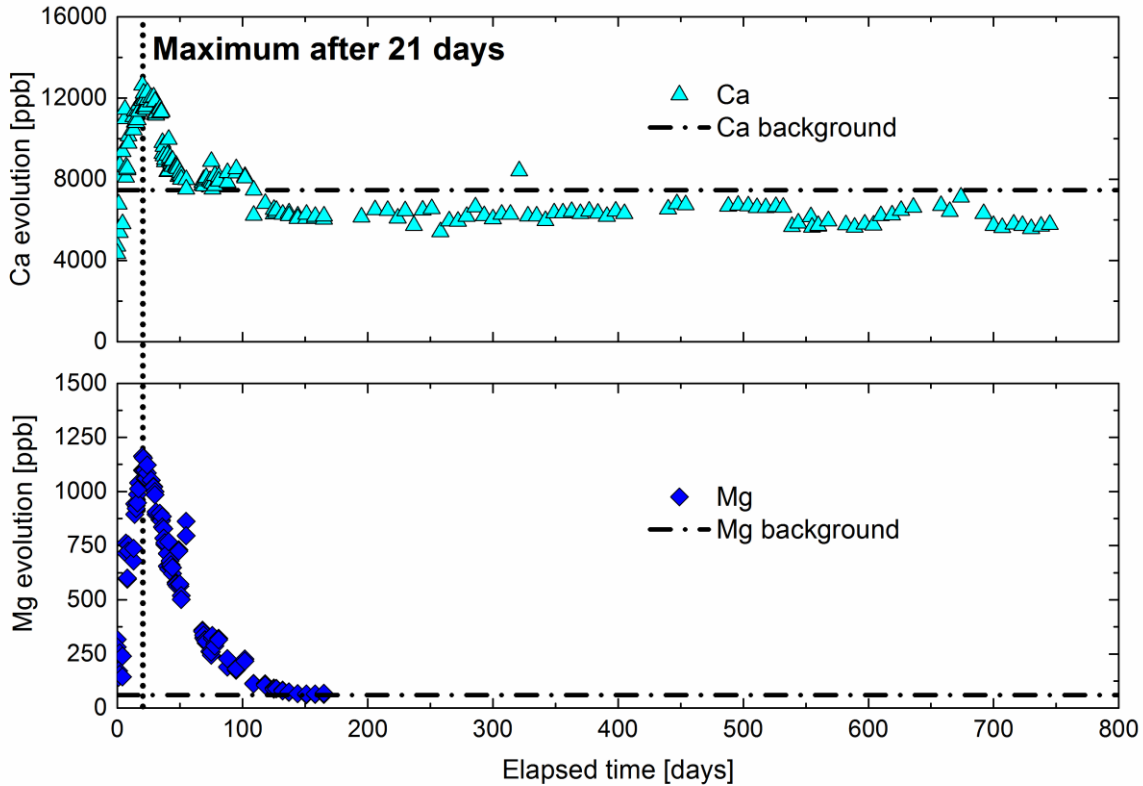


Figure 54: Calcium (top) and magnesium (bottom) evolution during the experiment.

Phase IV (Osmotic swelling and erosion phase):

Colloid concentrations obtained by optical LIBD increase after 150 days which goes along with a decrease in concentrations of the aforementioned elements. The ionic strength at 150 days run-time is calculated to 1.2 mM. Depletion of the accessory minerals leads to a decrease in ionic strength and consequently in osmotic swelling at the rim of the extruded bentonite sample as well as higher colloid stability. As a result, mean colloid concentrations of 1.05 mg/L with a minimum-maximum values between 0.06 - 6.1 mg/L (optical LIBD, Figure 55a) are detected during the further run-time. Size distributions obtained by s-curve LIBD show a bimodal distribution of 20 - 25 nm particles with a larger size fraction in the range of 150 - 300 nm in the early stage of the experiment ($t < 150$ d). A software update of the system necessitated new calibration of the system and is responsible for the gap in the s-curve LIBD data. Thereby the upper end of the calibration was expanded from 400 nm to 900 nm, whereas the smallest measurable particle size remained at 20 nm. The newly calibrated system detected smaller particles mainly in the range of 20 - 85 nm and no significant contribution by a bigger fraction. Test measurements with monomodal sized

polystyrene nanospheres showed that s-curve and optical LIBD deliver very comparable size and concentration data. Such measurements are performed on a regular basis.

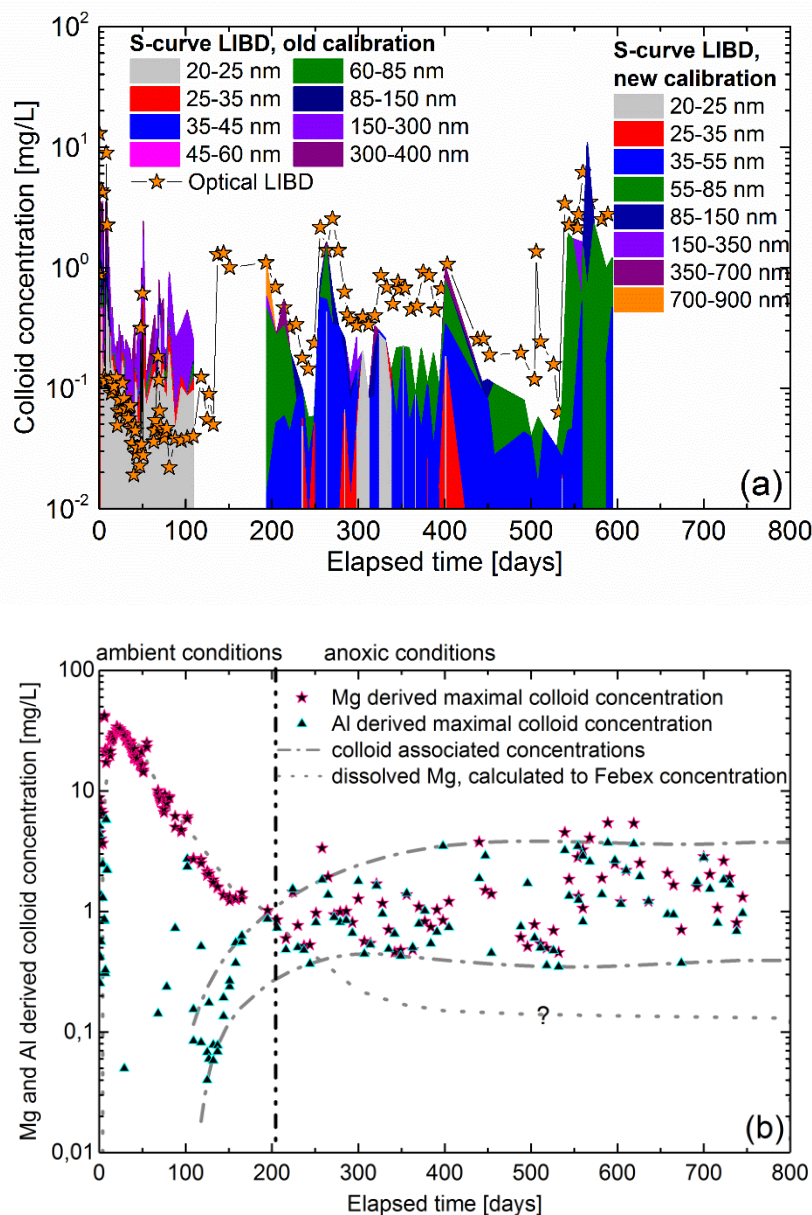


Figure 55: (a) Colloid concentration measured by LIBD and s-curve LIBD. The s-curve measurement gives a total concentration and a size distribution. The size fraction is given in the respective stacked diagram. The gap in the s-curve data is due to a software update during the experiment. (b) Colloid concentration calculated from the Mg and Al signal measured by ICP-MS.

In addition to LIBD analysis, colloid concentrations are calculated from the elemental composition of the effluents. According to the structural formula for the Febex bentonite $(\text{Na}_{0,31}\text{K}_{0,06})(\text{Si}_{3,91}\text{Al}_{0,09})(\text{Al}_{1,32}\text{Fe}_{0,24}\text{Mg}_{0,52})\text{O}_{10}(\text{OH})_2$, Al, Mg and Si concentrations can be used as they are main components of the Febex bentonite. Si values are not reliable due to the use of hydrofluoric acid which is used for colloid dissolution during the sample preparation. HF will leach additional Si from the glass elements of the ICP-MS device and the values are therefore discarded for colloid quantification. Low Al and Mg background in the GGW makes the calculation more reliable. Mg concentrations are at least slightly increased over the total experimental time by the exchange reaction described within the dissolution phase. The measured concentrations are therefore calculated to Febex colloid concentration with respect to the Febex structural formula. Only if Al and Mg derived colloid concentrations match, both elements can be expected as colloid associated. Under the assumption that the total amount of Mg and Al is originating from colloids, total colloid concentrations can be found in Table 17. As previously discussed Mg is also increased from the mixing of GGW with the bentonite porewater and the exchange reaction from the bentonite interlayer. These processes dominate the Mg concentration for the first 150 days of the experiment (Figure 55b). During this period very low Al derived colloid concentrations are detectable. Therefore, one can assume that a colloid phase originating from the Febex sample is not present at this point because of the higher ionic strength from porewater mixing, dissolution of accessory minerals and cation exchange reaction which decreases bentonite colloids stability. Al derived colloid concentrations start to increase after 100 days experimental duration and converge to Mg derived values after 200 days (Figure 55). After that, colloid release (erosion) becomes the Al and Mg concentration dominating process. Measured colloid concentrations scatter between 0.4 and 4.6 mg/L with a mean value of 1.4 mg/L but the trend is comparable to the LIBD measurement.

Table 17: Colloid mean concentration measured by three different methods over the bentonite erosion phase ($t > 200$ d). Mean values, lowest and highest limits are given.

| Method | Mean colloid concentration | Lowest colloid concentration | Highest colloid concentration |
|-----------------------|----------------------------|------------------------------|-------------------------------|
| Optical LIBD | 1.1 mg/L | 0.06 mg/L | 6.1 mg/L |
| s-curve LIBD | 0.7 mg/L | 0.03 mg/L | 10.9 mg/L |
| ICP-MS (Mg/Al-signal) | 1.4 mg/L | 0.4 mg/L | 4.6 mg/L |

Mg/Al derived colloid ratios of 1.25 and decreased Ca concentrations in comparison to the GGW background value over all samples in this period indicate the release of dissolved Mg in minor concentrations (20% of total Mg) by continuous cation exchange processes.

An average bentonite erosion rate is calculated over phase IV of the experiment and normalized to the contact area between bentonite source and GGW. Taking into account the sample diameter of 80 mm and the bentonite's swelling distance into the fracture of 18 mm, the contact area is built up by the circumference of 116 mm and the fracture height of 1 mm. The contact area calculates to $3.6 \cdot 10^{-4} \text{ m}^2$. The mean colloid concentration of 1.4 mg/L in combination with the mean flow rate of 45 $\mu\text{L}/\text{min}$ sums up to a total eroded mass of 33 mg in one year. The erosion rate can be calculated to $91 \pm 30 \text{ g}/(\text{m}^2 \cdot \text{a})$ in this simplified approach. It is likely that this calculation overestimates the erosion rate because it is assumed that the bentonite swelling into the fracture is homogeneous in all directions which is not the case (Figure 51). Due to the heterogeneous swelling distance, the contact area is larger and the contact area normalized erosion rate is most likely below the calculated value.

In comparison to literature data, the erosion rate of only $91 \pm 30 \text{ g}/(\text{m}^2 \cdot \text{a})$ seems low. Higher erosion rates have been reported by different institutions in the framework of the BELBaR project and are summarized in the final report [117]. Lowest erosion rate has been found by a group from ÚJV Řež but it is with a value of $400 \text{ g}/(\text{m}^2 \cdot \text{a})$ multiple times above the erosion rate reported in this work. Additional research groups, i.e. B+Tech OY and Clay Technology reported much higher erosion rates with lowest values between 12 to $82 \text{ kg}/(\text{m}^2 \cdot \text{a})$. It is remarkable that most of these experiments have been performed with a purified, homoionic exchanged bentonite sample or a mixture of different purified bentonites in addition with a synthetic contact water. Comparability with the investigated system is therefore limited. The complex combination of natural, unpurified bentonite and natural groundwater from GTS is mostly unsought.

7.2.2 LIT

LIT is an upscaling in-situ experiment under repository relevant near-natural conditions and simulates the intrusion of glacial melting water in a HLRW repository. The behavior of the bentonite buffer and the resulting erosion process as well as the interaction of the buffer and the eroded material with radionuclides are in focus of this experiment and investigated online at GTS and later in the INE laboratory.

7.2.2.1 LIT - online monitoring

Physical and geochemical key parameters are monitored on-line during the run-time of LIT. Data measured in the geochemistry cabinet shows periodic disturbances caused by an automatic valve in the line to the cabinet, which is used to change between online monitoring and sampling (Figure 33). There is no water flux in inline sensors of the cabinet during sampling. Therefore, spikes establish in the pH and redox potential monitoring during each sampling period and the data was smoothed to reveal the actual situation.

7.2.2.1.1 Swelling pressure evolution

Four pressure sensors are implemented in the source packer system to measure the swelling pressure evolution of the expanding bentonite source when contacted with the groundwater. Swelling pressure evolution is shown in Figure 56. Two sensors are installed on the lower interface between the packer and the bentonite source (TP_3 and TP_4) and two on the upper interface (TP_1 and TP_2). Pressure rises immediately after the installation of the packer system and reaches steady state on all pressure sensors within 20 days. Values of 900 ± 100 kPa are obtained on both sensors at the lower end of the sample and are stable over the total experimental time. Both pressure sensors measure very comparable values indicating homogeneous swelling in this region. Higher swelling pressure in the order of 1.4 (TP_2) to 1.9 MPa (TP_1) is obtained on the upper side of the packer. Both installed pressure sensors give different values indicating inhomogeneous swelling or some kind of sealing, preventing compensation of the swelling pressure between the sensors. The values remain constant until a pressure release occurred at TP_1 after 520 days. Thereby part of the pressure is released and a new equilibrium is established within 25 days at 1.5 MPa. Total pressure on TP_2 remains constant during the drop on TP_1. Concerning the dry density of the bentonite

source, which is 1.65 g/cm^3 , one would expect much higher swelling pressure in the order of 5.0 to 6.5 MPa [114]. Swelling pressure in LIT is significantly lower in comparison to the laboratory experiments as the bentonite source has some space to expand before it reaches the wall of the borehole and additional space as it may intrude into the fractured system. A metal sleeve had to be installed around the bentonite sample during installation for radiation security reasons and was pulled backwards when the sample was in place. The removal of the sleeve led to a gap between the sample and the tunnel wall of approximately 2-3 mm. The bentonite sample will expand to the tunnel wall when contacted with GW taking an additional volume of 16 to 21% in comparison to the sample volume. Thereby, the effective dry density is decreasing to only 1.37 to 1.45 g/cm^3 . Swelling pressure of 900 to 1100 kPa which is lying in between the experimental values is expected for this density region, according to Agus et al. [114]. The additional volume in the borehole was not compensated by using a bentonite sample with a higher degree of compaction to match repository conditions. This may limit the comparability of bentonite erosion and colloid generation within LIT to a HLRW repository. The addition of the synthetic Zn-montmorillonite in this experiment may also have an effect but cannot be evaluated as there is no data to compare the swelling properties of the synthetic montmorillonite and the Febex bentonite.

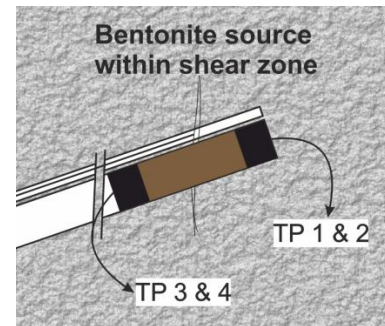
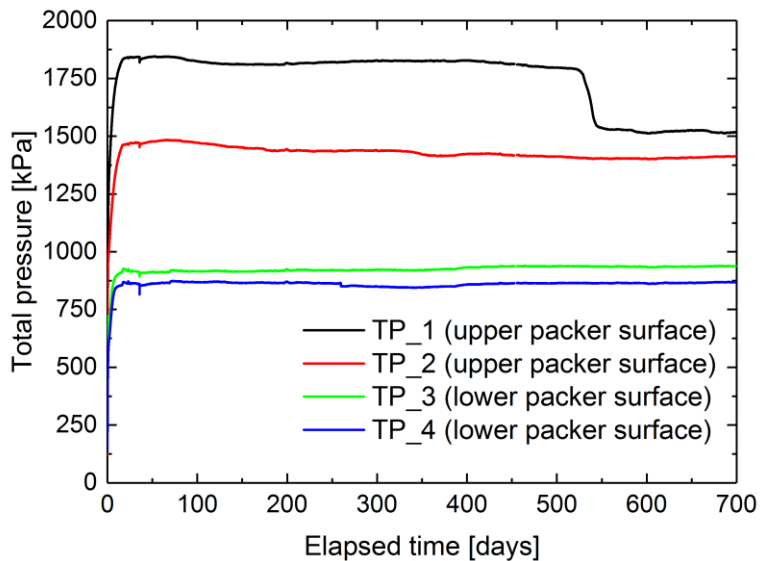


Figure 56: Swelling pressure evolution within the LIT bentonite source.

7.2.2.1.2 *Hydro-geochemical monitoring – pH, E_{SHE} , conductivity and conservative tracer evolution*

pH is measured in the near-field of the bentonite source (CFM11.02) as well as at the Pinkel outflow within the surface packer system. Both is shown in Figure 57. Especially the data obtained from the near-field shows periodic disturbances that have been explained in 7.2.2.1. A series of subsequent envelope functions was used for smoothing and only the smoothed data which exclude the disturbances to higher as well as to lower values will be discussed here. In a first step an upper envelope was calculated to fade out disturbances that gave data points below the true values. In a second step another envelope was applied to the first envelope to fade out the remaining disturbances, which gave values above the true values.

After implementation of the bentonite source, pH drops in the near-field from 9.6 to 9.1 ± 0.1 within 50 days and stays stable for 370 days. This is followed by a continuous increase to a maximum value of 10.1 ± 0.1 after 680 days. The steady increase in the second year of the experiment doesn't give true values but can be seen as alteration process of the pH electrode. The electrode was replaced after 690 days and pH is once again stable at 9.0 ± 0.1 . The pH drop around 690 days refers to the replacement of the electrode. The sink around 95 days can be explained by a longer period without flow through the geochemistry cabinet as it was bypassed for several days to facilitate continuous sampling during the first LIBD on-site campaign. The same effect is observed for E_{SHE} , electrical conductivity and fluorescence monitoring. In addition to the near-field pH values observed from CFM11.002 water samples are also collected at the Pinkel extraction point which is located at the tunnel wall. Samples from this spot show higher pH values around 9.4 ± 0.2 for the first year of LIT. A pH drop occurs at a run-time of 200 days and is caused by a power breakdown in the facility. New calibration of the pH probe after 310 days explains slightly lower values for the following data. The pH probe was replaced after 580 days as the former installed probe suffered from alteration. This is shown by the drift of 1.5 pH units in 100 days and the noisy signal prior replacement.

The redox potential is shown in Figure 57 and was also measured on both sampling spots giving very stable but also very different results. Reducing values are measured on the Pinkel extraction point with the exception of one drastic increase 300 days after the start of LIT which is caused by recalibration of the Eh probe. All values are however, in the range of -240 ± 60 mV and close to literature data (Möri et al., 2003). Considerably higher redox potentials have been measured in the

near-field of the bentonite source, which can be explained by interaction with the bentonite sample, for instance dissolution of accessory phases or mixing with the bentonite porewater. After an initial drop from 220 mV down to 160 mV followed by the bypassed period without flow in the geochemistry cabinet, a first plateau is obtained for a short period of 50 days at a redox potential of -50 mV. Afterwards $E_{h_{SHE}}$ increases to a second plateau which lasts for 450 days at a redox potential of 130 mV. Differences between the extraction points are caused by the interaction of the bentonite source with the surrounding groundwater. Due to the distance from the source to the Pinkel extraction point and the expected dilution on that way, the effect is only visible for the near-field monitoring.

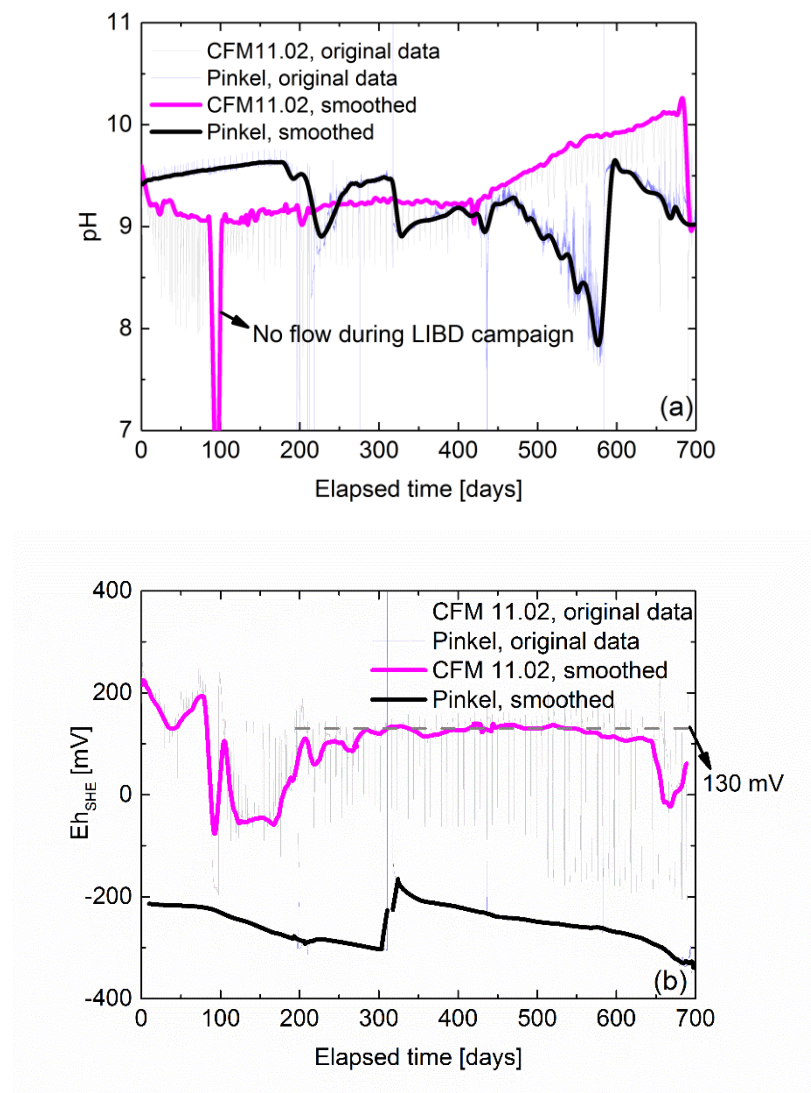


Figure 57: (a) pH and (b) redox potential evolution ($E_{h_{SHE}}$, corrected to standard hydrogen electrode) in the near-field of the bentonite source and on the tunnel wall respectively.

Electrical conductivity at the Pinkel extraction point is quite stable at $60 \pm 10 \mu\text{S}/\text{cm}$ for the first 300 days, showing only one re-calibration induced step 300 days after the start of LIT and slightly decreased values around $50 \pm 10 \mu\text{S}/\text{cm}$ for the remaining run-time (Figure 58). Values before and after this event are very stable. In contrast, the near field data shows a breakthrough curve that reaches a maximum of $170 \mu\text{S}/\text{cm}$ after 30 days and slowly levels off during the remaining run-time. Equilibrium is not reached within 700 days and values are still above the GW background. Increased values can be explained by the dissolution of accessory phases within the bentonite sample. Readily soluble phases like halite are responsible for the early maximum and the dissolution of hardly soluble phases like gypsum and the bentonite itself are responsible for the long tailing. The early maximum and the constant decrease of the values indicate stable contact between the bentonite source and the surrounding groundwater without serious disturbances by e.g. the release of air from the cavities within the bentonite source which may result in air bubbles around the sample and partly separation of the swelling bentonite from the groundwater or the spontaneous release of those air bubbles. Additional prove for good contact between the bentonite source and the groundwater can be found in the fluorescence signal of the conservative tracer, Amino G (Figure 58). Concentrations start rising around 20 days after emplacement and reach a maximum after 600 days. The detected tracer sums up to a released fraction of 1.3% of the total tracer mass within 700 days. The sharp peak around 200 days run-time is again caused by the power failure at GTS.

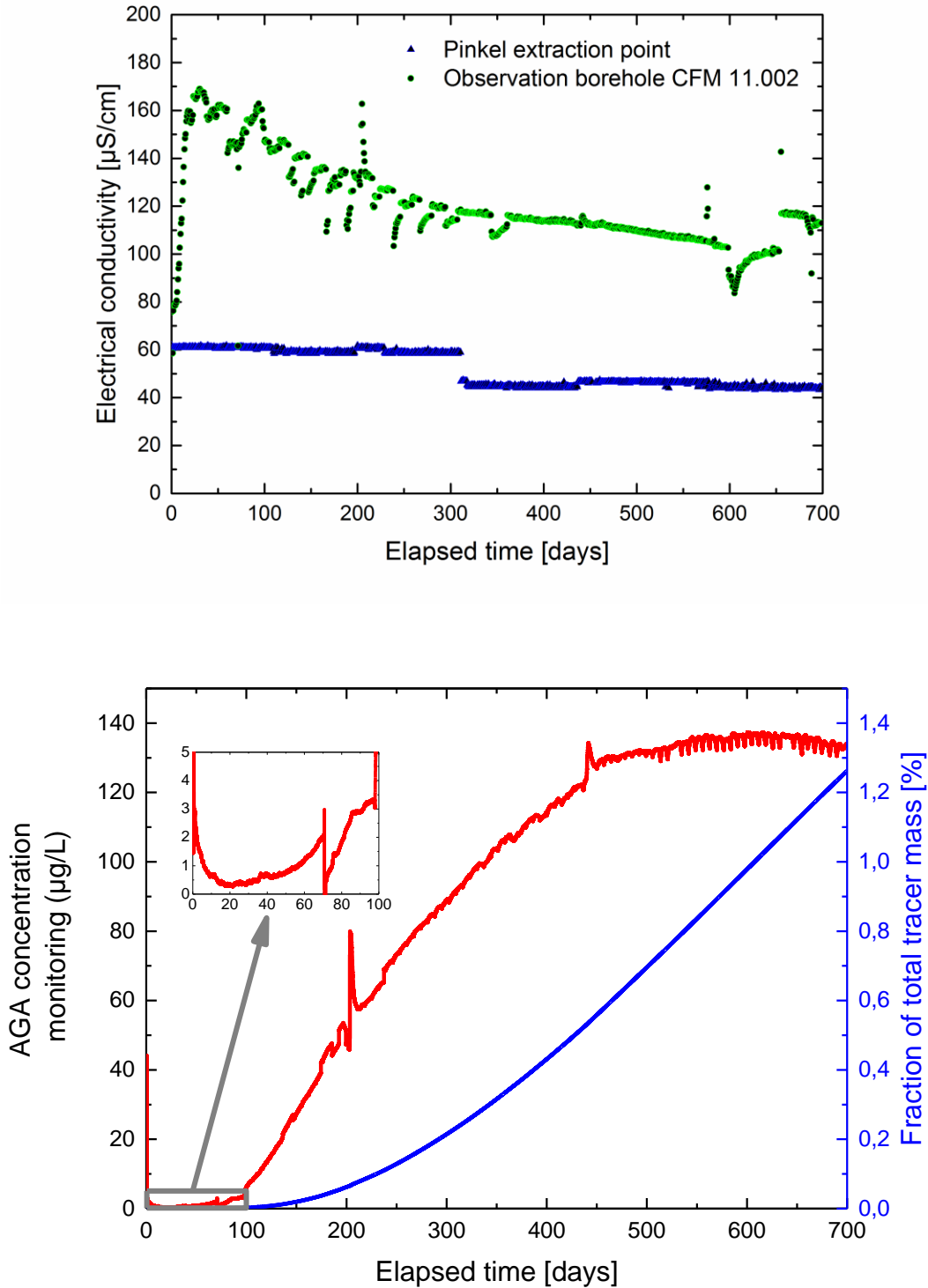


Figure 58: (top) electrical conductivity in the near-field of the bentonite source as well as on the tunnel wall and (bottom) conservative tracer evolution in the near-field of the bentonite sample.

7.2.2.2 LIT - sample analysis

Samples have been taken regularly from the near-field observation borehole CFM11.02 as well as from the Pinkel extraction point. An overview of the transferred samples with the respective sampling point and the sampling date can be found in the Annex (A-Figure 7). The effluent from CFM11.02 was collected under anoxic conditions in 15 mL septum sample vials until October, 2015 and in 40 mL septum vials afterwards at a flow rate of 20 $\mu\text{L}/\text{min}$, respectively. All pierced sample caps have been replaced against fresh ones prior to the transfer out of the argon glovebox and the transport from GTS to the INE laboratory to ensure anoxic conditions during transport. No samples from CFM11.02 were collected within the first 100 days due to a software malfunction. Large volume samples (1 L) have been collected with an autosampler (6712FR, Teledyne Isco Inc.) in parallel at the Pinkel extraction point at a flow rate of 20 mL/min under ambient conditions. Samples have been collected regularly.

Sample batches were transferred to the INE laboratories for further analysis twice a year. A sample list with the transfer date can be found in A-Table 7. A total of 98 samples from the near-field and 40 samples from the Pinkel extraction point have been received within the first two years of LIT. Due to the fact that samples from the Pinkel extraction point were highly diluted and didn't show observable interaction with LIT within the online monitoring, analysis focused mainly on the near-field samples.

7.2.2.2.1 Hydro-geochemical monitoring – pH, E_{SHE} and conservative tracer evolution

pH of the CFM11.02 samples is depicted in Figure 59. Stable pH of 9.1 ± 0.1 over all samples is very comparable to online data from GTS and indicates successful isolation of the samples from the atmosphere during the transport. Samples from the Pinkel extraction point have in contrast to the near-field samples been sampled and transported under oxic conditions. This results in a pH drift due to carbonization towards neutral values around 7.6 ± 0.3 . The concentration of the conservative tracer has been determined over the fluorescence signal (Figure 59). Values are again in-line with the online evolution described in Chapter 7.2.2.1. Monitoring of redox potentials in the laboratory was not possible for the 15 mL samples as the volume is not sufficient for a reliable measurement and the risk of leakage of the electrolyte within the electrode should be avoided.

Therefore the redox potential was only measured in case of the 40 mL samples and is with an E_{SHE} -value of 152 ± 32 mV ($n=5$) comparable to the online monitored data.

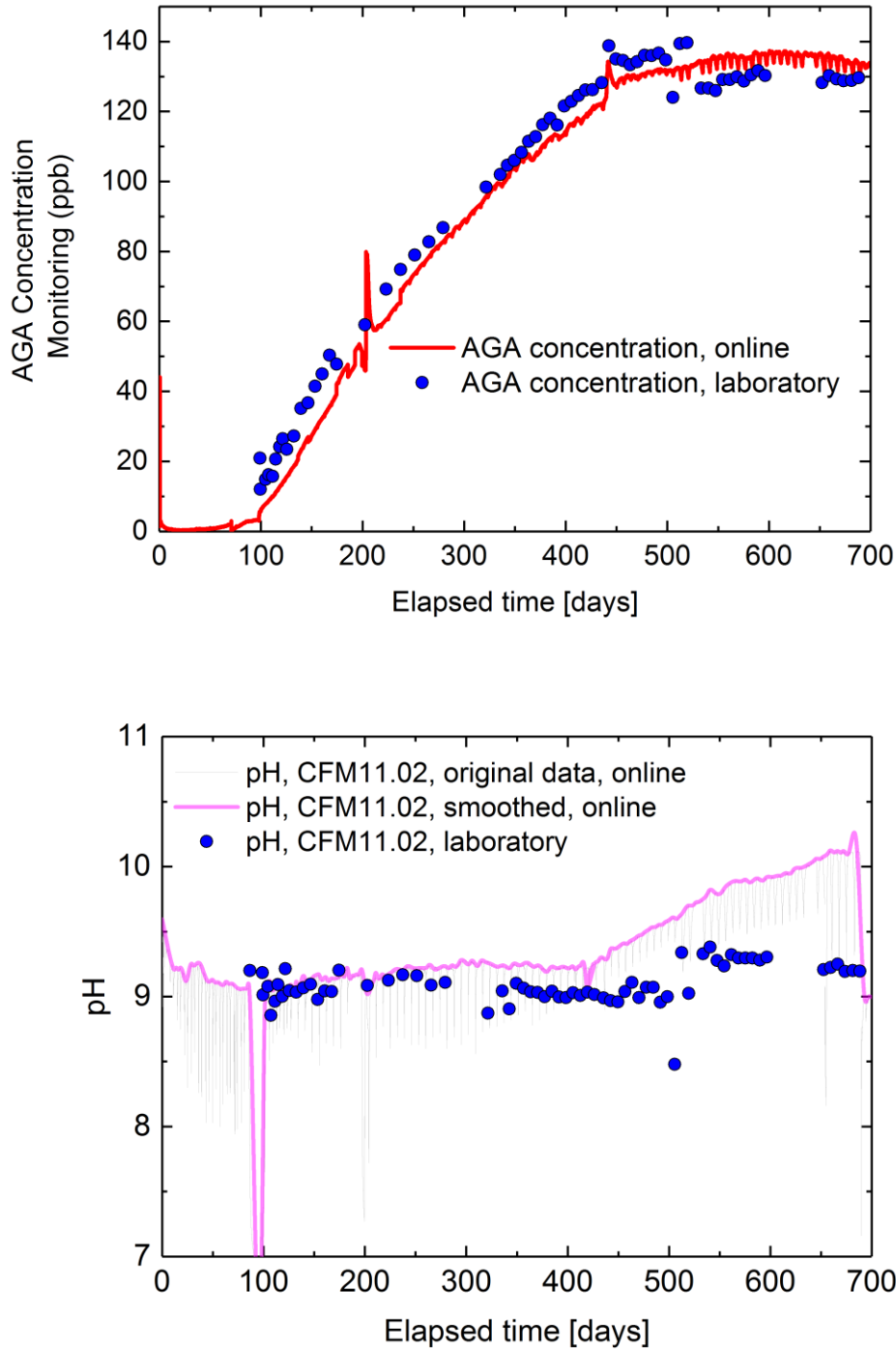


Figure 59: Comparison of online and laboratory data concerning (top) the conservative tracer concentration and (bottom) pH values.

7.2.2.2.2 *Elemental characterization*

Elemental composition of the cationic components was determined by ICP-MS and ion chromatography was applied for determination of the anion concentrations. ICP-MS measurements focused basically on the source forming main elements Zn, Mg, Al, and Ni as well as on elements connected with the dissolution of accessory minerals like Na in the case of halite and Ca in the context of gypsum. An overview on the remaining elements is achieved by the semi-quantitative TotalQuant method. Evolution of selected elements with the respective background value are presented in Figure 60. Increased concentrations in comparison to the GGW background have been measured for the bentonite source forming elements magnesium, aluminum and zinc. One event is remarkable. The concentrations are very stable until some fluctuations occur at a run-time around 510 days. It goes along with the pressure drop, described in 7.2.2.1.1. Slightly higher concentrations for a short period and subsequent lowest values over the total observation time in the case of Al (180 $\mu\text{g/L}$ before and 86 $\mu\text{g/L}$ after the event) and even values below the detection limit in case of Zn indicate an initial release of bentonite particles during the pressure drop and afterwards less connection between the bentonite source and the surrounding water. The effect of this event is in case of the Mg evolution not as clear as it is for Al and Zn and its concentration is in regard to the elemental composition (Table 18) of the source disproportionately high. An explanation can be found in the bentonite porewater and the Febex interlayer composition (Table 6 and Table 10). A continuous cation exchange reaction is a dominating process as it is described in 7.2.1.3. Mg evolution before the pressure drop is linearly decreasing from initially $\sim 500 \mu\text{g/L}$ to 230 $\mu\text{g/L}$ after 500 days, indicating that it is not only related with the Al concentration that remained stable during that time. It is rather a dilution process of the bentonite porewater until it is removed from the system.

Divalent cation concentration is important in the frame of bentonite erosion as increased concentrations limit the stability of the bentonite colloids. Calcium concentrations above the GGW background concentrations are observed for the first year of LIT and decrease steadily until a plateau below the background value is reached after ~ 400 days. The dissolution of gypsum, which can be found with a fraction of 0.14% in natural Febex bentonite, is the main source for additional calcium in the system. Therefore, GGW background (Table 2) corrected molar concentrations for both calcium and sulfate are depicted in Figure 60. It is remarkable that although the dissolution of gypsum releases the same amount of calcium and sulfate the elemental concentrations do not match.

The sulfate concentration is always $\sim 50 \mu\text{M}$ above the calcium concentration and in contrast to calcium never reaches values below the background. The same behavior has been observed in the artificial fracture set-up (Chapter 7.2.1.3) and can be explained by the exchange of calcium against sodium and magnesium within the bentonite interlayer. The unexpected release of Mg from the interlayer has been explained in 7.2.1.3.

Concerning the different experimental phases that have been observed and described within the bentonite erosion laboratory experiment (7.2.1) a clear separation of the postulated phases cannot be made. Phase I (washing) is located in the period without sampling (< 100 days). According to the evolution of the calcium concentration, Phase II (dissolution of accessories) should last until ~ 400 -500 days as Ca concentrations drop below the background value (Figure 60) and phase III (bentonite erosion) should follow up. Al concentrations are actually rising for a short period around 470 days but this is due to the before mentioned disturbance by the pressure drop an unreliable prediction.

Increased zinc and nickel concentrations as tracers for colloid release are detected from an experimental run-time of 100 days on. Samples taken before 100 days show strongly decreased concentrations. These samples have been taken continuously without break for geochemical monitoring during the first LIBD on-site campaign. The firstly decreased concentrations can be explained by a disequilibrium within the system due to a moderate change of the volumetric outflow from $20 \mu\text{L}$ to $50 \mu\text{L}$. Equilibrium recovered within 14 days and concentration plateaus at increased values of $14.5 \mu\text{g/L}$ and $1.7 \mu\text{g/L}$ formed for zinc and nickel, respectively. Concentrations for both elements show some scatter in the course of the experiment and mean concentrations slightly decrease to reach values of roughly $10 \mu\text{g/L}$ (Zn) and $1 \mu\text{g/L}$ (Ni) at a run-time of 500 days. Samples taken after the pressure drop described in 7.2.2.1.1 only contain measureable amounts of zinc and nickel in some exceptional cases. In most samples the concentrations are below the detection limit of ICP-MS ($< 5 \text{ ppt}$) supporting the theory that the incident that caused the pressure drop and limited Al concentrations also limited zinc and nickel concentrations and indicates that these elements are linked over a colloidal fraction.

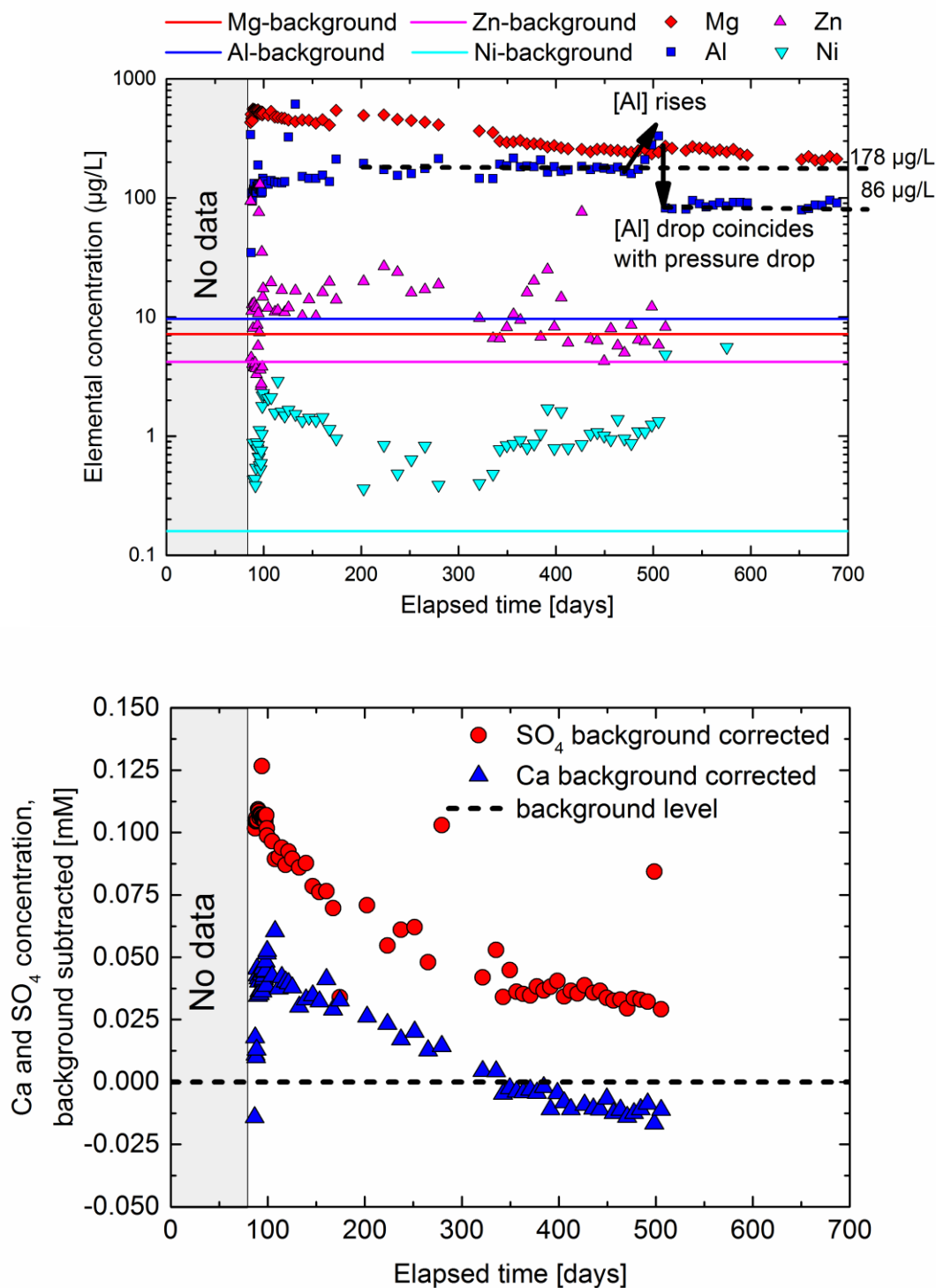


Figure 60: (top) Magnesium, aluminum and zinc evolution in comparison to the respective background value of Pinkel and (bottom) calcium and sulfate **molar** concentrations. The respective background concentrations (0.09 mM Ca and 0.06 mM SO₄ from Pinkel, n=21) are subtracted to compare the molar ratios regarding the dissolution of gypsum. Background values are given in Table 2.

7.2.2.2.3 Colloidal characterization

Colloid concentration and mean particle size are determined by LIBD with optical data acquisition and the results can be found in Figure 61. Linear dependence between particle density and size is based on the method as has been shown in 5.3.2. The increase in particle mean sizes and concentrations coincides with the drop of the Ca concentration below the detection limit (Figure 60, bottom).

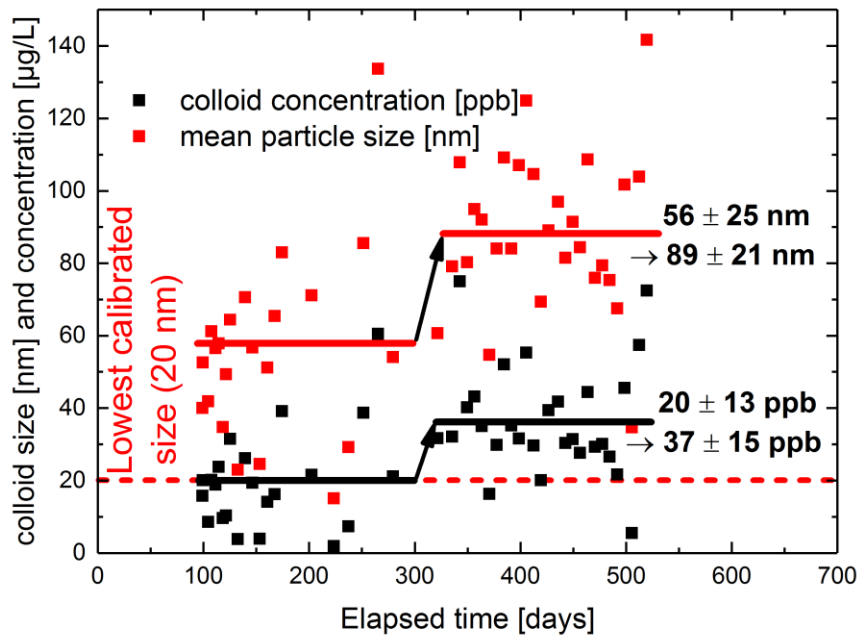


Figure 61: Colloid mean sizes and concentrations derived by LIBD with optical data acquisition.

Based on the structural formula of the Febex bentonite, (6.3.1.1) the elemental mass fractions of the main elements are calculated. The same is done for the admixture with the synthetic Zn-montmorillonite, which is in contact with the shear zone (6.3.2) and the synthetic Ni-montmorillonite in the tracer containing glass vials. These values are used to calculate colloid concentrations based on the ICP-MS data and under the assumption that the total Zn, Al and Ni concentration is colloid bound and originating from the midst bentonite rings or the tracer vials, respectively. Concerning the before mentioned elemental concentrations, maximum colloid concentrations of 1.4 mg/L and 1.7 mg/L are calculated from the zinc and aluminum concentrations, respectively. Ni concentrations can be applied to calculate the concentration of a released Ni-

colloid fraction. Average Ni colloid concentrations are calculated to 15 µg/L. A cross-link to the total colloid concentration is not possible because the Ni-colloids originate from a montmorillonite paste within the tracer vials and not from a dry compacted bentonite sample. Colloid release in both cases will differ. An alternative Ni source can be found in impurities of the Febex bentonite. A Ni-fraction of 0.003% was found in ICP-MS measurements of a Febex total digestion. In regard of the total Febex mass implemented in LIT, an additional Ni-mass of 70 mg is in the source term. Taking the total Ni amount within the tracer vials of 107 mg into account, additional Ni from the Febex bentonite cannot be neglected. An additional uncertainty can be found in the Nickel background in GGW as it is not a constant value. Depending on the extraction site Ni-background concentrations between 0.16 µg/L (Pinkel) to 3.2 µg/L (Annulus) have been measured. Former analysis of the GGW that was filled in barrels and transported to the INE laboratories in 2012 delivered Ni concentrations of 0.34, 0.93 and 1.83 µg/L. The Ni-background within Figure 60 originates from 21 measurements at the Pinkel extraction point because it is located in the same shear zone, close to the bentonite source and supposed to deliver reliable data. The background at Pinkel is low but shows severe fluctuations. This leads to a high standard deviation and a Ni-background concentration of 0.16 ± 0.18 µg/L.

Low Ni concentrations in the samples and the presence of additional colloid sources in the system makes it difficult to differentiate between dissolved and colloid bound Ni-fractions.

Table 18: Elemental composition of the bentonite rings emplaced within LIT.

| Element | Febex bentonite [weight-%] | Febex/Zn-Mnt admixture [weight-%] | Ni-montmorillonite [weight-%] |
|----------------------------------|-------------------------------|---|----------------------------------|
| Fraction of total sample mass | 76% | 24% | only in glass vials |
| Si | 29.1% | 29.2% | 29.5% |
| Al | 10.1% | 10.3% | 11.6% |
| Mg | 3.4% | 3.1% | --- |
| Zn | --- | 0.7% | --- |
| Ni | --- | --- | 6.0% |
| Fe | 3.6% | 3.2% | --- |

These results are in disagreement with the LIBD measurements, where colloid concentrations of roughly 40 ppb have been detected. Taking into account that 10.3% and 0.7% of the Zn-montmorillonite doped Febex bentonite consist of aluminum and zinc, respectively, the determined

elemental mass concentrations measured by ICP-MS gives up to 50-fold higher concentrations. Therefore, it was questionable if the total Al, Zn and Ni concentrations found were colloid associated or free in solution because dissolution of the bentonite cannot be excluded under GGW pH conditions. To clarify the discrepancy between ICP-MS and LIBD data, part of the samples have been ultra-centrifuged at 90,000 rpm (694,000 g) for one hour to distinguish between particulate bound and dissolved concentrations. Following ICP-MS measurements did not find any difference between centrifuged and untreated samples indicating that there is no or just a very small colloidal fraction. The colloidal fraction consists due to LIBD measurements out of less than 3% of the total aluminum and even less of the magnesium concentration which is in the range of the analytical uncertainty of ICP-MS and therefore not detectable.

7.2.2.2.4 *Radiochemical characterization*

The radionuclides introduced for the LIT experiment can be divided in fission and activation products (^{45}Ca , ^{75}Se , ^{99}Tc and ^{137}Cs) and actinides (^{233}U , ^{237}Np , ^{241}Am and ^{242}Pu). All fission products or rather elements at the mass respective channel have been detected during the SF-ICP-MS measurements. Selenium and cesium can be excluded in combination with the results obtained by gamma-spectroscopy as both radionuclides were below the detection limit of 0.03 Bq/mL. Calcium was not expected in the effluent as it was supposed to take part in the cation exchange process and should be immobilized in the bentonite's interlayer. As a consequence of the short lifetime of ^{45}Ca in combination with the allowed activity limit within LIT, only a very small amount of $2.4 \cdot 10^{-11}$ mol (710 kBq) were added to the tracer vials. If part of the calcium was in the effluent it would not be detectable by (SF-)ICP-MS because it is far below the detection limit of these techniques and because of a natural background of the isobaric scandium-45 that is part of GGW in much higher concentration. Nevertheless, trace amounts of ^{45}Ca would have been detectable in the radiochemical analysis (liquid scintillation counting, LSC), which was not the case. Calcium has a short half-life of only 162.2 days. 97% of the initial mass are already decayed within the first 3 years and later detection will be challenging.

A ^{99}Tc release from the bentonite source could be observed and is shown in Figure 62. Detected concentrations of nucleon number 99 are rising in parallel with the conservative tracer (Figure 62) but level off earlier after 300 days to reach values close to the detection limit after 600 days. Maximum concentrations of 15 ng/L have been determined by SF-ICP-MS but interference with

the isobaric ^{99}Ru cannot be neglected. There is no natural background for ^{99}Ru in GW and only ultra-trace amount of ^{99}Ru have been found in Febex bentonite. The ^{99}Ru portion within the bentonite source has been determined with ICP-MS of a Febex digestion and leads to a total amount of 1 mg. Recently performed accelerated mass spectroscopic (AMS) measurements of selected samples at the AMS device in Munich showed that the amount of ^{99}Tc is actually much lower than expected (< 5%) from SF-ICP-MS data.

Detection of uranium and the transuranic elements in the samples was not possible by HR ICP-MS. Values were very close or below the detection limits given for the measurements in GW of 4 pg/L in case of ^{242}Pu and even 2 pg/L for ^{233}U , ^{237}Np and ^{241}Am .

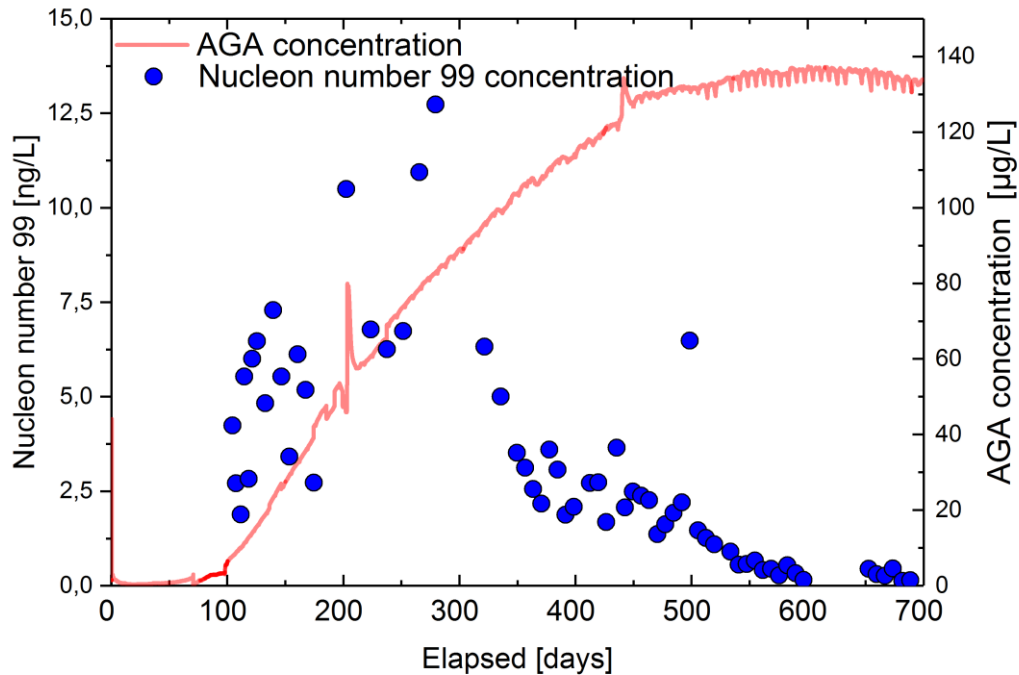


Figure 62: Nucleon number 99 release from LIT sampled from GTS borehole CFM11.02.

7.2.3 LIT mock-up

The LIT mock-up test was conducted in parallel to the LIT experiment with the aim to investigate comparable processes that relieve interpretation of the field experiment. Therefore, the mock-up test was designed as identical to LIT as possible.

7.2.3.1 Swelling pressure and distance

Swelling of the bentonite ring takes place during the first weeks of the experiment and is monitored with a camera, which is installed under the artificial fracture set-up. Pictures have been taken regularly every three hours. Swelling starts immediately upon contact of the bentonite sample with GGW in conjunction with the built-up of a swelling pressure. The biggest difference in swelling distance is observed during the first days of the experiments. After two weeks the sample expanded already 10 mm into the fracture (Figure 64). Swelling around the sample is not uniform and the equilibrium value is 10.5 ± 2 mm (Figure 63).

Swelling pressure did not built up within the first days of the experiment but with a delay of three days as pressure increased rapidly within the following eleven days to values around 250 kPa. A slower linear increase was observed over the following weeks until steady state was reached at 400 kPa after 60 days (Figure 64). The differences in swelling distance and pressure in comparison to the bentonite erosion experiment described in 7.2.1.1 can be explained by the differences of the bentonite samples. The use of a broken bentonite sample ring in this experiment reduced the total sample mass by 5-7%, limiting the dry density from initially $1,650 \text{ kg/m}^3$ to an effective dry density between $1,490$ to $1,520 \text{ kg/m}^3$. Less swelling pressure and reduced fracture intrusion are direct consequences. Swelling pressure up to 2 MPa is expected without swelling according to Agus et al. [114]. Again, the addition of the synthetic montmorillonite in this experiment may also have an effect but cannot be evaluated as there is no data to compare the swelling properties of the synthetic montmorillonite and the Febex bentonite. The pressure sensor was placed on top of the bentonite sample but a small gap between sample and sensor remained. This is the reason for the delay in the pressure data during the first days of the experiment.

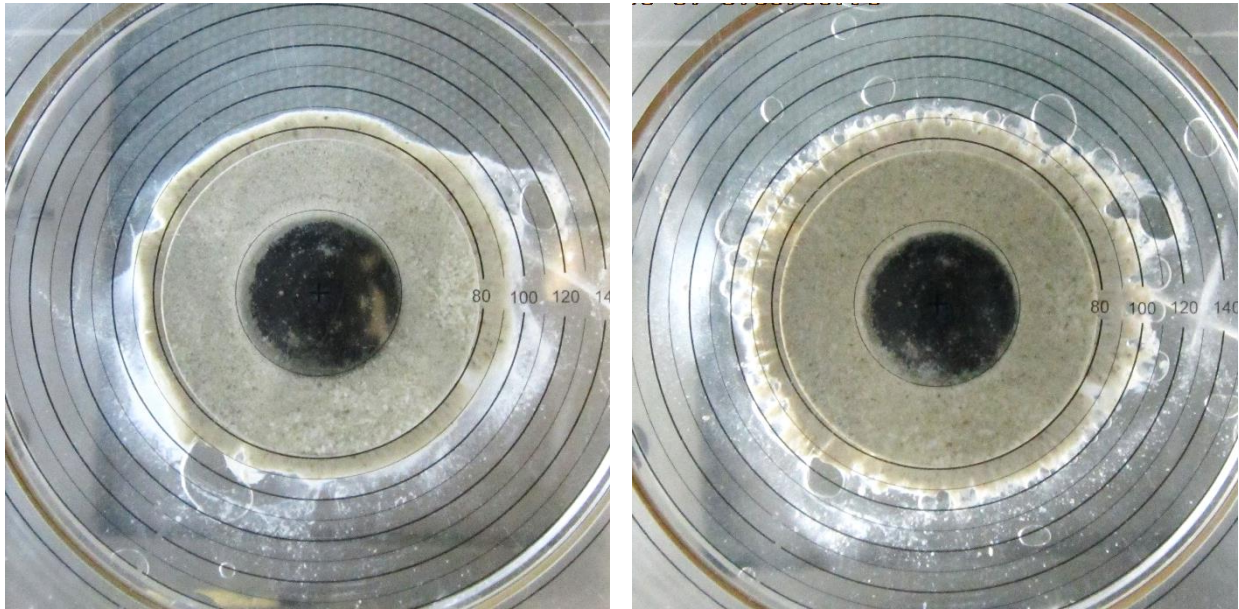


Figure 63: LIT-mock-up experiment (left) at a run-time of four days and (right) at a run-time of 56 days.

As already described in case of the pure Febex bentonite erosion test (7.2.1.1), an unsaturated bentonite sample was also used in this experiment. A water saturation process took place in the initial phase. GGW was sucked into the cavities and replaced entrapped air. As a consequence, air bubbles occurred regularly at the rim of the swelling zone during the first days of the experiment which were removed by slightly tilting of the set-up and moderately increasing the flow rate in parallel. This was necessary as the air bubbles otherwise would have stayed in the system effectively preventing the bentonite swelling process. The bentonite ring was fully saturated after two months and the swelling pressure reached steady state.

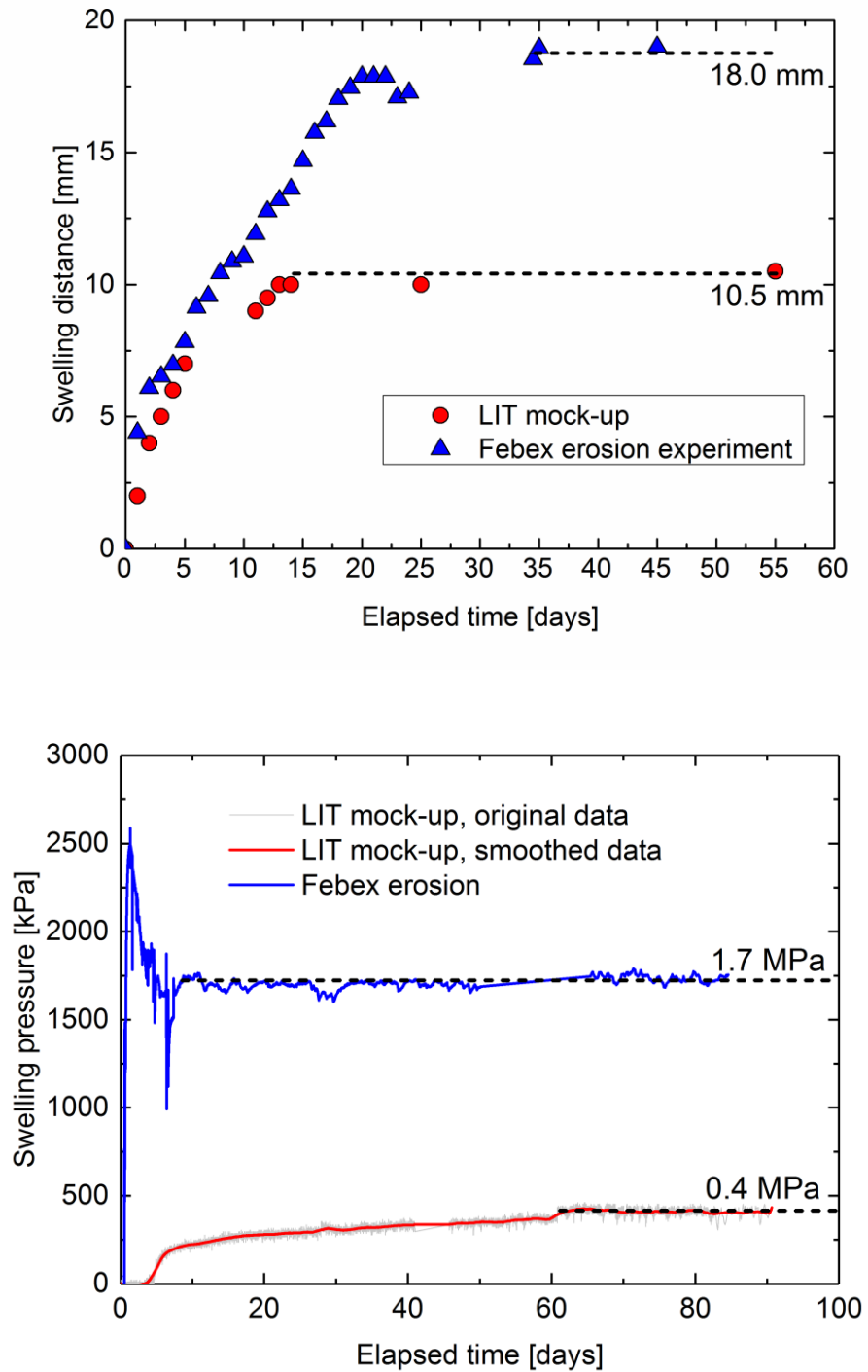


Figure 64: Results on swelling distance (top) in the 1 mm aperture and swelling pressure (bottom) within the set-up.

7.2.3.2 *Hydro-geochemical monitoring – pH, flow rate and conservative tracer evolution*

GGW is continuously pumped through the 1 mm artificial fracture. As the experiment is set up under anoxic conditions, carbon dioxide was excluded and has no influence on the pH as described in 0. A pH drop during the early stage of the experiment is monitored in Figure 65. Initial pH values around 8.5 differ clearly from the GGW literature value of 9.6 ± 0.2 [98] but rise steadily and reach steady state close to the initial value in the GGW containing barrels within 150 days. The overall shape of the pH evolution is comparable to LIT but the values differ due to varying sample dimensions and an additional dilution factor within LIT

Flow rate through the set-up was monitored during each sampling for 150 days as the eluted mass over time gives the volumetric flow rate. After 150 days sampling was changed from taking one sample of 15 mL at least every week to taking only one sample per week comprising the total effluent volume. The flow rate was initially adjusted to $49 \mu\text{L}/\text{min}$ but due to some alterations of the tubing the rate decreased to a plateau at $44 \pm 0.5 \mu\text{L}/\text{min}$ within 100 days (Figure 65). Modelling the flow velocity at the water-bentonite interface from the given volume flux with COMSOL Multiphysics yields a maximum velocity of $1.2 \cdot 10^{-5} \text{ m/s}$ (A-Figure 5) and a maximum shear stress of $3.3 \cdot 10^{-5} \text{ Pa}$ (A-Figure 6). These values are very comparable to the previous bentonite erosion laboratory experiment described in 0. The flow velocity distribution within the 1 mm fracture set-up at equilibrium swelling distance into the fracture is shown in A-Figure 4. Flow rate distribution and the flow rate evolution is very comparable to the pure Febex erosion experiment.

The release of the conservative tracer Amino-G was investigated by measuring the fluorescence intensity with an Aminco-Bowman Series 2 Luminescence Spectrometer (Thermo Inc.). It is shown in Figure 65. After 12 days the first tracer signal was detected rising to a maximum concentration around 1500 to 2000 ppb after 40 days experimental run-time. The Amino-G concentration decreased after this maximum value and was close to the detection limit but still measurable after 320 days. A total of 12.5 mg Amino G was released from the bentonite source. This represents a recovery of $49 \pm 2\%$ related to the total amount of AGA that was contained in the tracer vials. The even shape of the breakthrough curve suggests equal contact of the tracer containing vials with the surrounding groundwater over the overall experimental time. Limited Amino-G recovery can be explained by the assumption of degradation of the conservative tracer. Tracer glass vials used for this experiment were prepared for LIT, 22 months before the mock-up experiment was set-up. Left-over tracer vials from LIT emplacement have been stored unshaded in an Argon glove-box.

Additionally the fact that the experiment is unshaded may lead to further Amino-G degradation. Post-mortem analysis of the mock-up test is needed to quantify the remaining amount of the conservative tracer within the erosion cell.

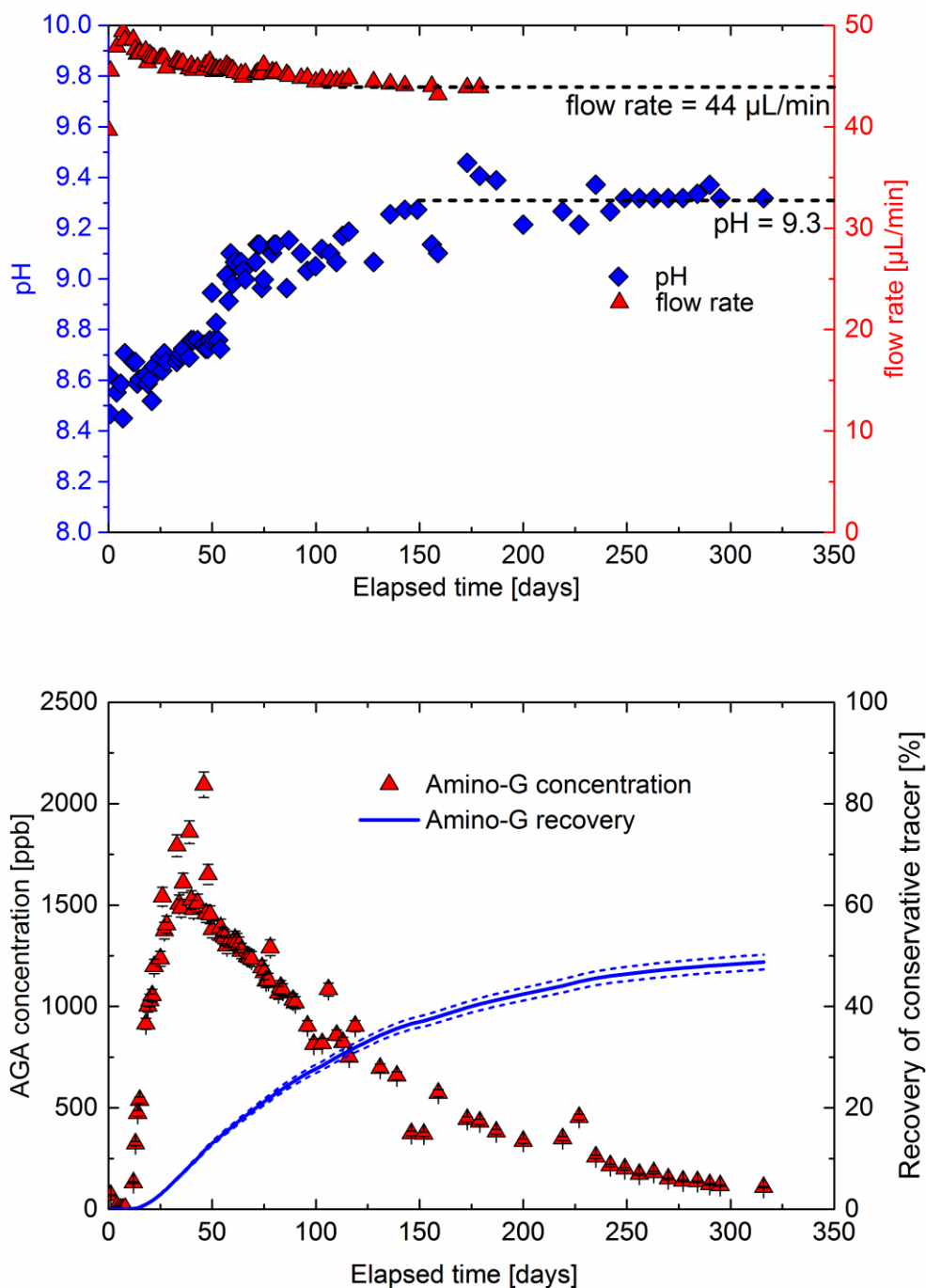


Figure 65: Evolution of pH, volumetric flow rate (top) and conservative tracer concentration and total recovery (bottom).

7.2.3.3 *Elemental characterization*

Elemental composition of the cations within the effluent (Figure 66a and b) was determined by ICP-MS and anions via ion chromatography (Figure 66c). ICP-MS measurements focused basically on the source forming main elements Al, Mg, Ni and Zn as well as on elements connected with the dissolution of accessory minerals like Na (halite) and Ca (gypsum).

Na and Ca concentrations as indicators for dissolution of accessory phases rise in the beginning of the experiment to level off after reaching a maximum at a run-time of 13 days. Background values are in case of Na concentrations not reached within the observed time-span but Ca concentrations reach the background value of 7.7 mg/L within 45 days. A steady state concentration below the GW background is reached at values of 6.0 ± 0.3 mg/L. A maximum for the Na concentrations is observed after 45 days with the five-fold background concentration and a steady state level is reached after 150 days with 17.2 ± 1.9 mg/L which is by 8 mg/L higher than the GW background. This observation can be explained with the continuous removal of Ca by the cation exchange process in combination with the release of Na from the bentonite's interlayer. Ca concentrations start rising above the GW background with a delay of seven days which can be explained by slow dissolution of hardly soluble gypsum [118] and the mixing of the GW with the bentonite's porewater (Table 10). Mg concentrations show a considerable increase in comparison to the background value over the total observation time. A maximal concentration of 5.2 mg/L is reached after 18 days which is nearly three orders of magnitude above the GW background concentration but still 50-fold below the porewater concentration. Equilibrium is reached within 160 days at significantly lower values of 89 ± 37 μ g/L which is only one order of magnitude above the GW background. The release of bentonite colloids are not responsible as source for the Mg concentration because there is no Al in most of the samples. Only the first three samples show a small Al content below 0.5 mg/L, respectively and no aluminum until a run-time of 170 days. This is an indication for hindered colloidal release due to the higher ionic strength which is mainly originating from the dissolution of accessory minerals. Ionic strength was calculated from the ICP-MS data and gives increased values of 3.3 mM at a run-time of 18 days and 1.1 mM at a run-time of 300 days, respectively. The combined concentration of the divalent cations alone at a run-time of 18 days ($c(M^{2+}) = 0.6$ mM) is high enough to prevent colloid formation [8].

In case of Ni, concentrations are always below the detection limit of the ICP-MS (< 5 ppt) and therefore not mentioned. Zn concentrations are increased over the entire run-time. A maximum of

90 $\mu\text{g/L}$ is observed after 14 days which is already close to the solubility limit reported for $\text{Zn}(\text{OH})_{2,s}$ by Reichle et al. [119]. Zn concentration decreases over time to values of 15 $\mu\text{g/L}$ after 50 days. [Zn] increases in the ongoing experiment and does not give a constant value but varies significantly between individual samples. Colloid concentrations are only calculated if both Al and Zn was detected in one sample. Al was only detectable in the very first samples and decreased below the detection limit of the ICP-MS after 170 days run-time. A mean Al concentration of 383 $\mu\text{g/L}$ was derived for the ongoing experiment. Zn mean concentration was measured with 190 $\mu\text{g/L}$ in the same period. Taking in account that the bentonite contains 10.3% and 0.7% Al and Zn (Table 18), respectively, maximum colloid concentration of 3.7 mg/L (Al) up to 27 mg/L are possible. Taking the low colloidal fraction within the effluent of the field experiment of only ~2% and assuming that this finding is transferrable to the laboratory experiment, the colloid fraction concentration reduces to ~70 (Al) - 500 (Zn) $\mu\text{g/L}$. This is only a weak assumption but further proof is currently not available.

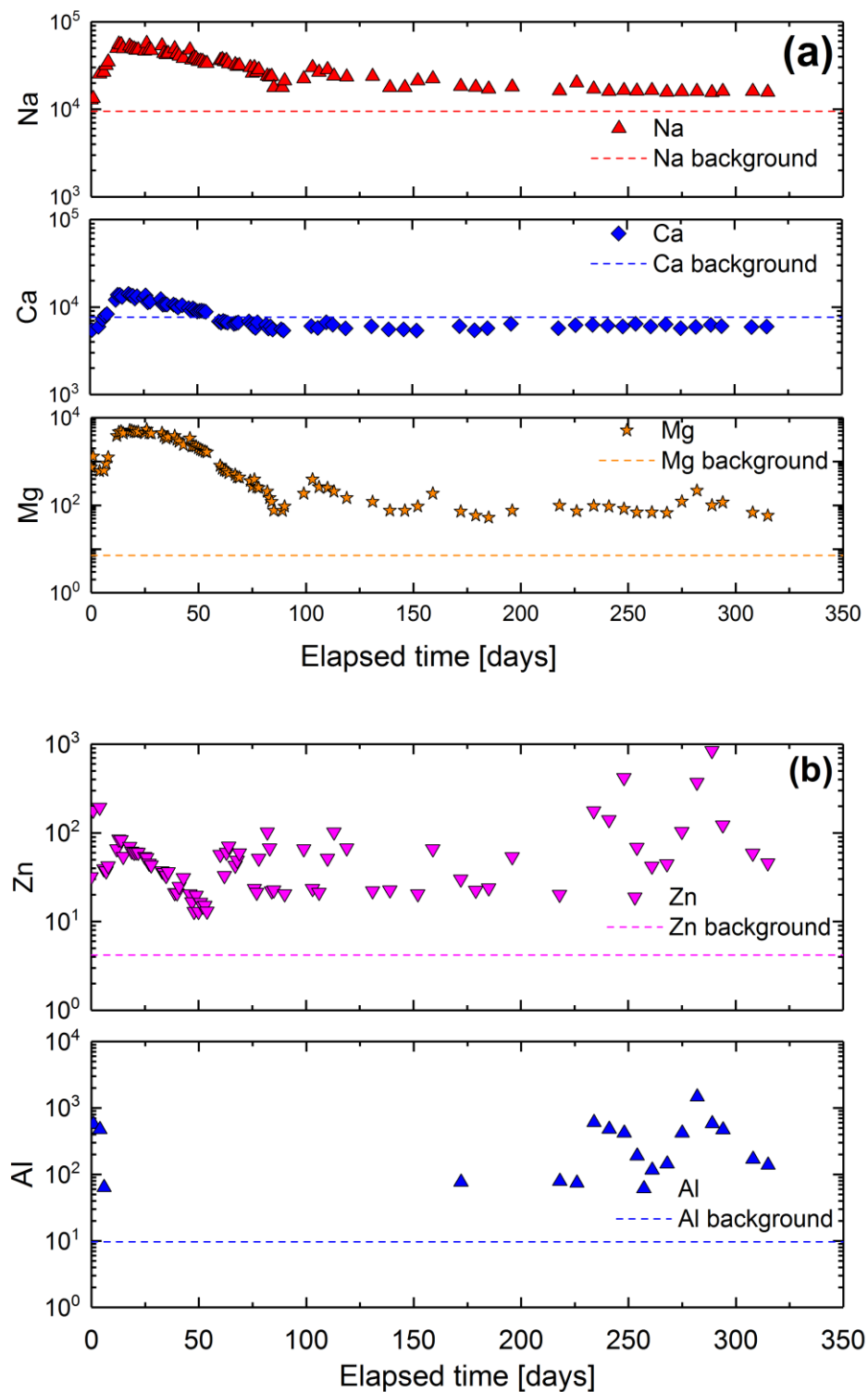
Evolution of the anionic components F, Cl and SO_4 can be found in Figure 66c. Cl and SO_4 concentrations are comparable to their counterion evolution in regard of the above mentioned accessory phases halite and gypsum. Cl concentrations are roughly one order of magnitude increased in the early samples before a run-time of 170 days. This can be explained with the analytical procedure. 15 mL samples have been taken for a run-time < 170 days and only 500 mL samples, collected over a week in the following. The small sample volume in the early stage of the experiment didn't allow to separate the sample into different aliquots. Therefore IC measurements have been conducted from the same sample after pH measurements and Cl-leaching from the filling of the electrode (3M KCl) leads to increased concentrations. Cl-leaching can be excluded for samples taken after 170 days as the sample volume was high enough to take different aliquots. Cl concentrations in case of the weekly samples (> 170 days) are at the GW background level. An early increase due to dissolution processes is likely but the data is due to Cl-leaching not reliable.

Analysis of the background corrected molar ratio between Ca and SO_4 can be found in Figure 66d. The ideal molar ratio for dissolution of gypsum is due to the equal ion charges 1. An early maximum at a molar ratio of ~1.7 can be found after 12 days and can be explained by the mixing of the GW with the bentonite porewater in which Ca is 4-fold higher concentrated than SO_4 . Ca- SO_4 -ratio shows a constant decrease over the following days. This observation in addition with the Na evolution supports the theory of the cation exchange process. Thereby additional Na is released

from and part of the Ca is bound in the interlayer. The additional Na concentration doesn't match to the decrease in Ca concentration as these are only two elements that take part in this process. Especially Mg which is compensating roughly 30% of the interlayer charge has to be taken into account.

Fluoride is not connected with the dissolution process of any accessory mineral phase in the system and its concentration is therefore stable at the GW level over the total experimental run-time.

In comparison to the erosion processes described in 7.2.1.3 all mentioned experimental phases, namely phase I (washing), phase II (crystalline swelling), phase III (dissolution) and finally phase IV (bentonite erosion) have been observed in the reported period of the LIT mock-up experiment. The washing phase is identified by the initial aluminum concentration around 0.5 mg/L, which decreases within the first samples under the detection limit. Increased Na and Ca concentrations are characteristic for the dissolution of accessory phases within the unpurified bentonite sample and used as indicator for phase III of the experiment. During dissolution, ionic strength is increased to 3.3 mM and colloid stability is limited. As a result Al concentrations as an indicator for a colloidal fraction drop under the detection limit and Ni is below the detection limit over all samples. An increase of the Al concentration is observed after 170 days in agree with the decrease in ionic strength, which favors colloid stability after 150 days run-time and indicates bentonite erosion.



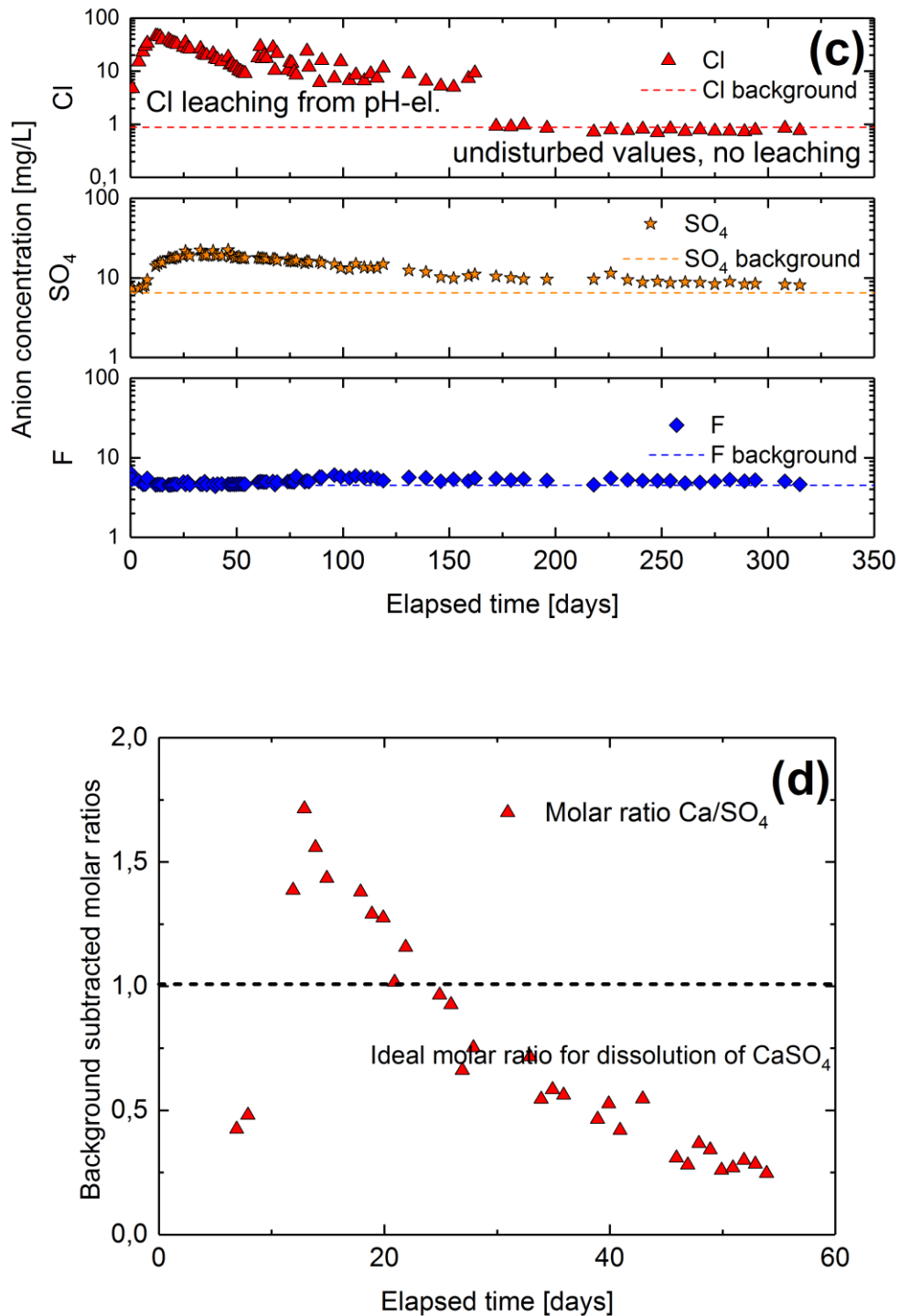


Figure 66: Elemental evolution of the main cations Na, Ca and Mg (a), the source forming cations Zn and Al (b), anions (c) as well as molar ratios of the components of the accessory mineral gypsum (d).

7.2.3.4 Radiochemical characterization

Gamma spectroscopy and SF-ICP-MS was applied for radiochemical characterization of the samples. Gamma spectroscopy focused only on the quantification of ^{75}Se , ^{137}Cs and ^{241}Am as the remaining radionuclides are due to a missing gamma emission not suitable for this technique. Like in case of the LIT samples none of the before mentioned radionuclides was found. All samples were below the detection limit of gamma spectroscopy. This can be seen as an additional indication against colloidal release at this stage because ^{137}Cs and ^{241}Am are supposed to be colloid associated. SF-ICP-MS was applied for all radionuclides. Due to the detection of the atomic mass several isobaric interferences were possible and may not be neglected (Table 12). Concentrations of the activation product ^{45}Ca and the fission products ^{75}Se and ^{137}Cs as well as the transuranic elements ^{241}Am and ^{242}Pu were below the detection limit of SF-ICP-MS.

Radionuclide release was detected in case of ^{99}Tc , ^{233}U and ^{237}Np already in the first samples and will be specified in the following (Figure 67). Technetium concentrations show a fast increase within the early phase of the experiment and reach a maximum of 500 ng/L after 14 days. Concentrations decrease over the remaining observation time to reach a plateau of 4 ± 0.7 ng/L after 240 days. As described in case of the LIT experiment (7.2.2.2.4) an overlap with nuclides of similar weight (^{98}Mo , ^{99}Ru and ^{100}Mo) cannot be excluded and ^{99}Tc concentrations may be lower. Again, AMS measurements could help to quantify the actual ^{99}Tc release but was not possible in the framework of this thesis. The delayed detection of the conservative tracer in comparison to the RNs can be explained by degradation of Amino-G because the tracer vials have not been shaded during storage. Additionally, the experiment was not shaded and part of the tracer may be degraded during sampling. This may explain that ^{99}Tc is detected before the conservative tracer. Similar behavior has been observed in case of ^{237}Np evolution. Concentrations above the detection limit are already present in the first samples and rise after a delay of 14 days to reach a stable 50 days lasting plateau around 15 ng/L within 27 days. ^{237}Np concentrations decrease to 1.6 ± 0.2 ng/L over time and are stable at this value after a run-time of 240 days for the remaining observation time. The plotted curves of technetium and neptunium concentrations do not show major disturbances, indicating that the tracer containing vials are constantly in contact with the groundwater. Disturbances at 150 and 230 days are visible in the evolution of ^{99}Tc and ^{237}Np concentrations as well as the Amino-G concentrations. This can be seen as proof of the high quality of the measurements as these changes are originating from the system and not from the measurement

techniques. The early detection of ^{99}Tc and ^{237}Np furthermore indicates that reduction from $^{99}\text{Tc(VII)}$ to $^{99}\text{Tc(IV)}$ and from $^{237}\text{Np(V)}$ to $^{237}\text{Np(IV)}$ can be excluded at this early stage because the tetravalent RN are strongly sorbing to the bentonite and bentonite colloids. Colloids are not detected at this stage.

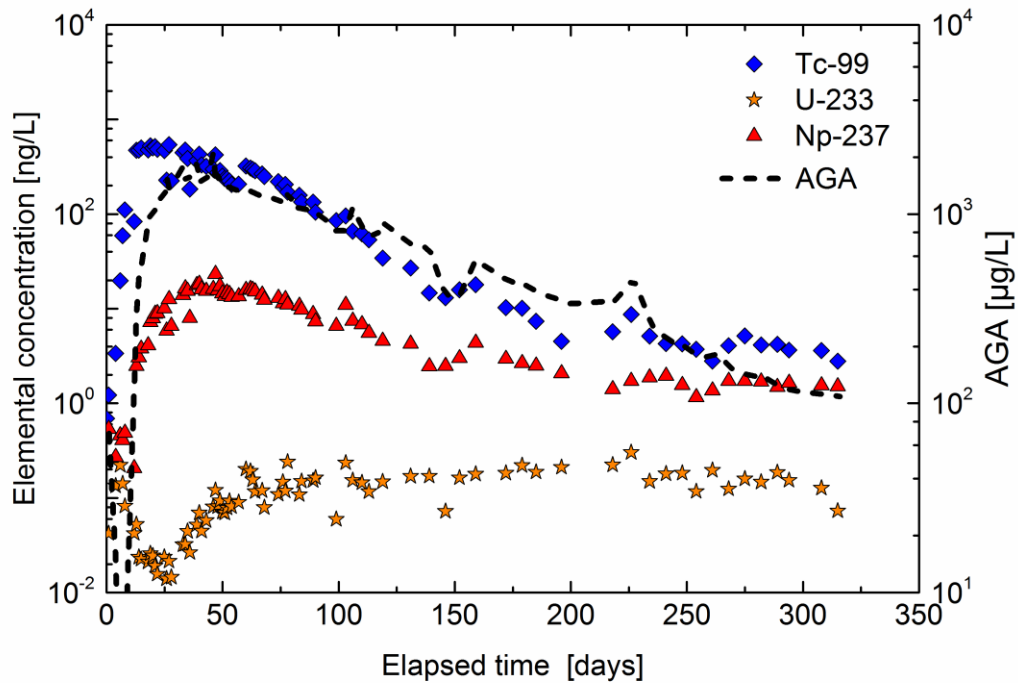


Figure 67: Radionuclide concentration in case of ^{99}Tc , ^{233}U and ^{237}Np . ^{99}Tc initially as Tc(VII) , ^{233}U initially as U(VI) and ^{237}Np initially as Np(V) .

In contrast to the before mentioned radionuclides, uranium shows an early maximum of 0.2 ng/L after only 7 days and levels off to reach a first plateau at 0.02 ng/L after 14 days. The orientation of the tracer vials that are opened towards the fracture is a possible explanation for the early U maximum. The tracer containing glass vials are in the initial phase of the experiment in direct contact to the GGW and the RNs can be released unhindered. Swelling of the bentonite will block this transport channel and can be responsible for the subsequent decrease of the U concentration. Elevated values are again detected after 30 days and are constant at 0.15 ± 0.05 ng/L for the total observation time. It is remarkable that the U speciation (7.1.3) changes during the first 50 days of the experiment. pH increases in the first 150 days of the experiment from 8.6 to 9.3 (Figure 65)

while Ca concentrations decrease from 0.36 mM to 0.15 mM. Thereby the Ca-UO₂ complexes described in Figure 39 gain importance in the first weeks and anionic UO₂(OH)₃⁻ is dominant during the further experiment. The neutral charged Ca₂UO₂(CO₃)₃ shows only weak sorption [120] and cannot explain the decreased uranium release during the first weeks of the experiment. Calculated speciation diagrams for the initial and the equilibrium stage of the experiment are shown in Figure 68 for the experimentally derived concentrations of U and Ca.

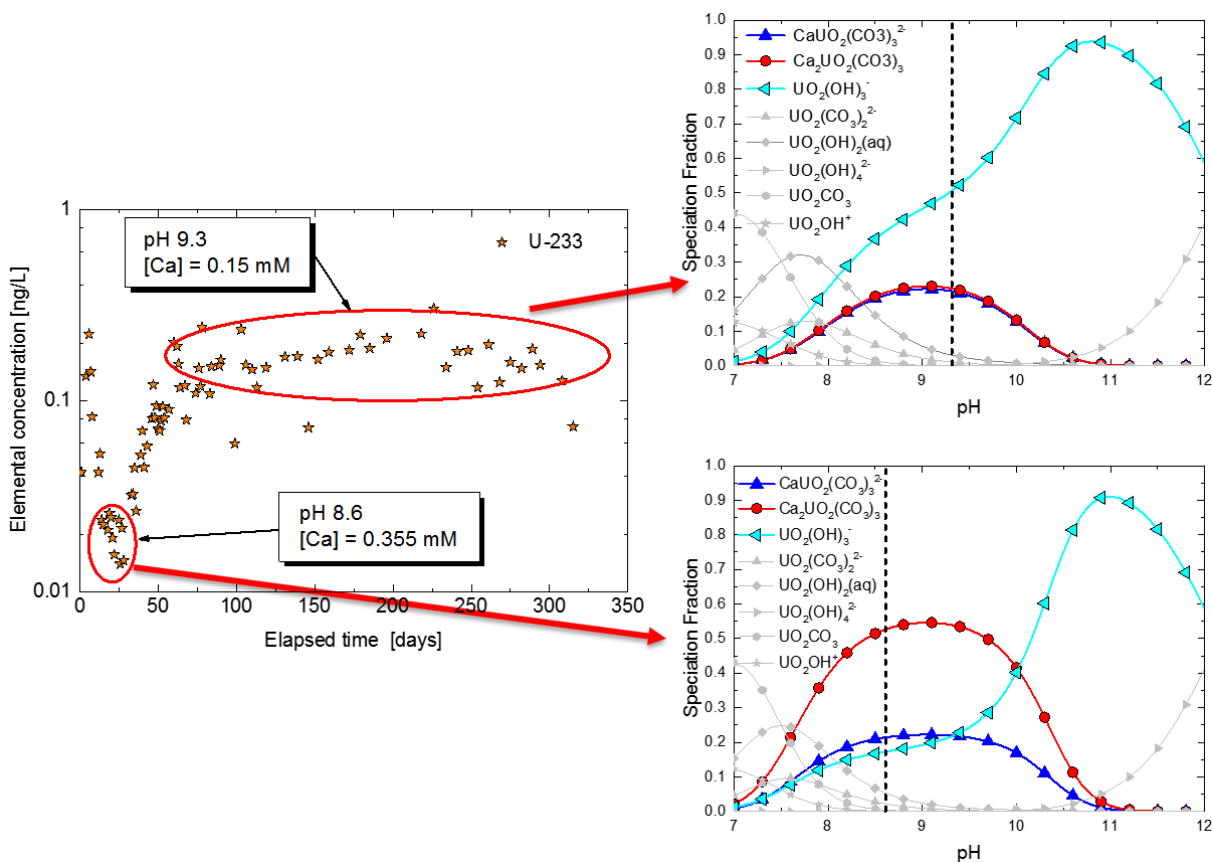


Figure 68: Uranium speciation for the LIT mock-up experiment calculated with Hydra/Medusa. Speciation changes over the run-time of the experiment.

Radionuclide recoveries over the first 320 days of the LIT mock-up experiment are calculated over the integral of the release curves. Quantitative recovery has been obtained for ⁹⁹Tc whereas the actinides show recoveries of only ~1% (Table 19). ⁹⁹Tc recoveries are surprisingly high in comparison to the recovered conservative tracer. This observation leads to two possible explanations. On the one hand side, ⁹⁹Tc recovery might be highly overrated due to isobaric (⁹⁹Ru) and neighboring (^{98/100}Mo) interferences during the ICP-MS measurement as has been seen in

samples originating from the LIT experiment (7.2.2.2.4). On the other hand side, it is possible that the conservative tracer degraded over time and led to decreased AGA concentrations in the effluent. As the set-up was not shaded during the experiment in order to take pictures and as AGA is sensitive to light, this possibility must not be neglected.

Reason for the differences in RN recoveries can be found in the RN speciation under the given conditions. Tc speciation under the relevant conditions is dominated by negatively charged TcO_4^- (Figure 38) while Np speciation is dominated by positively charged NpO_2^+ with a small fraction of $\text{NpO}_2\text{CO}_3^-$ as can be seen in Figure 40. The charge difference of the complexes influences the interaction with the negatively charged bentonite. TcO_4^- does not show retention on the bentonite but positively charged complexes like NpO_2^+ are supposed to be attracted by the oppositely charged surface. Furthermore, surface reduction from Np(V) to Np(IV) cannot be neglected because the system is close to the reduction borderline and lower E_{hSHE} values may be present at the bentonite surface [41].

Table 19: Radionuclide recoveries over the first 320 days of the LIT mock-up experiment.

| RN recoveries | |
|-------------------|----------|
| ^{99}Tc | 108±11% |
| ^{233}U | 0.8±0.1% |
| ^{237}Np | 1.3±0.2% |

8 Conclusions

Regarding the main goals of the prevailing thesis to produce kinetic parameters on the long-term sorption reversibility of various RNs on FG material, one can draw the following conclusions:

- Batch sorption experiments for the radionuclides ^{99}Tc , ^{233}U , ^{237}Np , ^{242}Pu and ^{243}Am on natural FG material under GW conditions have been conducted and provided distribution coefficients and kinetic reaction rates on the sorption process. Tc sorption is delayed, indicating a reductive sorption mechanism on the FG surface or in pores which is not expected under the experimental conditions. The same is observed for ^{237}Np sorption as a steady state of the sorption value is not reached during the entire sorption time. In case of ^{233}U and the strong sorbing RNs ^{242}Pu and ^{243}Am , steady state was observed within 14 days.
- Desorption processes in the binary system FG – GW were investigated in dependence of the sorption time. In case of the strong sorbing RNs ^{242}Pu and ^{243}Am , the reversible fraction is independent of the sorption time. The recoveries for these radionuclides are low. In contrast, ^{233}U and ^{237}Np sorption reversibility is sorption time depending. With increasing sorption time the reversible fraction decreases. A coupled sorption-reduction process can be assumed to explain this observation. RN release rates in a one-rate and a two-rate fit as well as the respective reversible RN fraction in dependence of the sorption time have been obtained.
- Introduction of bentonite colloids as competing surface leads to a significant release of the strong sorbing radionuclides ^{242}Pu and ^{243}Am in comparison to the binary system. Tc recovery is by addition of bentonite colloids as well many times higher than recovery in the binary system. The effect of bentonite colloid addition is in case of U and Np desorption less pronounced and a function of the sorption time. With increasing sorption time, the additional reversible fraction in the ternary system increases in comparison to the recovery in the binary system.
- Centrifugation tests showed that a major part of the released RNs in the ternary system is colloid bound. This observation leads to the assumption that the transfer of Tc from the FG over the dissolved species to the bentonite colloids takes place in the tetravalent oxidation state as the heptavalent TcO_4^- is not expected to interact with the colloid surface.

The process of bentonite erosion has been examined in-situ in terms of the LIT experiment as well as in artificial fractures on the laboratory scale. The following conclusions can be made:

- Bentonite erosion experiments of purified bentonite samples can be divided in a phase of bentonite saturation and swelling and the subsequent process of bentonite erosion. In case of natural unpurified bentonite samples, out washing of impurities and dissolution of accessory mineral phases in addition have to be taken into account. Furthermore cation exchange reactions take place if the bentonite sample is not in equilibrium with the contacting groundwater. The combination of these processes makes bentonite erosion under repository relevant conditions to a complex issue.
- Cation exchange processes cannot be neglected if the bentonite is not in equilibrium with the surrounding groundwater. As has been shown for natural Febex bentonite, Ca is stripped from the contact water and intercalated into the montmorillonite interlayer. In order to keep the charge balance, mainly Na but also minor quantities of Mg are at the same time released from the interlayer. The process is slow, which is surprising for a cation exchange process but can be explained by a diffusion limited transport in the bentonite source and only limited amounts of Ca in GW as rate limiting steps. Therefore the exchange process was visible over the entire experimental time.
- Swelling pressure evolution is monitored during the experiments in the artificial 1 mm fracture cell as well as in the LIT experiment. Dimension of the erosion experiments are undersized and swelling pressures in the range foreseen in case of a HLRW repository cannot establish. This is because swelling in open space around the sample and in the fractured system will reduce the density of the bentonite source. A bigger bentonite source will result in smaller decrease of the density during the swelling process and enable higher swelling pressures. Additionally, the literature data does not consider a reduction of the dry density during the swelling process.
- Colloid concentrations are in all cases surprisingly low. The ionic strength is during the early stage of the experiments with regard to the CCC high and colloid generation is unlikely. This is observed during the mixing with the bentonite pore water and the dissolution of accessory minerals. These processes control the ionic strength in the near-field during the first phase of the experiment. In the later course of the experiment, ionic strength decreases to the background level and colloids are supposed to be stable. At this

point, the bentonite may already have been transformed from a Na/Ca/Mg-dominated bentonite to a mainly Ca/Mg-dominated bentonite by continuous stripping of Ca from the groundwater. Bentonite erosion in case of bivalent interlayer cation dominated bentonites due to stronger interparticle electrostatic forces is suppressed in comparison to bentonites with a higher amount of monovalent interlayer cations.

- Regarding the radionuclides that have been released from the bentonite source in LIT, only limited amounts of Tc as the only radionuclide have been detected. Quantification with SF-ICP-MS is difficult due to interferences with isobaric ^{99}Ru in minor amounts as well as neighboring ^{98}Mo and ^{100}Mo , both in significant amounts. These interferences can be excluded by AMS (personal communication with Francesca Quinto), where only ~5% of the Tc determined with SF-ICP-MS have been confirmed. In terms of the LIT-mock-up experiment, U and Np have been detected beside Tc. The release of Tc and Np follow the conservative tracer evolution. U release is delayed which could be a result of a change in speciation due to pH variation. Quantitative recovery has been found for Tc but the interferences from ^{99}Ru and $^{98/100}\text{Mo}$ have not been corrected because AMS measurements for these samples have not been completed in the frame of this PhD. Recoveries of Np and U are low (~1%) indicating a retention process (sorption/reduction) within the bentonite.
- The colloid associated radionuclides ^{241}Am , ^{242}Pu and ^{137}Cs have neither been detected in the effluent of the mock-up experiment nor in the near-field of LIT, indicating very limited release and mobility of colloidal material as well as the respective dissolved RN species.
- The laboratory bentonite erosion experiment found during the erosion phase of the experiment an average, contact area normalized erosion rate of $91 \pm 30 \text{ g}/(\text{m}^2 \cdot \text{a})$. The rate low high in comparison to literature data but comparability is limited. In case of LIT, calculation of an erosion rate is not possible because it is not known how deep the bentonite source extruded into the fracture and therefore normalization over the contact area is not possible. Furthermore only a fraction of the eroded material can be sampled in the near-field observation boreholes.

9 *Open questions and future directions of research*

- RN sorption reversibility studies on FG material in absence and presence of bentonite colloids have been finalized in the course of this PhD. Kinetic parameters for sorption and sorption time depending RN release rates for the reversed reaction as well as reversible bound RN fractions in dependence of the sorption time in the binary and the ternary system have been determined. This data is supposed to be used as input parameters for migration models like COFRAME. The goal of this approach is the successful description of the long-term RN behavior in the tailing of CFM Run 12-02 and Run 13-05.
- The LIT experiment is currently going on and an increase of the flow velocity by extracting a higher volume in the near-field as well as a change of the near-field extraction point is planned for the later course of the experiment. The last action of the field activities within LIT will be the overcoring and the retrieval of the radionuclide holding bentonite source. Thereby a core containing the source as well as the near-field observation boreholes will be drilled into the shear zone to extract the source and the direct contact zone of the MI shear zone. It is mandatory that the bentonite source and the extruded bentonite in the fractured near-field stay intact during the overcoring process. Therefore a supporting feasibility study is planned to find a suitable way to conserve the sample during overcoring. This study includes the bentonite erosion experiment as they are due to the sample composition and the long run-time ideal for the final test before overcoring of LIT takes place. Once the bentonite sample is extracted from the shear zone, it will be disassembled and distributed among the CFM partner institutions for post-mortem analysis.
- The effluents of the bentonite erosion experiments in the artificial fracture cell have been collected for nearly the entire run-time of the experiment and the eroded material is still available but highly diluted. Radionuclide sorption/desorption experiments have not been conducted with natural eroded colloidal material so far as colloids produced from the bulk material by a centrifugation/resuspension method were used. In order to use the eroded colloids for future radionuclide sorption experiments, higher colloid concentrations are needed. Therefore, the effluent suspensions will be concentrated by ultra-filtration to

comparable colloid concentrations. It is planned to use these colloids either for new radionuclide sorption/desorption experiments and for comparison with former studies or as colloidal phase for a new radionuclide bentonite colloid tracer run at GTS.

10 References

1. SKB, *Long-term safety for KBS-3 repositories at Forsmark and Laxemar - a first evaluation; Main report of the SR-Can project*, in SKB Technical report TR-06-092006, Svensk Kärnbränsle-hantering AB: Stockholm, Sweden.
2. SKB, *Long-Term Safety for the Final Repository for Spent Nuclear Fuel at Forsmark*, in *Main Report of the SR-Site Project*. SKB technical report TR -11-012011, Svensk Kärnbränslehantering AB.
3. King F., L.C., Pedersen K., *An update of the state-of-the-art report on the corrosion of copper under expected conditions in a deep geologic repository*, 2010, SKB.
4. Huber, F.M., et al., *Radionuclide desorption kinetics on synthetic Zn/Ni-labeled montmorillonite nanoparticles*. *Geochimica Et Cosmochimica Acta*, 2015. **148**: p. 426-441.
5. Robinson, P. and A. Bath, *Workshop on Copper Corrosion and Buffer Erosion Stockholm 15-17 September 2010*, in SSM--2011-08
6. Degueldre, C. and A. Benedicto, *Colloid generation during water flow transients*. *Applied Geochemistry*, 2012. **27**(6): p. 1220-1225.
7. Alonso, U., T. Missana, and M. García-Gutiérrez, *Experimental Approach to Study the Colloid Generation from the Bentonite Barrier to Quantify the Source Term and to Assess its Relevance on the Radionuclide Migration*. *MRS Proceedings*, 2006. **985**.
8. Schaefer, T., et al., *Nanoparticles and their influence on radionuclide mobility in deep geological formations*. *Applied Geochemistry*, 2012. **27**(2): p. 390-403.
9. Geckeis, H., et al., *Results of the colloid and radionuclide retention experiment (CRR) at the Grimsel Test Site (GTS), Switzerland - impact of reaction kinetics and speciation on radionuclide migration*. *Radiochimica Acta*, 2004. **92**(9-11): p. 765-774.
10. Schäfer, T., et al., *U, Th, Eu and colloid mobility in a granite fracture under near-natural flow conditions*. *Radiochimica Acta*, 2004. **92**(9-11): p. 731-737.
11. Möri, A., et al., *The colloid and radionuclide retardation experiment at the Grimsel Test Site: influence of bentonite colloids on radionuclide migration in a fractured rock*. *Colloids and Surfaces A: Physicochemical and Engineering Aspects*, 2003. **217**(1-3): p. 33-47.
12. Bouby, M., et al., *Interaction of bentonite colloids with Cs, Eu, Th and U in presence of humic acid: A flow field-flow fractionation study*. *Geochimica Et Cosmochimica Acta*, 2011. **75**(13): p. 3866-3880.
13. Bouby, M., N. Finck, and H. Geckeis, *Flow field-flow fractionation (FIFFF) coupled to sensitive detection techniques: a way to examine radionuclide interactions with nanoparticles*. *Mineralogical Magazine*, 2012. **76**(7): p. 2709-2721.
14. Geckeis, H., et al., *Mineral-Water Interface Reactions of Actinides*. *Chemical Reviews*, 2013. **113**: p. 46.
15. Huber, F., et al., *Sorption reversibility kinetics in the ternary system radionuclide-bentonite colloids/nanoparticles-granite fracture filling material*. *Applied Geochemistry*, 2011. **26**(12): p. 2226-2237.
16. Miller, W., et al., *Geological Disposal of Radioactive Wastes and Natural Analogues 2000*: Elsevier Science.
17. Lagaly, G., *H. van Olphen: An Introduction to Clay Colloid Chemistry, 2nd Ed. John Wiley & Sons, New York, London, Sydney, Toronto 1977. 318 Seiten, Preis: £ 15.-, \$ 25.-*. *Berichte der Bunsengesellschaft für physikalische Chemie*, 1978. **82**(2): p. 236-237.

18. *Crystal Structures of Clay Minerals and their X-Ray Identification*, ed. G.W. Brindley and G. Brown 1980. 498.
19. Luckham, P.F. and S. Rossi, *The colloidal and rheological properties of bentonite suspensions*. Advances in Colloid and Interface Science, 1999. **82**(1-3): p. 43-92.
20. Steudel, A. and K. Emmerich, *Strategies for the successful preparation of homoionic smectites*. Applied Clay Science, 2013. **75-76**: p. 13-21.
21. Delavernhe, L., et al., *Influence of mineralogical and morphological properties on the cation exchange behavior of dioctahedral smectites*. Colloids and Surfaces A: Physicochemical and Engineering Aspects, 2015. **481**: p. 591-599.
22. Tombacz, E. and M. Szekeres, *Colloidal behavior of aqueous montmorillonite suspensions: the specific role of pH in the presence of indifferent electrolytes*. Applied Clay Science, 2004. **27**(1-2): p. 75-94.
23. Kazuya, O., S. Shinya, and M. Masaru, *Anisotropy in lithium ion conduction in laminated thin films of montmorillonite nanosheets*. Semiconductor Science and Technology, 2014. **29**(6): p. 064011.
24. Gouy, M., *Sur la constitution de la charge électrique à la surface d'un électrolyte*. J. Phys. Theor. Appl., 1910. **9**(1): p. 457-468.
25. Chapman, D.L., *LI. A contribution to the theory of electrocapillarity*. Philosophical Magazine Series 6, 1913. **25**(148): p. 475-481.
26. Hamaker, H.C., *The London—van der Waals attraction between spherical particles*. Physica, 1937. **4**(10): p. 1058-1072.
27. Sundberg, J., et al., *Modelling of thermal rock mass properties at the potential sites of a Swedish nuclear waste repository*. International Journal of Rock Mechanics and Mining Sciences, 2009. **46**(6): p. 1042-1054.
28. SKB, *Climate and climate-related issues for the safety assessment SR-Can*, in TR-06-232006, Svensk Kärnbränslehantering AB.
29. Norrish, K., *The swelling of montmorillonite*. Discussions of the Faraday Society, 1954. **18**(0): p. 120-134.
30. Delos, A., et al., *Size dispersion and colloid mediated radionuclide transport in a synthetic porous media*. Journal of Colloid and Interface Science, 2008. **324**(1-2): p. 212-215.
31. Posiva, *Buffer Erosion in Dilute Groundwater*, in Posiva 2012-44, K.N. Schatz T., Martikainen J., Sane P., Olin M., Seppälä A. , Editor 2013, Posiva: Oikiluoto.
32. Stumm, W. and J.J. Morgan, *Aquatic chemistry: chemical equilibria and rates in natural waters* 1996: Wiley.
33. Geckeis, H., et al., *Mineral–Water Interface Reactions of Actinides*. Chemical Reviews, 2013. **113**(2): p. 1016-1062.
34. Huber, F.M., *Impact of kinetics and flow path heterogeneity on nanoparticle/radionuclide migration*, 2012: Berlin.
35. Blume, H.P., et al., *Scheffer/Schachtschabel: Lehrbuch der Bodenkunde* 2009: Spektrum Akademischer Verlag.
36. Geckeis, H. and T. Rabung, *Actinide geochemistry: From the molecular level to the real system*. Journal of Contaminant Hydrology, 2008. **102**(3-4): p. 187-195.
37. Yalcintas, E., *Redox, solubility and sorption chemistry of technetium in dilute to concentrated saline systems* 2015.
38. Rard, J.A., et al., *Chemical thermodynamics of technetium* 1999: Elsevier Publishing Company.
39. Bruno J., D.L., Rollin C., Guimerà J., *Prediction of the solubility and speciation of RN in Febex and Grimsel waters*, 2000.
40. H., D., *Oskarshamn site investigation - Detecting the near surface redox front in crystalline rock - Results from drill cores KLX09B-G and KLX11B-F*, in P-08-44, SKB, Editor 2008, Centre University of Gothenburg.

41. Marsac, R., et al., *Neptunium redox speciation at the illite surface*. *Geochimica et Cosmochimica Acta*, 2015. **152**: p. 39-51.
42. Huber, F.M., et al., *Tc interaction with crystalline rock from Äspö (Sweden): Effect of in-situ rock redox capacity*. *Applied Geochemistry*.
43. Wood, W.W., T.F. Kraemer, and P.P. Hearn, *INTRAGRANULAR DIFFUSION - AN IMPORTANT MECHANISM INFLUENCING SOLUTE TRANSPORT IN CLASTIC AQUIFERS*. *Science*, 1990. **247**(4950): p. 1569-1572.
44. Neretnieks, I., *Diffusion in the rock matrix: An important factor in radionuclide retardation?* *Journal of Geophysical Research: Solid Earth*, 1980. **85**(B8): p. 4379-4397.
45. Alonso, U., et al., *Colloid diffusion in crystalline rock: An experimental methodology to measure diffusion coefficients and evaluate colloid size dependence*. *Earth and Planetary Science Letters*, 2007. **259**(3-4): p. 372-383.
46. Yoshino, T., *Electrical Properties of Rocks*, in *Encyclopedia of Solid Earth Geophysics*, H.K. Gupta, Editor 2011, Springer Netherlands: Dordrecht. p. 270-276.
47. Ota, K., et al., *Influence of the mode of matrix porosity determination on matrix diffusion calculations*. *Journal of Contaminant Hydrology*, 2003. **61**(1-4): p. 131-145.
48. Neretnieks Ivars, O.Y., *Diffusion data in granite: recommended values*, in *SKB Technical Report*, SKB, Editor 1997: Stockholm, Sweden.
49. Wickham, S.M., *Evaluation of colloid transport issues and recommendations for SKI performance assessments*, in *SKI-R--00-332000*.
50. Stoll, M., et al., *Impact of gravity, collector surface roughness and fracture orientation on colloid retention kinetics in an artificial fracture*. *Journal of Colloid and Interface Science*, 2016. **475**: p. 171-183.
51. Darbha, G.K., et al., *Site-Specific Retention of Colloids at Rough Rock Surfaces*. *Environmental Science & Technology*, 2012. **46**(17): p. 9378-9387.
52. Missana, T., et al., *Analysis of colloids erosion from the bentonite barrier of a high level radioactive waste repository and implications in safety assessment*. *Physics and Chemistry of the Earth*, 2011. **36**(17-18): p. 1607-1615.
53. Missana, T., U. Alonso, and M.J. Turrero, *Generation and stability of bentonite colloids at the bentonite/granite interface of a deep geological radioactive waste repository*. *Journal of Contaminant Hydrology*, 2003. **61**(1-4): p. 17-31.
54. Madsen, F.T., *Clay mineralogical investigations related to nuclear waste disposal*. *Clay Minerals*, 1998. **33**(1): p. 109-129.
55. Kaufhold, S. and R. Dohnmann, *Detachment of colloidal particles from bentonites in water*. *Applied Clay Science*, 2008. **39**(1-2): p. 50-59.
56. Huertas, F., et al., *Full-scale Engineered Barriers Experiment for a Deep Geological Repository for High-level Radioactive Waste in Crystalline Host Rock (FEBEX Project): Final Report 2000*: Directorate-General for Research.
57. Vilks, P. and M.-H. Baik, *Laboratory migration experiments with radionuclides and natural colloids in a granite fracture*. *Journal of Contaminant Hydrology*, 2001. **47**(2-4): p. 197-210.
58. Baik, M.-H., W.-J. Cho, and P.-S. Hahn, *Erosion of bentonite particles at the interface of a compacted bentonite and a fractured granite*. *Engineering Geology*, 2007. **91**(2-4): p. 229-239.
59. Missana, T., et al., *Role of bentonite colloids on europium and plutonium migration in a granite fracture*. *Applied Geochemistry*, 2008. **23**(6): p. 1484-1497.
60. J., G. and K. G., *The CRR Final Project Report Series III: Results of the Supporting Modelling Programme*, in *Technical Report*, Nagra, Editor 2003, Nagra.
61. Geckeis, H. and T. Missana, *The CRR Final Project Report Series II: Supporting Laboratory Experiments with Radionuclides and Bentonite Colloids*, in *Technical Report*, Nagra, Editor 2003, Nagra.

62. A., M., *The CRR Final Project Report Series I: Description of the Field Phase - Methodologies and Raw Data*, in *Technical Report*, Nagra, Editor 2003.
63. Blechschmidt, I., L. Schlickerieder, and G.W. Lanyon, *CFM Phase 2 - Field Set-up and Field Activities 2008-2009*, in *NAB 10-04*, Nagra, Editor 2010.
64. Blechschmidt, I., et al., *GTS Phase VI - CFM Phase 2: Field Activities mid-2011 to December 2012*, in *Arbeitsbericht NAB 12-11*, Nagra, Editor 2013.
65. Blechschmidt, I., et al., *GTS Phase VI - CFM Phase 2: Field Activities January to December 2013*, in *Arbeitsbericht NAB 13-44*, Nagra, Editor 2014.
66. Huber, F., *Colloid/nanoparticle formation and mobility in the context of deep geological nuclear waste disposal : Project KOLLORADO-2 ; Final Report*, 2014, KIT: Karlsruhe.
67. Huber, F., U. Noseck, and T. Schäfer, *Stability of compacted bentonite for radionuclide retardation – Experiments and modelling*, 2016, KIT: Karlsruhe.
68. Reiche, T., U. Noseck, and T. Schäfer, *Migration of Contaminants in Fractured-Porous Media in the Presence of Colloids: Effects of Kinetic Interactions*. *Transport in Porous Media*, 2016. **111**(1): p. 143-170.
69. M., J., *Bentonite Erosion TR-09-33*, 2009.
70. Moreno, L., L. Liu, and I. Neretnieks, *Erosion of sodium bentonite by flow and colloid diffusion*. *Physics and Chemistry of the Earth*, 2011. **36**(17-18): p. 1600-1606.
71. Kretzschmar, R. and T. Schäfer, *Metal Retention and Transport on Colloidal Particles in the Environment*. *Elements*, 2005. **1**(4): p. 205-210.
72. Missana, T., M. García-Gutiérrez, and Ú. Alonso, *Kinetics and irreversibility of cesium and uranium sorption onto bentonite colloids in a deep granitic environment*. *Applied Clay Science*, 2004. **26**(1–4): p. 137-150.
73. Quinto, F., et al., *Accelerator Mass Spectrometry of Actinides in Ground- and Seawater: An Innovative Method Allowing for the Simultaneous Analysis of U, Np, Pu, Am, and Cm Isotopes below ppq Levels*. *Analytical Chemistry*, 2015. **87**(11): p. 5766-5773.
74. Coplen Tyler, B., et al., *Isotope-abundance variations of selected elements (IUPAC Technical Report)*, in *Pure and Applied Chemistry*2002. p. 1987.
75. Meija, J., et al., *Isotopic compositions of the elements 2013 (IUPAC Technical Report)*, in *Pure and Applied Chemistry*2016. p. 293.
76. Linge, K.L. and K.E. Jarvis, *Quadrupole ICP-MS: Introduction to Instrumentation, Measurement Techniques and Analytical Capabilities*. *Geostandards and Geoanalytical Research*, 2009. **33**(4): p. 445-467.
77. Dawson, P.H., *Quadrupole Mass Spectrometry and Its Applications*2013: Elsevier Science.
78. Feldmann, I., et al., *Performance characteristics of inductively coupled plasma mass spectrometry with high mass resolution*. *Journal of Analytical Atomic Spectrometry*, 1994. **9**(9): p. 1007-1014.
79. Ekman, R., et al., *Mass Spectrometry: Instrumentation, Interpretation, and Applications*2008: Wiley.
80. Thermo-Fisher-Scientific, *Semi-Quantitative Environmental Analysis using the XSERIES 2 ICP-MS (Application Note)*, 2016.
81. Nölte, J., *ICP Emissionsspektrometrie für Praktiker: Grundlagen, Methodenentwicklung, Anwendungsbeispiele*2012: Wiley.
82. Planck, M., *Ueber das Gesetz der Energieverteilung im Normalspectrum*. *Annalen der Physik*, 1901. **309**(3): p. 553-563.
83. Einstein, A., *Zur Quantentheorie der Strahlung*1917.
84. Maiman, T.H., *Stimulated Optical Radiation in Ruby*. *Nature*, 1960. **187**(4736): p. 493-494.
85. Joseph Sneddon, T.L.T., Yong-Il Lee, *Lasers in Analytical Atomic Spectroscopy*1997.

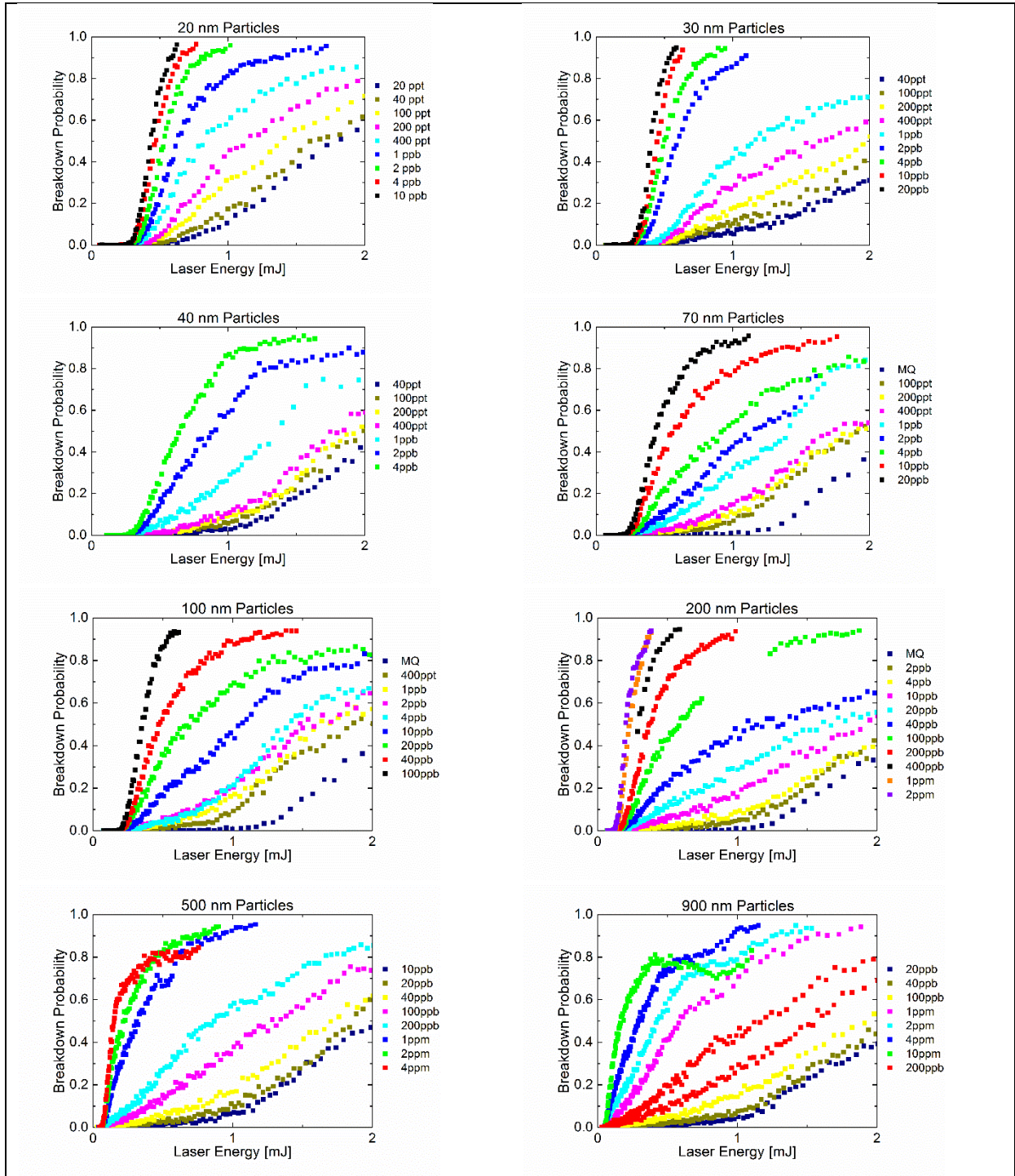
86. Cremers, D.A. and L.J. Radziemski, *LIBS Apparatus Fundamentals*, in *Handbook of Laser-Induced Breakdown Spectroscopy* 2013, John Wiley & Sons Ltd. p. 69-121.
87. Tunes, M.A., C.G. Schön, and N.U. Wetter. *Pulse-to-pulse stability analysis in a frequency-doubled, q-switched Nd: YAG rod-Laser*. in *SPIE NanoScience+ Engineering*. 2013. International Society for Optics and Photonics.
88. Barnes, N.P., et al., *Pulsed 4F3/2 to 4I9/2 operation of Nd lasers*. *Journal of the Optical Society of America B*, 1999. **16**(12): p. 2169-2177.
89. Semwal, K. and S.C. Bhatt, *Study of Nd³⁺ ion as a Dopant in YAG and Glass Laser*. *International Journal of Physics*, 2013. **1**(1): p. 15-21.
90. Maker P. D., T.R.W., *Study of Optical Effects Due to an Induced Polarization Third Order in the Electric Field Strength*. *Physical review*, 1965.
91. Hauser, W., et al., *A mobile laser-induced breakdown detection system and its application for the in situ-monitoring of colloid migration*. *Colloids and Surfaces A: Physicochemical and Engineering Aspects*, 2002. **203**(1–3): p. 37-45.
92. Walther, C., H.R. Cho, and T. Fanghanel, *Measuring multimodal size distributions of aquatic colloids at trace concentrations*. *Applied Physics Letters*, 2004. **85**(26): p. 6329-6331.
93. Scherbaum, F.J., R. Knopp, and J.I. Kim, *Counting of particles in aqueous solutions by laser-induced photoacoustic breakdown detection*. *Applied Physics B*, 1996. **63**(3): p. 299-306.
94. Walther, C. and W. Hauser, *Influence of laser beam characteristics and focusing optics on optical laser-induced breakdown detection*. *Applied Physics B-Lasers and Optics*, 2009. **97**(4): p. 877-886.
95. Latkoczy, C., et al., *Development of a mobile fast-screening laser-induced breakdown detection (LIBD) system for field-based measurements of nanometre sized particles in aqueous solutions*. *Journal of Environmental Monitoring*, 2010. **12**(7): p. 1422-1429.
96. Apted, M.J., et al., *Buffer erosion—An overview of concepts and potential safety consequences*. *SSM Report*, 2010. **31**.
97. Puls, R., *Use of low-flow or passive sampling techniques for sampling ground water.*, U.S.E.P.A, Editor 1993, U.S.E.P.A: Dallas. p. 205.
98. Schäfer T., N.U., *Colloid/Nanoparticle formation and mobility in the context of deep geological nuclear waste disposal (Project KOLLORADO-1; Final Report)*, in *Wissenschaftliche Berichte*, F. Karlsruhe, Editor 2010, INE: Karlsruhe.
99. Nagra, *Grimsel Test Site Investigation Phase V, The CRR Final Report Series II: Supporting laboratory experiments with radionuclides and bentonite colloids*. *Nagra Technical Report NTB 03-02*, T. Missana, et al., Editors. 2006, Nagra: Wettingen, Switzerland. p. 100.
100. Alexander, W.R., K. Ota, and B. Frieg, *The NAGRA-JNC in situ study of safety relevant radionuclide retardation in fractured crystalline rock II: the RRP project methodology development, field and laboratory tests*, 2001, NAGRA: Wettingen, Switzerland
101. Fernandez, A.M.R., P., *Analysis and distribution of waters in the compacted FEBEX bentonite: pore water chemistry and adsorbed water properties*. In: Alonso, E.E., Ledesma, A. (Eds.), *Advances in Understanding Engineered Clay Barriers*, in *Advances in understanding engineered clay barriers* 2005, Taylor and Francis Group: London. p. 257-275.
102. Fernandez, A.M., et al., *Analysis of the porewater chemical composition of a Spanish compacted bentonite used in an engineered barrier*. *Physics and Chemistry of the Earth*, 2004. **29**(1): p. 105-118.
103. Roberson, C.E. and J.D. Hem, *Solubility of aluminum in the presence of hydroxide, fluoride, and sulfate*, in *Water Supply Paper* 1969.
104. Reinholdt, M., et al., *Fluorine Route Synthesis of Montmorillonites Containing Mg or Zn and Characterization by XRD, Thermal Analysis, MAS NMR, and EXAFS Spectroscopy*. *European Journal of Inorganic Chemistry*, 2001. **2001**(11): p. 2831-2841.

105. Reinholdt, M., et al., *Hydrothermal Synthesis and Characterization of Ni-Al Montmorillonite-Like Phyllosilicates*. *Nanomaterials*, 2013. **3**(1): p. 48.
106. Neretnieks, I.L., Liu; Luis, Moreno, *Mechanisms and models for bentonite erosion*, in *Technical Report*, SKB, Editor 2009, Svensk Kärnbränslehantering, Swedish Nuclear Fuel and Waste Management Co: Stockholm.
107. Grenthe, I., et al., *Redox potentials and redox reactions in deep groundwater systems*. *Chemical Geology*, 1992. **98**(1-2): p. 131-150.
108. Guillaumont, R., F.J. Mompean, and O.N.E. Agency, *Update on the Chemical Thermodynamics of Uranium, Neptunium, Plutonium, Americium and Technetium* 2003: Elsevier.
109. Bernhard, G., et al., *Uranyl (VI) carbonate complex formation: Validation of the $\text{Ca}_2\text{UO}_2(\text{CO}_3)_3$ (aq.) species*. *Radiochimica Acta*, 2001. **89**(8): p. 511-518.
110. Endrizzi, F. and L. Rao, *Chemical Speciation of Uranium(VI) in Marine Environments: Complexation of Calcium and Magnesium Ions with $[(\text{UO}_2)(\text{CO}_3)_3]^{4-}$ and the Effect on the Extraction of Uranium from Seawater*. *Chemistry – A European Journal*, 2014. **20**(44): p. 14499-14506.
111. Brooks, S.C., et al., *Inhibition of bacterial U(VI) reduction by calcium*. *Environmental Science & Technology*, 2003. **37**(9): p. 1850-1858.
112. Bondietti, E.A. and C.W. Francis, *Geologic Migration Potentials of Technetium-99 and Neptunium-237*. *Science*, 1979. **203**(4387): p. 1337-1340.
113. Huber, F., et al., *Sorption reversibility kinetics in the ternary system radionuclide-bentonite colloids/nanoparticles-granite fracture filling material*. *Applied Geochemistry*, 2011. **26**(12): p. 2226-2237.
114. Agus, S.S. and T. Schanz, *A method for predicting swelling pressure of compacted bentonites*. *Acta Geotechnica*, 2008. **3**(2): p. 125-137.
115. Fernandez, A.M., J. Cuevas, and P. Rivas. *Pore water chemistry of the FEBEX bentonite*. in *MRS Proceedings*. 2000. Cambridge Univ Press.
116. Schafer, T., et al., *Nanoparticles and their influence on radionuclide mobility in deep geological formations*. *Applied Geochemistry*, 2012. **27**(2): p. 390-403.
117. BELBaR, *Final report on erosion processes under flowing water conditions*, H.M. Hansen E., Schatz T., Cervinka R., Editor 2015.
118. Colombani, J., *Measurement of the pure dissolution rate constant of a mineral in water*. *Geochimica Et Cosmochimica Acta*, 2008. **72**(23): p. 5634-5640.
119. Reichle, R.A., K.G. McCurdy, and L.G. Hepler, *Zinc Hydroxide: Solubility Product and Hydroxy-complex Stability Constants from 12.5–75 °C*. *Canadian Journal of Chemistry*, 1975. **53**(24): p. 3841-3845.
120. Schmeide, K., et al., *Interaction of U(VI) with Äspö diorite: A batch and in situ ATR FT-IR sorption study*. *Applied Geochemistry*, 2014. **49**: p. 116-125.

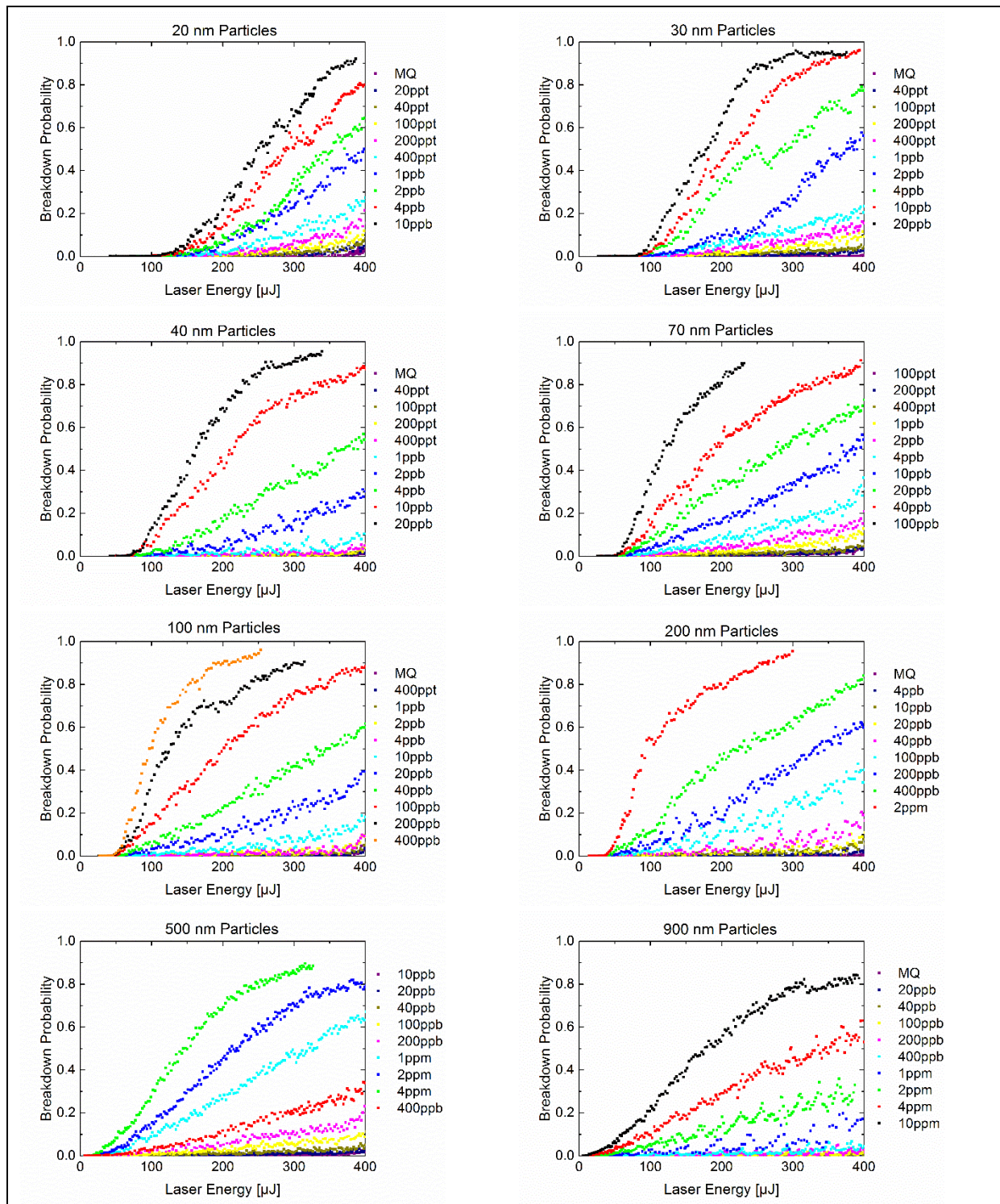




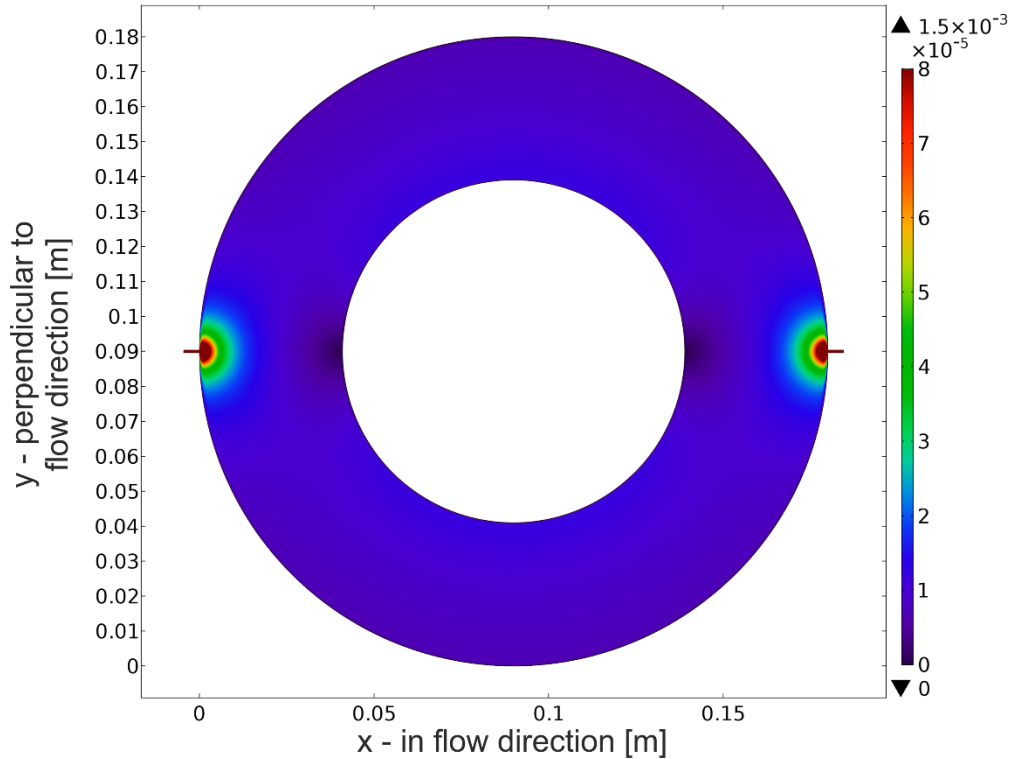
11 Annex



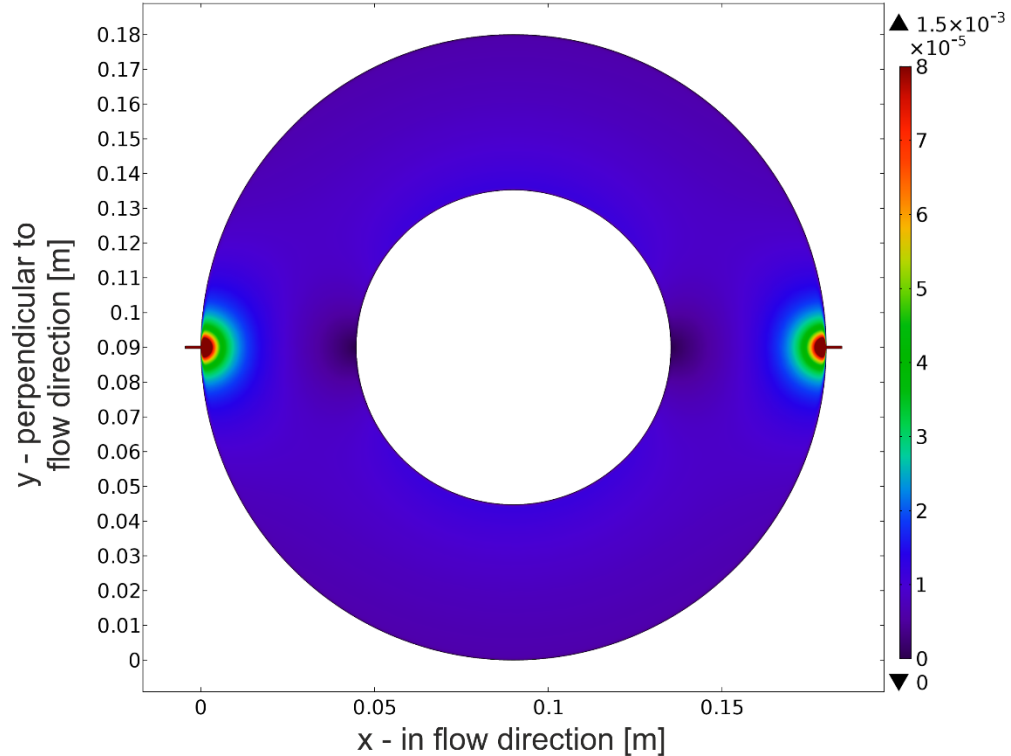
A-Figure 1: Calibration curves for polystyrene particles in different concentrations and particle sizes on the stationary s-curve LIBD.



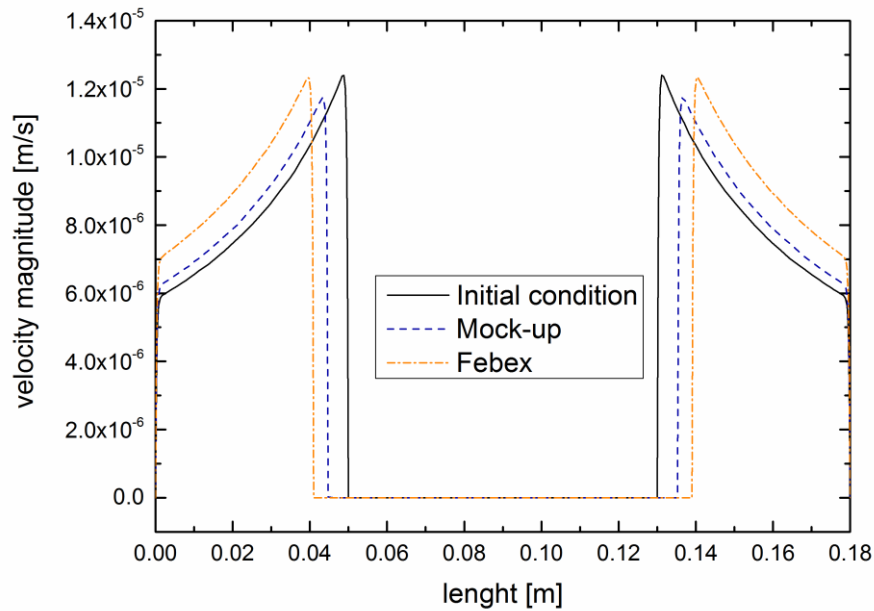
A-Figure 2: Calibration curves for polystyrene particles in different concentrations and particle sizes on the mobile s-curve LIBD.



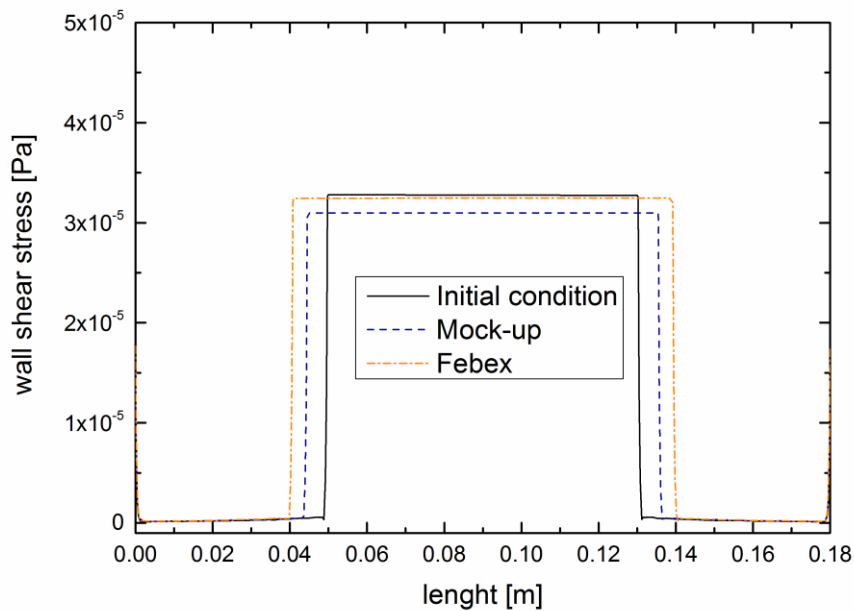
A-Figure 3: Flow velocity distribution in the Febex 1mm artificial fracture erosion experiment calculated with COMSOL Multiphysics for the equilibrium condition after swelling into the fracture.



A-Figure 4: Flow velocity distribution in the LIT mock-up 1mm artificial fracture erosion experiment calculated with COMSOL Multiphysics for the equilibrium condition after swelling into the fracture.



A-Figure 5: Flow velocity distribution of the bentonite erosion experiments in artificial 1mm fracture set-ups calculated with COMSOL Multiqphysics. Flow velocities are given over the maximum cross section perpendicular to the flow direction. The initial condition before swelling (continuous line) and the equilibrium conditions after swelling is shown for the Febex bentonite erosion test (7.2.1, red dotted line) and for the LIT mock-up experiment (0, blue dotted line)



A-Figure 6: Shear stress distribution of the bentonite erosion experiments in artificial 1mm fracture set-ups calculated with COMSOL Multiqphysics. Shear stress values are given over the maximum cross section perpendicular to the flow direction. The initial condition before swelling (continuous line) and the equilibrium conditions after swelling is shown for the Febex bentonite erosion test (7.2.1, red dotted line) and for the LIT mock-up experiment (0, blue dotted line)

A-Table 1: XRF analysis of FG material in different size fractions.

| Component | FG 500-1000µm [%] | FG 250-500µm [%] |
|--------------------------------|-------------------|------------------|
| SiO ₂ | 65,29 | 64,57 |
| Al ₂ O ₃ | 15,82 | 15,66 |
| Fe ₂ O ₃ | 3,76 | 3,87 |
| MnO | 0,07 | 0,07 |
| MgO | 2,37 | 2,42 |
| CaO | 1,55 | 1,71 |
| Na ₂ O | 4,72 | 4,54 |
| K ₂ O | 3,67 | 3,67 |
| TiO ₂ | 0,571 | 0,638 |
| P ₂ O ₅ | 0,16 | 0,16 |
| SO ₃ | 0,01 | 0,011 |
| Cr ₂ O ₃ | 0,001 | 0,0029 |
| NiO | 0,0002 | 0,0007 |
| LOI | 1,07 | 1,04 |
| Sum | 99,06 | 98,37 |

| Trace element | FG, 500-1000µm [ppm] | FG, 250-500µm [ppm] |
|---------------|----------------------|---------------------|
| Ba | 588 | 588 |
| Ce | 111 | 105 |
| Co | 32 | 40 |
| Cr | 16 | 18 |
| Cs | 9 | 7 |
| Cu | 1 | 2 |
| Ga | 20 | 21 |
| Gd | 6 | 6 |
| La | 56 | 55 |
| Nb | 29 | 34 |
| Nd | 49 | 46 |
| Ni | 6 | 5 |
| Pb | 10 | 12 |
| Pr | 12 | 11 |
| Rb | 219 | 215 |
| Sc | 9 | 9 |
| Sm | 13 | 11 |
| Sr | 173 | 179 |
| Th | 18,5 | 27,3 |
| U | 6,1 | 7 |
| V | 35 | 38 |
| W | 512 | 539 |
| Y | 55 | 60 |
| Zn | 65 | 66 |
| Zr | 265 | 285 |

A-Table 2: Input file for Hydra/Medusa calculations of ⁹⁹Tc speciation and predominance diagrams in GGW systems.

```

7, 16, 1, 0 /MEDUSA, t= 25 C, p= 1
H+
e-
TcO4-
F-
Cl-
CO3 2-
SO4 2-
H2CO3      , 16.681 2 0 0 0 0 1 0
HCO3-      , 10.329 1 0 0 0 0 1 0
TcO(OH)2   , 29.43  4 3 1 0 0 0 0
TcO4 2-    , -10.8  0 1 1 0 0 0 0
TcO4 3-    , -20.3  0 2 1 0 0 0 0
H2TcO4     , -1.1   2 1 1 0 0 0 0
HTcO4-     , -2.1   1 1 1 0 0 0 0
TcCO3(OH)2 , 48.68  6 3 1 0 0 1 0
TcCO3(OH)3- , 40.38  5 3 1 0 0 1 0
TcCO3(OH)4-3 , 21.116 4 4 1 0 0 1 0
TcO 2+     , 33.33  6 3 1 0 0 0 0
TcO(OH)+   , 31.93  5 3 1 0 0 0 0
TcO(OH)3-  , 18.53  3 3 1 0 0 0 0
TcO2Cl4 3- , 18.157 4 2 1 0 4 0 0
TcOC14-    , 26.367 6 2 1 0 4 0 0
TcOC15 2-  , 21.068 6 2 1 0 5 0 0
TcO2:1.6H2O(s) , 37.83  4 3 1 0 0 0 0
EH, e-, H+, TcO4-,
LAV, -7.0 -12.0
LAV, 8.451699 -8.451699
T, 1.5E-07
T, 2.4E-04
T, 3.5E-05
T, 5.9E-05
T, 7.1E-05

```

A-Table 3: Input file for Hydra/Medusa calculations of ^{233}U speciation and predominance diagrams in GW systems.

```

9, 49, 1, 0 /MEDUSA, t= 25 C, p= 1
H+
e-
UO2 2+
F-
Cl-
CO3 2-
SO4 2-
Si(OH)4
Ca 2+
H2CO3      , 16.681  2 0 0 0 0 1 0 0 0
HCO3-      , 10.329  1 0 0 0 0 1 0 0 0
U(OH) 3+   , 8.498   3 2 1 0 0 0 0 0 0
CaUO2(CO3)3 2- , 27.00   0 0 1 0 0 3 0 0 1
Ca2UO2(CO3)3(aq) , 30.84   0 0 1 0 0 3 0 0 2
U(OH)4(aq) , -0.962   0 2 1 0 0 0 0 0 0
(UO2)11CO3)6(OH)12-2, 36.42  -12 0 11 0 0 6 0 0 0
(UO2)2(OH)2 2+ , -5.62   -2 0 2 0 0 0 0 0 0
(UO2)2CO3(OH)3- , -0.855  -3 0 2 0 0 1 0 0 0
(UO2)2OH 3+ , -2.7    -1 0 2 0 0 0 0 0 0
(UO2)3(CO3)6 6- , 54.345  0 0 3 0 0 6 0 0 0
(UO2)3(OH)4 2+ , -11.9   -4 0 3 0 0 0 0 0 0
(UO2)3(OH)5+ , -15.55  -5 0 3 0 0 0 0 0 0
(UO2)3(OH)7- , -32.2   -7 0 3 0 0 0 0 0 0
(UO2)3O(OH)2(HCO3)+, 0.655  -3 0 3 0 0 1 0 0 0
(UO2)4(OH)7+ , -21.9   -7 0 4 0 0 0 0 0 0
OH-        , -14.0   -1 0 0 0 0 0 0 0 0
UO2(CO3)2 2- , 16.61   0 0 1 0 0 2 0 0 0
UO2(CO3)3 4- , 21.84   0 0 1 0 0 3 0 0 0
UO2(OH)2(aq) , -12.15  -2 0 1 0 0 0 0 0 0
UO2(OH)3-   , -20.25  -3 0 1 0 0 0 0 0 0
UO2(OH)4 2- , -32.4   -4 0 1 0 0 0 0 0 0
UO2(SO4)2 2- , 4.14    0 0 1 0 0 0 2 0 0
UO2(SO4)3 4- , 3.02    0 0 1 0 0 0 3 0 0
UO2+       , 1.484   0 1 1 0 0 0 0 0 0
UO2Cl+     , 0.17    0 0 1 0 1 0 0 0 0
UO2Cl2     , -1.1    0 0 1 0 2 0 0 0 0
UO2CO3     , 9.94    0 0 1 0 0 1 0 0 0
UO2F+      , 5.16    0 0 1 1 0 0 0 0 0
UO2F2      , 8.83    0 0 1 2 0 0 0 0 0
UO2F3-     , 10.9    0 0 1 3 0 0 0 0 0
UO2F4 2-   , 11.84   0 0 1 4 0 0 0 0 0
UO2HSiO3+  , -1.86   -1 0 1 0 0 0 0 1 0
UO2OH+     , -5.25   -1 0 1 0 0 0 0 0 0
UO2SO4     , 3.15    0 0 1 0 0 0 1 0 0
U(CO3)4 4- , 44.158  4 2 1 0 0 4 0 0 0
U(CO3)5 6- , 43.038  4 2 1 0 0 5 0 0 0
U(OH)4     , -0.962   0 2 1 0 0 0 0 0 0
U(SO4)2    , 19.548  4 2 1 0 0 0 2 0 0
UCl 3+     , 10.758  4 2 1 0 1 0 0 0 0
UF 3+      , 9.4200  4 2 1 1 0 0 0 0 0
UF2 2+     , 16.560  4 2 1 2 0 0 0 0 0
UF3+      , 21.890  4 2 1 3 0 0 0 0 0
UF4       , 26.340  4 2 1 4 0 0 0 0 0

```

UF5- , 27.730 4 2 1 5 0 0 0 0 0
UF6 2- , 29.800 4 2 1 6 0 0 0 0 0
UO2(CO3)3 5- , 8.434 0 1 1 0 0 3 0 0 0
UOH 3+ , 8.498 3 2 1 0 0 0 0 0 0
USO4 2+ , 15.618 4 2 1 0 0 0 1 0 0
UO2(am) , 7.533 0 2 1 0 0 0 0 0 0
UO2 2+, EH, H+,
LAV, -7.0 -12.0
LA, -3.042612
T, 8.2E-08
T, 2.4E-04
T, 3.5E-05
T, 5.9E-05
T, 7.1E-05
T, 1.2E-04
T, 2.0E-04

A-Table 4: Input file for Hydra/Medusa calculations of ^{237}Np speciation and predominance diagrams in GGW systems.

```

7, 28, 1, 0 /MEDUSA, t= 25 C, p= 1
H+
e-
CO3 2-
F-
Cl-
SO4 2-
Np 4+
H2CO3      , 16.681  2 0 1 0 0 0 0
HCO3-      , 10.329  1 0 1 0 0 0 0
Np(CO3)4-4 , 36.68   0 0 4 0 0 0 1
Np(CO3)5-6 , 35.61   0 0 5 0 0 0 1
Np(OH)2 2+ , -2.6    -2 0 0 0 0 0 1
Np(OH)3+   , -5.4    -3 0 0 0 0 0 1
Np(OH)4    , -9.8    -4 0 0 0 0 0 1
Np(OH)5-   , -20.0   -5 0 0 0 0 0 1
Np(SO4)2   , 7.09    0 0 0 0 0 2 1
NpCl 3+    , 1.5     0 0 0 0 1 0 1
NpF 3+     , 8.96    0 0 0 1 0 0 1
NpF2 2+    , 15.7    0 0 0 2 0 0 1
NpO2+      , -10.21  -4 -1 0 0 0 0 1
NpOH 3+    , 0.55    -1 0 0 0 0 0 1
NpSO4 2+   , 4.87    0 0 0 0 0 1 1
OH-        , -14.0   -1 0 0 0 0 0 0
Np(CO3)2-  , 15.995  0 1 2 0 0 0 1
Np(CO3)3-3 , 19.349  0 1 3 0 0 0 1
Np(OH)2+   , -10.405 -2 1 0 0 0 0 1
Np(OH)3    , -22.005 -3 1 0 0 0 0 1
NpO2(CO3)2-3 , -3.676 -4 -1 2 0 0 0 1
NpO2(CO3)2OH-4 , -15.515 -5 -1 2 0 0 0 1
NpO2(CO3)3-5 , -4.71  -4 -1 3 0 0 0 1
NpO2(OH)2- , -33.81  -6 -1 0 0 0 0 1
NpO2CO3-   , -5.25   -4 -1 1 0 0 0 1
NpO2F      , -9.01   -4 -1 0 1 0 0 1
NpO2OH     , -21.51  -5 -1 0 0 0 0 1
NpO2SO4-   , -9.77   -4 -1 0 0 0 1 1
NpO2(am)   , -0.70   -4 0 0 0 0 0 1
EH, e-, H+, Np 4+,
LAV, -7.0 -12.0
LAV, 8.451699 -8.451699
T, 5.9E-05
T, 2.4E-04
T, 3.5E-05
T, 7.1E-05
T, 5.5E-09

```

A-Table 5: Input file for Hydra/Medusa calculations of ^{242}Pu speciation and predominance diagrams in GGW systems.

```

7, 40, 8, 0 /MEDUSA, t= 25 C, p= 1
H+
e-
F-
Cl-
SO4 2-
CO3 2-
Pu 4+
Pu 3+      , 17.69  0 1 0 0 0 0 1
Pu(CO3)4 4-  , 37.0  0 0 0 0 0 4 1
Pu(CO3)5 6-  , 35.65  0 0 0 0 0 5 1
Pu(OH)2 2+   , 0.6   -2 0 0 0 0 0 1
Pu(OH)3+    , -2.3  -3 0 0 0 0 0 1
Pu(OH)4     , -8.5  -4 0 0 0 0 0 1
Pu(SO4)2    , 11.14  0 0 0 0 2 0 1
PuCl 3+     , 1.8   0 0 0 1 0 0 1
PuF 3+      , 8.84  0 0 1 0 0 0 1
PuF2 2+     , 15.7  0 0 2 0 0 0 1
PuO2+      , -17.45 -4 -1 0 0 0 0 1
PuOH 3+    , 0.6   -1 0 0 0 0 0 1
PuSO4 2+   , 6.89  0 0 0 0 1 0 1
Pu(CO3)2-  , 30.09  0 1 0 0 0 2 1
Pu(CO3)3-3  , 33.29  0 1 0 0 0 3 1
Pu(OH)3    , -8.01  -3 1 0 0 0 0 1
Pu(SO4)2-  , 23.39  0 1 0 0 2 0 1
PuCl 2+    , 18.89  0 1 0 1 0 0 1
PuCO3+    , 25.19  0 1 0 0 0 1 1
PuO2 2+   , -33.27 -4 -2 0 0 0 0 1
PuO2(CO3)3 5- , -12.42 -4 -1 0 0 0 3 1
PuO2(OH)2-  , -40.45 -6 -1 0 0 0 0 1
PuO2CO3-   , -12.33 -4 -1 0 0 0 1 1
PuO2OH     , -27.18 -5 -1 0 0 0 0 1
PuOH 2+    , 10.79  -1 1 0 0 0 0 1
PuSO4+    , 21.6   0 1 0 0 1 0 1
(PuO2)2(OH)2 2+ , -74.04 -10 -4 0 0 0 0 2
(PuO2)3(CO3)6 6- , -46.81 -12 -6 0 0 0 6 3
PuO2(CO3)2 2-  , -18.77 -4 -2 0 0 0 2 1
PuO2(CO3)3 4-  , -15.57 -4 -2 0 0 0 3 1
PuO2(OH)2     , -46.47 -6 -2 0 0 0 0 1
PuO2(OH)3-    , -58.27 -7 -2 0 0 0 0 1
PuO2(SO4)2 2- , -28.87 -4 -2 0 0 2 0 1
PuO2Cl+      , -32.57 -4 -2 0 1 0 0 1
PuO2Cl2     , -33.87 -4 -2 0 2 0 0 1
PuO2CO3     , -21.67 -4 -2 0 0 0 1 1
PuO2F+      , -28.71 -4 -2 1 0 0 0 1
PuO2F2      , -26.02 -4 -2 2 0 0 0 1
PuO2OH+    , -38.77 -5 -2 0 0 0 0 1
PuO2SO4    , -29.89 -4 -2 0 0 1 0 1
Pu(OH)3(c)  , 1.89  -3 1 0 0 0 0 1
Pu2(CO3)3(c) , 68.78  0 2 0 0 0 3 2
Pu2O3(cr)   , -15.22 -6 2 0 0 0 0 2
PuCO3OH(c)  , 24.89  -1 1 0 0 0 1 1
PuO2OH(am)  , -22.45 -5 -1 0 0 0 0 1
PuOCl(c)    , 6.290001

```

```

-2 1 0 1 0 0 1
PuO2(OH)2(c) , -38.77 -6 -2 0 0 0 0 1
PuO2CO3(s) , -19.07 -4 -2 0 0 0 1 1
Pu 4+, EH, H+,
LAV, -7.0 -12.0
LA, -2.53551
T, 2.4E-04
T, 3.5E-05
T, 7.1E-05
T, 5.9E-05
T, 6.0E-10

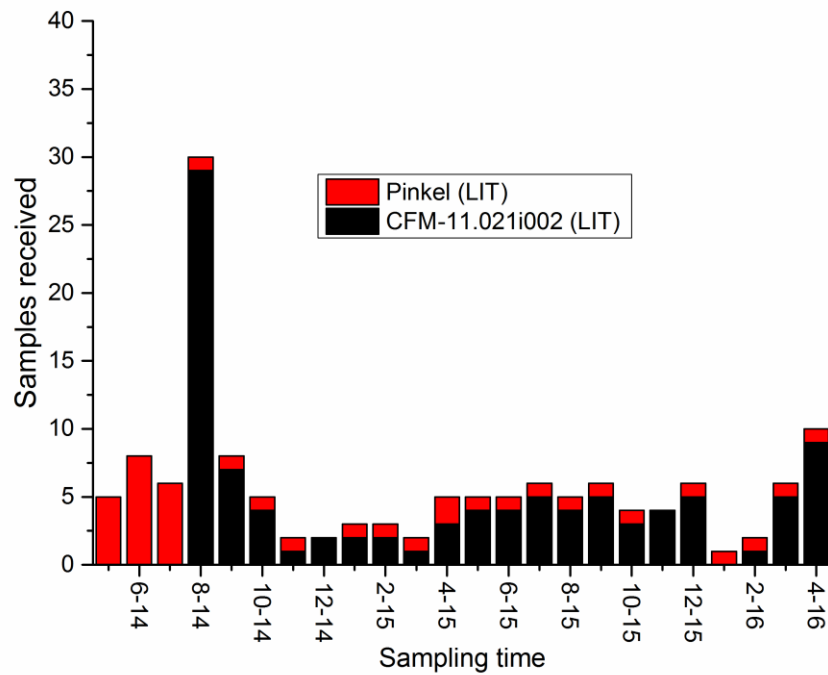
```

A-Table 6: Input file for Hydra/Medusa calculations of ^{243}Am speciation and predominance diagrams

```

7, 19, 1, 0 /MEDUSA, t= 25 C, p= 1
H+
e-
Am 3+
F-
Cl-
CO3 2-
SO4 2-
H2CO3 , 16.681 2 0 0 0 0 1 0
HCO3- , 10.329 1 0 0 0 0 1 0
Am(CO3)2- , 12.9 0 0 1 0 0 2 0
Am(CO3)3 3- , 15.0 0 0 1 0 0 3 0
Am(OH)2+ , -15.1 -2 0 1 0 0 0 0
Am(OH)3 , -26.2 -3 0 1 0 0 0 0
Am(SO4)2- , 3.7 0 0 1 0 0 0 2
AmCl 2+ , 0.24 0 0 1 0 1 0 0
AmCO3+ , 8.0 0 0 1 0 0 1 0
AmF 2+ , 3.4 0 0 1 1 0 0 0
AmF2+ , 5.8 0 0 1 2 0 0 0
AmOH 2+ , -7.2 -1 0 1 0 0 0 0
AmSO4+ , 3.3 0 0 1 0 0 0 1
OH- , -14.0 -1 0 0 0 0 0 0
Am(CO3)5 6- , -4.91 0 -1 1 0 0 5 0
AmO2(CO3)2 3- , -51.231 -4 -2 1 0 0 2 0
AmO2(CO3)3 4- , -65.731 -4 -3 1 0 0 3 0
AmO2(CO3)3 5- , -52.631 -4 -2 1 0 0 3 0
AmO2CO3- , -53.531 -4 -2 1 0 0 1 0
Am(OH)3(am) , -16.9 -3 0 1 0 0 0 0
EH, e-, H+, Am 3+,
LAV, -7.0 -12.0
LAV, 8.451699 -8.451699
T, 4.0E-10
T, 2.4E-04
T, 3.5E-05
T, 5.9E-05
T, 7.1E-05

```



A-Figure 7: Line-up of the LIT samples with extraction point and sampling time for off-site analysis.

A-Table 7: Line-up of the sample transfer from GTS to the laboratory.

| Samples received in | Number of samples from CFM 11.02 | Number of samples from Pinkel extraction point |
|---------------------|----------------------------------|--|
| 08-2014 | 25 | 19 |
| 11-2014 | 15 | - |
| 04-2015 | 9 | - |
| 06-2015 | - | 1 |
| 10-2015 | 25 | - |
| 5-2016 | 24 | 20 |



12 *List of Publications*

Oral presentations:

Friedrich F., Rinderknecht F., Schäfer T., “Update on erosion experiments and characterization of released material” Belbar 2nd Annual Meeting, Meiringen, June 16-18, 2014.

Rinderknecht F., Heck S., Huber F., Friedrich F., Geckeis H., Schäfer T., “Bentonite erosion in advection controlled systems”, BELBaR WP2 and WP4 meeting, Prague, October 30-31, 2014.

Rinderknecht F., Bouby M., Friedrich F., Heck S., Götz R., Huber F., Schäfer T., “Bentonite erosion experiments”, BELBaR 3rd Annual Meeting, Madrid, March 5-6, 2015.

Rinderknecht F., Quinto F., Lagos M., Heck A., Götz R., Huber F., Walschburger C., Schäfer T., “Radionuclide sorption reversibility on natural fracture filling material and different compacted bentonite derived clay nanoparticles” Goldschmidt, Prague, August 16-21, 2015.

Rinderknecht F., Heck S., Götz R., Huber F., Walschburger C., Garcia C., Hippel T., Hilpp S., Geyer F., Geckeis H., Schäfer T., “Erosion experiments: Results from LIT and mock-up tests”, CFM partner meeting, Karlsruhe, June 29-30, 2016.

Rinderknecht F., Quinto F., Lagos M., Heck S., Götz R., Walschburger C., Huber F., Schäfer T., “New results on radionuclide reversibility studies”, CFM partner meeting, Karlsruhe, June 29-30, 2016.

Poster presentations:

Rinderknecht F., Götz R., Huber F., Friedrich F., Delavernhe L., Geckeis H., “Bentonite erosion and colloid mediated transport of radionuclides in advection controlled systems”, MECC, Dresden, September 16-19, 2014.

Rinderknecht F., Bouby M., Friedrich F., Heck, S., Götz R., Huber F., Hilpp S., Geyer F., Geckeis H., Schäfer T., “Bentonite erosion experiments”, BELBaR 3rd Annual Meeting, Madrid, March 5-6, 2015.

Rinderknecht F., Friedrich F., Heck S., Götz R., Huber F., Schäfer T., Geckeis H., “Bentonite erosion in an artificial fracture set-up under near-natural conditions”, Clay colloids in aqueous systems, Berlin, February 3-4, 2016.

Rinderknecht F., Friedrich F., Heck S., Götz R., Huber F., Schäfer T., Geckeis H., “Bentonite erosion and colloid mediated transport of radionuclides in a natural shear zone at the Grimsel test site”, Clay colloids in aqueous systems, Berlin, February 3-4, 2016.

Publications:

Rinderknecht F., Huber F., Heck S., Schenk T., Walschburger C., Geyer F., Schäfer T., “Radionuclide sorption reversibility studies on fracture filling material in presence and absence of bentonite colloids”, in preparation.

Rinderknecht F., Huber F., Heck S., Schäfer T., “Long-term bentonite erosion in an artificial fracture under near-natural advective conditions”, in preparation